

# **Performance Enhancing Strategies For Silk Fibroin Based 3D Biomaterial For Bone Tissue Engineering**

By

**Nimisha Anant Parekh**

**AcSIR Registration Number 10BB17A26048**

A thesis submitted to the  
Academy of Scientific & Innovative Research  
for the award of the degree of  
DOCTOR OF PHILOSOPHY

in

SCIENCE

Under the supervision of  
**Dr. Anuya Nisal**



CSIR-National Chemical Laboratory



Academy of Scientific and Innovative Research  
AcSIR Headquarters, CSIR-HRDC campus  
Sector 19, Kamla Nehru Nagar,  
Ghaziabad, U.P. – 201 002, India

**April 2022**

# Certificate

This is to certify that the work incorporated in this Ph.D. thesis entitled, "Performance Enhancing Strategies For Silk Fibroin Based 3D Biomaterial For Bone Tissue Engineering", submitted by Nimisha Anant Parekh to the Academy of Scientific and Innovative Research (AcSIR) in fulfilment of the requirements for the award of the Degree of DOCTOR OF PHILOSOPHY in SCIENCE, embodies original research work carried-out by the student. We further certify that this work has not been submitted to any other University or Institution in part or full for the award of any degree or diploma. Research material(s) obtained from other source(s) and used in this research work has/have been duly acknowledged in the thesis. Image(s), illustration(s), figure(s), table(s) etc., used in the thesis from other source(s), have also been duly cited and acknowledged.



11<sup>th</sup> April 2022

Nimisha Parekh



11<sup>th</sup> April 2022

Anuya Nisal

## **STATEMENTS OF ACADEMIC INTEGRITY**

I Nimisha Anant Parekh, a Ph.D. student of the Academy of Scientific and Innovative Research (AcSIR) with Registration No. 10BB17A26048 hereby undertake that, the thesis entitled “Performance Enhancing Strategies For Silk Fibroin Based 3D Biomaterial For Bone Tissue Engineering” has been prepared by me and that the document reports original work carried out by me and is free of any plagiarism in compliance with the UGC Regulations on [“Promotion of Academic Integrity and Prevention of Plagiarism in Higher Educational Institutions \(2018\)”](#) and the CSIR Guidelines for *“Ethics in Research and in Governance (2020)”*.



**Signature of the Student**

Date :11<sup>th</sup> April 2021

Place :Pune

---

It is hereby certified that the work done by the student, under my supervision, is plagiarism-free in accordance with the UGC Regulations on [“Promotion of Academic Integrity and Prevention of Plagiarism in Higher Educational Institutions \(2018\)”](#) and the CSIR Guidelines for *“Ethics in Research and in Governance (2020)”*.



**Signature of the Supervisor**

Name :Dr. Anuya Nisal

Date :11<sup>th</sup> April 2022

Place :Pune

*This Dissertation is dedicated  
To  
My Family  
&  
Nutanben Pachchigar*

# Acknowledgements

I would like to take this opportunity to acknowledge the wonderful people, who have directly or indirectly helped me in my Ph.D. journey at CSIR-National Chemical Laboratory.

First and foremost, I want to express my deepest gratitude to my research supervisor Dr. Anuya Nisal for her invaluable guidance, constructive suggestions, countless discussions, and continuous support throughout my doctoral journey. She has been a source of positive energy; whether scientific or non-scientific. I sincerely appreciate her for providing all the time, motivational support, believing in my ability, and thank her for the care and affection that I received for the entire period of my doctoral research. My sincere regards are always due to her wonderful personality.

I would like to thank the Department of Science and Technology – Women Scientist Scheme A (DST-WOS-A), for giving me the award of research grant and fellowship. I am thankful to Dr. Ashish Lele (present Director), Dr. S. Chandrashekar and Prof. Ashwini Nangia, Prof. Sourav Pal (previous Directors), CSIR-National Chemical Laboratory for extending all possible infrastructural facilities to complete my research work.

I would like to extend my thanks to Dr. Venkateswarlu Panchagnula, with whom I did my M.Sc. dissertation. I would like to deeply thank one of the most important people in my professional life, Dr. Sayam Sen Gupta, with whom I started my actual journey towards a Ph.D. It has been a great pleasure to work in his team. Meaningful problem-solving discussions with him always encouraged me to stretch my efforts to fulfill my goal. He provided me with an opportunity to work

with different scientific groups that really nourished my career. I would like to thank Dr. Mugdha Gadgil for allowing me to work in her cell culture lab to conduct my research. I would also like to thank Dr. Guruswamy Kumaraswamy for his support along with Dr. Sayam Sen Gupta to establish a cell culture facility at PSE division. I am thankful to Dr. Asha S. K., Dr. Ashootosh V. Ambade and Dr. B. L. V. Prasad, with whom I worked on collaborative projects. Dr. Prasad is also my DAC member. I am also thankful to my other DAC committee members Dr. Dhanasekaran S. and Dr. Sreekumar Kurungot for their constructive, innovative and motivating suggestions.

I would also take this opportunity to thank the Fulbright commission of India (USIEF) and IIE for providing the Fulbright-Nehru doctoral research fellowship in the field of Bioengineering for the year 2020-2021.

I am thankful to Prof. Sidi Bencherif for believing in me and providing his lab infrastructure at Northeastern University, Boston, USA. My Fulbright work and experience would have not been complete without his guidance and continuous support. I would also like to thank Thibault Colombani, who has made a great contribution to my project work during my stay at Northeastern. Along with it, I would like to thank Khushbu Bhat, Mohammad Hamrangsekachae, Zachary Rogers, Jonathan Kelley, Katelyn Neuman, and Samata Jain for helping me and sharing with me a memorable USA lab experience.

I must say that it's been a great privilege for me to work with Dr. Anuya Nisal and her group. I would like to thank all my labmates, Isha Abhyankar, Swarali Hirlekar, Alaka T Panicker, Bijosh C K, Emmanuel Joseph (current labmates), Kartiki Kane, Vinita Dhaware, Swarali Joshi, Milanta Tom, Hensha Haneefa, Dr Venkat, Abhijit Shete and a team from Serigen Mediproducts Pvt. Ltd. (Raeesa Sayed, Shalmili Salunke, Dr. Rucha Deshpande, Dr. Swati Shukla ) for their helpful and cheerful attitude that made my research experience easy and enjoyable. I personally want

to thank my previous labmates, Basudeb, Munmun, Soumen, Kundan, Santanu, Praveen, Bhawana, Maria, for sharing good memories. I would like to thank Amarnath, Vishwa, Jyoti, Anuja, Reema, Aarti, Poulomi, Deepika, Nivedita, Jayshree, and Meghna for their help and support at NCL.

I offer my sincere regards to people and the teachers who have inspired me and helped me in all the way to my research career.

Last but not the least, the most pious and heartfelt gratitude goes to my life partner Anant. Without his constant support and encouragement, it would have been impossible to walk this journey. I credit him for whatever I am today. I am also deeply thankful to my father Sudhirkumar who supported me to achieve my basic education irrespective of all the difficulties he faced. My sincere thanks to my father-in-law Mr. Bhupendrabhai Parekh, and mother-in-law Jyotiben Parekh for their great understanding, strong support, love, and care. I must say that I am fortunate to have them as a parent in my life. My hats off to my dear children Khushi and Manan for their unconditional love, support, and understanding irrespective of their young age. Their contribution is immense and cannot be stated in words. I also thank all my other family members and friends and my well-wishers for their support.

Last but never least, I thank God for everything.

**Nimisha Anant Parekh**

---

# Synopsis

## **Introduction**

Every year millions of people suffer from tissue/organ loss or failure. Tissue/organ transplantation or use of biodegradable implants are promising solutions for repair or replacement of tissues/organs. The drawback for transplantation is the immunological response from the patient's body. This can be overcome by tissue engineering (TE) and/or regeneration. TE applies the principles of engineering and life sciences towards the development of biological substitutes that help to restore the lost tissues/organs. In tissue engineering, the major challenges have been the development of extracellular matrix (ECM) in a way that it can act as a scaffold to promote new tissue regeneration.

Bone is a highly vascularized tissue with a unique capacity to heal and regenerate without leaving a scar. 40% of women and 13% of men over 50 years old suffer with an osteoporotic fracture in their lifetime. Bone tissue engineering using natural and synthetic bone void fillers is therefore being looked at as a promising strategy for bone repair.

Many synthetic and natural polymeric scaffolds are currently being explored for bone tissue engineering (BTE). Natural polymeric scaffolds are favored due to their biocompatibility and versatility in supporting various biological functions. In the past two decades, Silk Fibroin (SF) has evolved as a promising biomaterial for tissue engineering and biomedical implant applications. It is naturally derived, biocompatible, biodegradable material and has excellent thermo-mechanical properties. SF can be easily chemically modified to obtain required functionality and can be processed into a variety of different forms using aqueous processing



---

techniques. Several studies have successfully demonstrated use of SF scaffolds for vascular, neural, bone, ligament, cartilage, skin, intervertebral disc, heart, ocular and spinal cord tissue regeneration. The silk from the *B.mori* silkworm, more commonly known as mulberry silkworm, can be produced with controlled quality in large commercial quantities. On the other hand, non-mulberry silk mostly from *A.mylitta* has also been in focus for bone tissue engineering (BTE) because of its hydrophilic nature, high mechanical strength and the inherent presence of cell binding motifs (e.g., RGD).

Different forms of SF based biomaterials for BTE includes SF-film, SF-hydrogels, SF- microparticle based 3D scaffold and SF-sponges. Thus, it is an objective of this thesis to further enhance the strategies for use of SF in BTE applications.

## **2. Statement of Problem**

The primary challenge in BTE includes development of three-dimensional (3D) scaffolds, which can also promote cell adhesion, proliferation, differentiation, resulting in superior healing of bone defects. Thus, the success of the regenerative process depends on the understanding of the interaction between the cells and the biomaterials used for scaffolds. Several biomaterials have been reported for BTE but none of them match the performance of an autograft.

SF is mainly produced by silkworms of the order Lepidoptera and different species of class Arachnida (spiders). Silkworm silks are the preferred materials and they are classified into mulberry (domestic) and non-mulberry (wild) varieties. Mulberry silk of silkworm *Bombyx mori* (BM) has been extensively explored and used for centuries in textiles and also sutures. For the last few decades BM has been extensively explored for biomedical applications. In the mulberry based SF scaffold system, in spite of the various developments there is scope for further improvement in scaffold formulations. Non-mulberry silk has established itself as a textile commodity. However, its transformation into a

---

biomaterial is a relatively new and exciting field as non-mulberry silk has an inherent RGD motif, which helps cell attachment, cell proliferation and differentiation. However, non-mulberry silk contains higher alanine content that results in a material with highly compacted beta sheets. This crystallinity prevents dissolution of the silk into any conventional solvents and hence limits the ability to process non-mulberry silk into various scaffolds. Therefore, the majority of reported literature of non-mulberry silk prefer extraction of silk directly from the silk gland of the non-mulberry silkworm. Processing from fibres/cocoons is challenging and also suffers with poor yield.

Biocompatibility of a biomaterial is also assessed by studying immune responses generated upon the interaction. Innate immunity is the non-specific first line of defense and includes a variety of cellular and molecular components, which initiate immune recognition and respond to foreign materials. On the other hand, adaptive immunity is triggered over a longer time period and responds with a high degree of specificity and the generation of memory. However, both these pathways are highly interconnected and these are the primary reasons why biomaterial transplant rejection is a major concern in healthcare. Hence there is a strong need to develop strategies to prevent attack from the immune system.

As a general rule for tissue engineering, scaffolds should be fabricated from materials that do not have the potential to elicit immunological or clinically detectable primary or secondary foreign body reactions in parallel to the formation of new tissue *in vivo*.

Thus, it is an objective of this thesis to develop strategies to further improve the performance of silk fibroin based biomaterials in bone tissue engineering. It is also an objective to develop innovative processing protocols to prepare non-mulberry silk scaffolds. Further, various *in-vitro* and *in vivo* studies have been done to study the immunological potential of these materials.

---

### 3. Objectives

This thesis aims to design different strategies to develop and modify 3D silk fibroin (both mulberry and non-mulberry silk) based biomaterials towards new bone tissue regeneration. Newly developed biomaterial was fully characterized physically and chemically by using various techniques like SEM, FTIR, TGA, contact angle, etc. The mechanical properties of the scaffold such as compression modulus and Young's modulus were also measured. Further, the *in-vitro* enzymatic degradation of the scaffolds was also studied. The biological properties of the scaffolds were evaluated by studying cell viability, cell proliferation and cell morphology. Finally, the developed scaffolds were assessed for their potential to differentiate primary cells or hMSCs into an osteogenic lineage (new bone formation cells) by measuring the differentiating markers (ALP, OCN, BMP-2, calcium mineralization) and their immunological response was also studied.

Specific strategies are mentioned below.

**Strategy 1** Surface coating with biopolymers on silk fibroin 3D microparticles based scaffold

**Strategy 2** Incorporation of bio-ceramics into silk fibroin 3D microparticles based scaffold

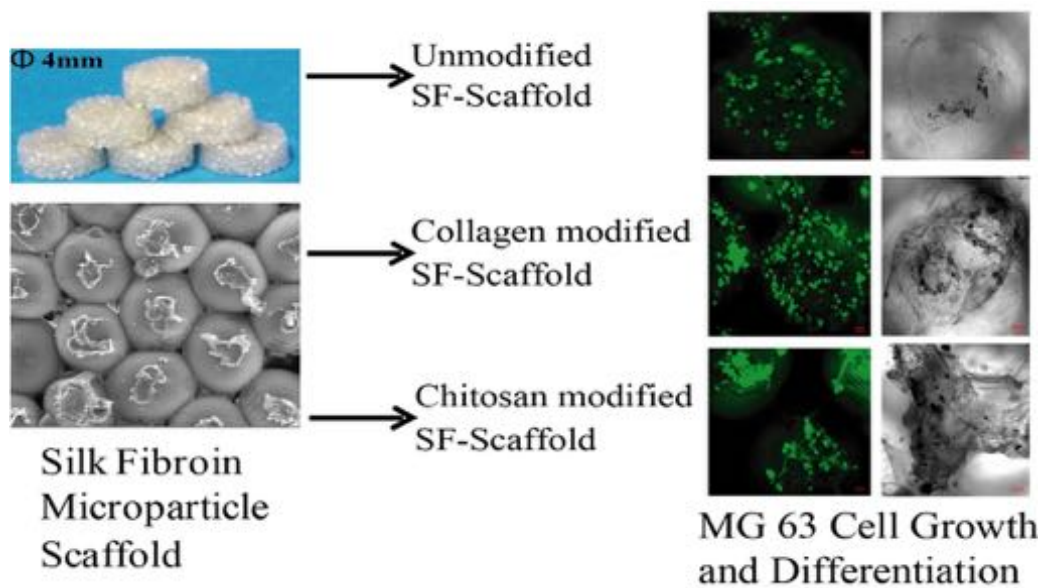
**Strategy 3** Novel processability of non-mulberry silk fiber: electrospun scaffold for bone tissue regeneration

**Strategy 4** Development of mulberry and non-mulberry silk fibroin based injectable cryogel

### 4. Methodology

**Strategy 1** *In-vitro* study of novel microparticle based silk fibroin scaffold with osteoblast-like cells for load-bearing osteo-regenerative applications

Silk Fibroin (SF) is today considered to be one of the most favorable materials for bone tissue engineering. SF microparticle based 3D scaffolds have appropriate pore size, pore interconnectivity and porosity, excellent mechanical properties and tunable bioresorption, while retaining the inherent biocompatibility of SF. These properties make them ideal candidates for osteoregenerative applications. This work reports the *in-vitro* cell viability, cell adhesion and proliferation with osteoblastic differentiation of MG 63 osteoblast-like cell line on these scaffolds. In addition, the surface of these scaffolds was also modified using collagen type I and chitosan biopolymers. The results show that although the SF scaffold does support *in-vitro* cell attachment, proliferation and differentiation, this performance can be further enhanced using the surface coating approach. Also, the ALP activity and bone mineralization was found to be particularly superior in the chitosan-modified scaffolds.

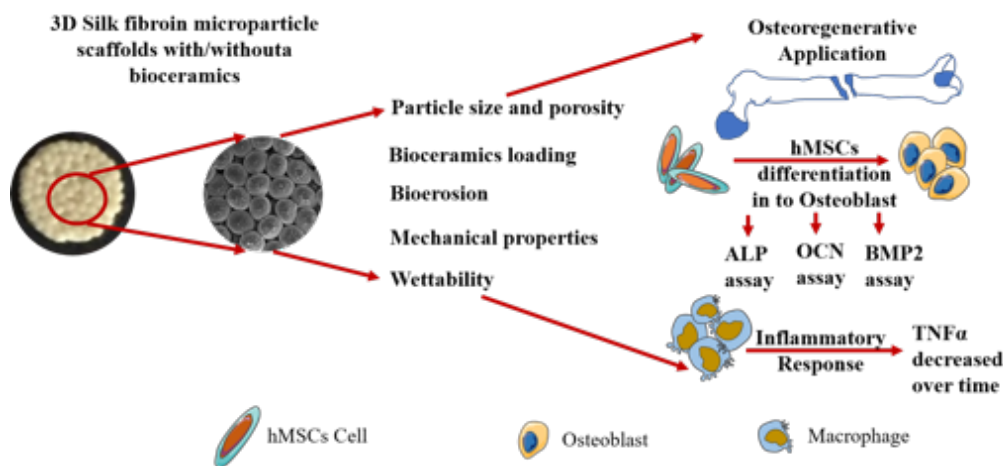


**Strategy 2 Silk Fibroin 3D Microparticle Scaffolds with Bioactive Ceramics: Chemical, Mechanical, and Osteoregenerative Characteristics**

Preparation of 3D scaffolds for bone tissue engineering (BTE) is a challenging task as it requires appropriate pore size and porosities, mechanical properties, and

controlled bioerosion rate. This study demonstrates the fabrication of silk fibroin (SF) 3D microparticle scaffolds with the incorporation of hydroxyapatite (HA) and calcium sulfate (CaS) as bioceramics.

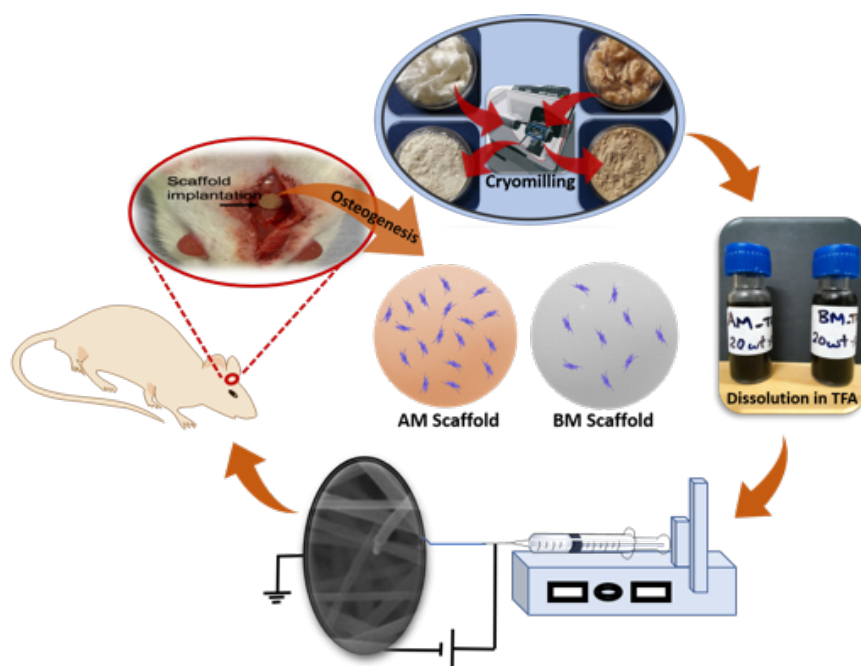
Physicochemical characterization shows 30% filler loading and 40% optimum porosity with  $>100\mu\text{m}$  pore size for these filled/unfilled scaffolds. Nanoindentation studies show improved Young's modulus at microparticle level with the incorporation of bioceramics. SF-HA scaffolds showed three-fold increase in Young's modulus, whereas SF-CaS showed two fold increase. *In-vitro* bioerosion study results in early bioerosion with SF-CaS scaffold, whereas prolonged bioerosion with SF-HA scaffold. *In-vitro* osteoregenerative potential is analyzed by estimating alkaline phosphatase (ALP), bone morphogenic protein-2 (BMP-2), and osteocalcin (OCN). SF-CaS supports early stage differentiation while SF-HA predominantly supports late stage. The expression of TNF- $\alpha$  suggests a reduced risk of immune rejection. This work, therefore, concludes that although SF supports bone tissue regeneration, the choice of bioceramic enhances the applicability in various clinical scenarios by providing a controlled bioerosion rate, tunable speed of osteo-regeneration, and improved load bearing capacities.



---

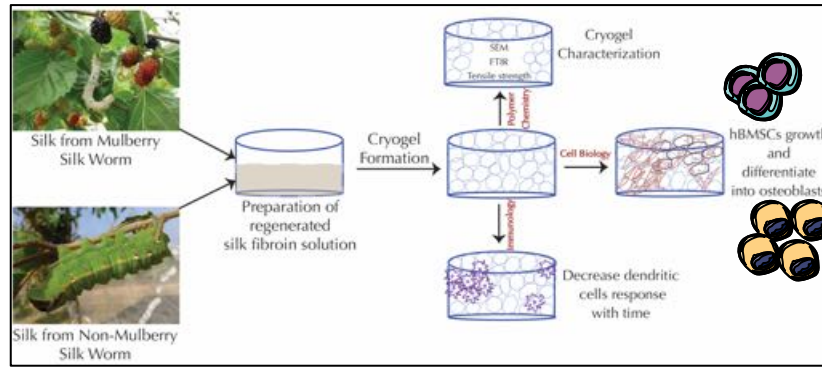
### **Strategy 3 Novel processability of non-mulberry silk fiber: electrospun scaffold for *in-vitro* and *in-vivo* bone tissue regeneration**

The dissolution of non-mulberry silk fiber is an arduous task in silk fibroin-based tissue engineering. In this study, to address this challenge, a unique protocol to process the *Antheraea mylitta* (AM) silk fiber was developed. The protocol enabled the preparation of a concentrated solution by combining cryomilling technique and its dissolution in trifluoroacetic acid (TFA). Electrospinning technique was used to prepare 3D scaffolds from 20 wt % silk fibroin solution. As a control, *Bombyx mori* (BM) silk was used. The secondary structure, solubility and surface morphology of both AM and BM were physico-chemically characterized. Results after cryo-milling techniques revealed reduction in beta sheet content of silk fibroin, which helped to enhance solubility. Methanol vapor annealing further brings the beta sheet content similar to its original level and maintains correct mechanical strength of natural silk fiber. *In-vitro* L929 cell growth and MG-63 cell adhesion data confirmed the enhanced cell attachment and growth in AM scaffold as compared to BM. hMSCs differentiation into osteogenic lineage was evaluated *in-vitro* by measuring the expression of ALP, BMP-2 and OCN. Results from the *in-vitro* study revealed enhanced osteogenic markers secretion at 28th day in AM scaffold. Finally, osteogenic potential of both AM and BM scaffold were evaluated by 4-week implantation study in rat calvarial defect. Histological evaluation of the sections stained with H&E and masson trichrome supports the *in-vitro* results and showed enhanced osteogenic potential of AM scaffolds.



#### **Strategy 4 Development of mulberry and non-mulberry silk fibroin based injectable cryogel**

This work demonstrates that chemical modification of silk fibroin with GMA (SFGMA) results in higher crosslinking sites on silk fibroin, which help to formulate injectable and highly compressible cryogels at subzero temperature with the initiator system of Tetramethylethylenediamine (TEMED) and Ammonium persulfate (APS). Addition of non-mulberry cryomilled microfibers (NMS) into mulberry silk based cryogel further enhanced the physical properties and biological performance of these cryogels. The SFGMA cryogels helped hMSCs to differentiate into osteogenic lineage. However, addition of NMS provides RGD motif and enhances osteogenic differentiation. *In-vitro* primary dendritic cells activation studies (CD86+, CD137+ and MHCII+ cell markers) reveals that all SFGMA and modified cryogels are not pro-inflammatory and SFGMA with NMS showed anti-inflammatory effect. Overall, methacrylated silk fibroin based cryogels would be a good candidate for bone tissue engineering applications and could also be explored for soft tissue engineering applications.



## 5. Summary

This thesis reports the different strategies to improve the chemical, physical and biological performance of 3D silk fibroin based biomaterial for new bone tissue engineering applications. The first strategy (1A) shows that *in-vitro* cell behavior of osteoblast-like cells (MG 63) on novel SF microparticle scaffolds for applications in load-bearing osteo-regenerative applications can be improved by a simple coating method by using collagen type I and chitosan biopolymers. The next strategy, focussed on enhancing the mechanical properties of SF micro-particle scaffolds by incorporating bio-ceramics viz calcium sulphate and hydroxyapatite. Mixing these ceramics into SF provides an opportunity to tune degradation rate of SF and also control the rate of osteo-regeneration process. The third strategy was focused on the non-mulberry silk fibroin (*A. mylitta*) processing technique to obtain a concentrated solution that was fabricated into a 3D scaffold by electrospinning technique. Evaluation of osteogenic potential revealed more cell attachment, growth and differentiation of stem cell with non-mulberry silk scaffold with respect to mulberry silk based scaffold both *in-vitro* and *in-vivo* in rat calvarial defect. To explore the advantage of both mulberry and non-mulberry silk fibroin, we also developed injectable cryogels in the last strategy. Functionalization of mulberry silk with methacrylate helped in the cryopolymerization. Incorporation of non-mulberry silk and Acrl-PEG-RGD significantly enhanced mechanical strength and osteogenic potential *in-vitro*. *In-vitro* activation study with BMDCs also confirmed the biocompatibility with all



---

developed cryogels while anti-inflammatory effect was observed with incorporation of non-mulberry silk and Acrl-PEG-RGD.

## 6. Future directions

Recent advances in the development of scaffold based drug delivery systems have been viewed as potential alternatives, due to sustained drug release at targeted sites. Ideally, augmentation of osteoporotic fractures with osteoconductive bone grafts reduces the occurrence of secondary fracture by releasing the incorporated drug and also provides a scaffold for ingrowth of new bone at the bone defected site. In the last two decades, there have been several reports on the use of silk fibroin as a biomaterial generated for tissue engineering applications. The chemical and biological properties of silk fibroin provide an advantage to modulate its design as per the required application.

SF can be used as a vehicle for the delivery of alendronate drug. The unique mechanical property, non-cytotoxic nature, and ability of SF can support the differentiation of mesenchymal stem cells along the osteogenic lineage and help in faster new bone formation and release of alendronate drug helps to treat osteoporosis. Thus, proposed SF-alendronate combination provides a dual advantage as a treatment for osteoporosis and as a platform for new bone tissue regeneration.

## 7. Publications

### International Journal Publications

1. **Nimisha Parekh\***, Chandani Hushye, Saniya Warunkar, Sayam Sen Gupta and Anuya Nisal\*, *In-vitro* study of novel microparticle based Silk Fibroin scaffold with osteoblast-like cells for load-bearing osteo-regenerative applications, RSC Advances, 2017, 7, 26551 – 26558.
2. **Nimisha Parekh\***, Rucha V. Deshpande, Swati G. Shukla, and Anuya A. Nisal\*, "Silk Fibroin 3D Microparticle Scaffolds with Bioactive Ceramics:

---

Chemical, Mechanical, and Osteoregenerative Characteristics”, Adv. Eng. Mater. 2020, DOI: 10.1002/adem.202000458

3. Novel processability of non-mulberry silk fiber: electrospun scaffold for *in-vitro* and in-vivo bone tissue regeneration (**Manuscript under review, International Journal of Biological Macromolecules**)
4. Mulberry and non-mulberry silk based injectable cryogel (**Manuscript under preparation**)

---

# Content

DEDICATION.....	ii
CERTIFICATE.....	iii
STATEMENTS OF ACADEMIC INTEGRITY.....	iv
ACKNOWLEDGEMENTS.....	v
SYNOPSIS.....	viii
TABLE OF CONTENTS.....	xxi
LIST OF FIGURES.....	xxvi
LIST OF TABLES.....	xxxvi
LIST OF ACRONYMS.....	xxxvii

---

## Table of Contents

### Table of Contents

<b>Chapter 1 Introduction .....</b>	<b>1</b>
<b>1.1 Introduction.....</b>	<b>1</b>
<b>1.2 Motivation and Objectives .....</b>	<b>2</b>
<b>1.3 Organization of Thesis .....</b>	<b>3</b>
<b>1.4 References .....</b>	<b>6</b>
<b>Chapter 2 Literature Review.....</b>	<b>11</b>
<b>2.1 Bone biology and tissue engineering.....</b>	<b>11</b>
2.1.1 Bone as a Tissue .....	11
2.1.2 Tissue Engineering.....	14
2.1.3 Bone Tissue Engineering.....	15
2.1.4 Bone grafts substitute and it's limitations.....	19
<b>2.2 Introduction to Silk .....</b>	<b>20</b>
2.2.1 Silk as a Protein .....	20
2.2.2 Silk Fibroin in Tissue Engineering.....	22
2.2.3 Silk Fibroin in Bone Tissue Engineering .....	25
<b>2.3 Motivation and Objective of Present Work.....</b>	<b>28</b>
<b>2.4 Reference: .....</b>	<b>29</b>
<b>Chapter 3 Surface coating with biopolymers on silk fibroin micro-particle based scaffold 41</b>	
<b>3.1 Abstract .....</b>	<b>42</b>
<b>3.2 Literature Review .....</b>	<b>42</b>

---

<b>3.3</b>	<b>Experimental Section – Materials and Methods .....</b>	<b>46</b>
3.3.1	SF-scaffold preparation.....	46
3.3.2	Surface modification.....	47
3.3.3	Surface characterisation by scanning electron microscopy.....	48
3.3.4	Cell culture .....	48
3.3.5	Cell viability .....	48
3.3.6	Cell adhesion and proliferation.....	49
3.3.7	Cell morphology by actin cytoskeleton staining .....	49
3.3.8	Osteogenic differentiation by ALP Assay.....	50
3.3.9	Extracellular mineral(Ca <sup>2+</sup> ) deposition and quantification.....	51
<b>3.4</b>	<b>Results and Discussion.....</b>	<b>52</b>
3.4.1	Cell viability and proliferation studies.....	54
3.4.2	Osteogenic differentiation .....	59
<b>3.5</b>	<b>Conclusions.....</b>	<b>63</b>
<b>3.6</b>	<b>References .....</b>	<b>64</b>
<b>Chapter 4 Incorporation of bio-ceramics into silk fibroin 3D microparticles based scaffold 72</b>		
<b>4.1</b>	<b>Abstract .....</b>	<b>73</b>
<b>4.2</b>	<b>Literature Review .....</b>	<b>74</b>
<b>4.3</b>	<b>Experimental Section – Materials and Methods .....</b>	<b>75</b>
4.3.1	Preparation of silk fibroin microparticles and scaffolds .....	76
4.3.2	Particle size determination .....	77
4.3.3	Confirmation of secondary structure in SF and presence of bioceramics 77	
4.3.4	Surface morphology and elemental analysis.....	77
4.3.5	Thermogravimetric Analysis (TGA).....	78
4.3.6	Mechanical properties of microparticles .....	78

---

---

4.3.7	Mechanical properties of 3D scaffolds.....	78
4.3.8	Surface wettability of 3D scaffolds.....	79
4.3.9	Bioerosion in proteolytic environment .....	79
4.3.10	<i>In-vitro</i> cytotoxicity (MTT assay) assay:.....	79
4.3.11	Quantitative hMSCs proliferation (Picogreen dsDNA Assay) .....	79
4.3.12	Cell morphology by actin cytoskeleton staining .....	80
4.3.13	Osteoblast differentiation on SF, SF-HA and SF-CaS scaffolds .....	81
4.3.14	Detection of inflammatory response .....	83
4.3.15	Statistical Analysis. ....	83
<b>4.4</b>	<b>Results .....</b>	<b>84</b>
4.4.1	Preparation of microparticles and 3D scaffolds .....	84
4.4.2	Particle size determination .....	84
4.4.3	Confirmation of secondary structure in SF and in presence of bioceramics .....	86
4.4.4	Surface morphology and elemental analysis.....	87
4.4.5	Thermogravimetric analysis (TGA) .....	90
4.4.6	Mechanical Properties of microparticles.....	92
4.4.7	Mechanical properties of 3D scaffolds.....	92
4.4.8	Surface wettability of 3D scaffolds.....	93
4.4.9	Bioerosion in proteolytic environment .....	94
4.4.10	<i>In-vitro</i> cytotoxicity (MTT assay) assay.....	95
4.4.11	Quantitative hMSCs proliferation (Picogreen dsDNA Assay) .....	96
4.4.12	Actin cytoskeleton staining.....	97
4.4.13	Detection of osteoblast differentiation markers.....	98
4.4.14	Detection of Inflammatory response .....	100
<b>4.5</b>	<b>Discussion .....</b>	<b>100</b>
<b>4.6</b>	<b>Conclusions.....</b>	<b>105</b>
<b>4.7</b>	<b>References .....</b>	<b>106</b>

---

<b>Chapter 5</b>	<b><i>Development of non-mulberry electrospun scaffold</i></b>	<b>112</b>
<b>5.1</b>	<b>Abstract</b>	<b>113</b>
<b>5.2</b>	<b>Literature Review</b>	<b>114</b>
<b>5.3</b>	<b>Experimental Section – Materials and Methods</b>	<b>115</b>
5.3.1	Materials	115
5.3.2	Degumming of silk	116
5.3.3	Cryomilling of AM and BM fiber, dissolution and its characterization..	116
1.		116
5.3.4	AM and BM dissolution	117
5.3.5	FTIR analysis	117
5.3.6	XRD analysis	118
5.3.7	Preparation of scaffolds	118
5.3.8	Electron microscopy analysis	118
5.3.9	<i>In-vitro</i> cytotoxicity (MTT assay) assay:	119
5.3.10	<i>In-vitro</i> cell adhesion (seeding) assay	119
5.3.11	hMSCs proliferation assay (Alamar Blue Assay)	119
5.3.12	hMSCs differentiation into osteogenic lineage	120
5.3.13	Detection of extracellular calcium deposition	122
5.3.14	<i>In- vitro</i> inflammatory response (TNF- $\alpha$ )	123
5.3.15	Rat calvarial defect model for <i>in vivo</i> new bone regeneration	124
5.3.16	Histopathology	125
5.3.17	Statistical analysis	125
<b>5.4</b>	<b>Results</b>	<b>126</b>
5.4.1	Cryomilling of AM and BM fiber, dissolution and its characterization..	126
5.4.2	<i>In-vitro</i> cytotoxicity assay	133
5.4.3	<i>In-vitro</i> cell adhesion assay	134
5.4.4	hMSCs proliferation assay (Alamar Blue Assay)	135
5.4.5	hMSCs differentiation into osteogenic lineage	136

---

5.4.6	<i>In-vitro</i> inflammatory response (TNF- $\alpha$ ).....	138
5.4.7	Rat calvarial defect model for <i>in-vivo</i> new bone regeneration.....	139
<b>5.5</b>	<b>Discussion .....</b>	<b>141</b>
<b>5.6</b>	<b>Conclusions.....</b>	<b>145</b>
<b>5.7</b>	<b>References .....</b>	<b>145</b>
<b>Chapter 6</b>	<b><i>Development of mulberry and non-mulberry silk fibroin-based injectable scaffold .....</i></b>	<b>152</b>
<b>6.1</b>	<b>Abstract .....</b>	<b>153</b>
<b>6.2</b>	<b>Literature Review .....</b>	<b>154</b>
<b>6.3</b>	<b>Experimental Section – Materials and Methods .....</b>	<b>157</b>
6.3.1	Materials .....	157
6.3.2	Synthesis of methacrylated silk fibroin (SFMA) .....	158
6.3.3	Chemical Characterization of SFMA.....	158
6.3.4	Cryomilling of non-mulberry silk fiber (NMS).....	159
6.3.5	Preparation of SFMA and SFMA with NMS/MPA/APR Cryogels .....	160
6.3.6	Injectability Test .....	160
6.3.7	Physical Characterization of Cryogels .....	160
6.3.8	<i>In-vitro</i> cell adhesion efficiency .....	162
6.3.9	<i>In-vitro</i> cell viability and cytoskeleton staining .....	162
6.3.10	hMSCs proliferation assay and cytoskeleton staining .....	163
6.3.11	hMSCs differentiation into osteogenic lineage .....	164
6.3.12	Generation of BMDCs and <i>in vitro</i> dendritic cell (DC) activation assay.	165
6.3.13	<i>In-vivo</i> biocompatibility assessment .....	166
6.3.14	Statistical analysis.....	166
<b>6.4</b>	<b>Results .....</b>	<b>167</b>
6.4.1	Synthesis and characterization of SFMA .....	167
6.4.2	Preparation of SFMA-based Cryogels.....	172



---

6.4.3	Physical Characterization of SFMA-based Cryogels .....	173
6.4.4	<i>In-vitro</i> cell adhesion efficiency .....	177
6.4.5	<i>In-vitro</i> HDF cell viability and cytoskeleton staining .....	177
6.4.6	hMSCs proliferation assay and cytoskeleton staining .....	179
6.4.7	hMSCs differentiation into osteogenic lineage .....	180
6.4.8	<i>In-vitro</i> bone marrow-derived dendritic cells (BMDCs) activation assay 182	
6.4.9	<i>In-vivo</i> biocompatibility assessment .....	183
<b>6.5</b>	<b>Discussion .....</b>	<b>185</b>
<b>6.6</b>	<b>Conclusions.....</b>	<b>187</b>
<b>6.7</b>	<b>References .....</b>	<b>188</b>
<b>Chapter 7</b>	<b><i>Conclusions and Future Work .....</i></b>	<b>196</b>
<b>7.1</b>	<b>Summary and Conclusions.....</b>	<b>196</b>
<b>7.2</b>	<b>Scope of Future Work .....</b>	<b>199</b>
7.2.1	Formation of SF scaffold with/without Alendronate drug.....	201
7.2.2	Primary cell culture study .....	202
7.2.3	Future advance study .....	203
<b>7.3</b>	<b>References .....</b>	<b>203</b>

---

## List of Figures

<b>Figure 2-1</b> Hierarchical structure of bone tissue from macro to nanoscale. Reproduce with the permission from Elsevier	12
<b>Figure 2-2</b> Bone Tissue with different types of cells	13
<b>Figure 2-3</b> Schematic representation of sail from a stem cell to mature osteoblast and markers expressed at each stage of differentiation <sup>10</sup>	13
<b>Figure 2-4</b> Schematic representation of different types of 3D scaffolds for various tissue engineering applications. <sup>13</sup>	15
<b>Figure 2-5</b> Market research report for bone surgeries <sup>16</sup>	16
<b>Figure 2-6</b> Different types of biomaterials for BTE	17
<b>Figure 2-7</b> Different methods used for the fabrication of bone grafts. A) solvent casting, B) thermally induced phase separation, C) sol-gel method, D) microsphere sintering method, E) electrospinning technique and F) pore generation by particulate leaching/emulsification freeze-drying/gas foaming methods. <sup>2</sup>	18
<b>Figure 2-8</b> Biomaterials used for scaffold fabrication in BTE <sup>22</sup>	19
<b>Figure 2-9</b> Hydrophilic (Silk I) and Hydrophobic (Silk II) components of Silk Fibroin	22
<b>Figure 2-10</b> Year wise Silk production	24
<b>Figure 2-11</b> Different biophysical Properties of SF as a biomaterial to support cell- material interaction	24
<b>Figure 2-12</b> Different biophysical properties of mulberry and non-mulberry SF for biomedical applications	25

---

<b>Figure 2-13</b> The most reported form of SF based 3D scaffolds for BTE	28
<b>Figure 3-1</b> Schematic representation of SF-Scaffold preparation and surface modification	48
<b>Figure 3-2</b> Standard calibration curve for Alkaline Phosphatase Assay	52
<b>Figure 3-3</b> Standard Calibration curve for Ca estimation by O-cresolphthalein complexone colourimetric assay	53
<b>Figure 3-4</b> SEM images of SF, Coll-SF and CS-SF	55
<b>Figure 3-5</b> Viable MG63 cell density counted by trypan blue dye exclusion method (Data are represented as the mean $\pm$ SD of two independent experiments)	56
<b>Figure 3-6</b> Epi-fluorescence images of Live (Green) and Dead (red) MG63 cells grown on SF, Coll-SF and CS-SF. All images were taken at the same exposure time, and the scale bar is 50 $\mu$ m	57
<b>Figure 3-7</b> Live/Dead images of AO channel; Elongated MG63 cell morphology on 3rd day of seeding with modified scaffold (Scale bar – 20 $\mu$ m)	57
<b>Figure 3-8</b> Cell adhesion and proliferation assay (MTT Assay) of MG63 cultured on SF, Coll-SF and CS-SF till seven days. Data are presented as the mean $\pm$ SD of two independent experiments.	58
<b>Figure 3-9</b> Actin cytoskeleton staining of MG63 cells with Alexa fluor phalloidin 488 and nucleus were counterstained with DAPI. The scale bar is 20 $\mu$ m.	59
<b>Figure 3-10</b> CS-SF scaffold - Actin cytoskeleton staining of MG63 cells with Alexa fluor phalloidin 488 and nucleus were counterstained with DAPI	60

---

<b>Figure 3-11</b> ALP assay- MG63 cells cultured on SF, Coll-SF and CS-SF till seven days. Absorbance was taken at 405 nm, and data are presented as the mean $\pm$ SD of two independent experiments	62
<b>Figure 3-12</b> Calcium deposition by Alizarin Red S staining. Arrow indicates deposited calcium nodules. All bright field images were taken at the same exposure time, and the scale bar is 50 $\mu$ m	63
<b>Figure 3-13</b> Calcium deposition of MG63 cells after seven days.	64
<b>Figure 4-1</b> Alkaline phosphatase assay - Calibration curve	83
<b>Figure 4-2</b> Detection of BMP 2 by ELISA - Calibration curve	83
<b>Figure 4-3</b> Detection of osteocalcin by ELISA - Calibration curve	84
<b>Figure 4-4 Particle size distribution of SF, SF-25% HA, SF-50% HA, SF-25% CaS and SF-50% CaS micro-particles was analyzed using optical microscope. Images of at least 20 micro-particles were captured by using 10x objective and diameter was calculated using ZenPro</b>	<b>86</b>
<b>Figure 4-5</b> Confirmation of secondary structures. SF, SF-25% HA, SF-50% HA, SF-25% CaS and SF-50% CaS micro-particles were analyzed using FTIR-ATR	87
<b>Figure 4-6</b> SEM analysis of SF micro-particles with and without bio-ceramic. Figure 3a-3e has a 200 $\mu$ m scale and represent particle sphericity and evenly distributed bioceramics in bioceramics filled particle. Figure 3f-3j has a 500 $\mu$ m scale and represent scaffold morphology with pores between the particle joints. Figure 3k-3o were shown at a 50 $\mu$ m scale and representing the tight adhesion of two particles with each other in a scaffold.	89

---

<b>Figure 4-7</b> EDX spectra of SF and bioceramics filled microparticles	91
<b>Figure 4-8</b> Thermogravimetric analysis of SF, SF-25% HA, SF-50% HA, SF-25% CaS and SF-50% CaS micro-particles. TGA analysis was performed from 25°C to 900°C at a heating rate of 10°C/min in an air atmosphere using a TGA Q5000 machine	92
<b>Figure 4-9</b> (a) Nanoindentation: SF, SF-50% HA and SF-50% CaS particles Data represented as average Young's Modulus (GPa) $\pm$ Std. Dev. (n=3) *p<0.05. (b) Wet compression modulus: bulk mechanical properties of SF, SF-50% HA and SF-50% CaS scaffolds, Data represented as average compression modulus $\pm$ Std. Dev. ns: Not significant difference.	93
<b>Figure 4-10</b> Surface wettability of 3D scaffolds. Surface wettability of 3D scaffolds of SF, SF-50% HA and SF-50% CaS was analyzed by measuring the contact angle. Data represented as average contact angle $\pm$ Std. Dev. (n=3)	95
<b>Figure 4-11</b> Physical appearance of protease XIV enzyme-treated SF, SF-50% HA and SF-50% CaS scaffolds	96
<b>Figure 4-12</b> <i>In-vitro</i> bio-erosion in the proteolytic environment. SF, SF-50%HA and SF-50% at different time points day 7, day 14 and day 28. Data represented as an average weight loss $\pm$ std. dev. (n=3) *p<0.05	96
<b>Figure 4-13</b> <i>In-vitro</i> L929 cell viability assay (MTT assay) on SF, SF-50% HA and SF-50% CaS scaffolds. * # Significantly not different (p > 0.05). Others are significantly different (p < 0.05)	97

---

**Figure 4-14** hMSCs cell growth. (a) PicoGreen assay: dsDNA concentration was measured using Quant-iT PicoGreen dsDNA kit at day 7, day 14 and day 28-time points. Data represented as DNA concentration (ng/ml)  $\pm$  Std. Dev. (n=3). \*p< 0.05. (b) Actin staining: Morphology of hMSCs seeded on SF, SF-50% HA and SF-50% CaS scaffolds were observed by actin-cytoskeleton at the end of day 28 of culture.

98

**Figure 4-15** Osteogenic differentiation and inflammatory response. (a) ALP activity was measured from conditioned media collected at day7, day 14 and day 28. ALP activity was normalized with the total protein loaded and expressed as ALP activity / 100 $\mu$ g of protein. (b) BMP-2 expression was estimated from conditioned media on day 1 and day 28 using ELISA. (c) Expression of osteocalcin was also estimated by ELISA from conditioned media on day 1 and day 28. (d) Inflammatory reaction against the SF, SF-50% HA and SF-50% CaS by estimating expression level of TNF- $\alpha$ . Data represented as Average  $\pm$  Std. Dev. (n=3). ns= not significant difference. \* p< 0.05.

100

**Figure 5-1** Degummed and cryomilled fiber of BM and AM 118

**Figure 5-2** Calibration curve for ALP estimation 122

**Figure 5-3** Calibration curve for BMP-2 estimation 122

**Figure 5-4** Calibration curve for osteocalcin estimation 123

**Figure 5-5** Brief overview of the creation of calvarial defect, scaffold implantation and closure of the defect 125

---

<b>Figure 5-6</b> Secondary structure analysis of AM and BM. a. FTIR spectra of AM, BM fiber and powder, b. FTIR Spectra from 1400 to 1800 cm <sup>-1</sup> , c & d $\beta$ -sheet and random coil % in AM and BM respectively	128
<b>Figure 5-7</b> X-ray Diffraction studies of AM and BM - fiber and powder	129
<b>Figure 5-8</b> SEM of cryomilled (a) AM and (b) BM powder	130
<b>Figure 5-9</b> Dissolution of silk fiber and its cryomilled form in TFA	131
<b>Figure 5-10</b> Solution of AM and BM fiber and cryomilled powder in TFA	132
<b>Figure 5-11</b> 20 wt % AM and BM cryomilled powder in TFA	133
<b>Figure 5-12</b> SEM images of electrospun scaffolds from (a) AM before annealing, (b) BM before annealing, (c) AM after annealing and (d) BM after annealing	134
<b>Figure 5-13</b> <i>In-vitro</i> L929 cell viability was analyzed by MTT assay on AM and BM scaffolds. Data are represented by average cell viability with respect to plate control $\pm$ Std. Dev. (n=3)	135
<b>Figure 5-14</b> Relative percent MG63 cell seeding efficiency for AM and BM scaffolds	135
<b>Figure 5-15</b> <i>In-vitro</i> hMSCs cell proliferation: Data represented as average normalized factor $\pm$ std. dev. (n=3). *p< 0.05. a) Alamar blue assay in normal cell growth media. b) Alamar blue assay in osteogenic differentiation media	136
<b>Figure 5-16</b> Osteogenic potential by estimating expression of alkaline phosphatase (ALP) activity, bone morphogenic protein-2 (BMP-2) and Osteocalcin levels (OCN). (a) ALP activity was normalized with the total protein loaded and expressed as ALP activity / 100 $\mu$ g of protein. (b) Expression of OCN were	

---

represented as average OCN (ng/ml)  $\pm$  std. dev. (n=3) (c) BMP-2 expression was represented as average BMP-2 (pg/ml)  $\pm$  std. dev. (n=3) (c) BMP-2 expression was represented as average BMP-2 (pg/ml)  $\pm$  std. dev. (n=3) \*p<0.05. (d) Quantification of calcium deposition: calcium deposition by alizarin red S staining which was extracted by using acetic acid at the end of 28 days by measuring the absorbance at 405nm 138

**Figure 5-17** Ca<sup>2+</sup> deposition stained by Alizarin Red S staining at the end of 28 days 139

**Figure 5-18** TNF- $\alpha$  activity. Data represented as average  $\pm$  std. dev. (n=2) \*p< 0.05 140

**Figure 5-19** Rat calvarial defect model for in-vivo new bone regeneration. Fig 4A: standard H&E staining. Black arrow: old bone; Yellow arrow: new bone formation; Blue arrow: fibrous tissue formation; Red arrow: scaffold. Fig 4B: Masson trichrome staining. White star: mineralized bone; Yellow arrow: fibrous tissue 141

**Figure 5-20** *In-vitro* hMSCs cell growth in normal growth media (NGM) and osteogenic media (OstM). Data are represented by average cell viability with respect to plate control  $\pm$  Std. Dev. (n=3) 144

**Figure 6-1** Schematic for the fabrication of SFMA A) fabrication of chemically modified SF with GMA; a. degumming of SF b. Washing of degummed SF fibers DI water; c. Dissolution of SF into 9.3M Lithium Bromide solution; d. Addition of GMA and TEA; e. Dialysis with Dialysis with DI water; f. lyophilization; g. lyophilized



---

SFMA. B) Incorporation of functional methacrylate groups into SF by epoxide ring-opening polymerization reaction and a possible site for the modification includes -NH<sub>2</sub>, -OH and -COOH.<sup>42</sup> 172

**Figure 6-2** Chemical characterization of SFMA by <sup>1</sup>H NMR and FTIR: A) <sup>1</sup>H NMR spectra of pure SF and SFMA in D<sub>2</sub>O, 1d reaction between GMA and SF is indicated by SFMA 1 while 2d reaction by SFMA 2. B) <sup>1</sup>H NMR spectra of SFMA before and after cryogelation. C) FTIR spectra of pure SF, SFMA. D) Beta sheet percentage in pure SF and SFMA and E) Viscosity measurement of pure SF and SFMA. 174

**Figure 6-3** Procedure for the fabrication of SFMA. Injectable SFMA cryogel by using TEMED and APS as an initiator system at -20°C for 16-18h 175

**Figure 6-4** Mechanical characterization of SFMA-based cryogels: A) Comparative compression modulus of SFMA Cryogels. B) 10 compressive cycles of SFMA. C) 10 compressive cycles of SFMA + 0.5% NMS. D) 10 compressive cycles of SFMA + 1% NMS. E) 10 compressive cycles of SFMA + 0.5% MPA. Values represent mean and SD (n = 5). Data were analysed using two-way analysis of variance (ANOVA) (\* p < 0.05) 177

**Figure 6-5** Physical characterization of SFMA cryogels: A) Cryogel polymer wall staining B) Average pore size C) Pore interconnectivity D) Swelling Ratio E) Scanning electron micrograph and F) *in-vitro* enzymatic degradation of cryogels. Values represent mean and SD (n = 5). Data were analysed using one-way/two-way analysis of variance (ANOVA) (\* p < 0.05) 178

---

**Figure 6-6** Cell seeding efficiency of cryogels: HDF cells adhere to cryogels after 24h. Values represent mean and SD (n = 5). Data were analyzed using one-way/two-way analysis of variance (ANOVA) (\* p < 0.05) 179

**Figure 6-7** (A) Viability of HDFn on the cryogels after day 1 and 3 incubation period. B) Confocal images of HDFn cells cultured on cryogels. The polymer walls of cryogels are labelled with Rhodamine (red), cell nuclei with DAPI (blue), dead cells with far- red fixable dead cell staining (yellow), and cytoskeleton with Alexa Fluor 488-phalloidin (green). All cryogels were fabricated at -20 °C and values represent mean and SD (n = 5). 180

**Figure 6-8** *In-vitro* hMSCs human mesenchymal stem cells grown in complete growth media: (A) Alamar blue assay at day 7, 14 and 28 on cryogels seeded with hMSCs. B) Confocal images of actin cytoskeleton - stained with Alexa Fluor 488-phalloidin (green). C) SFMA+1% NMS cryogel was artificially coloured in red while actin filaments appeared in green. 182

**Figure 6-9** Osteogenic potential by estimating expression of alkaline phosphatase (ALP) activity, Osteocalcin levels (OCN), bone morphogenic protein-2 (BMP-2) and Calcium extraction: A) ALP activity was normalized with the total protein loaded and expressed as Units/mg/mL of protein B) Expression of osteocalcin estimated by ELISA. OCN level was normalized with the total protein loaded and expressed as ng/mg/mL of protein C) BMP-2 expression was estimated using ELISA. BMP-2 activity was normalized with the total protein loaded and expressed as pg/mg/mL of protein D) Quantification of calcium deposition: calcium deposition by alizarin

---

red S staining, which was extracted at the end of 28 day. Values represent mean, and SD (n = 5), and data were analyzed using ANOVA (\* p < 0.05). 184

**Figure 6-10** *In-vitro* activation of BMDCs: (A) CD11c+CD86+ (B) CD11c+CD317+ and (C) CD11c+MHCII+ BMDCs stimulated after exposure to SFMA (Gel 1), SFMA+0.5%NMS (Gel 2), SFMA+1%NMS (Gel 3) and SFMA+0.5% APR (Gel 4) cryogels for 24 h. Lipopolysaccharide (LPS) at 200 ng/mL was used as a positive control and cryogel-free medium as a negative control (Media). Values represent mean and SD (n = 5). Data were analyzed using ANOVA (\* p < 0.05) **Error!**

**Bookmark not defined.**

**Figure 6-11** *In-vivo* biocompatibility assessment. H&E staining of SFMA cryogels (dimension: 4mm x 4mm x 1mm) scaffold sections explanted on day 3 and 28 following subcutaneous injections in the dorsal flanks of C57BL/6 mice: (A) H&E staining highlights the macroporous polymeric network of cryogels, infiltrated leukocytes (dark blue dots), fibrin formation (purple), and surrounding tissues (cryogel-free) B) Masson's trichrome staining. Images are representative of n = 5 samples per condition. 187

**Figure 7-1** Schematic for the formation of SF microparticle/freeze dried scaffolds with/without alendronate drug loading. Freeze dried SF Scaffold (FD-SF); alendronate drug loaded SF scaffold (FD-SF+Ald); Microparticle SF Scaffold (M-SF) and alendronate drug loaded SF scaffold (FD-SF+Ald); Microparticle SF Scaffold (M-SF) and alendronate drug loaded microparticle SF scaffold (M-SF+Ald) 204

---

<b>Figure 7-2</b> <i>In-vitro</i> MG-63 cell growth on FD-SF, FD-SF+Ald, M-SF and M-SF+Ald scaffolds up to 7 days	205
---	-----

## List of Tables

<b>Table 2-1</b> Physico-chemical properties of different silk fibroin from different origin	22
<b>Table 3-1</b> Comparison properties of our newly developed SF microparticle scaffold with other reported silk scaffolds	46
<b>Table 4-1</b> Particle size distribution by optical microscopic technique	86
<b>Table 4-2</b> Crystallinity index calculated by using Peakfit v4.1 software	88
<b>Table 4-3</b> TGA analysis: remaining weight percent at different temperatures of SF and bioceramics filled microparticles	93

---

## List of Acronyms

		<b>C</b>	
(3-(4, 5-Dimethylthiazol-2-yl)-2, 5-diphenyltetrazolium bromide)		calcium sulfate (CaS)	74
MTT	50	Committee for the Purpose of Control and Supervision of Experiments on Animals (CPCSEA)	124
	<b>1</b>		
1-Butyl-3-Methylimidazolium Acetate (BMIAc)	115	crystallinity index CI 78	
	<b>A</b>		
Alkaline phosphatase			
ALP	3	deionized water (DI)	79
analysis of variance (ANOVA)	126		
<i>Antheraea mylitta</i>			
A. mylitta	2	Energy-dispersive X-ray spectroscopy (EDX)	79
Arg-Gly-Asp (RGD)	157	extra cellular matrix (ECM)	155
	<b>B</b>		
beta-tricalcium phosphate			
TCP	75	Fourier transform infrared spectroscopy FTIR	3
<i>Bombyx mori</i>			
(B. mori)	2		
bone marrow-derived dendritic cells (BMDCs)	158	Glycidyl methacrylate GMA	5
Bone morphogenic protein-2			
BMP-2	3		
bone tissue engineering (BTE)	1	haematoxylin and eosin (H&E)	168
		Hexafluoroisopropanol	

---

HFIP	47	<b>P</b>	
human dermal fibroblasts (hDFs)	158	paraformaldehyde (PFA)	168
Human mesenchymal stem cells hMSCs	3	<b>R</b>	
hydroxyapatite HA	12	recombinant human BMP-2 rhBMP-2	27
<b>I</b>		regenerated silk fibroin (RSF)	75
Institutional Animal Ethics Committee (IAEC)	124	room temperature (RT)	166
<b>L</b>		<b>S</b>	
Lipopolysaccharide (LPS)	139	scanning electron microscopy SEM	3
Lithium bromide (LiBr)	77	silk fibroin (SF)	2
<b>M</b>		<b>T</b>	
Masson's trichrome (MT)	168	Thermogravimetric analysis TGA	3
Mesenchymal stem cells MSCs	11	three-dimensional 3D	1
methacrylated SF (SFMA)	154	tissue engineering (TE)	1
<b>N</b>		Toll like receptors (TLRs)	105
non-mulberry SF NMS	5	transforming growth factor- $\beta$ (TGF- $\beta$ )	44
<b>O</b>		trifluoroacetic acid TFA	5
Osteocalcin OCN	3		

---

# Chapter 1 Introduction

## 1.1 Introduction

Every year millions of people suffer from tissue/organ loss or failure. Tissue/Organ transplantation is a promising solution for the repair or replacement of damaged tissues/organs.<sup>1</sup> The drawback of transplantation is the immunological response from the patient's body. This can be overcome by tissue engineering (TE)/regeneration. TE applies the principles of engineering and life sciences to develop biological substitutes that help restore the lost tissues/organs.<sup>2,3</sup> Bone is the prime structural tissue in the body and has a load-bearing capacity. The bone tissue has the ability to regenerate by itself and minor bone fractures heal with minimum external intervention. However, a reunion of large bone defects needs external intervention. Bone graft substitutes are biomaterials that help in healing by recruiting native cells to form new bone tissue.<sup>4,5</sup> This process requires an integration of chemical, physical, and biological science and forms the basis of bone tissue engineering (BTE).<sup>6</sup> The primary challenge in BTE includes the development of a three-dimensional (3D) scaffold, which is not only biocompatible but also promotes cell adhesion, proliferation, and differentiation resulting in superior healing of bone defects.<sup>7,8</sup> Thus, the success of the regenerative process depends on understanding the interaction of cells and biomaterials. Several natural and synthetic biomaterials have been reported for BTE.<sup>9,10</sup>

More recently, silk fibroin (SF) has emerged as a promising biomaterial for BTE.<sup>11</sup> SF is the protein-polymer extracted from the cocoons of *Bombyx mori* (*B. mori*) and since ancient times it has been used as a medical suture.<sup>12</sup> The silk from the *B. mori* can be produced with controlled quality in large commercial quantities. It can be

easily chemically modified to obtain the required functionality.<sup>13</sup> It can be processed into various forms using aqueous processing techniques.<sup>14-16</sup> Additionally, different non-mulberry silks such as *Antheraea mylitta* (*A. mylitta*) and *Antheraea pernyi*, and *Antheraea assamensis* are also used as biomaterials.<sup>13,17,18</sup> In the case of non-mulberry silk, the transformation from a textile commodity to biomaterials is new and exciting.<sup>19-21</sup> Non-mulberry SF has an inherent RGD peptide sequence, which is desirable for cell attachment, proliferation, and differentiation.<sup>22-24</sup>

## 1.2 Motivation and Objectives

Bone is the load-bearing tissue where the coexistence of two different properties, i) porosity and ii) mechanical strength results in challenges in developing biomaterial for BTE application.<sup>25</sup> As a general rule for tissue engineering, scaffolds should be fabricated from materials that invoke low immune reactions upon implantation.<sup>26,27</sup> SF is a US-FDA approved biomaterial. SF has the ability to undergo a conformational transition from a completely amorphous state (alpha helix & random coil) to a predominantly crystalline state (beta sheets).<sup>28,29</sup> This property can be leveraged to develop various protocols to prepare SF scaffolds that have a range of mechanical properties. For example, stiff and hard load-bearing scaffolds or soft elastic injectable hydrogel scaffolds.<sup>30-32</sup>

Despite the various developments in the mulberry silk-based SF scaffold system, there is scope for further improvement in the development of various scaffold formulations that can be used in various clinical scenarios.<sup>14,33,34</sup> However, non-mulberry silk contains higher alanine blocks that result in a material with increased beta-sheet content. These localized highly crystalline domains prevent the dissolution of the silk into any conventional solvents and limits the ability to process non-mulberry silk into various scaffolds.<sup>35,36</sup>



Thus, this thesis is focused on developing different 3D scaffold systems by using natural SF (both mulberry and non-mulberry silk). The developed scaffold was fully characterized physically and chemically using various techniques like scanning electron microscopy (SEM), Fourier Transform Infrared Spectroscopy (FTIR), Thermogravimetric analysis (TGA), contact angle, etc. The mechanical properties of the scaffold, such as compression modulus and Young's modulus, were also measured. Further, the *in-vitro* enzymatic degradation of the scaffold was also studied. The biological properties of the scaffolds were evaluated by studying the cell viability, cell proliferation and cell morphology. Finally, the developed scaffolds were assessed for their potential to differentiate primary cells or human mesenchymal stem cells (hMSCs) into an osteogenic lineage (new bone formation cells). These experiments were performed by measuring the differentiating osteogenic markers such as Alkaline phosphatase (ALP), Osteocalcin (OCN), Bone morphogenic protein-2 (BMP-2), and calcium mineralization. Further, the scaffolds were examined for their immunological response.

Following specific objectives (strategies) are included in the thesis.

1. Surface coating with biopolymers on micro-particle-based SF scaffold
2. Incorporation of bio-ceramics into SF micro-particle-based scaffold
3. Development of non-mulberry silk electrospun scaffold
4. Development of mulberry and non-mulberry SF based injectable scaffold

## **1.3 Organization of Thesis**

The dissertation is presented in seven chapters and a summary of each chapter is given below.

### **Chapter 1: Introduction**

This chapter provides an overview of the thesis. It highlights the motivation for the work and outlines the specific objectives. Further it also provides an overview of the organization of the thesis.

## **Chapter 2: Literature review**

This chapter begins with a general introduction to bone tissue and summarizes an overview of advancements in BTE, bone graft substitutes/ bone void fillers, and their limitations. This chapter also discusses the physical, chemical, and structural properties of SF and explores the application of SF in BTE. The chapter ends by describing the motivation and objective of the present thesis.

## **Chapter 3: Surface coating with biopolymers on micro-particle-based SF scaffold**

In this chapter, microparticles from SF have been formulated, which were fused by using a regenerated SF solution to prepare a load-bearing 3D microparticle-based SF scaffold. The surface coating strategy was explored using collagen and chitosan biopolymers to enhance the osteogenic potential of the microparticle-based SF scaffold.

## **Chapter 4: Incorporation of bio-ceramics into SF micro-particle- based scaffold**

In this chapter, microparticles from SF have been formulated by using conventional bio-ceramics. Bio-ceramics loaded microparticles were fused using a regenerated SF solution to make a 3D microparticle based SF scaffold. Bioceramics influence the mechanical properties at the particle level and provide

mechanostimulation to stem cells to improve the osteogenic potential of microparticle-based SF scaffold.

### **Chapter 5: Development of non-mulberry electrospun SF-based scaffold**

In this chapter, a highly concentrated SF solution from the fiber of *A. Mylitta* silkworm was prepared in trifluoroacetic acid (TFA) from cryomilled powder. Cryomilling reduces the crystalline structure of silk fiber and enables faster and efficient dissolution. Silk from *B. mori* was processed similarly and used as a control. Electrospun fiber mat was prepared from mulberry and non-mulberry silk solution and was evaluated for BTE using *in-vitro* and *in vivo* experiments.

### **Chapter 6: Development of mulberry and non-mulberry SF based injectable scaffold**

This chapter incorporated the methacrylated group into silk fibroin using the epoxide ring-opening polymerization method. Chemical modification of silk fibroin using glycidyl methacrylate (GMA) enhances crosslinking sites on SF, which help to formulate injectable and highly compressible cryogels. The addition of non-mulberry SF (NMS) cryomilled microfibers into mulberry SF-based cryogel further enhanced the physical properties and biological performance of cryogels for BTE. *In-vitro* primary dendritic cells activation studies (CD86+, CD137+, and MHCII+ cell markers) reveal that all cryogels are not pro-inflammatory. The addition of NMS results in an anti-inflammatory effect.

### **Chapter 7: Conclusions and future work**

This chapter presents an overall summary of the work done for this dissertation and describes the significant outcomes of the studies. Future directions based on the work reported in this thesis are also discussed.

## 1.4 References

- (1) Henkel, J.; Woodruff, M. A.; Epari, D. R.; Steck, R.; Glatt, V.; Dickinson, I. C.; Choong, F. M.; Schuetz, M. A.; Hutmacher, D. W. Bone Regeneration Based on Tissue Engineering Conceptions – A 21st Century Perspective. **2013**, 216–248. <https://doi.org/10.4248/BR201303002>.
- (2) Hao, Z.; Song, Z.; Huang, J.; Huang, K.; Panetta, A.; Gu, Z.; Wu, J. The Scaffold Microenvironment for Stem Cell Based Bone Tissue Engineering. *Biomater. Sci.* **2017**, 5 (8), 1382–1392. <https://doi.org/10.1039/c7bm00146k>.
- (3) Langer, R.; Vacanti, J. P. - ARTICLES Tissue Engineering. *Science (80-. )*. **1993**, 260 (May), 920–926.
- (4) Fernandez de Grado, G.; Keller, L.; Idoux-Gillet, Y.; Wagner, Q.; Musset, A. M.; Benkirane-Jessel, N.; Bornert, F.; Offner, D. Bone Substitutes: A Review of Their Characteristics, Clinical Use, and Perspectives for Large Bone Defects Management. *J. Tissue Eng.* **2018**, 9. <https://doi.org/10.1177/2041731418776819>.
- (5) Roberts, T. T.; Rosenbaum, A. J. Bone Grafts, Bone Substitutes and Orthobiologics. *Organogenesis* **2012**, 8 (4), 114–124. <https://doi.org/10.4161/org.23306>.
- (6) Stevens, M. M. Biomaterials for Bone Tissue Engineering. *Mater. Today* **2008**, 11 (5), 18–25. [https://doi.org/10.1016/S1369-7021\(08\)70086-5](https://doi.org/10.1016/S1369-7021(08)70086-5).
- (7) Rozalia Dimitriou, Elena Jones, D. M. and P. V. G. Bone Regeneration: Current Concepts and Future Directions Rozalia. *BMC Med.* **2011**, 43.

- (8) Mödinger, Y.; Teixeira, G. Q.; Neidlinger-Wilke, C.; Ignatius, A. Role of the Complement System in the Response to Orthopedic Biomaterials. *Int. J. Mol. Sci.* **2018**, *19* (11). <https://doi.org/10.3390/ijms19113367>.
- (9) Troy, E.; Tilbury, M. A.; Power, A. M.; Wall, J. G. Nature-Based Biomaterials and Their Application in Biomedicine. *Polymers (Basel)*. **2021**, *13* (19), 1–37. <https://doi.org/10.3390/polym13193321>.
- (10) Carson, J. S.; Bostrom, M. P. G. Synthetic Bone Scaffolds and Fracture Repair. *Injury* **2007**, *38* (SUPPL. 1). <https://doi.org/10.1016/j.injury.2007.02.008>.
- (11) Midha, S.; Murab, S.; Ghosh, S. Osteogenic Signaling on Silk-Based Matrices. *Biomaterials* **2016**, *97*, 133–153. <https://doi.org/10.1016/j.biomaterials.2016.04.020>.
- (12) Fiorenzo G. Omenetto and David L. Kaplan. New Opportunities for an Ancient Material Fiorenzo. *Science (80-. )*. **2010**, *329* (5991), 528–531. <https://doi.org/10.1126/science.1188936.New>.
- (13) Sen, K.; Babu K, M. Studies on Indian Silk. I. Macrocharacterization and Analysis of Amino Acid Composition. *J. Appl. Polym. Sci.* **2004**, *92* (2), 1080–1097. <https://doi.org/10.1002/app.13609>.
- (14) Melke, J.; Midha, S.; Ghosh, S.; Ito, K.; Hofmann, S. Silk Fibroin as Biomaterial for Bone Tissue Engineering. *Acta Biomater.* **2015**, *31*, 1–16. <https://doi.org/10.1016/j.actbio.2015.09.005>.
- (15) Mottaghitalab, F.; Hosseinkhani, H.; Shokrgozar, M.; Mao, C.; Yang, M.; Farokhi, M. Silk as a Potential Candidate for Bone Tissue Engineering. *J. Control. release* **2015**, *215*, 112–128.
- (16) Rockwood, D. N.; Preda, R. C.; Yücel, T.; Wang, X.; Lovett, M. L.; Kaplan, D. L. Materials Fabrication from Bombyx Mori Silk Fibroin. **2011**, No. September. <https://doi.org/10.1038/nprot.2011.379>.
- (17) Singh, B. N.; Pramanik, K. Tissue and Cell Fabrication and Evaluation of Non-Mulberry Silk Fibroin Reinforced Chitosan Based Porous Composite Scaffold

Old for Cartilage Tissue Engineering. **2018**, 55 (October), 83–90. <https://doi.org/10.1016/j.tice.2018.10.003>.

(18) Darshan, G. H.; Kong, D.; Gautrot, J.; Vootla, S. Physico-Chemical Characterization of Antheraea Mylitta Silk Mats for Wound Healing Applications. *Sci. Rep.* **2017**, 7 (1), 1–11. <https://doi.org/10.1038/s41598-017-10531-7>.

(19) Konwarh, R.; Bhunia, B. K.; Mandal, B. B. Opportunities and Challenges in Exploring Indian Non-Mulberry Silk for Biomedical Applications. *Proc. Indian Natl. Sci. Acad.* **2017**, 83 (1), 85–101. <https://doi.org/10.16943/ptinsa/2017/41288>.

(20) Gupta, P.; Adhikary, M.; M, J. C.; Kumar, M.; Bhardwaj, N.; Mandal, B. B. Biomimetic, Osteoconductive Non-Mulberry Silk Fiber Reinforced Tricomposite Scaffolds for Bone Tissue Engineering. *ACS Appl. Mater. Interfaces* **2016**, 8 (45), 30797–30810. <https://doi.org/10.1021/acsami.6b11366>.

(21) Mandal, B. B.; Kundu, S. C. Non-Mulberry Silk Gland Fibroin Protein 3-D Scaffold for Enhanced Differentiation of Human Mesenchymal Stem Cells into Osteocytes. *Acta Biomater.* **2009**, 5 (7), 2579–2590. <https://doi.org/10.1016/j.actbio.2009.02.033>.

(22) Naskar, D.; Nayak, S.; Dey, T.; Kundu, S. C. Non-Mulberry Silk Fibroin Influence Osteogenesis and Osteoblast-Macrophage Cross Talk on Titanium Based Surface. *Sci. Rep.* **2014**, 4, 4745. <https://doi.org/10.1038/srep04745>.

(23) Acharya, C.; Ghosh, S. K.; Kundu, S. C. Silk Fibroin Film from Non-Mulberry Tropical Tasar Silkworms: A Novel Substrate for *in-vitro* Fibroblast Culture. *Acta Biomater.* **2009**, 5 (1), 429–437. <https://doi.org/10.1016/j.actbio.2008.07.003>.

(24) Behera, S.; Naskar, D.; Sapru, S.; Bhattacharjee, P.; Dey, T.; Ghosh, A. K.; Mandal, M.; Kundu, S. C. Hydroxyapatite Reinforced Inherent RGD Containing Silk Fibroin Composite Scaffolds: Promising Platform for Bone Tissue Engineering. *Nanomedicine Nanotechnology, Biol. Med.* **2017**, 13 (5), 1745–1759. <https://doi.org/10.1016/j.nano.2017.02.016>.

- (25) Koons, G. L.; Diba, M.; Mikos, A. G. Materials Design for Bone-Tissue Engineering. *Nat. Rev. Mater.* **2020**, *5* (8), 584–603. <https://doi.org/10.1038/s41578-020-0204-2>.
- (26) Qu, H.; Fu, H.; Han, Z.; Sun, Y. Biomaterials for Bone Tissue Engineering Scaffolds: A Review. *RSC Adv.* **2019**, *9* (45), 26252–26262. <https://doi.org/10.1039/c9ra05214c>.
- (27) Lin, X.; Patil, S.; Gao, Y. G.; Qian, A. The Bone Extracellular Matrix in Bone Formation and Regeneration. *Front. Pharmacol.* **2020**, *11* (May), 1–15. <https://doi.org/10.3389/fphar.2020.00757>.
- (28) Kaplan, D.; Adams, W. W.; Farmer, B.; Viney, C. Chapter 1 Silk: Biology, Structure, Properties, and Genetics. **1994**, 2–16.
- (29) Wilson, D.; Valluzzi, R.; Kaplan, D. Conformational Transitions in Model Silk Peptides [In Process Citation]. *Biophys J* **2000**, *78* (5), 2690–2701.
- (30) Nisal, A.; Sayyad, R.; Dhavale, P.; Khude, B.; Deshpande, R. Silk Fibroin Micro-Particle Scaffolds with Superior Compression Modulus and Slow Bioresorption for Effective Bone Regeneration. **2018**, No. April, 1–10. <https://doi.org/10.1038/s41598-018-25643-x>.
- (31) Parekh, N.; Hushye, C.; Warunkar, S.; Gupta, S. Sen; Nisal, A. RSC Advances *In-vitro* Study of Novel Microparticle Based Silk. *RSC Adv.* **2017**, *7*, 26551–26558. <https://doi.org/10.1039/C7RA03288A>.
- (32) Roohaniesfahani, I.; Wang, J.; No, Y. J.; de Candia, C.; Miao, X.; Lu, Z.; Shi, J.; Kaplan, D. L.; Jiang, X.; Zreiqat, H. Modulatory Effect of Simultaneously Released Magnesium, Strontium, and Silicon Ions on Injectable Silk Hydrogels for Bone Regeneration. *Mater. Sci. Eng. C* **2019**, *94* (December 2017), 976–987. <https://doi.org/10.1016/j.msec.2018.10.053>.
- (33) Fazal, N.; Latief, N. Bombyx Mori Derived Scaffolds and Their Use in Cartilage Regeneration: A Systematic Review. *Osteoarthr. Cartil.* **2018**, *26* (12), 1583–1594. <https://doi.org/10.1016/j.joca.2018.07.009>.

(34) Alaribe, F. N.; Manoto, S. L.; Motaung, S. C. K. M. Scaffolds from Biomaterials: Advantages and Limitations in Bone and Tissue Engineering. *Biologia (Bratisl)*. **2016**, *71* (4), 353–366. <https://doi.org/10.1515/biolog-2016-0056>.

(35) Andiappan, M.; Kumari, T.; Sundaramoorthy, S.; Meiyazhagan, G.; Manoharan, P.; Venkataraman, G. Comparison of Eri and Tasar Silk Fibroin Scaffolds for Biomedical Applications. *Prog. Biomater.* **2016**, *5* (2), 81–91. <https://doi.org/10.1007/s40204-016-0047-5>.

(36) Naskar, D.; Sapru, S.; Ghosh, A. K.; Reis, R. L.; Dey, T.; Kundu, S. C. Nonmulberry Silk Proteins : Multipurpose Ingredient in Bio-Functional Assembly Nonmulberry Silk Proteins : Multipurpose Ingredient in Bio-Functional Assembly. **2021**.



## Chapter 2 Literature Review

Bone is a unique tissue that continuously resorbs and neoforms in the body. Bone defects can be caused due to age, trauma, accidents, infections, and/or other disease conditions. Hence, bone is the second most transplanted tissue. This chapter begins with a literature review that covers relevant details about the structure of bone, regenerative medicine, BTE, the prevalent solutions, and their limitations. Section 2.2 includes a discussion about the unique features of the SF that make it favorable material for BTE. This chapter concludes by outlining the objectives of the thesis.

### 2.1 Bone biology and tissue engineering

#### 2.1.1 Bone as a Tissue

Bone is a 3D structure composed of 10-20% organic matrix, 60-70% inorganic matrix and 9-20% water by weight in addition to various proteins, polysaccharides and lipids as shown in **Figure 2-1**. There is a balance between bone resorption and bone formation that results in a continuous process of bone remodeling. Mesenchymal stem cells (MSCs), osteoblasts (bone-forming cells),

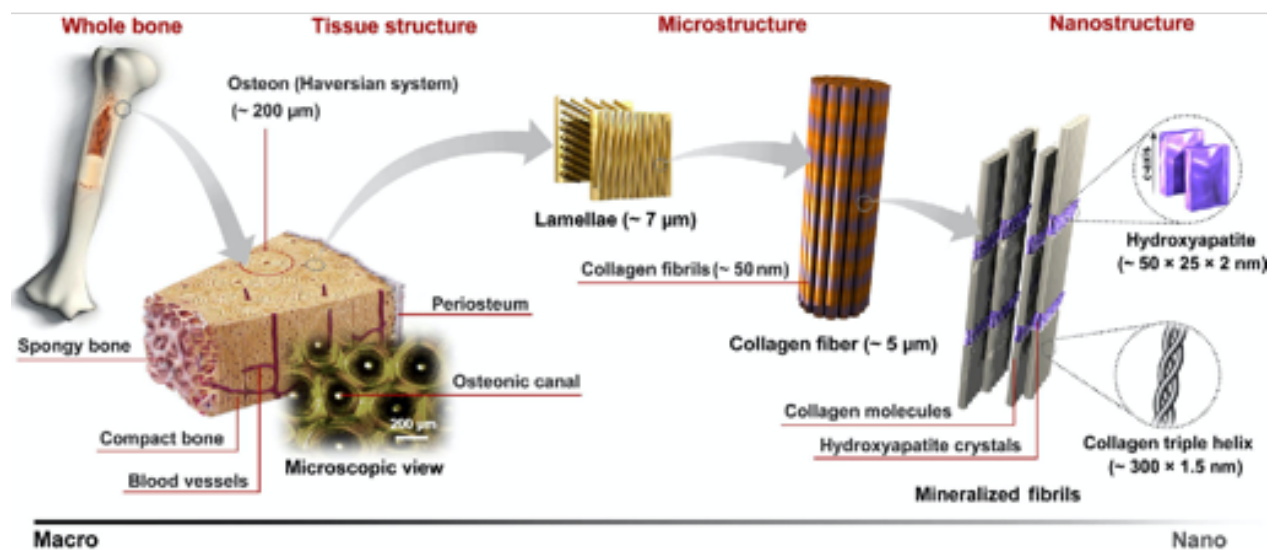


**Figure 2-1** Hierarchical structure of bone tissue from macro to nanoscale. Reproduce with the permission from Elsevier

and ultimately osteocytes play an essential role during bone formation. In a bone formation process, multipotent mesenchymal stem cells (MSCs) (present in the bone marrow or other tissues) are differentiated into osteoblasts.<sup>3</sup>

Osteoclasts are the cells that are responsible for bone resorption. All types of bone cells are depicted in **Figure 2-2**. The bone-ECM is a non-cellular three-dimensional structure secreted by cells into the extracellular space. Organic bone-ECM significantly consists of 90% collagen type I and 10% non-collagenous proteins. The primary function of collagen is to provide mechanical support in the form of a scaffold for osteoblast cells. The inorganic component of bone is hydroxyapatite (HA) –  $(\text{Ca}_5(\text{PO}_4)_3\text{OH})$ . Biomineralization is the process responsible for collagen production on which HA get deposited.<sup>4</sup>

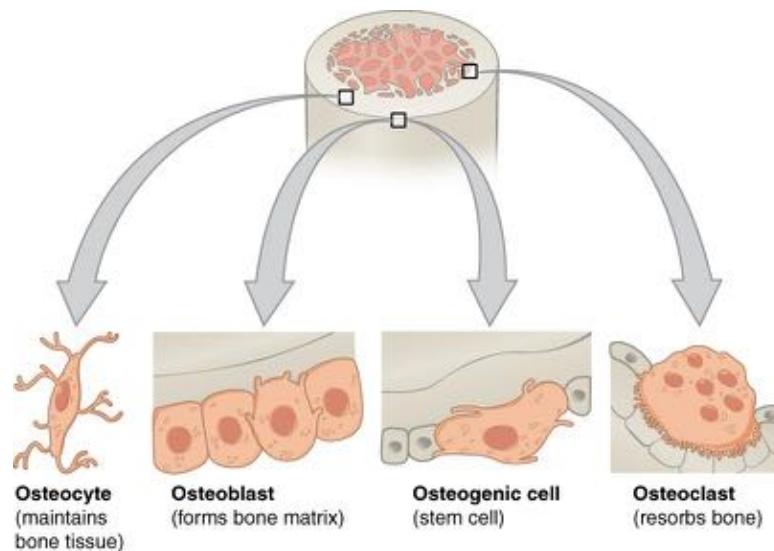


**Figure 2-2** Bone Tissue with different types of cells ([https://en.wikipedia.org/wiki/Bone#/media/File:604\\_Bone\\_cells.jpg](https://en.wikipedia.org/wiki/Bone#/media/File:604_Bone_cells.jpg))

The osteogenic differentiation of MSCs can be explained by different steps that include a) commitment step – responsible for lineage-specific progenitor cells formation b) proliferative phase of osteoprogenitors - cell cycle-associated genes and signals for histone are expressed c) ECM secretion and maturation of osteoblasts d) osteoid mineralization by mature osteoblasts and osteocytes differentiation. This complex process is highly regulated by several markers and/or expression of transcription factors.<sup>5-9</sup> This transformation of a stem cell to mature osteoblast with the expression of various biomarkers has been depicted in **Figure 2-3**.

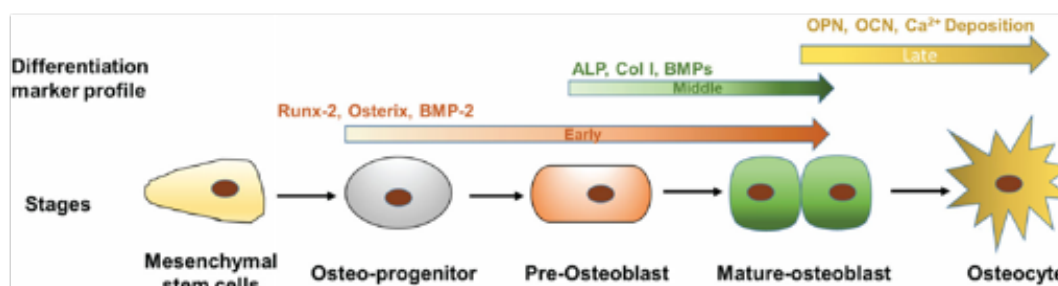


**Figure 2-3** Schematic representation of differentiation from a stem cell to mature osteoblast and markers expressed at each stage of differentiation<sup>10</sup>

## 2.1.2 Tissue Engineering

In 1988, the term “tissue engineering” (TE) was introduced by Professor Robert Nerem at UCLA Symposium on Molecular and Cellular Biology.<sup>11</sup> This TE term elaborated and structured by Langer and Vacanti, 1993. TE is defined as the application of life sciences and engineering principles to develop a basic understanding of the functional and structural relationships of natural and pathological mammalian tissues. Further, TE includes the development of bio-substitutes that can be utilized to restore, maintain, or improve tissues damaged or lost by various disease conditions. Every year millions of people suffer from tissue/organ loss or failure. Tissue/Organ transplantation is a promising solution for the repair or replacement of tissue/organ. The drawback of transplantation is the immunological response from the patient’s body. This can be overcome by tissue engineering (TE)/regeneration, which applies the principles of engineering and life sciences to develop biological substitutes that help restore the lost tissues/organs. In TE, the major challenges have been the development of biocompatible material, which can perfectly mimic the ECM in such a way that it can act as a scaffold for tissue regeneration. The success of the regenerative process depends on understanding the interactions between the cells and the type of material and its physicochemical characteristics. As tissue has a 3D structure, biomaterials used for TE application in the form of 3D have shown to have enhanced potential.<sup>12,13</sup> Different types of scaffolds like microparticle or microparticle based solid scaffold, fibrous woven or non-woven scaffolds, hydrogel, crygels or 3D printed scaffolds are explored for different types of TE applications. **Figure 2-4** depicts the various types of 3D biomaterials for TE applications.

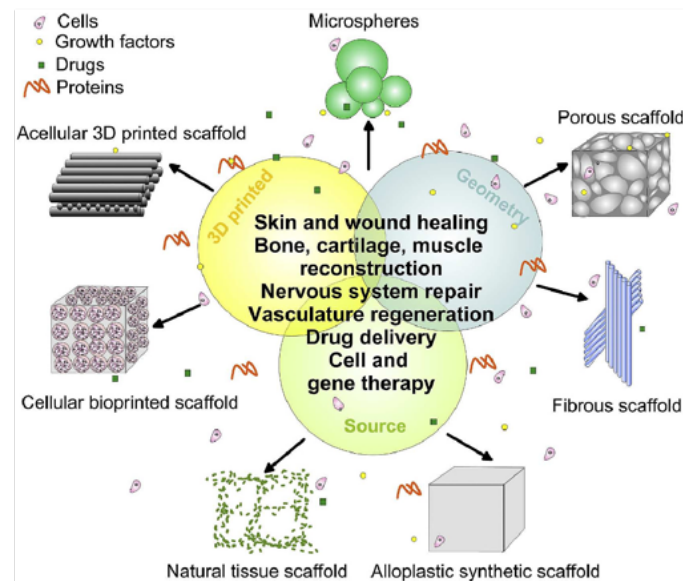


**Figure 2-4** Schematic representation of different types of 3D scaffolds for various tissue engineering applications.<sup>13</sup>

### 2.1.3 Bone Tissue Engineering

Bone is 3D highly vascularized tissue with a unique capacity to heal and regenerate without leaving a scar.<sup>14</sup> Over the years, bone disorders have seen a steep rise in numbers not only in India, but also in the world. The primary causes for bone disorders are ageing, obesity and/or poor physical activity.<sup>15</sup>

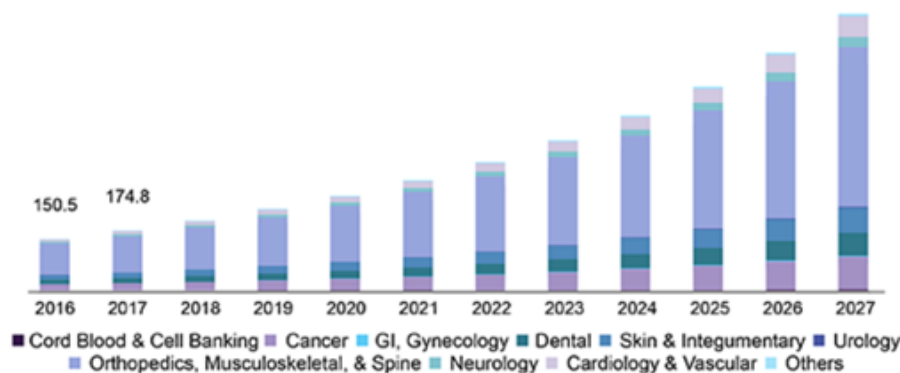


**Figure 2-5** Market research report for bone surgeries<sup>16</sup>

As per the U.S. Medicare and Medicaid facility, there are around 900,000 surgeries performed every year that require bone replacement or reconstruction. Also, a whopping 15 million fractures are reported annually as presented in **Figure 2.5**. 40% of women and 13% of men over 50 years old suffer from an osteoporotic fracture in their lifetime.<sup>17</sup> 200 women worldwide are affected by osteoporosis.<sup>18</sup>

BTE is being currently explored as a potential alternative to conventional auto/allogenic bone grafts as it has a significantly lower risk of disease transmission. BTE involves the use of a 3D scaffold that provides a substrate for cell attachment. The scaffold material may be bioactive or functional through incorporation of molecules/drugs. Thus the scaffold plays a very crucial role in the success of BTE. The ideal scaffold should have a 3D architecture with optimum pore size and porosity for effective diffusion of nutrients and migration of cells. Biomaterial must have the appropriate mechanical strength suitable to provide structural support. Ultimately, the scaffold must provide the proper chemical, biological and morphological clues so that cells can form good quality new bone tissue.<sup>3,19</sup>

BGS is a material used to fill cavities/defects in bone. These materials should be biocompatible, bioactive, osteoconductive and osteoinductive with a controlled

degradation rate that matches with the rate of ECM deposition. Therefore selection/fabrication of scaffold is a critical parameter in bone graft design.<sup>20</sup> BGS can either be derived from biological sources or synthetic sources.<sup>21</sup> BGS can be classified as autografts (derived from the same individual/person), allografts (derived from same species) or xenografts (derived from other species) as mentioned in **Figure 2-6**.

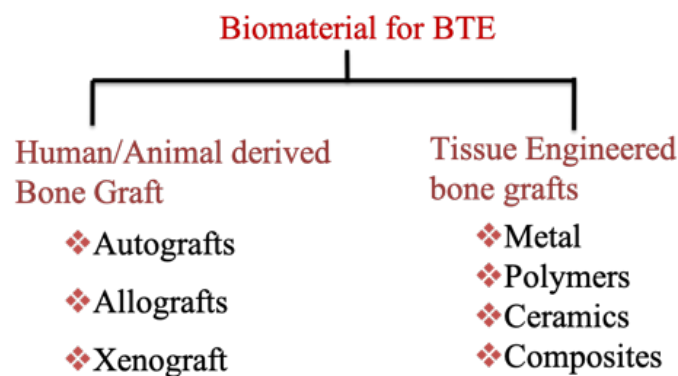


**Figure 2-6** Different types of biomaterials for BTE

Synthetic BGS involve the use of various materials such as ceramics, polymers, metals, and their blends/composites.<sup>2</sup> Various techniques such as solvent casting (where different types of porogen is used to obtain porous scaffold), thermally induced phase separation (where temperature difference is used to get polymer rich phase and solvent rich phase to obtained scaffold), microsphere sintering, electrospinning non-woven fibrous mats, woven mats, solution to gel method to obtained sponge like hydrogel or cryogels (with controlled sub-zero temperature) have been used to fabricate BGS. Some of the most commonly used methods are summarized in **Figure 2-7**.

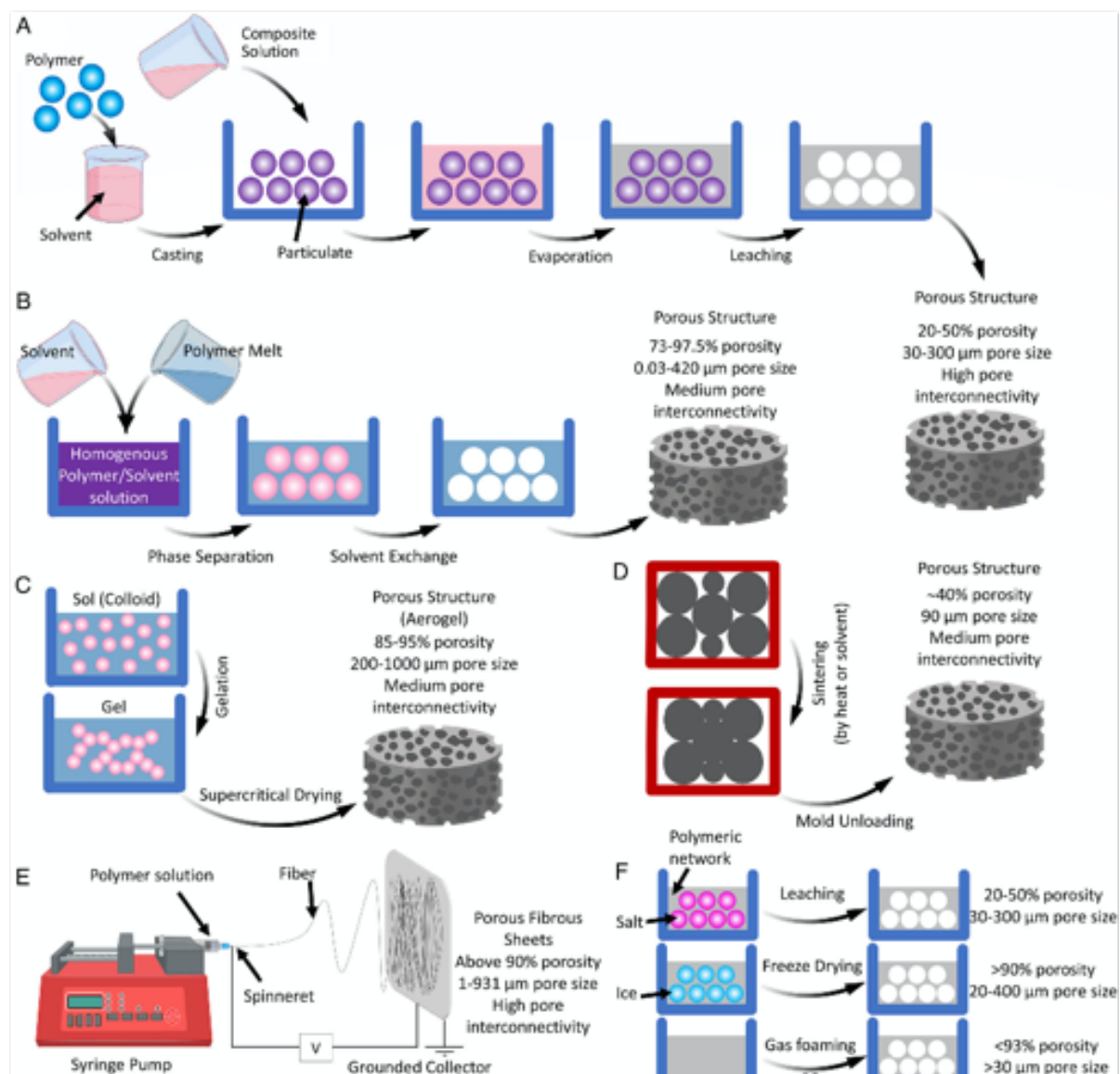


**Figure 2-7** Different methods used for the fabrication of bone grafts. A) solvent casting, B) thermally induced phase separation, C) sol-gel method, D) microsphere sintering method, E) electrospinning technique and F) pore generation by particulate leaching/emulsification freeze-drying/gas foaming methods.<sup>2</sup>

Another method commonly used to classify the bone void fillers is classification based on nature of origin. Bio-engineered bone graft materials broadly include bio-ceramics, polymers, and hydrogels/cryogels due to their excellent biocompatibility, tuneable chemical composition, incorporation of functional groups and biodegradation.<sup>20</sup> Commonly used different types of bone graft



materials are listed in **Figure 2-7**. The advantages and limitations of the conventionally used BGS materials is discussed in the next section.

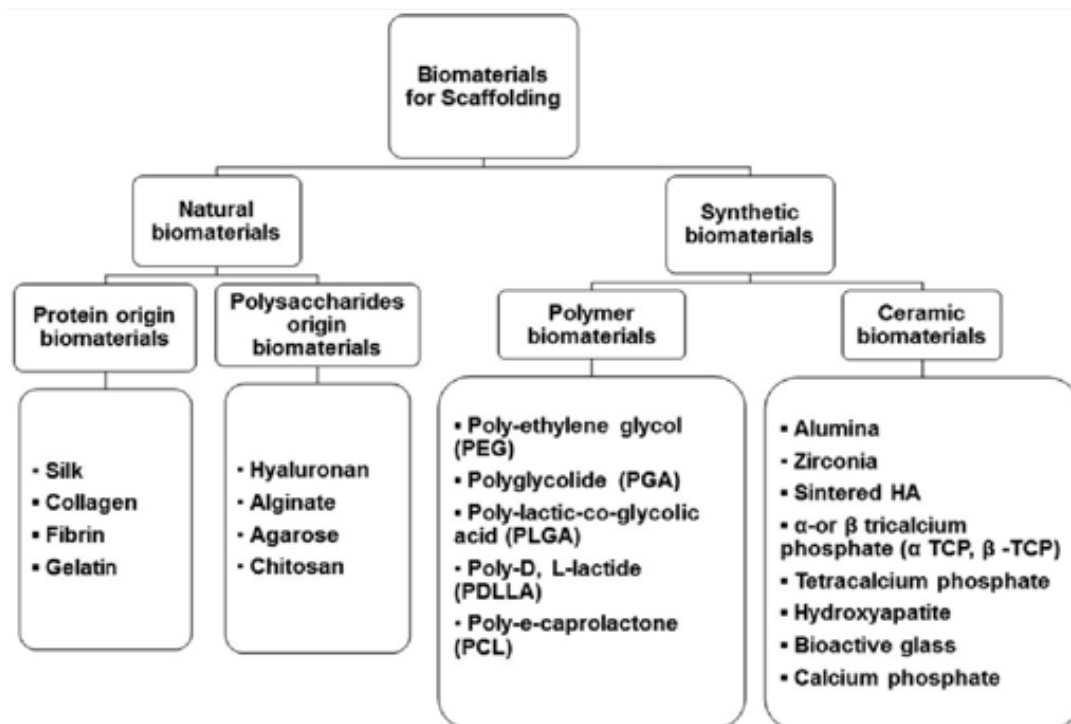


**Figure 2-8** Biomaterials used for scaffold fabrication in BTE<sup>22</sup>

### 2.1.4 Bone grafts substitute and it's limitations

Autografts are the gold standard for the treatment of bone defects.<sup>23</sup> Autografts easily integrate into host bone tissue because of osteogenic properties and immune similarity. However, donor site morbidity, dual surgery at different places, long surgery time, risk of infection are limitations for the use of autografts. Allografts and xenografts are more prone to failure and rejections because of immunogenic reactions. High risk of disease transmission also limits the use of available material.<sup>24,25</sup> Therefore, tissue-engineered bone grafts have emerged as a promising alternative. Bio-ceramics have high biocompatibility and are chemically similar to natural bone. However, bioceramics are highly brittle.<sup>21,26</sup> Also, the rate of bio-degradation with respect to rate of new bone formation is not

matched.<sup>27-29</sup> Different types of natural (protein-based and polysaccharide-based) and synthetic polymers (polymers and ceramic-based) are also explored as biomaterials because of their cost-effectiveness, less toxicity, high reproducibility, controllable mechanical/chemical/physical properties. However, higher hydrophobicity, lack of cell adhesion moiety, and poor osteoinductive/conductive properties limit their use in BTE.<sup>20,30</sup>

Natural biomaterials are being increasingly evaluated in BTE because of their biocompatibility. Natural biomaterials also provide an opportunity for chemical/functional modifications as per the desired application. A variety of natural materials like chitosan, agarose, hyaluronan, fibrin, collagen, and SF are explored for BTE.<sup>31</sup> SF has emerged as a promising biomaterial in BTE and details about silk as a polymer for BTE will be discussed in the subsequent sections.

## 2.2 Introduction to Silk

### 2.2.1 Silk as a Protein

Silk is a proteinaceous natural polymer. Silk is produced in the silk gland of many insects including spiders, flies, beetles, mites, and scorpions. But the silk which is most extensively commercially produced and used by Lepidopterans larvae belong to the family *Bombycidae* and family *Saturniidae*.<sup>4,32,33</sup> *Bombyx mori* is the most illustrative member of the family *Bombycidae* and is more commonly known as mulberry silkworm (domestic silkworm). The *Saturniidae* family, comprises non- mulberry species, including Indian species a) *Antheraea mylitta* (tasar silkworm), b) *Antheraea assamensis* (muga silkworm) and c) *Samia ricini* (eri silkworm); and Chinese species d) *Antheraea pernyi* (temperate oak tasar silkworm) and Japanese species *Antheraea yamamai* (oak silkworm).<sup>34</sup> In spite of

excellent strength to weight ratio, spider silk has restricted use because of its difficulty in large scale culture and limited availability.<sup>35</sup>

Among the different types of SF, *B. mori* is one of the best characterized silk. Silk is composed of two major proteins: 1) 70-80% of Silk Fibroin – a fibrous protein (SF) and 20-30% sericin – a globular protein. SF located in the core of the silk fiber is coated with sericin (20–310kDa). Thermochemical treatment, also known as degumming, is used to remove the glue-like protein sericin. SF, the structural protein, contains light (~25kDa), heavy chains (~325kDa), and fibrohexamerin or P25 (30kDa).<sup>36</sup> The core sequence of the heavy chain is comprised of alanine (43%), glycine (30%), and serine (12%) - a repeated motif. SF contains three common crystalline structures silk I, II, and III.<sup>37,38</sup> The hydrophilic domain of SF is known as silk I/  $\alpha$ -silk which can be easily converted to hydrophobic silk II through changes in temperature, physical spinning, and solvent effects, such as exposure to methanol and potassium chloride.<sup>39,40</sup> In Silk II SF molecules are arranged into  $\beta$ -sheets which is responsible for the crystallinity of SF. Silk III has a helical structure that assembles at air-water interfaces.<sup>41</sup> Both Silk I and II structure of SF have been depicted in **Figure 2-8**. The molecular weight of the structural protein of the majority of silk worms' SF with its repetitive amino acid sequence(s), tensile strength, and % crystallinity is mentioned in **Table 2-1**.

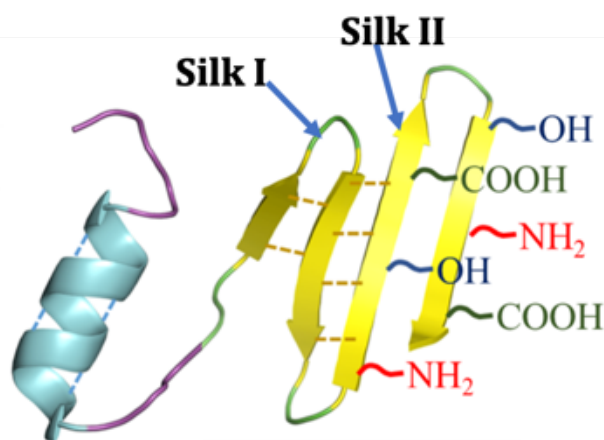


**Figure 2-9** Hydrophilic (Silk I) and Hydrophobic (Silk II) components of Silk Fibroin

Silkworm	Structural Protein	repetitive amino acid sequence	Tensile strength (GPa)	% Crystallinity	Ref
<i>B. mori</i>	Fibroin H-Chain-350 KD L-Chain-26 KD P25 (glycoprotein) - 30 KD	GAGAGS GAGAGY	0.57±0.12	30.5-33.7	34,42-44
<i>A. assamensis</i>	Fibroin H-Chain-230 KD	AAA(A) <sub>5-15</sub>	0.36±0.10	34.7	42,44,45
<i>A. mylitta</i>	Fibroin H-Chain-197 KD	AAAAAAAAAAAAASS	0.25±0.45	39.5	45-47
<i>A. pernyi</i>	Fibroin H-Chain-220 KD	AAAAAAAAAAAAAAG S	0.43±0.08	30.9	42,46
<i>A. yamamai</i>	Fibroin H-Chain-218 KD	AAAAAAAAAAAAASS	0.39±0.07	32.5	42,45
<i>P. ricini</i>	Fibroin H-Chain-230 KD	YGGDGG(A) <sub>12</sub> GGAG	0.47±0.11	25.8	42-44

**Table 2-1** Physico-chemical properties of different silk fibroin from different origin

## 2.2.2 Silk Fibroin in Tissue Engineering

In tissue engineering, biomaterials play an important role. Biomaterials are bio-tolerable rather than truly inert. India is the second largest producer of silkworm silk (Refer **Figure 2-10**) and it is also the only country producing different varieties of silk.<sup>44</sup> Silk has been reported from most ancient times for its use as a medical suture in 131-211 A.D by Aelius Galenus – a Greek physician.<sup>49</sup> SF is a promising candidate for tissue engineering and biomedical implant applications

as the biophysical properties of SF are favorable for cells to interact with material<sup>50</sup> (Refer to **Figure 2-11**). It is biocompatible, biodegradable, and has excellent thermo-mechanical properties.<sup>51</sup> The silk from the silkworm *B. mori* can be produced with controlled quality in large commercial quantities. It can be easily chemically modified to obtain the required functionality. It can be processed into a variety of different forms using aqueous processing techniques.<sup>52,53</sup> On the other hand different types of non-mulberry silks such as *Antheraea mylitta* and *Antheraea pernyi*, *Antheraea assamensis* have also been evaluated as biomaterials. Non-mulberry silk contains higher alanine amino acids.<sup>54,55</sup> This results in higher beta sheet and reduces the ability to process this silk.<sup>44,56</sup> This is why most reported literature on non-mulberry silk uses silk extracted directly from the silkworm's silk gland.<sup>57-59</sup> Different biophysical properties of mulberry and non-mulberry SF is depicted in **Figure 2-12** A variety of different cell lines including mesenchymal stem cells<sup>60</sup>, fibroblasts<sup>61</sup>, osteoblasts<sup>62</sup>, myoblasts<sup>63</sup>, chondrocytes<sup>64</sup>, keratinocytes<sup>65</sup> and neurons<sup>66</sup> have been demonstrated to adhere and extensively proliferate on SF matrices. Several studies have successfully demonstrated use of SF scaffold for vascular, neural, bone, ligament, cartilage, skin, intervertebral disc, heart, ocular and spinal cord tissue regeneration.<sup>67</sup> The inherent mechanical, chemical and physiological properties of SF provide an excellent platform for BTE, which is elaborated in next section.

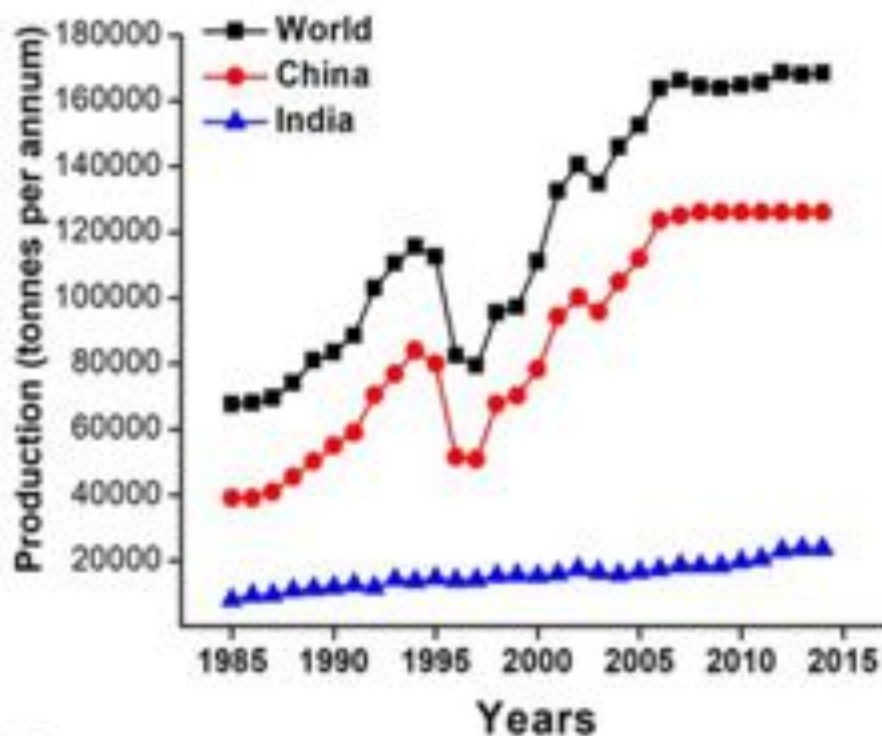


Figure 2-10 Year wise Silk production<sup>48</sup>

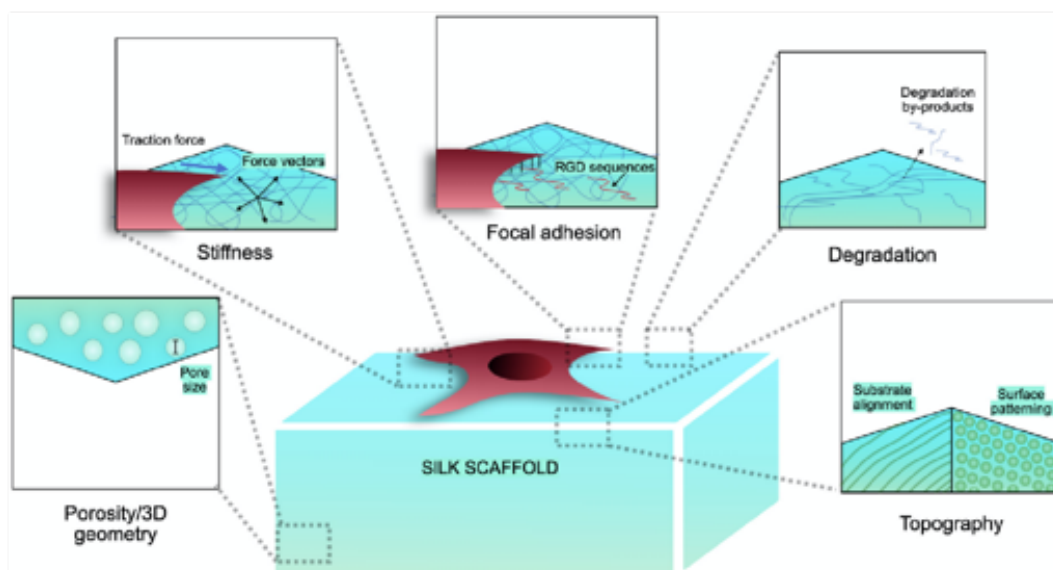
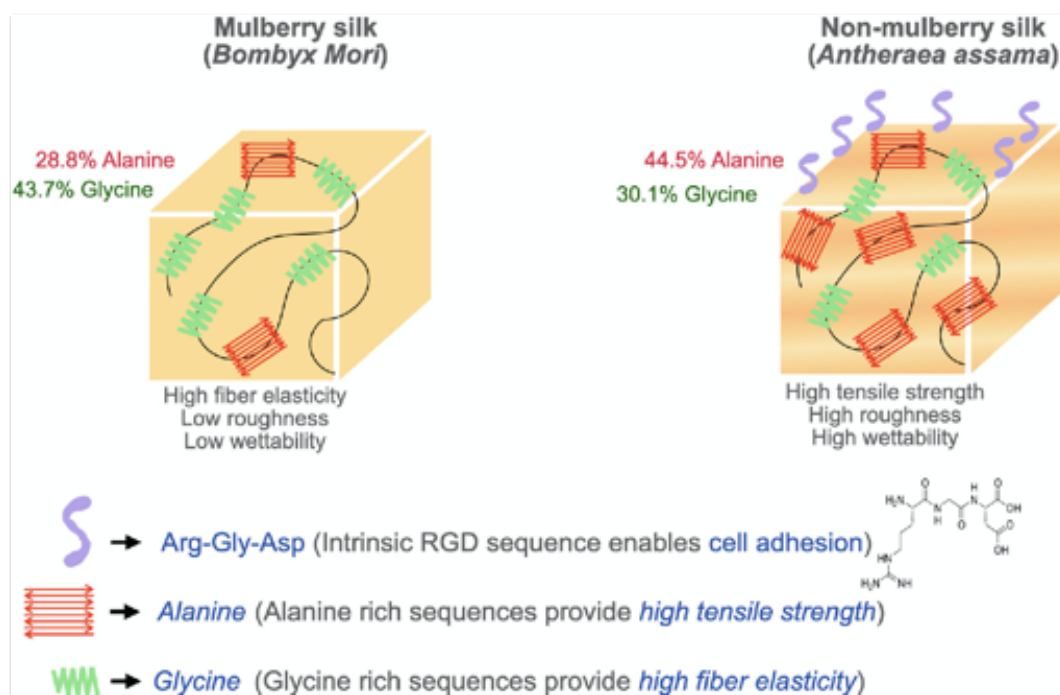


Figure 2-11 Different biophysical Properties of SF as a biomaterial to support cell-material interaction.<sup>68</sup>



**Figure 2-12** Different biophysical properties of mulberry and non-mulberry SF for biomedical applications.<sup>68</sup>

### 2.2.3 Silk Fibroin in Bone Tissue Engineering

Quality of life is majorly dependent on the musculoskeletal system where bone plays a major role. Bone can be damaged because of injuries, osteoarthritis, osteogenesis, trauma, etc. Bone repair is a complex process involving a cascade of many osteogenic events. Different types of cells, signaling molecules, and ECM proteins work together at the site of bone injury. Therefore, bone grafts material/fillers should be biocompatible, bioactive, osteoconductive and osteoinductive with a controlled degradation rate that matches the rate of ECM deposition.

SF is the oldest natural polymer having evolutionary history spanning over 380 million years. In different BTE applications, SF has been shown to function as an effective and versatile polymer. Moreover, the use of SF is the greener approach as silk protein is obtained from the cocoon and silk glands. Meinel *et al.* successfully fabricated an SF-based scaffold by using pure SF for implantation in critical-size

calvarial defects in mice.<sup>69</sup> Nanofibrous meshes developed from the SF showed good quality bone formation in rabbit calvarial defect model.<sup>70</sup> SF provides opportunity to tune its surface property.<sup>41,62</sup> During the processing of silk fibroin, conformational changes are noted. Treating SF with methanol gradually transforms silk I to silk II and Jones *et al.* reported more cell attachment and osteogenic differentiation in methanol vapor treated SF and also observed more osteoblasts in compare to osteoclasts providing a better model for co-culture.<sup>71</sup> Further, excellent literature is available on the use of SF in BTE.<sup>53,72-77</sup> The most common forms of SF-based 3D scaffolds like films, microspheres, woven and non-woven fibrous mats, sponge, hydrogel/cryogel are depicted in **Figure 2-13**. A simple surface coating strategy with SF further enhances the performance of the scaffold. Kweon *et al.* compared the osteogenic potential of hydroxyapatite (HA)-coated silk scaffolds and HA-coated collagen scaffolds. They showed that HA coated SF scaffolds can promote more bone regeneration than HA-coated collagen scaffolds.<sup>78</sup> SF is also used in many studies to achieve biomineralization. For example, Nagano *et al.* fabricated genetically modified SF with the incorporation of the poly-glutamic acid site that acts as an active site for calcium ion (Ca) binding. Their results showed higher Ca-binding activity in transgenic SF than native SF, which might be due to the introduction of hydrophilic Ca-binding sites into the hydrophobic H-chain of SF. After implanting this transgenic SF-based scaffold into the femoral epicondyle in a rabbit model, early mineralization and bone formation were observed.<sup>79</sup> SF also provides flexibility for blending with a variety of polymers and functional molecules to enhance its advantageous properties. SF-coated poly( $\epsilon$ -caprolactone) (PCL) nanofibers are used to enhance the mechanical and biological behavior of biphasic calcium phosphate (BCP) scaffolds. The proliferation and differentiation rates of osteoblasts were increased in the SF/PCL scaffold compared to that in the BCP/PCL and BCP scaffolds.<sup>80</sup> A considerable amount of research has been done on SF-based materials for growth factor delivery. BMP-2 has been reported as a potent growth factor for inducing the differentiation of hMSCs into osteoblasts. It was reported that an SF scaffold with



recombinant human BMP-2 (rhBMP-2) could promote enhanced bone regeneration than an SF scaffold without rhBMP-2. This observation put forward a more attractive strategy for the use of SF combined with a growth factor for clinical applications.<sup>81</sup> There are good reviews available that provide detailed information about the different processing techniques, a different form of SF, and its combination with other materials/polymers for BTE. Many silk-based scaffolds to regenerate bone tissues or other parts of the skeletal system that includes cartilage and ligament both *in-vitro* and *in vivo* are also reported successfully.

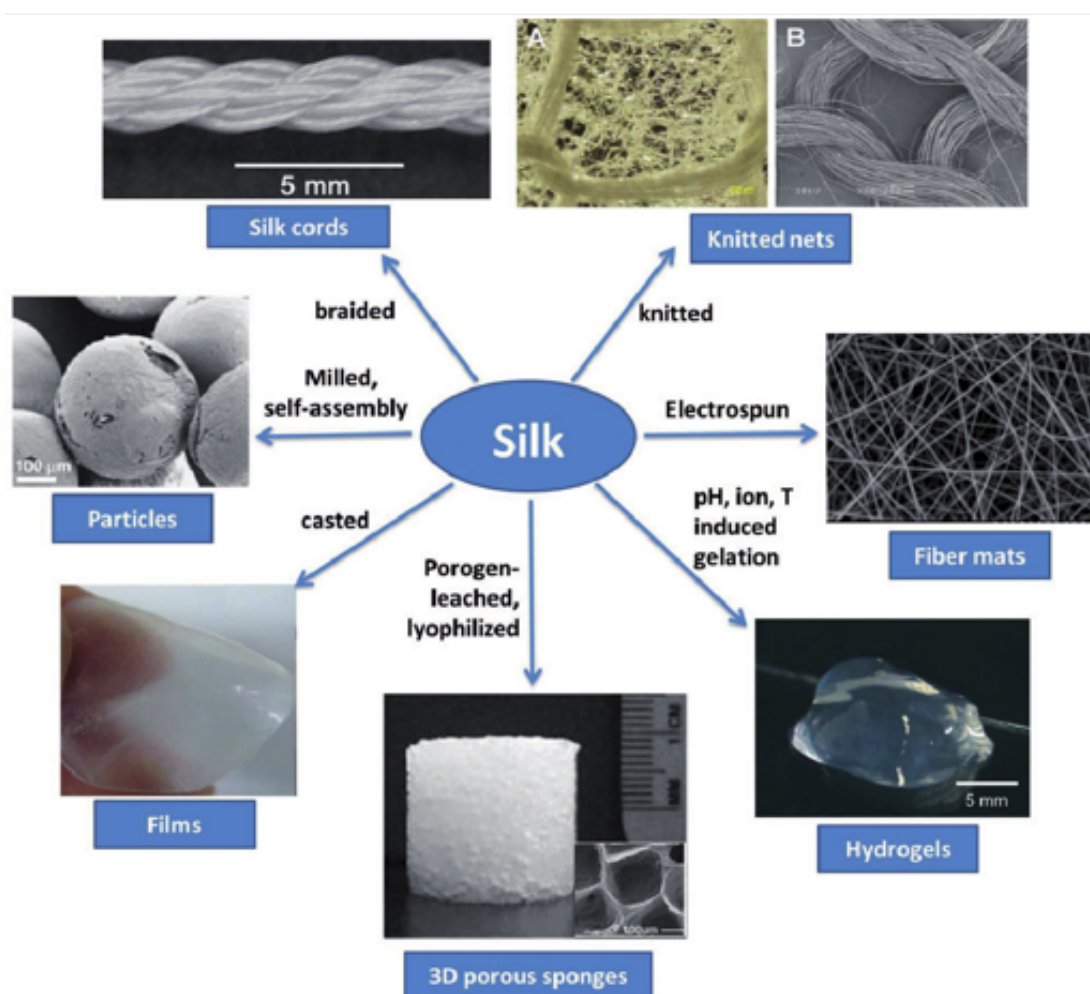


**Figure 2-13** The most reported form of SF based 3D scaffolds for BTE<sup>82</sup>

## 2.3 Motivation and Objective of Present Work

Bone is the rigid organ that supports and protects other organs/tissue. This unique property of bone is attributed to the soft collagen protein and stiffer apatite minerals. Unlike in other tissues, many bone fractures heal without the formation of scar, and new bone is regenerated with its pre-existing properties. It is eventually indistinguishable from the adjacent uninjured native bone. However, many surgical procedures such as spine fusion and sinus augmentation require bone substitutes. Each of these conditions requires a different form, structure, and shape to support BTE. Critical size bone defects require solid load-bearing bone graft fillers. In multi-fracture sites or cranial/craniofacial defects or minor cracks, non-load bearing injectable biomaterials play an important role.

All available bone graft substitutes are not suitable for every clinical use, and the bone graft substitutes must be chosen depending on the clinical condition. Also, a majority of the biomaterials placed on the market possess osteoconductive properties. However, very few offer osteoinductive properties. Even though many technologies have been developed with the consideration of chemical/material/biological aspects, translation of such technologies into clinical applications is still a major challenge. Along with the technical challenge, the scalability of the production methods huddles the clinical translation.

Most of the available strategies for BTE exhibit relatively satisfactory results. However, there are drawbacks and limitations associated with their use as well as with their availability. There are controversial reports about their efficacy and cost-effectiveness even. Furthermore, by looking at the current scenario there are no heterologous or synthetic or natural bone substitutes available that have similar biological or mechanical properties compared with native bone. Therefore, there is a necessity to develop novel alternatives or adjuncts to cope with the standard method used for bone regeneration.

In bone graft substitute, SF – a natural polymer is a promising candidate as SF is a US-FDA approved, biocompatible, biodegradable, less immunogenic biomaterial.

Therefore the present thesis work includes different strategies that aim to address the majority of prerequisites for optimal bone healing with mechanical stability, osteoconductive matrices, osteoinductive factors/molecules, cells that have potential to differentiate into osteogenic lineage. Different strategies as mentioned below form the objectives of a 3D scaffold system that can provide over all solutions to both load-bearing and non-load-bearing bone defects by using SF as a biomaterial and to enhance its osteo-regenerative capabilities.

Objective 1 - Surface coating with biopolymers on micro-particle-based SF scaffold

Objective 2 - Incorporation of bio-ceramics into SF micro-particle-based scaffold

Objective 3 - Development of non-mulberry SF electrospun scaffold

Objective 4 - Development of mulberry and non-mulberry SF based injectable scaffold

## 2.4 Reference:

- (1) Jin, Y.; Kundu, B.; Cai, Y.; Kundu, S. C.; Yao, J. Bio-Inspired Mineralization of Hydroxyapatite in 3D Silk Fibroin Hydrogel for Bone Tissue Engineering. *Colloids Surfaces B Biointerfaces* **2015**, *134*, 339–345. <https://doi.org/10.1016/j.colsurfb.2015.07.015>.
- (2) Ghelich, P.; Kazemzadeh-Narbat, M.; Hassani Najafabadi, A.; Samandari, M.; Memić, A.; Tamayol, A. (Bio)Manufactured Solutions for Treatment of Bone Defects with an Emphasis on US-FDA Regulatory Science Perspective. *Adv. NanoBiomed Res.* **2022**, 2100073.

- <https://doi.org/10.1002/anbr.202100073>.
- (3) Willems, N. M. B. K.; Langenbach, G. E. J.; Everts, V.; Zentner, A. The Microstructural and Biomechanical Development of the Condylar Bone: A Review. *Eur. J. Orthod.* **2014**, *36* (4), 479–485. <https://doi.org/10.1093/ejo/cjt093>.
- (4) Bhattacharjee, P.; Kundu, B.; Naskar, D.; Kim, H. W.; Maiti, T. K.; Bhattacharya, D.; Kundu, S. C. Silk Scaffolds in Bone Tissue Engineering: An Overview. *Acta Biomater.* **2017**, *63*, 1–17. <https://doi.org/10.1016/j.actbio.2017.09.027>.
- (5) Aubin, J. E. Regulation of Osteoblast Formation and Function. *Reviews in Endocrine and Metabolic Disorders.* **2001**, pp 81–94. <https://doi.org/10.1023/A:1010011209064>.
- (6) Huang, Z.; Nelson, E. R.; Smith, R. L.; Goodman, S. B. The Sequential Expression Profiles of Growth Factors from Osteroprogenitors to Osteoblasts in Vitro. *Tissue Eng.* **2007**, *13* (9), 2311–2320. <https://doi.org/10.1089/ten.2006.0423>.
- (7) **2012** - McNamara - Osteogenic Markar.Pdf.
- (8) Wei Huang, Shuying Yang, Jianzhong Shao, and Y.-P. L. Signaling and Transcriptional Regulation in Osteoblast Commitment and Differentiation. *Front Biosci* **2013**, *12*, 3068–3092. <https://doi.org/10.1038/jid.2014.371>.
- (9) Rutkovskiy, A.; Stensl kken, K.-O.; Vaage, I. J. Osteoblast Differentiation at a Glance. *Med. Sci. Monit. Basic Res.* **2016**, *22*, 95–106. <https://doi.org/10.12659/msmbr.901142>.
- (10) Deshpande, R.; Shukla, S. Silk Fibroin and Ceramic Scaffolds : Comparative in Vitro Studies for Bone Regeneration. **2021**, No. March, 1–12. <https://doi.org/10.1002/btm2.10221>.
- (11) Eltom, A.; Zhong, G.; Muhammad, A. Scaffold Techniques and Designs in Tissue Engineering Functions and Purposes: A Review. *Adv. Mater. Sci. Eng.* **2019**, *2019*. <https://doi.org/10.1155/2019/3429527>.

- (12) Ikada, Y. Challenges in Tissue Engineering. *J. R. Soc. Interface* **2006**, 3 (10), 589–601. <https://doi.org/10.1098/rsif.2006.0124>.
- (13) Nikolova, M. P.; Chavali, M. S. Recent Advances in Biomaterials for 3D Scaffolds: A Review. *Bioact. Mater.* **2019**, 4 (August), 271–292. <https://doi.org/10.1016/j.bioactmat.2019.10.005>.
- (14) Page, C. O. F.; Griffith, L. G.; Naughton, G. Tissue Engineering — Current Challenges and Expanding Opportunities. **2002**, 295 (February).
- (15) Wu, A.-M.; Bisignano, C.; James, S. L.; Abady, G. G.; Abedi, A.; Abu-Gharbieh, E.; Alhassan, R. K.; Alipour, V.; Arabloo, J.; Asaad, M.; Asmare, W. N.; Awedew, A. F.; Banach, M.; Banerjee, S. K.; Bijani, A.; Birhanu, T. T. M.; Bolla, S. R.; Cámera, L. A.; Chang, J.-C.; Cho, D. Y.; Chung, M. T.; Couto, R. A. S.; Dai, X.; Dandona, L.; Dandona, R.; Farzadfar, F.; Filip, I.; Fischer, F.; Fomenkov, A. A.; Gill, T. K.; Gupta, B.; Haagsma, J. A.; Haj-Mirzaian, A.; Hamidi, S.; Hay, S. I.; Ilic, I. M.; Ilic, M. D.; Ivers, R. Q.; Jürisson, M.; Kalhor, R.; Kanchan, T.; Kavetsky, T.; Khalilov, R.; Khan, E. A.; Khan, M.; Kneib, C. J.; Krishnamoorthy, V.; Kumar, G. A.; Kumar, N.; Laloo, R.; Lasrado, S.; Lim, S. S.; Liu, Z.; Manafi, A.; Manafi, N.; Menezes, R. G.; Meretoja, T. J.; Miazgowski, B.; Miller, T. R.; Mohammad, Y.; Mohammadian-Hafshejani, A.; Mokdad, A. H.; Murray, C. J. L.; Naderi, M.; Naimzada, M. D.; Nayak, V. C.; Nguyen, C. T.; Nikbakhsh, R.; Olagunju, A. T.; Otstavnov, N.; Otstavnov, S. S.; Padubidri, J. R.; Pereira, J.; Pham, H. Q.; Pinheiro, M.; Polinder, S.; Pourchamani, H.; Rabiee, N.; Radfar, A.; Rahman, M. H. U.; Rawaf, D. L.; Rawaf, S.; Saeb, M. R.; Samy, A. M.; Sanchez Riera, L.; Schwebel, D. C.; Shahabi, S.; Shaikh, M. A.; Soheili, A.; Tabarés-Seisdedos, R.; Tovani-Palone, M. R.; Tran, B. X.; Travillian, R. S.; Valdez, P. R.; Vasankari, T. J.; Velazquez, D. Z.; Venketasubramanian, N.; Vu, G. T.; Zhang, Z.-J.; Vos, T. Global, Regional, and National Burden of Bone Fractures in 204 Countries and Territories, 1990–2019: A Systematic Analysis from the Global Burden of Disease Study **2019**. *Lancet Heal. Longev.* 2021, 2 (9), e580–e592. [https://doi.org/10.1016/s2666-7568\(21\)00172-0](https://doi.org/10.1016/s2666-7568(21)00172-0).

- (16) Tissue Engineering Market Size, Industry Analysis Report, 2027. *Finance* **2020**, 1–7.
- (17) Kruger, M. J.; Nell, T. A. Bone Mineral Density in People Living with HIV: A Narrative Review of the Literature. *AIDS Res. Ther.* **2017**, *14* (1), 1–17. <https://doi.org/10.1186/s12981-017-0162-y>.
- (18) Global Bone Graft and Substitutes Market Report, 2021-2028. **2021**, 1–8.
- (19) Vidal, L.; Kampleitner, C.; Brennan, M.; Hoornaert, A.; Layrolle, P. Reconstruction of Large Skeletal Defects: Current Clinical Therapeutic Strategies and Future Directions Using 3D Printing. *Front. Bioeng. Biotechnol.* **2020**, *8* (February). <https://doi.org/10.3389/fbioe.2020.00061>.
- (20) Fernandez de Grado, G.; Keller, L.; Idoux-Gillet, Y.; Wagner, Q.; Musset, A. M.; Benkirane-Jessel, N.; Bornert, F.; Offner, D. Bone Substitutes: A Review of Their Characteristics, Clinical Use, and Perspectives for Large Bone Defects Management. *J. Tissue Eng.* **2018**, *9*. <https://doi.org/10.1177/2041731418776819>.
- (21) Carson, J. S.; Bostrom, M. P. G. Synthetic Bone Scaffolds and Fracture Repair. *Injury* **2007**, *38* (SUPPL. 1). <https://doi.org/10.1016/j.injury.2007.02.008>.
- (22) Alaribe, F. N.; Manoto, S. L.; Motaung, S. C. K. M. Scaffolds from Biomaterials: Advantages and Limitations in Bone and Tissue Engineering. *Biologia (Bratisl)*. **2016**, *71* (4), 353–366. <https://doi.org/10.1515/biolog-2016-0056>.
- (23) Schmidt, A. H. Autologous Bone Graft: Is It Still the Gold Standard? *Injury* **2021**, *52*, S18–S22. <https://doi.org/10.1016/j.injury.2021.01.043>.
- (24) Roberts, T. T.; Rosenbaum, A. J. Bone Grafts, Bone Substitutes and Orthobiologics. *Organogenesis* **2012**, *8* (4), 114–124. <https://doi.org/10.4161/org.23306>.
- (25) Stevenson S, Li XQ, M. B. The Fate of Cancellous and Cortical Bone after Transplantation of Fresh and Frozen Tissue-Antigen-Matched and

- Mismatched Osteochondral Allografts in Dogs. *J. Bone Jt. Surg.* **1991**, 73 (8), 1143–1156.
- (26) Eggli PS, Müller W, S. R. Porous Hydroxyapatite and Tricalcium Phosphate Cylinders with Two Different Pore Size Ranges Implanted in the Cancellous Bone of Rabbits. A Comparative Histomorphometric and Histologic Study of Bony Ingrowth and Implant Substitution. *Clin. Orthop. Relat. Res.* **1998**, No. 232, 127–138.
- (27) Gao, C.; Deng, Y.; Feng, P.; Mao, Z.; Li, P.; Yang, B.; Deng, J.; Cao, Y.; Shuai, C.; Peng, S. Current Progress in Bioactive Ceramic Scaffolds for Bone Repair and Regeneration. *Int. J. Mol. Sci.* **2014**, 15 (3), 4714–4732. <https://doi.org/10.3390/ijms15034714>.
- (28) Stefan Zwingenberger, Christophe Nich, Roberto D. Valladares, Zhenyu Yao, Maik Stiehler, and S. B. G. Recommendations and Considerations for the Use of Biologics in Orthopedic Surgery. **2012**, 26 (4), 245–256. <https://doi.org/10.2165/11631680-000000000-00000.Recommendations>.
- (29) Nikakhtar, Y.; Shafiei, S. S.; Fathi-roudsari, M.; Asadi-Eydivand, M.; ShiraliPour, F. Preparation and Characterization of Electrospun Polycaprolactone/Brushite Scaffolds to Promote Osteogenic Differentiation of Mesenchymal Stem Cells. *J. Biomater. Sci. Polym. Ed.* **2022**, 0 (0), 1–21. <https://doi.org/10.1080/09205063.2022.2041786>.
- (30) Rozalia Dimitriou, Elena Jones, D. M. and P. V. G. Bone Regeneration: Current Concepts and Future Directions Rozalia. *BMC Med.* **2011**, 43.
- (31) Troy, E.; Tilbury, M. A.; Power, A. M.; Wall, J. G. Nature-Based Biomaterials and Their Application in Biomedicine. *Polymers (Basel)*. **2021**, 13 (19), 1–37. <https://doi.org/10.3390/polym13193321>.
- (32) Taura, J. R. S. Jin and Kaplan - Mechanism of Silk Processing in Insects and Spiders. **2003**, 926 (2002), 1057–1061.
- (33) Sutherland, T. D.; Young, J. H.; Weisman, S.; Hayashi, C. Y.; Merritt, D. J. Insect

- Silk: One Name, Many Materials. *Annu. Rev. Entomol.* **2010**, *55*, 171–188. <https://doi.org/10.1146/annurev-ento-112408-085401>.
- (34) Kundu, S. C.; Kundu, B.; Talukdar, S.; Bano, S.; Nayak, S.; Kundu, J.; Mandal, B. B.; Bhardwaj, N.; Botlagunta, M.; Dash, B. C.; Acharya, C.; Ghosh, A. K. Invited Review: Nonmulberry Silk Biopolymers. *Biopolymers* **2012**, *97* (6), 455–467. <https://doi.org/10.1002/bip.22024>.
- (35) Muthumanickam, A.; Subramanian, S. Comparative Study on Eri Silk and Mulberry Silk Fibroin Scaffolds for Biomedical Applications. **2013**, 143–154. <https://doi.org/10.1007/s13726-012-0113-3>.
- (36) Kaplan, D.; Adams, W. W.; Farmer, B.; Viney, C. Chapter 1 Silk: Biology, Structure, Properties, and Genetics. **1994**, 2–16.
- (37) Mottaghitlab, F.; Hosseinkhani, H.; Shokrgozar, M.; Mao, C.; Yang, M.; Farokhi, M. Silk as a Potential Candidate for Bone Tissue Engineering. *J. Control. release* **2015**, *215*, 112–128.
- (38) Nguyen, T. P.; Nguyen, Q. V.; Nguyen, V. H.; Le, T. H.; Huynh, V. Q. N.; Vo, D. V. N.; Trinh, Q. T.; Kim, S. Y.; Van Le, Q. Silk Fibroin-Based Biomaterials for Biomedical Applications: A Review. *Polymers (Basel)*. **2019**, *11* (12), 1–25. <https://doi.org/10.3390/polym11121933>.
- (39) Tetsuo Asakura, Yu Suzuki, Yasumoto Nakazawa, G. P. H. J. L. Y. Elucidating Silk Structure Using Solid-State NMR. *Soft Matter* **2013**, *9*, 1440–11450.
- (40) Wilson, D.; Valluzzi, R.; Kaplan, D. Conformational Transitions in Model Silk Peptides [In Process Citation]. *Biophys J* **2000**, *78* (5), 2690–2701.
- (41) vepari C., K. D. L. Silk as Biomaterial. **2007**, *32* (8–9), 991–1007. <https://doi.org/10.1016/j.pestbp.2011.02.012>.Investigations.
- (42) Malay, A. D.; Sato, R.; Yazawa, K.; Watanabe, H.; Ifuku, N.; Masunaga, H.; Hikima, T.; Guan, J.; Mandal, B. B.; Damrongsakkul, S.; Numata, K. Relationships between Physical Properties and Sequence in Silkworm Silks. *Sci. Rep.* **2016**, *6* (June), 1–11. <https://doi.org/10.1038/srep27573>.



- (43) Katanchalee Mai-ngam, Kanhokthorn Boonkitpattarakul, J. J. & Bunpot M. Evaluation of the Properties of Silk Fibroin Films from the Non-Mulberry Silkworm *Samia Cynthia Ricini* for Biomaterial Design. *J. Biomater. Sci. Polym. Ed.* **2011**, 22 (15), 2001–2022.
- (44) Sen, K.; Babu K, M. Studies on Indian Silk. I. Macrocharacterization and Analysis of Amino Acid Composition. *J. Appl. Polym. Sci.* **2004**, 92 (2), 1080–1097. <https://doi.org/10.1002/app.13609>.
- (45) Adarsh Gupta, K.; Mita, K.; Arunkumar, K. P.; Nagaraju, J. Molecular Architecture of Silk Fibroin of Indian Golden Silkworm, *Antheraea Assama*. *Sci. Rep.* **2015**, 5, 1–17. <https://doi.org/10.1038/srep12706>.
- (46) Reddy, N.; Yang, Y. Structure and Properties of Cocoons and Silk Fibers Produced by *Hyalophora Cecropia*. *J. Mater. Sci.* **2010**, 45 (16), 4414–4421. <https://doi.org/10.1007/s10853-010-4523-3>.
- (47) Das, S., Chattopadhyay, R., Gulrajani, M. L., Sen, K. Study of Property & Structural Variants of Mulberry and Tasar Silk Filaments. *Autex Res. J.* **2005**, 5 (2), 81–86.
- (48) Bandyopadhyay, A.; Chowdhury, S. K.; Dey, S.; Moses, J. C.; Mandal, B. B. Silk : A Promising Biomaterial Opening New Vistas REVIEW. *J. Indian Inst. Sci.* **2019**, 99 (3), 445–487. <https://doi.org/10.1007/s41745-019-00114-y>.
- (49) Goel, A. Surgical Sutures - A Review. *Delhi J. Ophthalmol.* 2016, 26 (3), 159–162. <https://doi.org/10.7869/djo.161>.
- (50) Midha, S.; Murab, S.; Ghosh, S. Osteogenic Signaling on Silk-Based Matrices. *Biomaterials* **2016**, 97, 133–153. <https://doi.org/10.1016/j.biomaterials.2016.04.020>.
- (51) Fiorenzo G. Omenetto and David L. Kaplan. New Opportunities for an Ancient Material Fiorenzo. *Science (80-. )*. **2010**, 329 (5991), 528–531. <https://doi.org/10.1126/science.1188936>.New.
- (52) Gregory H. Altman, Frank Diaz, Caroline Jakuba, Tara Calabro,

- RebeccaL.Horan, JingsongChen, HelenLu, JohnRichmond, D. K. Silk-Based Biomaterials. *Biomaterials* **2003**, *24*, 401–416.
- (53) Melke, J.; Midha, S.; Ghosh, S.; Ito, K.; Hofmann, S. Silk Fibroin as Biomaterial for Bone Tissue Engineering. *Acta Biomater.* **2015**, *31*, 1–16. <https://doi.org/10.1016/j.actbio.2015.09.005>.
- (54) Singh, B. N.; Pramanik, K. Tissue and Cell Fabrication and Evaluation of Non-Mulberry Silk Fibroin Fiber Reinforced Chitosan Based Porous Composite Scaffold for Cartilage Tissue Engineering. **2018**, *55* (October), 83–90. <https://doi.org/10.1016/j.tice.2018.10.003>.
- (55) Darshan, G. H.; Kong, D.; Gautrot, J.; Vootla, S. Physico-Chemical Characterization of Antheraea Mylitta Silk Mats for Wound Healing Applications. *Sci. Rep.* **2017**, *7* (1), 1–11. <https://doi.org/10.1038/s41598-017-10531-7>.
- (56) Andiappan, M.; Kumari, T.; Sundaramoorthy, S.; Meiyazhagan, G.; Manoharan, P.; Venkataraman, G. Comparison of Eri and Tasar Silk Fibroin Scaffolds for Biomedical Applications. *Prog. Biomater.* **2016**, *5* (2), 81–91. <https://doi.org/10.1007/s40204-016-0047-5>.
- (57) Konwarh, R.; Bhunia, B. K.; Mandal, B. B. Opportunities and Challenges in Exploring Indian Non-Mulberry Silk for Biomedical Applications. *Proc. Indian Natl. Sci. Acad.* **2017**, *83* (1), 85–101. <https://doi.org/10.16943/ptinsa/2017/41288>.
- (58) Gupta, P.; Adhikary, M.; M, J. C.; Kumar, M.; Bhardwaj, N.; Mandal, B. B. Biomimetic, Osteoconductive Non-Mulberry Silk Fiber Reinforced Tricomposite Scaffolds for Bone Tissue Engineering. *ACS Appl. Mater. Interfaces* **2016**, *8* (45), 30797–30810. <https://doi.org/10.1021/acsami.6b11366>.
- (59) Mandal, B. B.; Kundu, S. C. Non-Mulberry Silk Gland Fibroin Protein 3-D Scaffold for Enhanced Differentiation of Human Mesenchymal Stem Cells

- into Osteocytes. *Acta Biomater.* **2009**, 5 (7), 2579–2590. <https://doi.org/10.1016/j.actbio.2009.02.033>.
- (60) Parekh, N. A.; Deshpande, R. V.; Shukla, S. G.; Nisal, A. A. Silk Fibroin 3D Microparticle Scaffolds with Bioactive Ceramics: Chemical, Mechanical, and Osteoregenerative Characteristics. *Adv. Eng. Mater.* **2020**, 2000458, 1–11. <https://doi.org/10.1002/adem.202000458>.
- (61) Sween Gilotr, Dimple Chouhan, Nandana Bhardwaj, Samit Kumar Nandi, B. B. M. Potential of Silk Sericin Based Nanofibrous Mats for Wound Dressing Applications. *Mater. Sci. Eng. C* **2018**, 420–432.
- (62) Parekh, N.; Hushye, C.; Warunkar, S.; Gupta, S. Sen; Nisal, A. RSC Advances In Vitro Study of Novel Microparticle Based Silk. *RSC Adv.* **2017**, 7, 26551–26558. <https://doi.org/10.1039/C7RA03288A>.
- (63) Shivaprasad Manchineella, Greeshma Thrivikraman, Khadija K. Khanum, Praveen C. Ramamurthy, Bikramjit Basu, T. G. Pigmented Silk Nanofibrous Composite for Skeletal Muscle Tissue Engineering. *Adv. Healthc. Mater.* **2016**, 25, 1222–1232.
- (64) Pen-Hsiu Grace Chao, Supansa Yodmuang, Xiaoqin Wang, Lin Sun, David L. Kaplan, and G. V.-N. Silk Hydrogel for Cartilage Tissue Engineering. *J Biomed Mater Res B Appl Biomater* **2010**, 95 (1), : 84–90.
- (65) Levin, B.; Redmond, S. L.; Rajkhowa, R.; Eikelboom, R. H.; Atlas, M. D.; And; Marano, R. J. Utilising Silk Fibroin Membranes as Scaffolds for the Growth of Tympanic Membrane Keratinocytes, and Application to Myringoplasty Surgery. *J. Laryngol. Otol.* **2012**, 127 (S1), S13–S20.
- (66) Adrián Magaz, Ben F. Spencer, John G. Hardy, Xu Li, Julie E. Gough, and J. J. B. Modulation of Neuronal Cell Affinity on PEDOT–PSS Nonwoven Silk Scaffolds for Neural Tissue Engineering. *ACS Biomater. Sci. Eng.* **2020**, 6 (12), 6906–6916.
- (67) Jao, D.; Mou, X.; Hu, X. Tissue Regeneration: A Silk Road. *J. Funct. Biomater.*

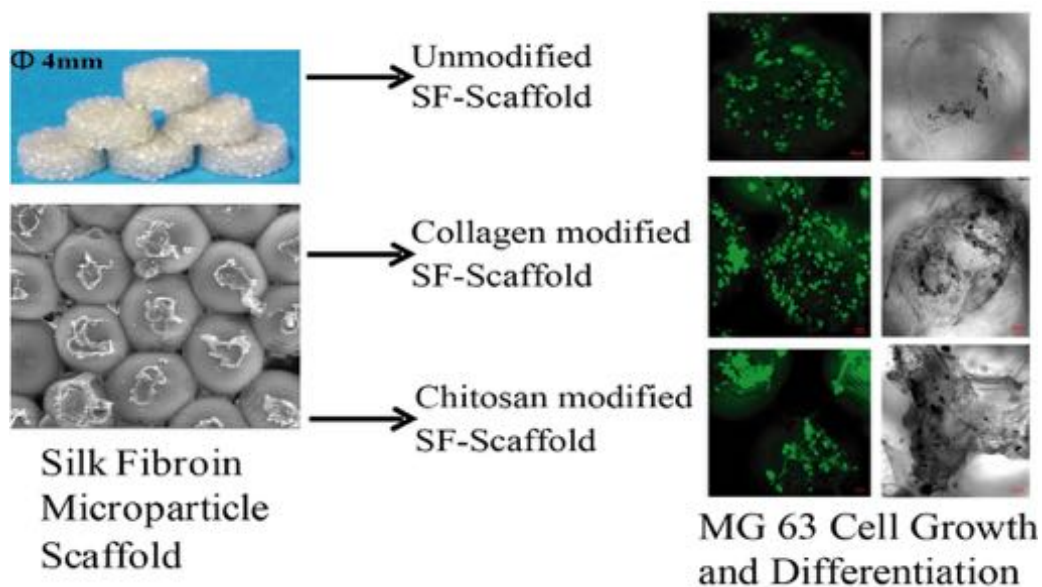
- 2016**, 7 (3), 22. <https://doi.org/10.3390/jfb7030022>.
- (68) Kochhar, D.; Debari, M. K.; Abbott, R. D.; Abbott, R. D. The Materiobiology of Silk: Exploring the Biophysical Influence of Silk Biomaterials on Directing Cellular Behaviors. **2021**, 9 (June), 1–11. <https://doi.org/10.3389/fbioe.2021.697981>.
- (69) Meinel, L.; Fajardo, R.; Hofmann, S.; Langer, R.; Chen, J.; Snyder, B.; Vunjak-Novakovic, G.; Kaplan, D. Silk Implants for the Healing of Critical Size Bone Defects. *Bone* **2005**, 37 (5), 688–698. <https://doi.org/10.1016/j.bone.2005.06.010>.
- (70) Jo, Y. Y.; Kim, S. G.; Kwon, K. J.; Kweon, H. Y.; Chae, W. S.; Yang, W. G.; Lee, E. Y.; Seok, H. Silk Fibroin-Alginate-Hydroxyapatite Composite Particles in Bone Tissue Engineering Applications in Vivo. *Int. J. Mol. Sci.* **2017**, 18 (4). <https://doi.org/10.3390/ijms18040858>.
- (71) Jones, G. L.; Motta, A.; Marshall, M. J.; El Haj, A. J.; Cartmell, S. H. Osteoblast: Osteoclast Co-Cultures on Silk Fibroin, Chitosan and PLLA Films. *Biomaterials* **2009**, 30 (29), 5376–5384. <https://doi.org/10.1016/j.biomaterials.2009.07.028>.
- (72) Nisal, A.; Sayyad, R.; Dhavale, P.; Khude, B.; Deshpande, R. Silk Fibroin Micro-Particle Scaffolds with Superior Compression Modulus and Slow Bioresorption for Effective Bone Regeneration. **2018**, No. April, 1–10. <https://doi.org/10.1038/s41598-018-25643-x>.
- (73) Mandal, B. B.; Grinberg, A.; Seok, E.; Panilaitis, B.; Kaplan, D. L. High-Strength Silk Protein Scaffolds for Bone Repair. *Pnas* **2012**, 109 (20), 7699–7704. <https://doi.org/10.1073/pnas.1119474109>.
- (74) Singh, Y. P.; Moses, J. C.; Bhunia, B. K.; Nandi, S. K.; Mandal, B. B. Hierarchically Structured Seamless Silk Scaffolds for Osteochondral Interface Tissue Engineering. *J. Mater. Chem. B* **2018**, 6 (36), 5671–5688. <https://doi.org/10.1039/c8tb01344f>.

- (75) Behera, S.; Naskar, D.; Sapru, S.; Bhattacharjee, P.; Dey, T.; Ghosh, A. K.; Mandal, M.; Kundu, S. C. Hydroxyapatite Reinforced Inherent RGD Containing Silk Fibroin Composite Scaffolds: Promising Platform for Bone Tissue Engineering. *Nanomedicine Nanotechnology, Biol. Med.* **2017**, *13* (5), 1745–1759. <https://doi.org/10.1016/j.nano.2017.02.016>.
- (76) Naskar, D.; Nayak, S.; Dey, T.; Kundu, S. C. Non-Mulberry Silk Fibroin Influence Osteogenesis and Osteoblast-Macrophage Cross Talk on Titanium Based Surface. *Sci. Rep.* **2014**, *4*, 4745. <https://doi.org/10.1038/srep04745>.
- (77) Kasoju, N.; Bora, U. Silk Fibroin in Tissue Engineering. *Adv. Healthc. Mater.* **2012**, *1* (4), 393–412. <https://doi.org/10.1002/adhm.201200097>.
- (78) Kweon, H.; Lee, S.-W.; Hahn, B.-D.; Yong-Chan Lee, D.; Kim, S.-G. Hydroxyapatite and Silk Combination-Coated Dental Implants Result in Superior Bone Formation in the Peri-Implant Area Compared With Hydroxyapatite and Collagen Combination-Coated Implants. *J. Oral Maxillofac. Surg.* **2014**.
- (79) Nagano, A.; Tanioka, Y.; Sakurai, N.; Sezutsu, H.; Kuboyama, N.; Kiba, H.; Tanimoto, Y.; Nishiyama, N.; Asakura, T. Regeneration of the Femoral Epicondyle on Calcium-Binding Silk Scaffolds Developed Using Transgenic Silk Fibroin Produced by Transgenic Silkworm. *Acta Biomater.* **2011**, *7* (3), 1192–1201. <https://doi.org/10.1016/j.actbio.2010.10.032>.
- (80) Roohani-Esfahani, S. I.; Lu, Z. F.; Li, J. J.; Ellis-Behnke, R.; Kaplan, D. L.; Zreiqat, H. Effect of Self-Assembled Nanofibrous Silk/Polycaprolactone Layer on the Osteoconductivity and Mechanical Properties of Biphasic Calcium Phosphate Scaffolds. *Acta Biomater.* **2012**, *8* (1), 302–312. <https://doi.org/10.1016/j.actbio.2011.10.009>.
- (81) C Kirker-Head, Karageorgiou V, S Hofmann, R Fajardo, O Betz, H P Merkle, M Hilbe, B von Rechenberg, J McCool, L Abrahamsen, A Nazarian, E Cory, M. C. D. K. and L. M. BMP-Silk Composite Matrices Heal Critically Sized Femoral

Defects. *Bone* **2007**, *41* (2), 247–255.  
<https://doi.org/10.1016/j.bone.2007.04.186>.BMP-Silk.

- (82) Yao, D.; Liu, H.; Fan, Y. Silk Scaffolds for Musculoskeletal Tissue Engineering. *Exp. Biol. Med.* **2016**, *241* (3), 238–245.  
<https://doi.org/10.1177/1535370215606994>.

# Chapter 3 Surface coating with biopolymers on silk fibroin micro-particle based scaffold



This chapter is adapted from the following publication:

“*In-vitro* study of novel microparticle based Silk Fibroin scaffold with osteoblast-like cells for load-bearing osteo-regenerative applications”, **Nimisha Parekh\***, Chandani Hushye, Saniya Warunkar, Sayam Sen Gupta and Anuya Nisal\*, RSC Advances, **2017**, 7, 26551 – 26558.

## 3.1 Abstract

SF is considered one of the most favorable materials for bone tissue engineering today. We have prepared novel SF microparticle-based 3D scaffolds with appropriate pore size, pore interconnectivity and porosity, excellent mechanical properties, and tuneable bioresorption, while retaining SF's inherent biocompatibility. These properties make them ideal candidates for osteo-regenerative applications. Here, we report the *in-vitro* cell viability, adhesion, and proliferation with osteoblastic differentiation of MG63 osteoblast-like cell line on these scaffolds. In addition, we have also modified the surface of these scaffolds using Collagen Type I and chitosan biopolymers. Our results show that although the SF scaffold does support *in-vitro* cell attachment, proliferation and differentiation, this performance can be significantly enhanced using the surface coating approach. Also, the alkaline phosphatase (ALP) activity and bone mineralisation were significantly enhanced in the chitosan modified scaffolds.

This Chapter begins with Section 3.2, which describes a review of literature that outlines the challenges associated with bone tissue engineering and requirements for further modifications in available SF based biomaterials. Section 3.3 discusses the methodology used for the formation and surface modification of microparticle-based SF scaffolds and their characterisation, while Section 3.4 discusses results in detailed experiments. Section 3.5 concludes Chapter 1A.

## 3.2 Literature Review

Bone tissue engineering (BTE) has emerged as a promising method for accelerated healing of damaged bone tissues.<sup>1</sup> BTE involves use of a 3D scaffold that supports cell attachment and natural tissue formation, thus mimicking the biological



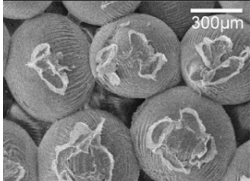
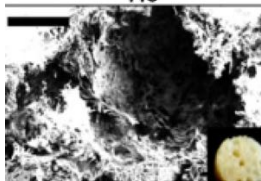
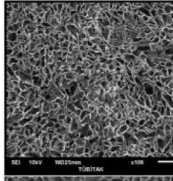
extracellular matrix. There are, therefore, stringent requirements on the properties of the scaffold that can be used in BTE.<sup>2-4</sup>

Calcium phosphate and bioresorbable bioactive glass-based micro-porous ceramic scaffolds have been extensively explored for use in BTE because of their similar chemistry with bone tissue.<sup>5</sup> However, they are limited by their brittleness.<sup>5</sup> In contrast, various natural and synthetic polymeric 3D platforms have been extensively studied for BTE, and they exhibit better biocompatibility and mechanical properties.<sup>6</sup> However, polymer-based matrices typically do not possess the mechanical properties of ceramics and rapidly degrade *in-vivo*; thus, they remain nondurable for load-bearing applications required in BTE. Recently, much interest has been focused on composite materials, which attempt to combine the advantages of both polymers and ceramics. However, a 3D scaffold composed of 100% biopolymer has composite materials' properties is desirable.<sup>7,8</sup>

In this context, from the last two decades, SF has emerged as a promising material for BTE on account of its excellent biocompatibility, tuneable bioresorption, easy processability and thermo-mechanical stability.<sup>1,9-11</sup> SF allows easy chemical modification,<sup>12</sup> to obtain required functionality and be processed into 3D materials like hydrogels, sponges, fibres, microspheres, and electrospun fiber mats.<sup>13-17</sup>

The unique mechanical properties and tuneable bioresorption rate of these 3D scaffolds allow attachment, proliferation and differentiation of mesenchymal stem cells along the osteogenic lineage for BTE.<sup>18-24</sup> The efficacy of these 3D scaffolds from SF gets enhanced when they are surface-functionalized with integrin-binding RGD motifs, collagen, chitosan, gelatin and growth factors like transforming growth factor- $\beta$  (TGF- $\beta$ ), VEG-F and bone morphogenic protein (BMPs).<sup>25-27</sup> However, the main limitation of the scaffolds discussed above is that they are primarily soft in nature and do not have high load-bearing capacity, which is essential for BTE. Recently, high strength SF scaffold for BTE, which possess a high

load-bearing ability, has been reported by a few groups.<sup>28-30</sup> Ak et al. have described a novel method of cryo-gelation using a cross-linker molecule.<sup>28</sup> Also, Mandal et al. have described scaffolds prepared using salt leaching and reinforced with SF microfibers. Nisal et al. have recently developed novel processing protocols to produce unique 3D scaffolds of silk fibroin using SF micro-particles.<sup>31,32</sup> Here, the SF microparticles are produced by a collection of drops of SF solution in a bath. These micro-particles are then fused using a dilute solution of SF in water. This novel protocol was then used to produce 3D scaffolds with excellent mechanical properties (Dry compression modulus 10-100MPa, Wet compression modulus of 25MPa), which is one of the main prerequisites for BTE and property is property lacking in most 100% SF based scaffolds.<sup>33</sup> The bulk porosity in scaffolds is in the range of 40-60%, and the pore sizes are of the order of 50-500 $\mu$ m. It has been well documented that microparticle based scaffolds have improved pore interconnectivity and better control on pore size and porosity.<sup>34</sup> The conformation of SF protein in the microparticle can be controlled, which implies that the bioresorption of the scaffold can be tuned. In addition to these advantages, the methodology of scaffold fabrication is flexible enough to incorporate various functionalities such as growth factors, fillers and drug molecules, amongst others. These properties make this scaffold unique for BTE compared to other scaffolds recently reported. A comparison of properties with other load-bearing SF- scaffolds are reported in **Table 3-1**.

Property	SF microparticle scaffold	Mandalet <i>al.</i> 2012	Aket <i>al.</i> 2012
Method of preparation	SF micro-particles fused using aq. SF solution	Salt leaching using SF: HFIP solutions with reinforcing SF microfibers	Gelation reaction of frozen SF solutions
Pore size ( $\mu\text{m}$ )	50 - 500	500 - 600	10 - 30
Porosity (%)	40 - 60 %	69 - 90 %	90 %
Dry Compression modulus (MPa)	60 - 100	Not reported	2 - 48
Wet Compression modulus (MPa)	0.1 - 30	0.1 - 12	Not reported
Bioresorption	Tunable (invivo few months to 2 years)	Not reported	Not reported
Scanning Electron Microscopy images			

**Table 3-1** Comparison properties of our newly developed SF microparticle scaffold with other reported silk scaffolds

This chapter explores the *in-vitro* cell morphology, cell viability, cell adhesion and proliferation with osteoblastic differentiation of MG63 osteoblast-like cell line on these scaffolds containing 100% SF and having high mechanical strengths. In addition, in this chapter, we report a simple method to enhance the performance of this SF-Scaffold for BTE by surface coating the scaffolds with collagen Type I and chitosan biopolymers. Collagen, a dominant component of the ECM in bone tissue, is known to favour cell adhesion and provide the correct chemical cues for osteogenic differentiation.<sup>35-37</sup> On the other hand, chitosan is known for its inherent osteogenic potential and has been a well-documented biopolymer for BTE.<sup>38-42</sup> We show the *in-vitro* cell viability, adhesion, and proliferation with osteoblastic differentiation of MG-63 osteoblast-like cells in collagen (Coll-SF)/chitosan (CS-SF) coated SF scaffolds and compared their performance to the uncoated scaffolds.

## **3.3 Experimental Section – Materials and Methods**

### **3.3.1 SF-scaffold preparation**

SF-Scaffold has been prepared as per the protocol mentioned in the earlier work.<sup>29,30</sup> In brief, a 4ml syringe was filled with the SF-HFIP solution. A syringe pump with a infuse rate of 1ml/min was used, and the drops of SF-Hexafluoroisopropanol (HFIP) solution were collected in a stirred methanol coagulant bath. The particles so formed were kept in a methanol bath for 3h. Fresh methanol was then replenished after 3h, and the particles were further incubated in methanol for 12h. The micro-particles were allowed to air dry, and the 3D SF

scaffold was prepared by fusing these SF micro-particles in a cylindrical mould using an aqueous SF solution, as shown in **Figure 3-1**.

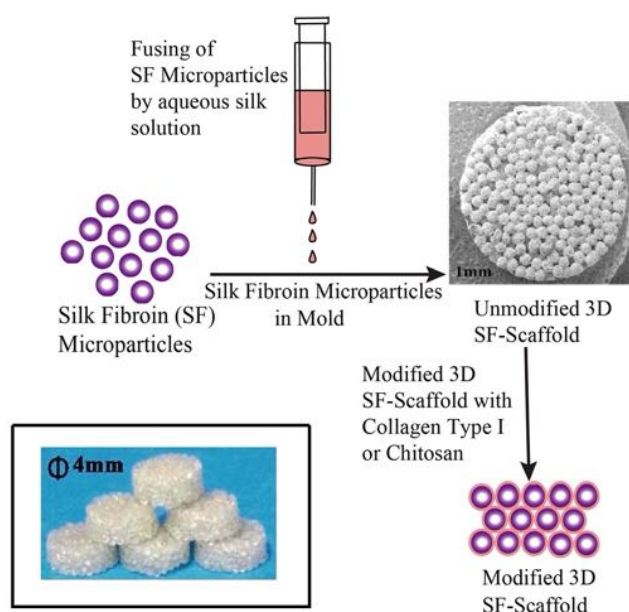


**Figure 3-1** Schematic representation of SF-Scaffold preparation and surface modification

### 3.3.2 Surface modification

For Collagen: 1 mg/mL sterile collagen solution (Sigma) was diluted ten times using sterile DI water. An SF scaffold was kept in the well of a 96 well plate. 100  $\mu$ L of the collagen solution prepared was added to each well and incubated at room temperature for 12h. The remaining solution was then pipetted out, and the scaffold was dried at 4°C for 12h. The scaffold was stored at 4°C until further use.

For Chitosan: 1wt% chitosan (Sigma) solution was prepared in 0.05M acetic acid. 100 $\mu$ L of this chitosan solution was added per scaffold to the SF scaffold and kept at 60°C for 20 minutes in an oven to obtain a dry CS-SF scaffold.

### **3.3.3 Surface characterisation by scanning electron microscopy**

The uncoated and coated SF scaffolds were observed for surface features using a Scanning Electron Microscope (SEM). Before SEM imaging, the samples were sputter-coated with a 5nm gold (Au) coating with a Polaron SC 6420 sputter coater. The image was captured on a Quanta 200 3D SEM equipped with a tungsten filament gun, operating at WD 10.6mm and 20kV. Images of representative areas at suitable magnification were captured.

### **3.3.4 Cell culture**

MG63 human osteoblast-like cells were purchased from National Centre for Cell Science (NCCS), Pune, Maharashtra, India. Cells were maintained in DMEM (Gibco) with 10% FBS (Gibco).

### **3.3.5 Cell viability**

#### **3.3.5.1 Trypan blue assay**

MG-63 cells were maintained in complete media containing DMEM with 10% FBS. Before seeding the cells, scaffolds were incubated in full media at 37°C with 5% CO<sub>2</sub> for 12h. 5 x 10<sup>4</sup> cells per scaffold in 100µL of entire media were seeded on SF, Coll-SF and CS-SF scaffolds. Cells were trypsinized and counted on the day 1, 3, 5, and 7 in the Neubauer chamber using the standard trypan blue method.

#### **3.3.5.2 Live/Dead Assay**

MG-63 cells were seeded on SF, Coll-SF, CS-SF scaffolds at a density of 5 x 10<sup>4</sup> in DMEM containing 10% FBS. Cells were incubated at 37°C with 5% CO<sub>2</sub> for up to 7

days. During incubation, on the 1<sup>st</sup>, 3<sup>rd</sup>, 5<sup>th</sup>, and 7<sup>th</sup> day, cells were stained with Live/Dead staining solution that comprises of 10 $\mu$ L of 7.5mM propidium iodide and 1 $\mu$ L of 0.67mM acridine orange (both stocks were prepared in PBS) in 1mL of DMEM containing 10% FBS. Cells were incubated at 37°C with 5% CO<sub>2</sub> for ~25 minutes. Later, cells were washed two times with PBS and images were captured by epifluorescence microscopy using Axio Observer Z1 Carl Zeiss Microscope.

### **3.3.6 Cell adhesion and proliferation**

Cell adhesion and proliferation were determined by MTT (3-(4, 5-Dimethylthiazol-2-yl)-2, 5-diphenyltetrazolium bromide) assay. Before seeding the cells, SF, Coll-SF and CS-SF scaffolds were incubated in complete media at 37°C with 5% CO<sub>2</sub> for 12h. MG63 cells were seeded in a flat-bottomed non-adhesive 96-well plate at a density of 5 x 10<sup>4</sup> cells per scaffold in 100 $\mu$ L of complete media. The dish was incubated at 37°C with 5% CO<sub>2</sub> for 24h. During incubation, on the 1<sup>st</sup>, 3<sup>rd</sup>, 5<sup>th</sup>, and 7<sup>th</sup> day, the media was replaced with filter-sterilized MTT (0.45mg/mL) prepared in DMEM containing 10% FBS and further incubated for 4h at 37°C with 5% CO<sub>2</sub>. MTT reagent was replaced by DMSO 100 $\mu$ L/well. The addition of DMSO dissolves the formazan crystals formed by the reaction of the sample with MTT, and the developed color was measured at 550 nm using a micro-titre plate reader (Multiskan EX, Thermo Scientific). Each absorbance was taken to be the mean of triplicate measurements.

### **3.3.7 Cell morphology by actin cytoskeleton staining**

MG-63 cells were seeded on SF, Coll-SF, CS-SF scaffolds at a density of 5 x 10<sup>4</sup> in DMEM containing 10% FBS. Cells were incubated at 37°C with 5% CO<sub>2</sub> for up to 7 days. During incubation, on the 3<sup>rd</sup>, 5<sup>th</sup>, and 7<sup>th</sup> day, actin cytoskeleton staining was performed using the following protocol: Scaffolds were washed with PBS followed

by the cell fixation with 4% paraformaldehyde for 15 minutes at room temperature. The cells were washed with PBS two times and permeabilized with 0.1% Triton X-100 (Sigma-Aldrich) for 5 minutes. The cells were again subjected to PBS washing two times and incubated with 5% BSA for 20 minutes at room temperature to avoid non-specific binding. Actin filaments were stained by 1:100 dilution of Alexa fluor 488 phalloidin (Thermo Fisher Scientific) prepared in PBS and incubated for 30 minutes in the dark at room temperature. Cell's nucleus was counterstained with DAPI at 300nM concentration for 4 minutes at room temperature and washed with PBS. Images were captured by epifluorescence microscopy using Axio Observer Z1 Carl Zeiss Microscope.

### **3.3.8 Osteogenic differentiation by ALP Assay**

ALP activity was assayed using a colourimetric ALP kit (Abcam, U.K.). Briefly, MG-63 cells were seeded on SF, Coll-SF, CS-SF scaffolds at a density of  $5 \times 10^4$  cells per scaffold in 10 $\mu$ L of complete media. The cells were allowed to be settled for 5-7 minutes at 37°C with 5% CO<sub>2</sub>. The additional 90 $\mu$ L media for cells was added, and the cell culture plate was then incubated at 37°C with 5% CO<sub>2</sub> for 7 days. On the 2<sup>nd</sup> day of the experiment, seeding media was replaced with osteogenic differentiation media (Invitrogen). During incubation, on the 3<sup>rd</sup>, 5<sup>th</sup>, and 7<sup>th</sup> day, spent media from cell-seeded scaffolds was collected, and 80 $\mu$ L of the spent media was incubated with 50 $\mu$ L of p-nitrophenyl phosphate (5mM) solution at room temperature for 1h in the dark. At the end of the incubation, enzyme activity was stopped by adding 20 $\mu$ L of stop solution. Simultaneously, the standard curve was plotted as shown in **Figure 3-2** as per the manufacturer's instruction. The amount of p-nitrophenol produced was measured by measuring absorbance at 405nm.



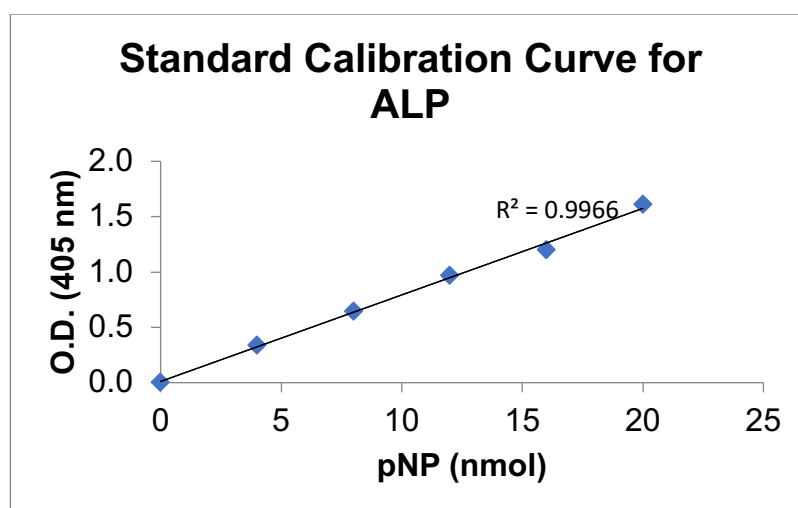


*Figure 3-2 Standard calibration curve for Alkaline Phosphatase Assay*

### 3.3.9 Extracellular mineral( $\text{Ca}^{2+}$ ) deposition and quantification

At the end of the 7<sup>th</sup> day, mineralised calcium deposition was analyzed with Alizarin Red S staining. In brief, MG-63 cells were seeded on SF, Coll-SF, CS-SF scaffolds at a density of  $5 \times 10^4$  cells per scaffold in 10 $\mu\text{L}$  of complete media. The cells were allowed to be settled for 5-7 minutes at 37°C with 5%  $\text{CO}_2$ . The additional 90 $\mu\text{L}$  media for cells was added, and the cell culture plate was then incubated at 37°C with 5%  $\text{CO}_2$  for 7 days. The day after seeding, the media was replaced with osteogenic differentiation media (Invitrogen). On the 7<sup>th</sup> day, scaffolds were fixed with 4% formaldehyde at room temperature for 10 min. They were later washed with PBS and then stained with 2% Alizarin Red (Sigma) solution for 20 minutes at room temperature. After staining, the scaffolds were washed two times with DI water. Calcium deposition was observed under a bright-field by the Axio Observer Z1 microscope from Carl Zeiss.

Calcium deposition was further confirmed by quantifying total calcium content. In brief, at the end of the 7<sup>th</sup> day, scaffolds were washed with PBS, and the deposited calcium was extracted with 0.5mL of 5% trichloroacetic acid for 30 minutes. At the end of incubation, Calcium was quantified using O-cresolphthalein complexone colourimetric assay (Sigma). The developed color was measured at 575nm, and the background color was subtracted from the experimental reading to quantify the Ca content. The standard calibration curve was prepared per manufacturer instructions as shown here in **Figure 3-3**.

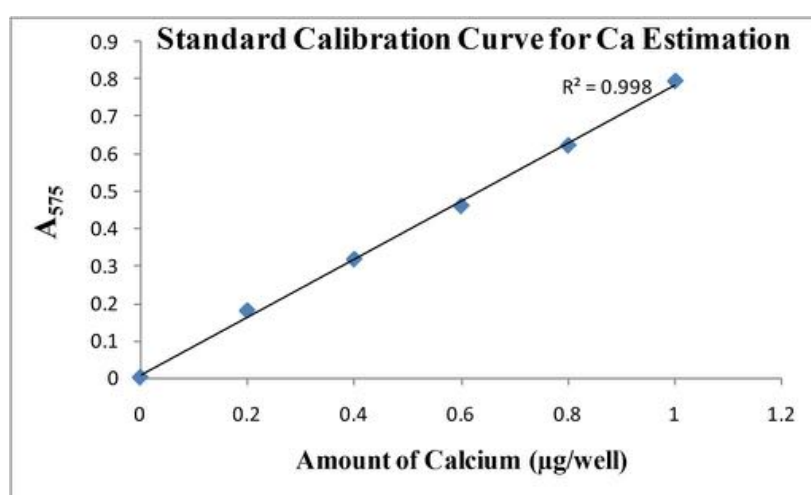


**Figure 3-3** Standard Calibration curve for Ca estimation by O-cresolphthalein complexone colourimetric assay

## 3.4 Results and Discussion

SF based scaffolds have been prepared using various methods like lyophilisation, salt leaching, electrospinning, ice crystal templating, etc. These materials have shown promise in BTE. We used a 3D microparticle SF-Scaffold, which was prepared using a methodology developed in our laboratory. Preliminary studies on this 3D microparticle SF-Scaffold (such as mechanical integrity, pore size and

pore volume and rate of bioresorption) match the requirements for a scaffold in BTE, as mentioned in **Table 3-1**. We have introduced a surface modification of the SF-Scaffold to improve cell adhesion and proliferation further. Our process involves coating the surface of this microparticle scaffold using collagen Type I and chitosan- biopolymers known to enhance cell adhesion and proliferation.

The method involved incubating the SF-Scaffolds with the biopolymer and annealing and coating the surface. The morphological features of the surface coating were studied using Scanning Electron Microscopy (SEM). **Figure 3-4** shows the SEM images of SF scaffold (SF) and surface-modified scaffolds treated with collagen (Coll-SF) and chitosan (CS-SF). The SEM images of the SF scaffold (**Figure 3-4a**) shows micro-particles packed together in a hexagonal packing. The surface of SF micro-particles is essentially the dried silk solution used to fuse these particles. The interparticle pore sizes are visible and are of the order 100-500 $\mu$ m. The collagen modified SF scaffold shows the presence of additional material domains dispersed throughout the surface. (**Figure 3-4b**). These could be attributed to the collagen coating. Similar material domains were also observed in the chitosan treated scaffold (**Figure 3-4c**). It has been found that a minimum pore size of 30 $\mu$ m is necessary for effective cell migration and colonization.<sup>43</sup> As shown in **Figure 3-4**, the method used for coating here does not alter the pore size of the scaffold. This implies that the surface modification technique will not inhibit the transport of nutrients and waste diffusion or cell migration in the scaffold.

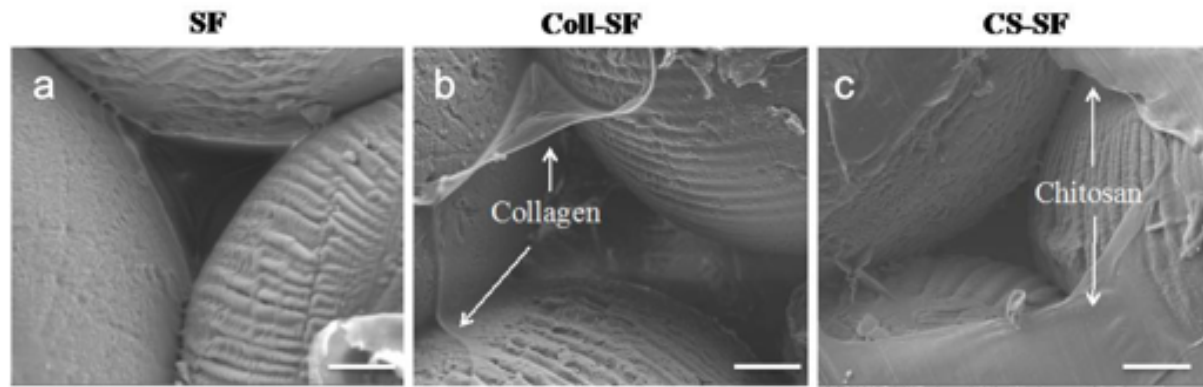


**Figure 3-4** SEM images of SF, Coll-SF and CS-SF

### 3.4.1 Cell viability and proliferation studies

The uncoated and coated SF scaffolds were evaluated using *in-vitro* cell culture studies. MG-63 cells were chosen for this study as it has a high proliferation rate, *In-vitro* studies performed in a 7-day experiment are therefore sufficient to provide reliable and sensitive information on the performance of this material as a possible scaffold for BTE.<sup>44-46</sup> Cell viability of MG-63 was assayed quantitatively by using trypan blue dye exclusion method and qualitatively by performing live/dead imaging by using acridine orange (AO) and propidium iodide (PI) stains. **Figure 3-5** shows the viable cell count on the 1<sup>st</sup>, 3<sup>rd</sup>, 5<sup>th</sup>, and 7<sup>th</sup> day after seeding the MG-63 on SF, Coll-SF and CS-SF scaffolds. It can be seen from **Figure 3-5** that the SF scaffold does support the attachment of the MG63 cells. Also, as the experiment progresses, the number of viable cells on the SF scaffold increases. However, coating or surface modifying the scaffolds results in increased attachment and proliferation of cells.

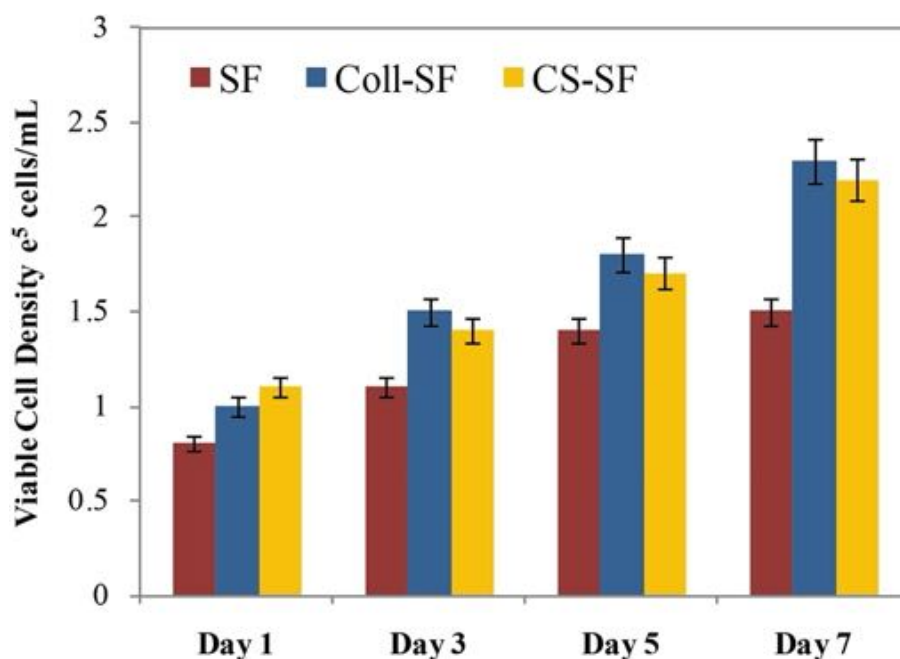


**Figure 3-5** Viable MG-63 cell density counted by trypan blue dye exclusion method (Data are represented as the mean  $\pm$  SD of two independent experiments)

On a given day of the experiment, the Coll-SF scaffolds and CS-scaffolds have a higher number of viable cells than the uncoated SF scaffold. However, the viability of the cells on the Coll-SF and CS-SF scaffold is comparable, and no significant differences between these two scaffolds were observed here. The trends observed in cell viability were further corroborated using live-dead imaging.

**Figure 3-6** shows the individual channel images of AO and PI on the 1<sup>st</sup>, 3<sup>rd</sup>, 5<sup>th</sup> and 7<sup>th</sup> day after seeding the MG-63 on SF, Coll-SF and CS-SF scaffold. For the SF scaffold, MG-63 cells did adhere to the micro-particle surface. Also, there were increased numbers of viable cells visible as the days increased. Insignificant or no red coloured spots in these images indicate the absence of dead cells on these scaffolds. Similar trends in cell proliferation were also observed for the surface modified scaffolds. Also, the number of cells observed for modified scaffolds is always higher than the uncoated SF scaffold. The elongated and spread cell

morphology was most clearly visible on the Coll-SF scaffold compared to the other two scaffolds used in the study, as seen in **Figure 3-7**. Another interesting observation was that, as the experiment progressed, cells formed clumps on the CS-SF scaffold.

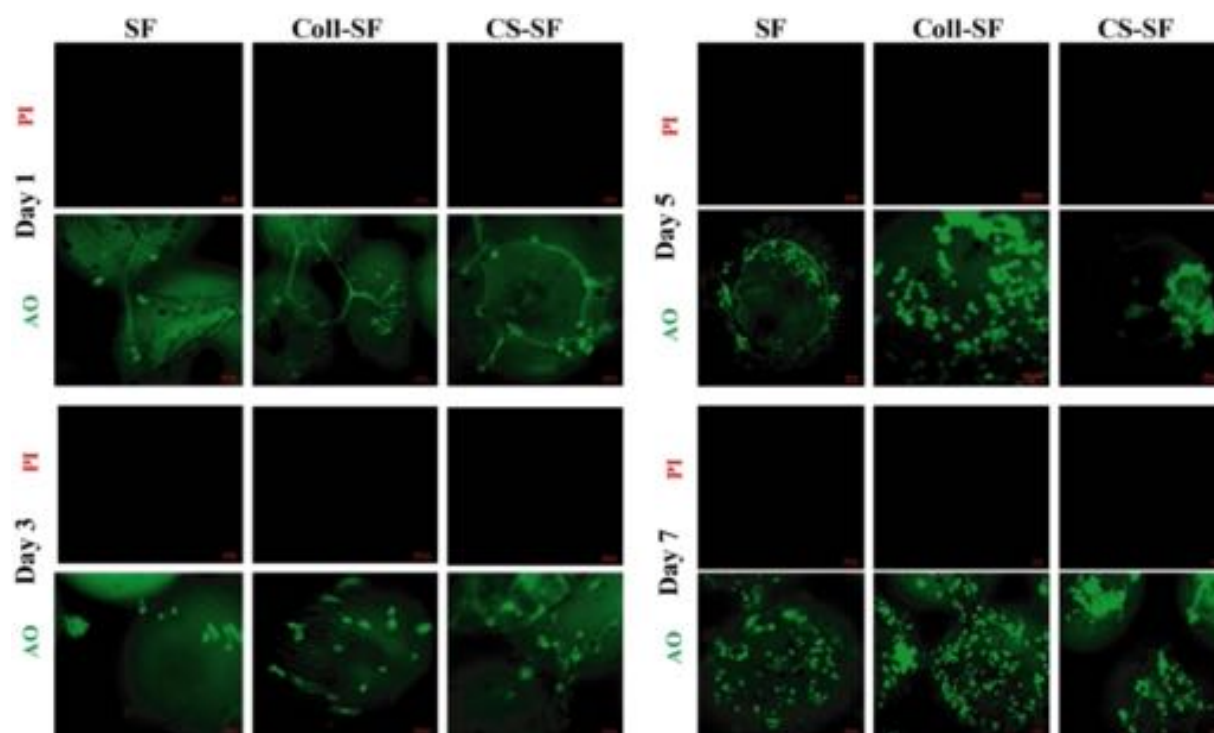


**Figure 3-6** Epi-fluorescence images of Live (Green) and Dead (red) MG-63 cells grown on SF, Coll-SF and CS-SF. All images were taken at the same exposure time, and the scale bar is 50  $\mu\text{m}$

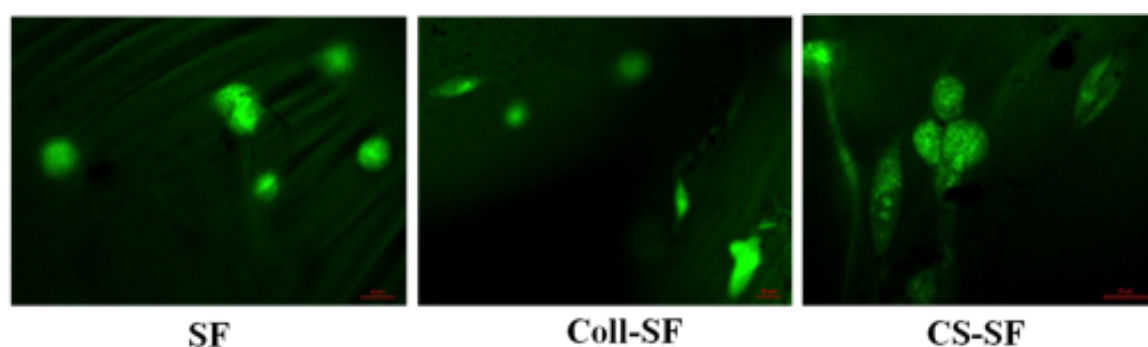


**Figure 3-7** Live/Dead images of AO channel; Elongated MG63 cell morphology on 3rd day of seeding with modified scaffold (Scale bar – 20  $\mu\text{m}$ )

This clumping was not observed in the SF or Coll-SF scaffold. It has been reported that the degree of acetylation of chitosan is responsible for the clustering of cells.<sup>43</sup> Here, we used 15 – 25% acetylated chitosan to modify the surface, and our observation is in agreement with the reported literature.<sup>38,43</sup>

Cell adhesion and proliferation was also analyzed using MTT assay. Cells were analyzed on the 1<sup>st</sup>, 3<sup>rd</sup>, 5<sup>th</sup>, and 7<sup>th</sup> days after seeding the MG-63 on SF, Coll-SF and CS-SF scaffolds and the data are shown in **Figure 3-8**. As shown in Figure 3.8, the SF scaffold supports adhesion and the proliferation of the cells. The viable cell count nearly doubled on the 7<sup>th</sup> day after incubation. Similar trends in cell proliferation were also observed for the Coll-SF and CS-SF scaffolds. Increased absorbance due to viable cells was monitored with both surface-modified scaffolds compared to unmodified silk scaffolds. These results are in-line with those observed in trypan blue and live-dead assay experiments.

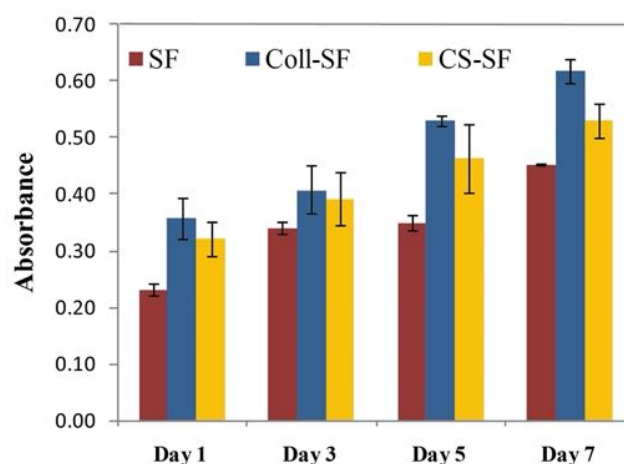


**Figure 3-8** Cell adhesion and proliferation assay (MTT Assay) of MG-63 cultured on SF, Coll-SF and CS-SF till seven days. Data are presented as the mean  $\pm$  SD of two independent experiments.

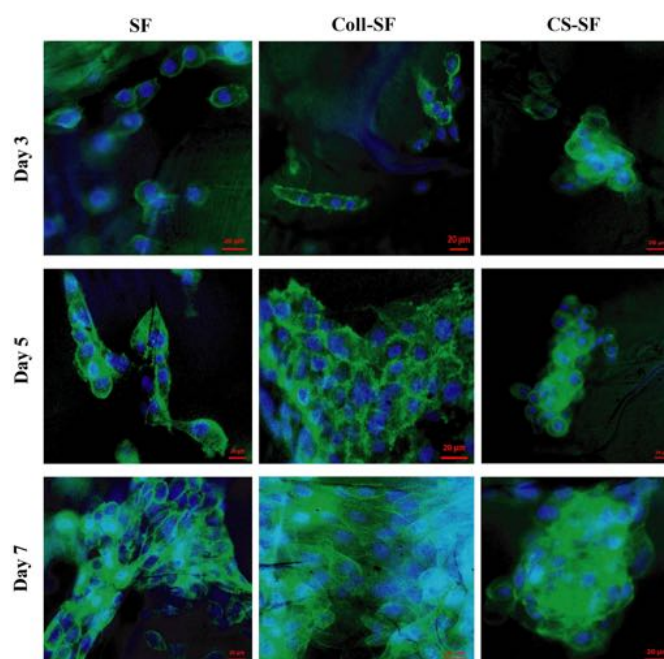


**Figure 3-9** Actin cytoskeleton staining of MG-63 cells with Alexa fluor phalloidin 488 and nucleus were counterstained with DAPI. The scale bar is 20  $\mu\text{m}$ .

Cell morphology and cell adhesion were evaluated by F-actin cytoskeleton staining with Alexa fluor 488 phalloidin. **Figure 3-9** shows the actin cytoskeleton of MG-63 grown on SF, Coll-SF and CS-SF scaffolds. The images show considerable cell growth with clear morphology of cells concerning all three scaffolds. More elongated cell morphology with an increased number of cells was visual with Coll-SF than SF and CS-SF. Also, we observed some cells spread out for the CS-SF scaffolds, but the predominant morphology was spherical, as shown in **Figure 3-10**. This variation in morphology of the cells can be attributed to the spread in the degree of acetylation in the chitosan used for experimentation. Both the results are in agreement with MTT and live/dead assay results.



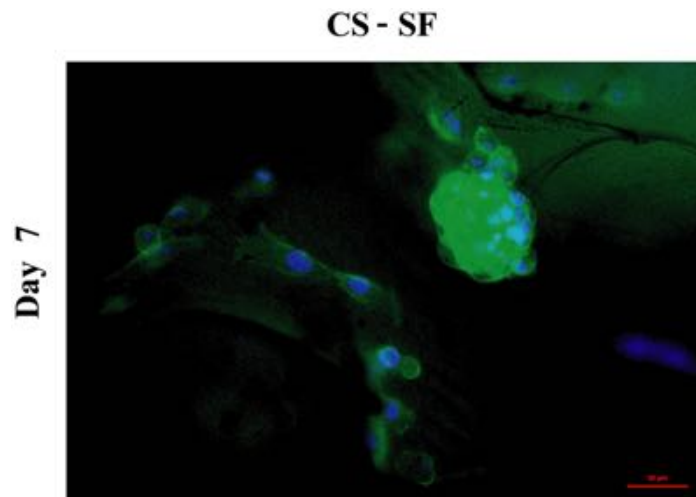


**Figure 3-10** CS-SF scaffold - Actin cytoskeleton staining of MG-63 cells with Alexa fluorophore and nucleus were counterstained with DAPI

In short, data obtained from the trypan blue dye extraction method, live/dead assay and cell proliferation assayed by MTT showed improved performance of the biopolymer coated scaffolds towards cell adhesion, viability and proliferation. This is in line with several reports where collagen and chitosan have improved cell adhesion and proliferation. Collagen Type I is the dominant component of the ECM in bone tissue and hence provides the right chemical cues for cell recognition. The integrins present on the cell surface are known to recognize the triple helix structure of collagen. Also, it has been acknowledged that collagen plays a vital role in cytoskeleton reorganization and signal transduction, which regulates cell adhesion and proliferation.<sup>47</sup> Chitosan has been used in BTE and is shown to induce the proliferation of osteoblast cells. The chemical structure of chitosan is similar to glycosaminoglycans (GAGs), which is an essential component in ECM. This has been cited as one of the possible reasons for the improved adhesion of cells to chitosan. Our data support these observations made in the literature.

### 3.4.2 Osteogenic differentiation

Bone is a mineralized connective tissue, which is continuously bio-resorbed and neoformed. The formation of new bone tissue requires commitment from the cells towards the osteogenic lineage. The osteoblasts are responsible for the synthesis of the bone matrix, and as the cells proliferate, it shows higher ALP activity and mineral deposition. Thus, in addition to cell adhesion and proliferation, understanding the functioning of cells is also of prime importance in BTE. In this study, we used ALP activity and calcium deposition to monitor the osteogenic differentiation of MG-63 cells on unmodified and modified scaffolds.

ALP is an early to mid stage marker for the osteogenic differentiation process, and it is secreted into the ECM, playing a crucial role in bone ECM mineralization. In our study, **Figure 3-11**, we detected measurable ALP activity with all three scaffolds and within the standard calibration curve as per **Figure 3-2**. The ALP activity was evident on Day 3 for the SF scaffold and was significantly enhanced on day 7. For the Coll-SF scaffold, similar increased ALP activity was also observed for day 7. On the 3rd and 7th days, the ALP activity between the three types of scaffold studied was comparable, with the CS-SF scaffold showing the highest ALP activity. However, on the 5th day, the ALP activity in the CS-SF scaffold was significantly higher than the other two scaffolds studied. Here, the absorbance for the CS-SF scaffold was nearly double that of the SF and Coll-SF scaffold.

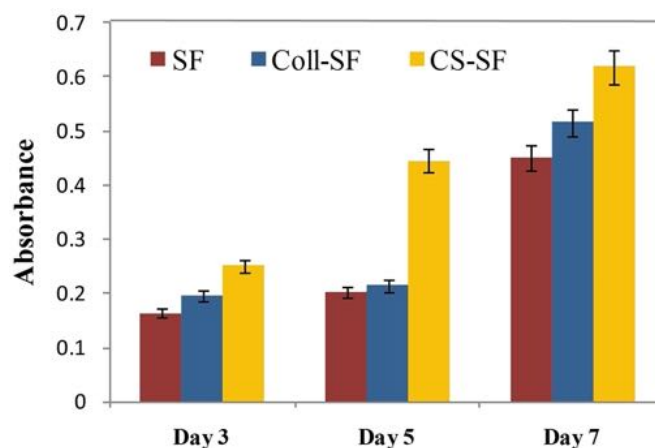


**Figure 3-11** ALP assay- MG63 cells cultured on SF, Coll-SF and CS-SF till seven days. Absorbance was taken at 405nm, and data are presented as the mean  $\pm$  SD of two independent experiments

The presence of the ALP enzyme is the early predetermining marker as the cells start to differentiate into the osteogenic lineage. Throughout the assay, we got higher ALP activity with chitosan modified scaffold. The invigorating effect of chitosan on osteogenesis has been extensively reported.<sup>47,48</sup> However, the exact mechanism of this osteogenic behaviour is unknown. One of the possible reasons that have been discussed is the cationic charge on chitosan.<sup>49</sup> Also, it has been suggested that high molecular weight (>10kDa) of chitosan results in improved osteogenic behaviour of MG-63 cells. The molecular weight of chitosan used here is 190-310kDa, and thus, our observation is in sync with the literature.<sup>47,50</sup>

Due to the osteoblastic differentiation initiation process, alizarin red S staining was used to detect *in-vitro* extra-cellular mineral (calcium) deposition. After the 7th day of seeding the MG-63 cells, calcium deposited nodules were detected on all three scaffolds, as seen in **Figure 3-12**. The amount of deposition was less in the SF scaffold. This deposition has been considerably increased with both the CS-SF and Coll-SF scaffolds, evident in the images. As part of the differentiation

process, calcium deposition nodules stained by alizarin red also increased with scaffold modification. More deposition was observed with chitosan modified scaffold. For the Coll-SF scaffolds, this improvement can be attributed.

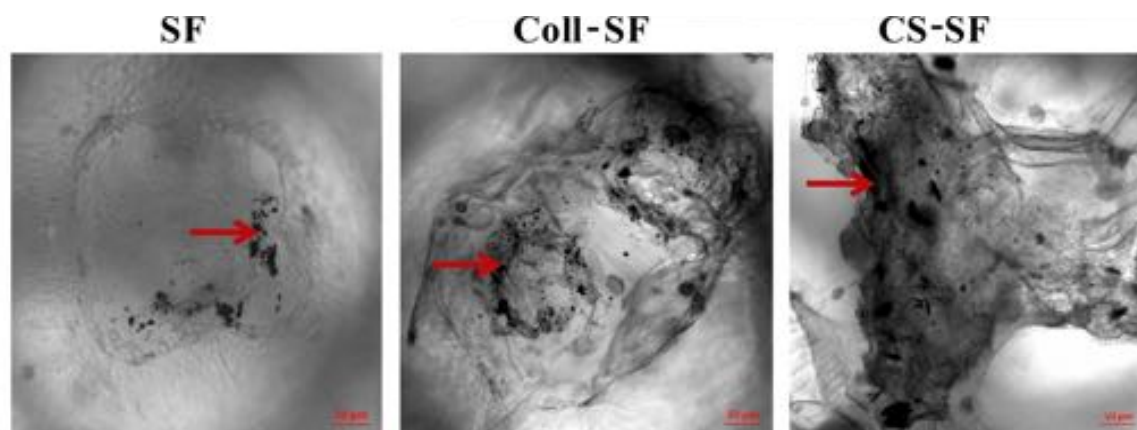


**Figure 3-12** Calcium deposition by Alizarin Red S staining. Arrow indicates deposited calcium nodules. All bright field images were taken at the same exposure time, and the scale bar is 50 $\mu$ m

to the GER sequence in collagen, which acts as an integrin-binding site.<sup>51</sup> However, our ALP activity assay did not show significant differences between SF and Coll-SF scaffolds. But, calcium mineralization was found to be better in Coll-SF as compared to the SF scaffold. Further, the total Calcium deposition amount was quantified using O-cresolphthalein complexone colourimetric assay as per the results mentioned in **Figure 3-13**. Calcium deposition was quantified by using a calibration curve as per **Figure 3-3**. Higher Calcium content was observed with chitosan-modified scaffolds than SF and Coll-SF scaffolds. These results in agreement with the observations observed in ALP and alizarin red S staining studies.

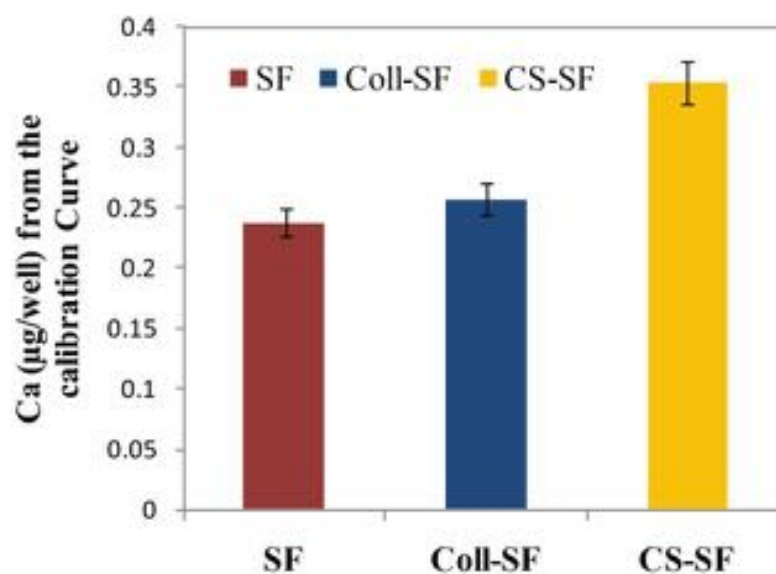


Figure 3-13 Calcium deposition of MG63 cells after seven days.

### 3.5 Conclusions

We report in this Chapter the *in-vitro* cell behaviour of osteoblast-like cells on novel SF microparticle scaffolds for applications in load-bearing osteoregenerative applications. Additionally, we have modified the surface of these scaffolds using natural biopolymers – Collagen Type I and Chitosan. Our results suggest that SF micro-particle scaffold supports cell attachment, proliferation, and differentiation. This behaviour can be further enhanced by coating the surface of these scaffolds with Collagen Type I and Chitosan biopolymers. Although the cell attachment, viability and morphology were superior in collagen modified scaffolds, the osteogenic differentiation is better in chitosan-modified scaffolds. The efficacy of these scaffolds for load-bearing bone tissue engineering application in suitable animal model is necessary to validate the findings of this *in-vitro* studies.

## 3.6 References

- (1) Melke, J.; Midha, S.; Ghosh, S.; Ito, K.; Hofmann, S. Silk Fibroin as Biomaterial for Bone Tissue Engineering. *Acta Biomater.* **2015**, *31*, 1–16. <https://doi.org/10.1016/j.actbio.2015.09.005>.
- (2) Le, X.; Poinern, G. E. J.; Ali, N.; Berry, C. M.; Fawcett, D. Engineering a Biocompatible Scaffold with Either Micrometre or Nanometre Scale Surface Topography for Promoting Protein Adsorption and Cellular Response. *Int. J. Biomater.* **2013**, *2013*, 1–16. <https://doi.org/10.1155/2013/782549>.
- (3) Liu, X.; Ma, P. X. Polymeric Scaffolds for Bone Tissue Engineering. *Ann. Biomed. Eng.* **2004**, *32* (3), 477–486. <https://doi.org/10.1023/B:ABME.0000017544.36001.8e>.
- (4) Hutmacher, D. W. Scaffolds in Tissue Engineering Bone and Cartilage. *Biomaterials* **2000**, *21* (24), 2529–2543. [https://doi.org/10.1016/S0142-9612\(00\)00121-6](https://doi.org/10.1016/S0142-9612(00)00121-6).
- (5) Ding, S.-J.; Wei, C.-K.; Lai, M.-H. Bio-Inspired Calcium Silicate-Gelatin Bone Grafts for Load-Bearing Applications. *J. Mater. Chem.* **2011**, *21* (34), 12793–12802. <https://doi.org/10.1039/C1JM11171J>.
- (6) Sachlos, E.; Czernuszka, J. T. Making Tissue Engineering Scaffolds Work. Review on the Application of Solid Freeform Fabrication Technology to the Production of Tissue Engineering Scaffolds. *Eur. Cells Mater.* **2003**, *5*, 29–40. <https://doi.org/10.22203/eCM.v005a03>.
- (7) Troy, E.; Tilbury, M. A.; Power, A. M.; Wall, J. G. Nature-Based Biomaterials and Their Application in Biomedicine. *Polymers (Basel)*. **2021**, *13* (19), 1–37. <https://doi.org/10.3390/polym13193321>.
- (8) Carson, J. S.; Bostrom, M. P. G. Synthetic Bone Scaffolds and Fracture Repair. *Injury* **2007**, *38* (SUPPL. 1). <https://doi.org/10.1016/j.injury.2007.02.008>.

- (9) Kasoju, N.; Bora, U. Silk Fibroin in Tissue Engineering. *Adv. Healthc. Mater.* **2012**, *1* (4), 393–412. <https://doi.org/10.1002/adhm.201200097>.
- (10) Koh, L. D.; Cheng, Y.; Teng, C. P.; Khin, Y. W.; Loh, X. J.; Tee, S. Y.; Low, M.; Ye, E.; Yu, H. D.; Zhang, Y. W.; Han, M. Y. Structures, Mechanical Properties and Applications of Silk Fibroin Materials. *Prog. Polym. Sci.* **2015**, *46*, 86–110. <https://doi.org/10.1016/j.progpolymsci.2015.02.001>.
- (11) Thurber, A. E.; Omenetto, F. G.; Kaplan, D. L. *In Vivo* Bioresponses to Silk Proteins. *Biomaterials* **2015**, *71*, 145–157. <https://doi.org/10.1016/j.biomaterials.2015.08.039>.
- (12) Das, S.; Pati, D.; Tiwari, N.; Nisal, A.; Sen Gupta, S. Synthesis of Silk Fibroin-Glycopolypeptide Conjugates and Their Recognition with Lectin. *Biomacromolecules* **2012**, *13* (11), 3695–3702. <https://doi.org/10.1021/bm301170u>.
- (13) vepari C., K. D. L. Silk as Biomaterial. **2007**, *32* (8–9), 991–1007. <https://doi.org/10.1016/j.pestbp.2011.02.012>. Investigations.
- (14) Nisal, A.; Dhanalakshmi, M.; Lele, A.; Prasad, B. L. V; Bellare, J. Hydrophilic Electrospun Silk Fibroin Non-Woven Mats Anuya Nisal , M . Dhanalakshmi and Ashish Lele , Polymer Science and Engineering Dept . National The Prepared Electrospinning Solutions Were Characterized. *Proc. 70th Annu. Tech. Conf. Exhib. Mumbai, India, December 6-7, Soc. Plast. Eng.* **2012**, 270–275.
- (15) Nisal, A.; Kalelkar, C.; Bellare, J.; Lele, A. Rheology and Microstructural Studies of Regenerated Silk Fibroin Solutions. *Rheol. Acta* **2013**, *52* (10–12), 833–840. <https://doi.org/10.1007/s00397-013-0723-5>.
- (16) Dubey, P.; Nawale, L.; Sarkar, D.; Nisal, A.; Prabhune, A. Sphorolipid Assisted Tunable and Rapid Gelation of Silk Fibroin to Form Porous Biomedical Scaffolds. *RSC Adv.* **2015**, *5* (43), 33955–33962.

- <https://doi.org/10.1039/C5RA04317D>.
- (17) Dubey, P.; Kumar, S.; Aswal, V. K.; Ravindranathan, S.; Rajamohanan, P. R.; Prabhune, A.; Nisal, A. Silk Fibroin-Sophorolipid Gelation: Deciphering the Underlying Mechanism. *Biomacromolecules* **2016**, *17* (10), 3318–3327. <https://doi.org/10.1021/acs.biomac.6b01069>.
- (18) Meinel, L.; Betz, O.; Fajardo, R.; Hofmann, S.; Nazarian, A.; Cory, E.; Hilbe, M.; McCool, J.; Langer, R.; Vunjak-Novakovic, G.; Merkle, H. P.; Rechenberg, B.; Kaplan, D. L.; Kirker-Head, C. Silk Based Biomaterials to Heal Critical Sized Femur Defects. *Bone* **2006**, *39* (4), 922–931. <https://doi.org/10.1016/j.bone.2006.04.019>.
- (19) Saha, S.; Kundu, B.; Kirkham, J.; Wood, D.; Kundu, S. C.; Yang, X. B. Osteochondral Tissue Engineering in Vivo: A Comparative Study Using Layered Silk Fibroin Scaffolds from Mulberry and Nonmulberry Silkworms. *PLoS One* **2013**, *8* (11), 1–10. <https://doi.org/10.1371/journal.pone.0080004>.
- (20) Kundu, B.; Rajkhowa, R.; Kundu, S. C.; Wang, X. Silk Fibroin Biomaterials for Tissue Regenerations ☆. *Adv. Drug Deliv. Rev.* **2013**, *65* (4), 457–470. <https://doi.org/10.1016/j.addr.2012.09.043>.
- (21) Gupta, P.; Adhikary, M.; M, J. C.; Kumar, M.; Bhardwaj, N.; Mandal, B. B. Biomimetic, Osteoconductive Non-Mulberry Silk Fiber Reinforced Tricomposite Scaffolds for Bone Tissue Engineering. *ACS Appl. Mater. Interfaces* **2016**, *8* (45), 30797–30810. <https://doi.org/10.1021/acsami.6b11366>.
- (22) Ghanaati, S.; Unger, R. E.; Webber, M. J.; Barbeck, M.; Orth, C.; Kirkpatrick, J. A.; Booms, P.; Motta, A.; Migliaresi, C.; Sader, R. A.; Kirkpatrick, C. J. Scaffold Vascularization in Vivo Driven by Primary Human Osteoblasts in Concert with Host Inflammatory Cells. *Biomaterials* **2011**, *32* (32), 8150–8160.



- <https://doi.org/10.1016/j.biomaterials.2011.07.041>.
- (23) Unger, R. E.; Sartoris, A.; Peters, K.; Motta, A.; Migliaresi, C.; Kunkel, M.; Bulnheim, U.; Rychly, J.; James Kirkpatrick, C. Tissue-like Self-Assembly in Cocultures of Endothelial Cells and Osteoblasts and the Formation of Microcapillary-like Structures on Three-Dimensional Porous Biomaterials. *Biomaterials* **2007**, *28* (27), 3965–3976. <https://doi.org/10.1016/j.biomaterials.2007.05.032>.
- (24) Fuchs, S.; Jiang, X.; Schmidt, H.; Dohle, E.; Ghanaati, S.; Orth, C.; Hofmann, A.; Motta, A.; Migliaresi, C.; Kirkpatrick, C. J. Dynamic Processes Involved in the Pre-Vascularization of Silk Fibroin Constructs for Bone Regeneration Using Outgrowth Endothelial Cells. *Biomaterials* **2009**, *30* (7), 1329–1338. <https://doi.org/10.1016/j.biomaterials.2008.11.028>.
- (25) Karageorgiou V., Tomkins M., Fajardo R., Meinel L., Snyder B., Wade K., Chen J., Vunjak-Novakovic V., K. D. L. Porous Silk Fibroin 3-D Scaffolds for Delivery of Bone Morphogenetic Protein-2 in Vitro and in Vivo. *J. Biomed. Mater. Res. Part A* **2006**, *33*, 324–334. <https://doi.org/10.1002/jbm.a>.
- (26) Chung, H. J.; Park, T. G. Surface Engineered and Drug Releasing Pre-Fabricated Scaffolds for Tissue Engineering. *Adv. Drug Deliv. Rev.* **2007**, *59* (4–5), 249–262. <https://doi.org/10.1016/j.addr.2007.03.015>.
- (27) Zhang, W.; Zhu, C.; Ye, D.; Xu, L.; Zhang, X.; Wu, Q.; Zhang, X.; Kaplan, D. L.; Jiang, X. Porous Silk Scaffolds for Delivery of Growth Factors and Stem Cells to Enhance Bone Regeneration. *PLoS One* **2014**, *9* (7), 1–9. <https://doi.org/10.1371/journal.pone.0102371>.
- (28) Mandal, B. B.; Grinberg, A.; Seok, E.; Panilaitis, B.; Kaplan, D. L. High-Strength Silk Protein Scaffolds for Bone Repair. *Pnas* **2012**, *109* (20), 7699–7704. <https://doi.org/10.1073/pnas.1119474109>.
- (29) Ak, F.; Oztoprak, Z.; Karakutuk, I.; Okay, O. Macroporous Silk Fibroin

- Cryogels. *Biomacromolecules* **2013**, *14* (3), 719–727.  
<https://doi.org/10.1021/bm3018033>.
- (30) Collins, A. M.; Skaer, N. J. V; Gheysens, T.; Knight, D.; Bertram, C.; Roach, H. I.; Oreffo, R. O. C.; Von-Aulock, S.; Baris, T.; Skinner, J.; Mann, S. Bone-like Resorbable Silk-Based Scaffolds for Load-Bearing Osteoregenerative Applications. *Adv. Mater.* **2009**, *21* (1), 75–78.  
<https://doi.org/10.1002/adma.200802239>.
- (31) Nisal, A.; Venugopalan, P.; Sinha, N. Silk Based Porous Scaffold and a Process for the Preparation Thereof. WO2014125505 A1, 2014.  
<https://doi.org/10.1021/bm200062a>.
- (32) Nisal, A.; Venugopalan, P.; Khude, B. Highly Crystalline Spherical Silk Fibroin Micro- Particles and a Process for Preparation Thereof. WO2016110873 A1, 2016.
- (33) Nisal, A.; Sayyad, R.; Dhavale, P.; Khude, B.; Deshpande, R. Silk Fibroin Micro-Particle Scaffolds with Superior Compression Modulus and Slow Bioresorption for Effective Bone Regeneration. **2018**, No. April, 1–10.  
<https://doi.org/10.1038/s41598-018-25643-x>.
- (34) Dhandayuthapani, B.; Yoshida, Y.; Maekawa, T.; Kumar, D. S. Polymeric Scaffolds in Tissue Engineering Application: A Review. *Int. J. Polym. Sci.* **2011**, *2011* (ii). <https://doi.org/10.1155/2011/290602>.
- (35) Vandrovcová, M.; Douglas, T.; Hauk, D.; Grössner-Schreiber, B.; Wiltfang, J.; Bačáková, L.; Warnke, P. H. Influence of Collagen and Chondroitin Sulfate (CS) Coatings on Poly-(Lactide-Co-Glycolide) (PLGA) on MG 63 Osteoblast-like Cells. *Physiol. Res.* **2011**, *60* (5), 797–813.
- (36) Ferreira, A. M.; Gentile, P.; Chiono, V.; Ciardelli, G. Collagen for Bone Tissue Regeneration. *Acta Biomater.* **2012**, *8* (9), 3191–3200.  
<https://doi.org/10.1016/j.actbio.2012.06.014>.

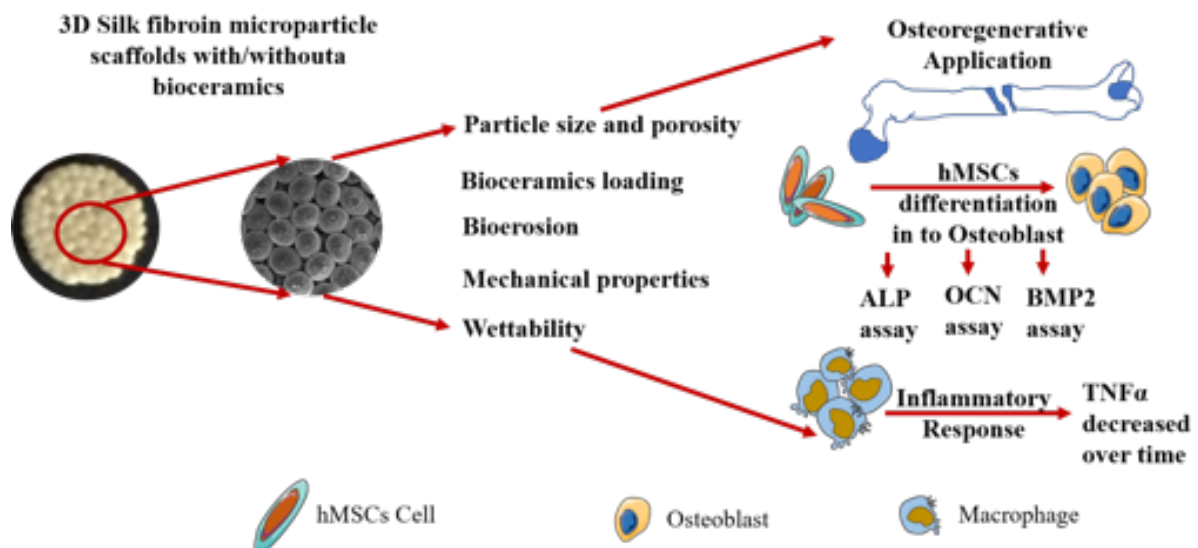
- (37) Lee, M. H.; You, C.; Kim, K. H. Combined Effect of a Microporous Layer and Type I Collagen Coating on a Biphasic Calcium Phosphate Scaffold for Bone Tissue Engineering. *Materials (Basel)*. **2015**, *8* (3), 1150–1161. <https://doi.org/10.3390/ma8031150>.
- (38) Lee, J. Y.; Nam, S. H.; Im, S. Y.; Park, Y. J.; Lee, Y. M.; Seol, Y. J.; Chung, C. P.; Lee, S. J. Enhanced Bone Formation by Controlled Growth Factor Delivery from Chitosan-Based Biomaterials. *J. Control. Release* **2002**, *78* (1–3), 187–197. [https://doi.org/10.1016/S0168-3659\(01\)00498-9](https://doi.org/10.1016/S0168-3659(01)00498-9).
- (39) Venkatesan, J.; Kim, S. K. Chitosan Composites for Bone Tissue Engineering - An Overview. *Mar. Drugs* **2010**, *8* (8), 2252–2266. <https://doi.org/10.3390/md8082252>.
- (40) Costa-Pinto, A. R.; Reis, R. L.; Neves, N. M. Scaffolds Based Bone Tissue Engineering: The Role of Chitosan. *Tissue Eng. Part B Rev.* **2011**, *17* (5), 331–347. <https://doi.org/10.1089/ten.teb.2010.0704>.
- (41) Zeng, S.; Liu, L.; Shi, Y.; Qiu, J.; Fang, W.; Rong, M.; Guo, Z.; Gao, W. Characterization of Silk Fibroin/Chitosan 3D Porous Scaffold and In Vitro Cytology. *PLoS One* **2015**, *10* (6), e0128658. <https://doi.org/10.1371/journal.pone.0128658>.
- (42) LogithKumar, R.; KeshavNarayan, A.; Dhivya, S.; Chawla, A.; Saravanan, S.; Selvamurugan, N. A Review of Chitosan and Its Derivatives in Bone Tissue Engineering. *Carbohydr. Polym.* **2016**, *151*, 172–188. <https://doi.org/http://dx.doi.org/10.1016/j.carbpol.2016.05.049>.
- (43) Amaral, I. F.; Sampaio, P.; Barbosa, M. A. Three-Dimensional Culture of Human Osteoblastic Cells in Chitosan Sponges: The Effect of the Degree of Acetylation. *J. Biomed. Mater. Res. - Part A* **2006**, *76* (2), 335–346. <https://doi.org/10.1002/jbm.a.30522>.
- (44) Liu, B.; Wu, S.; Han, L.; Zhang, C. B-Catenin Signaling Induces the

- Osteoblastogenic Differentiation of Human Pre-Osteoblastic and Bone Marrow Stromal Cells Mainly Through the Upregulation of Osterix Expression. *Int. J. Mol. Med.* **2015**, 1572–1582. <https://doi.org/10.3892/ijmm.2015.2382>.
- (45) Yang, M.; Shuai, Y.; He, W.; Min, S.; Zhu, L. Preparation of Porous Scaffolds from Silk Fibroin Extracted from the Silk Gland of Bombyx Mori (B. Mori). *Int. J. Mol. Sci.* **2012**, 13 (6), 7762–7775. <https://doi.org/10.3390/ijms13067762>.
- (46) Pautke, C.; Schieker, M.; Tischer, T.; Kolk, A.; Neth, P.; Mutschler, W.; Milz, S. Characterization of Osteosarcoma Cell Lines MG-63, Saos-2 and U-2OS in Comparison to Human Osteoblasts. *Anticancer Res.* **2004**, 24 (6), 3743–3748. <https://doi.org/10.1016/j.bone.2013.01.009>.
- (47) Fakhry, A.; Schneider, G. B.; Zaharias, R.; Şenel, S. Chitosan Supports the Initial Attachment and Spreading of Osteoblasts Preferentially over Fibroblasts. *Biomaterials* **2004**, 25 (11), 2075–2079. <https://doi.org/10.1016/j.biomaterials.2003.08.068>.
- (48) Zhang, Y.; Ni, M.; Zhang, M.; Ratner, B. Calcium Phosphate – Chitosan Composite Scaffolds for Bone Tissue Engineering. *Tissue Eng.* **2003**, 9 (2), 337–345.
- (49) Yang, X.; Chen, X.; Wang, H. Acceleration of Osteogenic Differentiation of Preosteoblastic Cells by Chitosan Containing Nanofibrous Scaffolds. *Biomacromolecules* **2009**, 10 (10), 2772–2778. <https://doi.org/10.1021/bm900623j>.
- (50) Lee, K.; Jin, G.; Jang, C. H.; Jung, W.-K.; Kim, G. Preparation and Characterization of Multi-Layered Poly( $\epsilon$ -Caprolactone)/Chitosan Scaffolds Fabricated with a Combination of Melt-Plotting/in Situ Plasma Treatment and a Coating Method for Hard Tissue Regeneration. *J. Mater. Chem. B* **2013**,

1 (42), 5831. <https://doi.org/10.1039/c3tb21123a>.

- (51) Knight, C. G.; Morton, L. F.; Onley, D. J.; Peachey, A. R.; Messent, J.; Smethurst, P. A.; Danny, S.; Farndale, R. W.; Michael, J.; Knight, C. G.; Morton, L. F.; Onley, D. J.; Peachey, A. R.; Messent, A. J.; Smethurst, P. A.; Tuckwell, D. S.; Farndale, R. W.; Barnes, M. J. PROTEIN CHEMISTRY AND STRUCTURE : Identification in Collagen Type I of an Integrin  $\alpha 2 \beta 1$ -Binding Site Containing an Essential GER Sequence Identification in Collagen Type I of an Integrin  $\alpha 2 \beta 1$ -Binding Site Containing an Essential GER Sequence \*. **1998**, 273 (50), 33287–33294. <https://doi.org/10.1074/jbc.273.50.33287>.

# Chapter 4 Incorporation of bio-ceramics into silk fibroin 3D microparticles based scaffold



This chapter is adapted from the following publication:

“Silk Fibroin 3D Microparticle Scaffolds with Bioactive Ceramics: Chemical, Mechanical, and Osteo-regenerative Characteristics”, **Nimisha A. Parekh\***, Rucha V. Deshpande, Swati G. Shukla, and Anuya A. Nisal\*, *Adv. Eng. Mater.* **2020**, DOI: 10.1002/adem.202000458.

## 4.1 Abstract

Preparation of 3D scaffolds for bone tissue engineering (BTE) is a challenging task as it requires appropriate pore size and porosities, excellent mechanical properties and controlled rate of bioerosion. The focus of this work is the fabrication of silk fibroin (SF) 3D microparticle scaffolds with the incorporation of hydroxyapatite (HA) and calcium sulfate (CaS) as bioceramics. Physicochemical characterization shows ~30% filler loading, ~ 40% bulk porosity with >100  $\mu\text{m}$  pore size for these filled/unfilled scaffolds. Nanoindentation studies show improved Young's modulus at the microparticle level with the incorporation of bioceramics. There is a three-fold increase in Young's Modulus in the case of SF-HA while a two-fold increase for SF-CaS. *In-vitro* bioerosion study results in early bioerosion with SF-CaS scaffold while prolonged bioerosion with SF-HA scaffold. *In-vitro* osteo-regenerative potential is analyzed by estimating ALP, BMP-2 and OCN. SF-CaS supports the early stage differentiation as compared to SF-HA scaffolds, which predominantly support late stage differentiation. The reduced expression of TNF- $\alpha$ , suggests a lower risk of immune rejection. This work, therefore, concludes that although SF scaffolds support bone tissue regeneration, the choice of bioceramics enhances the applicability in various clinical scenarios by providing a controlled rate of bioerosion, tuneable speed of osteo-regeneration and improved load-bearing capacities.

This Chapter begins with Section 4.2, which describes a review of literature that outlines the use of bio-ceramics in BTE and its limitation as a biomaterial. Section 4.3 discusses the methodology used for the formation and their physical-chemical characterisation, while Section 4.4 discusses the results of the experiments. Section 4.5 provides discussion followed by Section 4.6 which concludes Chapter 4. All references used for this Chapter are compiled in Section 4.7.

## 4.2 Literature Review

More recently, synthetic ceramics have shown promise for this application of bone void filling because of their chemical similarity to ceramics present in natural bone. Commonly used bioceramics include hydroxyapatite (HA), beta-tricalcium phosphate (TCP) and more recently calcium sulfate (CaS).<sup>1,2</sup> These materials are biocompatible, support cell adhesion, proliferation and growth of bone cells. Though these bioceramics are used as bone void fillers, they have certain limitations: they are intrinsically brittle and lack the required mechanical properties. Also, some of them have faster bioresorption rates (eg. CaS and TCP) while others do not completely bioresorb (eg. HA). In this context, to achieve native bone-like properties, the current trend in BTE is to use a composite of bioceramics and a biocompatible polymer.<sup>3,4</sup>

SF - a natural biopolymer, has come up as a potential candidate for BTE, owing to its biocompatibility, mechanical properties, tunable biodegradation rate and ease of processability. SF can be easily modulated to obtain the required functionality and different forms.<sup>5-11</sup> Different SF based biomaterials including SF-films<sup>12</sup>, SF-3D scaffold<sup>13,14</sup>, SF-reinforced biomaterials<sup>15</sup> have proven to be successful for bone regeneration purposes.

Nisal *et al.* have earlier reported a method to prepare silk fibroin micro-particle scaffolds that have shown a high potential in BTE.<sup>14</sup> These SF microparticle scaffolds have excellent mechanical properties, pore interconnectivity and a superior ability to promote osteo-regeneration. The objective of this work was to prepare regenerated silk fibroin (RSF) microparticle scaffolds filled with nano-hydroxyapatite (HA) or calcium sulfate (CaS). The addition of these fillers would further enhance the mechanical properties of these scaffolds and would thereby contribute towards the osteo-regenerative potential. We compare and evaluate



the performance of these microparticles and scaffolds vis-à-vis pure SF scaffolds. We have characterised the microparticles and their scaffolds for the physico-chemical properties using spectroscopic and thermal techniques. We have also characterized the mechanical properties at the microparticle length scale using the nano-indentation technique. Further, the bulk compression modulus of the scaffolds was also measured. The scaffolds were evaluated for their potential in supporting bone tissue regeneration through *in-vitro* studies. We monitored the growth and differentiation of human mesenchymal stem cells (hMSCs) on the filled/unfilled scaffolds. We also studied the immune response towards these scaffolds upon exposure to human leukemia monocytic cell line, THP-1 cells. We report that the addition of bioactive ceramics to microparticle based SF scaffolds provides the flexibility to prepare bone void fillers with controlled rates of bioerosion and tuneable osteo-regeneration, while surprisingly it does not alter the bulk mechanical performance of the scaffolds.

### **4.3 Experimental Section – Materials and Methods**

SF cocoons were purchased from Central Sericultural Research & Training Institute (CSRTI), Mysore, Sodium Bicarbonate (NaHCO<sub>3</sub>) purchased from Merck (1.93237.0521), Lithium Bromide (Li-Br) (cat#213225), nano-Hydroxyapatite (HA) (cat# 677418), Protease XIV (cat#P5147) enzyme were procured from Sigma Aldrich, Hexafluoroisopropanol (HFIP) from Gujarat Fluorochemicals Ltd. & medical grade Calcium Sulfate was used in the study. All cell culture reagents, IMDM (cat#12440-046), RPMI (cat#A10491-01), fetal bovine serum (FBS) (cat#10082-147), FBS for hMSCs (cat#12662-011), Alamar blue (cat#1987309), MTT (cat#M6494), StemPro osteogenic differentiation kit (cat# A1007201), Picogreen assay kit (cat# P11496), ELISA kits for detection of BMP-2 (cat#EHBMP2), osteocalcin (cat# BMS2020INST), TNF- $\alpha$  (cat# BMS223-4) were

purchased from Invitrogen, ALP detection kit (cat# ab83369) was procured from Abcam. hMSCs (cat#PT-2501) were purchased from Lonza and revived and stored as per suppliers' specifications. In all experiments on hMSC's, cells from passage number 3 were used. The THP-1 cell line was procured from National Centre for Cell Sciences, Pune.

### **4.3.1 Preparation of silk fibroin microparticles and scaffolds**

Silk fibroin microparticles and scaffolds were prepared as per the protocol described earlier. <sup>13</sup> *B. mori* cocoons were boiled in 0.5 w/v% of NaHCO<sub>3</sub> solution twice for 30 minutes each for sericin removal. Collected fibroin was vacuum dried at 60°C followed by dissolution in 9.3M Lithium bromide (LiBr) at 60°C for 4h. This solution was dialyzed extensively against water and the centrifuged solution was lyophilized at -55°C for 6h to obtain an SF sponge. The powder was dissolved in HFIP and this SF-HFIP solution was mounted on a syringe pump and the drops of SF-HFIP solution were coagulated in a methanol bath. The particles were incubated in a methanol bath for 24h with frequent changes of fresh methanol. The micro-particles were allowed to air dry and stored at room temperature till further use. Composite microparticles were prepared by adding 25wt% and 50wt% HA and/or CaSO<sub>4</sub> powder with respect to the weight of SF in the SF-HFIP solution. 3D scaffolds of SF and SF-bioceramics in the form of cylinders of various diameters and heights were prepared using dilute SF solution. Once microparticles were added to the mould, RSF was added on the top of the microparticles, which has been kept at 60°C under vacuum for 30-45 minutes. This high temperature resulted in drying of the aqueous silk solution, fusing the microparticles together and also inducing beta-sheet formation in the aqueous silk solution. This process results in making the glue water-insoluble. These microparticles and 3D scaffolds

are further referred to as SF-25% HA, SF-50% HA, SF-25% CaS and SF-50% CaS indicating both the type of filler and the filler loading percentage.

### **4.3.2 Particle size determination**

Particle size was analysed using optical microscopy (Carl Zeiss Axio Observer Z1 microscope). 20 particles were imaged and the diameter was calculated from the obtained area from ZenPro 2012 software from Carl Zeiss.

### **4.3.3 Confirmation of secondary structure in SF and presence of bioceramics**

All SF and bioceramics filled SF microparticles were analyzed using FTIR from Perkin Elmer (Spectrum GX) coupled with Golden Gate Diamond ATR at the resolution of  $4\text{ cm}^{-1}$  in the range of  $1400$  to  $1800\text{ cm}^{-1}$  and 32 scans were recorded. The amide I peak obtained in the spectral regime of  $1580$  to  $1720\text{ cm}^{-1}$  was deconvoluted to analyze the secondary structure of fibroin protein. Peakfit v4.1 software was used to calculate the crystallinity index (CI). The CI was measured as per the protocol described in our earlier publication Nisal *et al.* 2018. Briefly, the amide I peak in the  $1600$ - $1700\text{ cm}^{-1}$  region was deconvoluted into 12 peaks using the second derivative method and the CI was calculated as the ratio of areas of peak assigned to beta sheets to the areas of peaks assigned to random coil and alpha helix.

### **4.3.4 Surface morphology and elemental analysis**

The surface of SF microparticles with or without bio-ceramics was analyzed using a Quanta 200 3D scanning electron microscope (SEM). Prior to imaging, all samples were sputter-coated with a 5nm gold coating using a Polaron SC6420 sputter coater. Elemental mapping was performed by Energy-dispersive X-ray

spectroscopy (EDX) analysis by using Leica Stereoscan-440 SEM equipped with a Phoenix EDX attachment.

### **4.3.5 Thermogravimetric Analysis (TGA)**

TGA was performed on an accurately weighed sample from 25°C to 900°C at a heating rate of 10°C/min in an air atmosphere using a TGA Q5000 machine from TA instruments.

### **4.3.6 Mechanical properties of microparticles**

Mechanical properties of microparticles were analyzed by nanoindentation. Microparticles were mounted in epoxy using the cold mounting method followed by gentle cloth diamond polishing before the indentation test. Indentation was performed on SF, SF-50% HA and SF-50% CaS particles on a nanoindenter - Bruker NanoInc, Minneapolis, USA, Model: TI Premier using a Berkovich tip approx. 300nm diameter. 10mN load as a constant parameter was applied and displacement was recorded. 20 indentations per sample were recorded and an average modulus was calculated.

### **4.3.7 Mechanical properties of 3D scaffolds**

Bulk mechanical properties of SF, SF-50% HA and SF-50% CaS scaffolds, (8mm in diameter and 5mm in height) were analyzed using Bose Electroforce 3200 Series III machine equipped with a 450N load cell at compression speed of 0.005 mm/sec, a preset load of -1N and scan time of 40Sec. Scaffolds were immersed into deionized (DI) water for about 2h and then used for compression test. A stress-strain graph was plotted and compression modulus was reported.

### **4.3.8 Surface wettability of 3D scaffolds**

Surface wettability of the 3D scaffold of SF, SF-50% HA and SF-50% CaS was analyzed by measuring the contact angle. A stable sessile drop of 4 $\mu$ L of DI water was used and the equilibrium contact angle was reported as the average of at least three measurements for each type of sample.

### **4.3.9 Bioerosion in proteolytic environment**

*In-vitro* weight loss study was conducted by using protease XIV enzyme. SF, SF-50% HA and SF-50% CaS scaffolds were incubated in the enzymatic solution (2Units/ml) at 37°C for a maximum of 28 days with time points of day 7, day 14 and day 28. The experiment was performed in triplicates at each time point. The freshly prepared filter-sterilized enzymatic solution was replenished every 48h. On the 7<sup>th</sup>, 14<sup>th</sup> and 28<sup>th</sup> day, scaffolds were washed with PBS, dried in a vacuum oven at 60°C overnight and weighed. Average weight loss was calculated with respect to the initial weight of the individual scaffold.

### **4.3.10 *In-vitro* cytotoxicity (MTT assay) assay:**

MTT assay was performed to study cytotoxicity of developed scaffolds by using L929 fibroblast cell line as per protocol mentioned in Nisal *et al.*, 2018.

### **4.3.11 Quantitative hMSCs proliferation (Picogreen dsDNA Assay)**

Sterilized SF, SF-50% HA, SF-50% CaS scaffolds were placed in a 96 well flat-bottomed non-adherent cell culture plate and hMSCs were seeded. hMSCs were seeded at a density of  $5 \times 10^4$  cells per scaffold in 10 $\mu$ L of complete media (IMDM + 10% MSCs-FBS). The cells were allowed to settle for 5–7 minutes at 37°C, 5% CO<sub>2</sub> atmosphere. Additional 90 $\mu$ L media was added to the tissue culture plate, which was then incubated at 37°C for 28 days in a 5% CO<sub>2</sub> atmosphere. Media was replenished after every 48h.

*In-vitro* quantitative cell proliferation was analyzed by measuring DNA concentration. dsDNA concentration was analyzed on the 7<sup>th</sup>, 14<sup>th</sup> and 28<sup>th</sup> day using Quant-iT PicoGreen dsDNA kit. On the day of analysis, scaffolds were collected and digested in 1mL of papain solution (125mg/mL of papain in 10mM L-cysteine, 100mM phosphate, and 10 mM EDTA at pH 6.3) for 16h at 60°C. After incubation, samples were centrifuged at 14000 rpm for 10 minutes, the supernatant was collected and stored at -80°C for further analysis. DNA contents were measured by using a Picogreen dsDNA assay kit according to the manufacturer's protocol. Fluorescence was measured at 535nm using a multimode detector and concentration of dsDNA was reported in ng/mL.

#### **4.3.12 Cell morphology by actin cytoskeleton staining**

Morphology of hMSCs seeded on SF, SF-50% HA and SF-50% CaS scaffolds was observed by actin staining of the cytoskeleton at the end of 28 days using the protocol described earlier.<sup>14</sup> Scaffolds were washed with (1X) PBS and 4% paraformaldehyde was used as a fixative for 15 minutes at 25°C. The washing protocol was repeated two times. Cell permeabilization was done using 0.1% Triton X-100 (Sigma-Aldrich) for 5 minutes followed by a double PBS wash. Cells were incubated with 5% BSA for 20 minutes at room temperature. Alexa fluor 488

phalloidin was prepared in PBS 1:100 ratio and incubated for 30 minutes at room temperature in the dark to stain the actin filaments. 300nM solution of DAPI was used as a counterstain for the nucleus. Scaffolds were washed again and images were captured on Axio Observer Z1 microscope (Carl Zeiss).

### **4.3.13 Osteoblast differentiation on SF, SF-HA and SF-CaS scaffolds**

Sterilized SF, SF-50%HA, SF-50%CaS scaffolds were placed in a 96 well tissue culture treated plate and hMSCs were seeded. Seeding density were kept at  $5 \times 10^4$  cells per scaffold in 10 $\mu$ L of complete media (IMDM + 10% MSCs-FBS). The plate was kept for 5–7 minutes at 37°C, 5% CO<sub>2</sub> atmosphere followed by the addition of 90 $\mu$ L media and incubated at the same temperature for 24h. The next day, media was removed and osteogenic differentiation media was added. Fresh osteogenic media was replenished after every 48h. Osteoblast differentiation was analyzed by estimation of levels of ALP, BMP-2 and Osteocalcin. On the day of analysis, spent culture media was taken out and stored at -80°C for marker analysis.

#### **4.3.13.1 Expression of alkaline phosphatase (ALP)**

The activity of ALP was measured by using ALP colourimetric assay as per the protocol mentioned in earlier **Chapter3, Section 3.3.8**. At each use a separate ALP calibration curve is recommended to calculate ALP concentration in samples. The calibration curve used in this experiment is depicted in **Figure 4-1**.

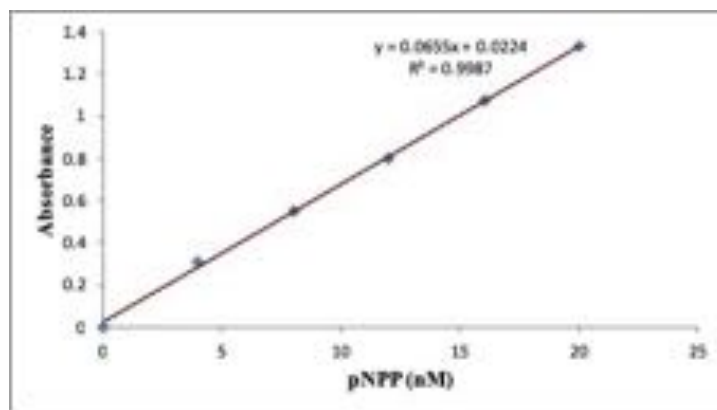


Figure 4-1 Alkaline phosphatase assay - Calibration curve

### **4.3.13.2 Expression of BMP-2 and Osteocalcin**

Both BMP-2 and osteocalcin were analyzed on day 1 and day 28. On the day of analysis, spent media was collected. Standard ELISA for both markers was carried out as per the manufacturer's instruction. The individual calibration curve as depicted in **Figure 4-2** for BMP-2 and **Figure 4-3** for osteocalcin expression were developed to calculate concentration in samples respectively.

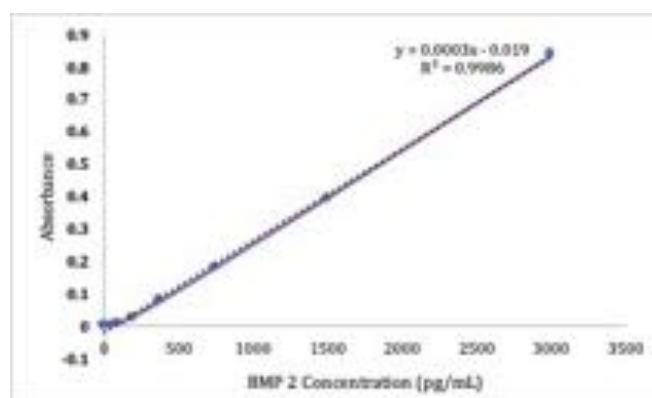
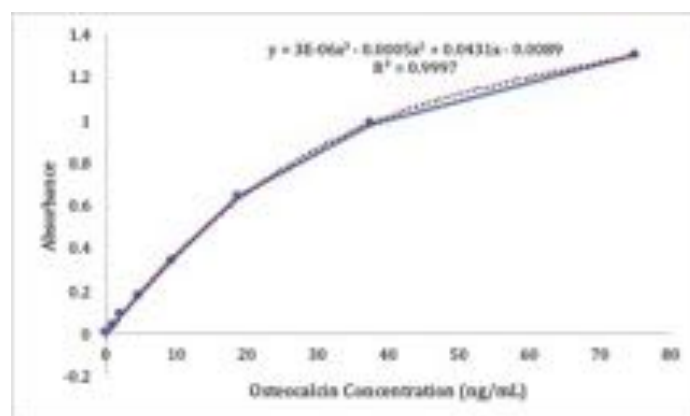


Figure 4-2 Detection of BMP 2 by ELISA - Calibration curve





**Figure 4-3** Detection of osteocalcin by ELISA - Calibration curve

### 4.3.14 Detection of inflammatory response

Inflammatory reactions against the SF, SF-50% HA and SF-50% CaS were analyzed by estimating the expression level of TNF- $\alpha$  in human monocytic cell line (THP-1) cells.  $8 \times 10^3$  cells per scaffold per well were seeded and cultured in 1ml complete media and incubated at 37°C in a 5% CO<sub>2</sub> atmosphere up to day 7 and media was changed after every 48h. On day 1 and day 7 spent media was collected and used to calculate expression levels of TNF- $\alpha$  by using a standard ELISA kit. Two independent experiments with duplicates reading in each set were taken and results are reported in terms of absorbance.

### 4.3.15 Statistical Analysis.

Statistical analysis was done by using one-way and two-way analysis of variance (ANOVA) with Tukey's post-hoc test by using Past 3 software. A value of  $p < 0.05$  was considered statistically significant.

## 4.4 Results

### 4.4.1 Preparation of microparticles and 3D scaffolds

Five variants of microparticles were prepared and analysed for particle size, surface morphology, filler content and protein conformation using various microscopic, spectroscopic and thermal characterization techniques. The pure SF microparticles were translucent golden brown in colour while SF-25/50% HA and SF-25/50% CaS microparticles were white opaque in appearance. Scaffolds were prepared in two different sizes of 2mm (h) x 4mm (D) and 4mm (h) x 8mm (D) in cylindrical moulds. In all experiments, scaffolds of 4mm (Dia) size were used except mechanical testing where 8mm (D) sized scaffolds were used.

### 4.4.2 Particle size determination

**Figure 4-4** summarises the results of image analysis performed on optical microscopic images. SF microparticles have an average particle size of 0.52mm. No significant difference in microparticle size was seen after the incorporation of 25% HA or CaS. Absolute values of particle diameter are given in **Table 4-1**. Average microparticle size was high in microparticles with 50wt% of HA (diameter-0.60mm) or CaS (diameter-0.57mm) as compared to SF microparticles. For monodispersity measurement,  $d_{90}/d_{10}$  ratio was calculated by measuring the diameters of 25 particles. The diameter was sorted in an ascending manner. The  $d_{90}$  describes the diameter where ninety percent of the particles have a smaller particle size and ten percent has a larger particle size. Therefore a ratio closer to 1, indicates that the particles are monodisperse. Notably, all microparticles exhibited a  $d_{90}/d_{10}$  ratio~1, indicating that the microparticles are monodispersed.

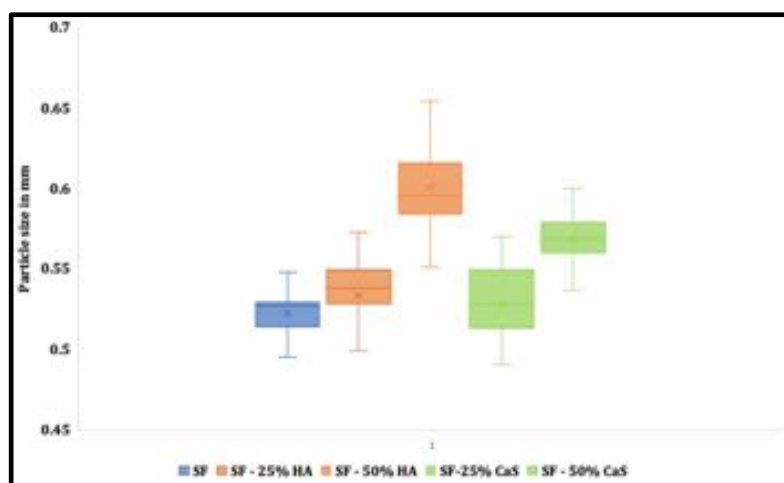


**Figure 4-4** Particle size distribution of SF, SF-25% HA, SF-50% HA, SF-25% CaS and SF-50% CaS micro-particles was analyzed using optical microscope. Images of at least 20 micro-particles were captured by using 10x objective and diameter was calculated using ZenPro

	SF	SF-25% HA	SF-50% HA	SF-25% CaS	SF-50% CaS
Avg Diameter (mm)	0.52	0.52	0.60	0.51	0.57
Minimum Diameter (mm)	0.49	0.50	0.55	0.49	0.49
Maximum Diameter (mm)	0.55	0.59	0.65	0.57	0.61
Standard Deviation	0.01	0.02	0.03	0.02	0.03
D10	0.50	0.51	0.55	0.49	0.54
D50	0.53	0.54	0.59	0.53	0.57
D90	0.54	0.58	0.65	0.55	0.59
D90/D10	1.08	1.15	1.18	1.13	1.09

**Table 4-1** Particle size distribution by optical microscopic technique

### 4.4.3 Confirmation of secondary structure in SF and in presence of bioceramics

Fourier Transform Infrared spectroscopy (FTIR) in the attenuated total reflection (ATR) mode was performed to quantify the secondary protein conformation and to verify the presence of incorporated bioceramics. Spectra is represented in **Figure 4-5**. The presence of a peak at  $1018\text{cm}^{-1}$ , in both 25wt% and 50wt% SF-HA microparticles, confirmed HA incorporation in SF microparticles. Similarly, the presence of a peak at  $1083\text{cm}^{-1}$  in both 25wt% and 50wt% SF-CaS microparticles confirmed the successful incorporation of CaS. The Amide I peak observed between  $1600\text{-}1700\text{cm}^{-1}$  was also deconvoluted to evaluate the secondary structure of the SF protein. The ratio of the beta-sheets present in the sample to the ratio of a random coil and alpha-helix structures has been described as a crystallinity index (CI). The CI has been tabulated in supporting information. As can be seen from the data in **Table 4-2**, the addition of various fillers and the quantity of the filler did not have a significant effect on the crystallinity index. The CI of the material was found to be  $\sim 1.5$ , indicating a predominance of beta-sheet conformation in all the microparticles.

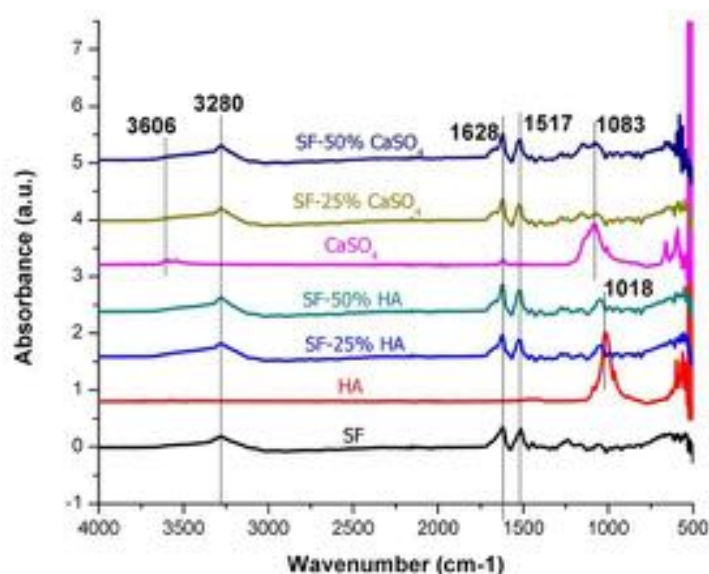


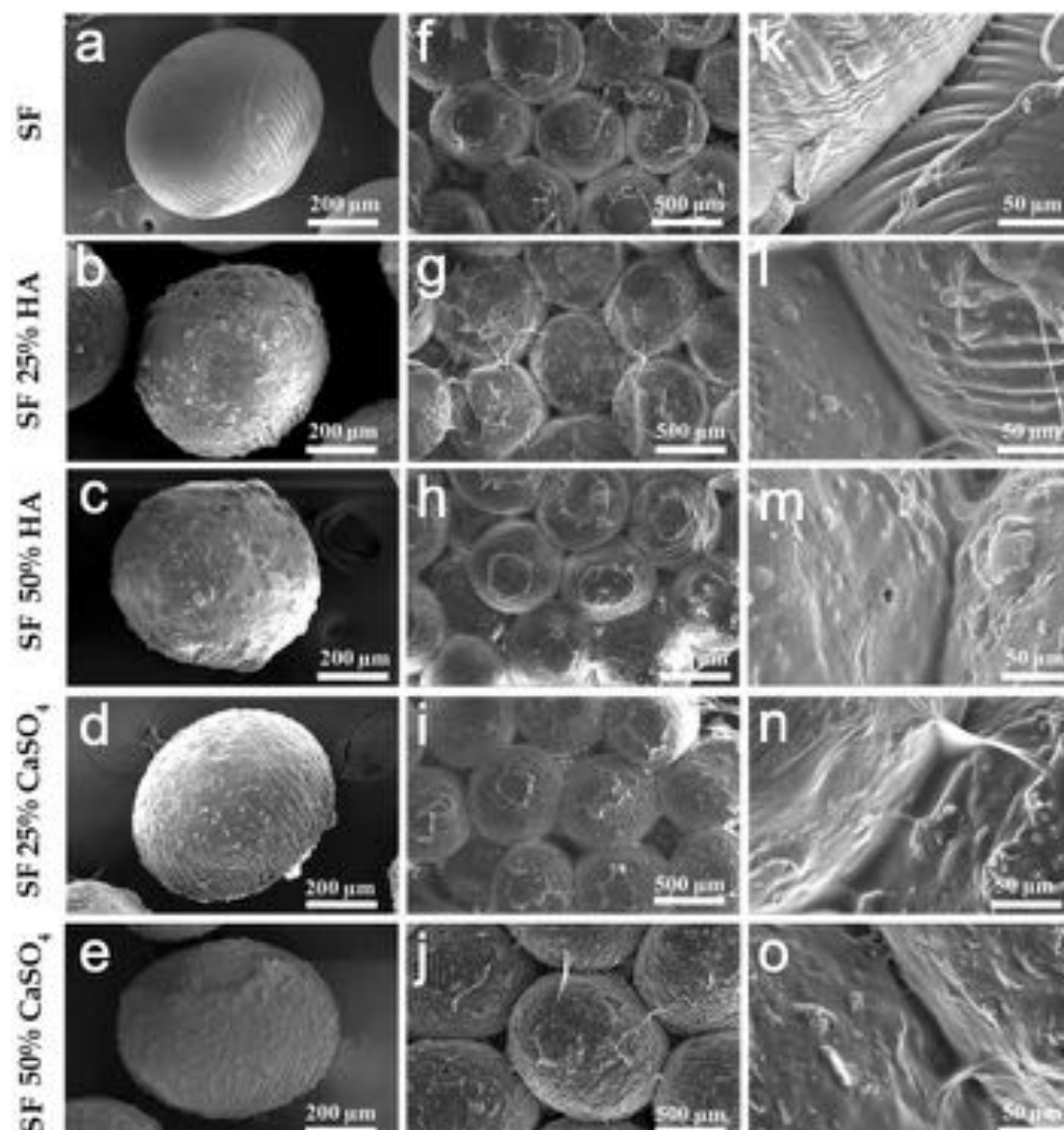
**Figure 4-5** Confirmation of secondary structures. SF, SF-25% HA, SF-50% HA, SF-25% CaS and SF-50% CaS micro-particles were analyzed using FTIR-ATR

	SF	SF-25% HA	SF-50% HA	SF-25% CaS	SF-50% CaS
Crystalline Index	1.60	1.53	1.5	1.6	1.5

**Table 4-2** Crystallinity index calculated by using Peakfit v4.1 software

#### 4.4.4 Surface morphology and elemental analysis

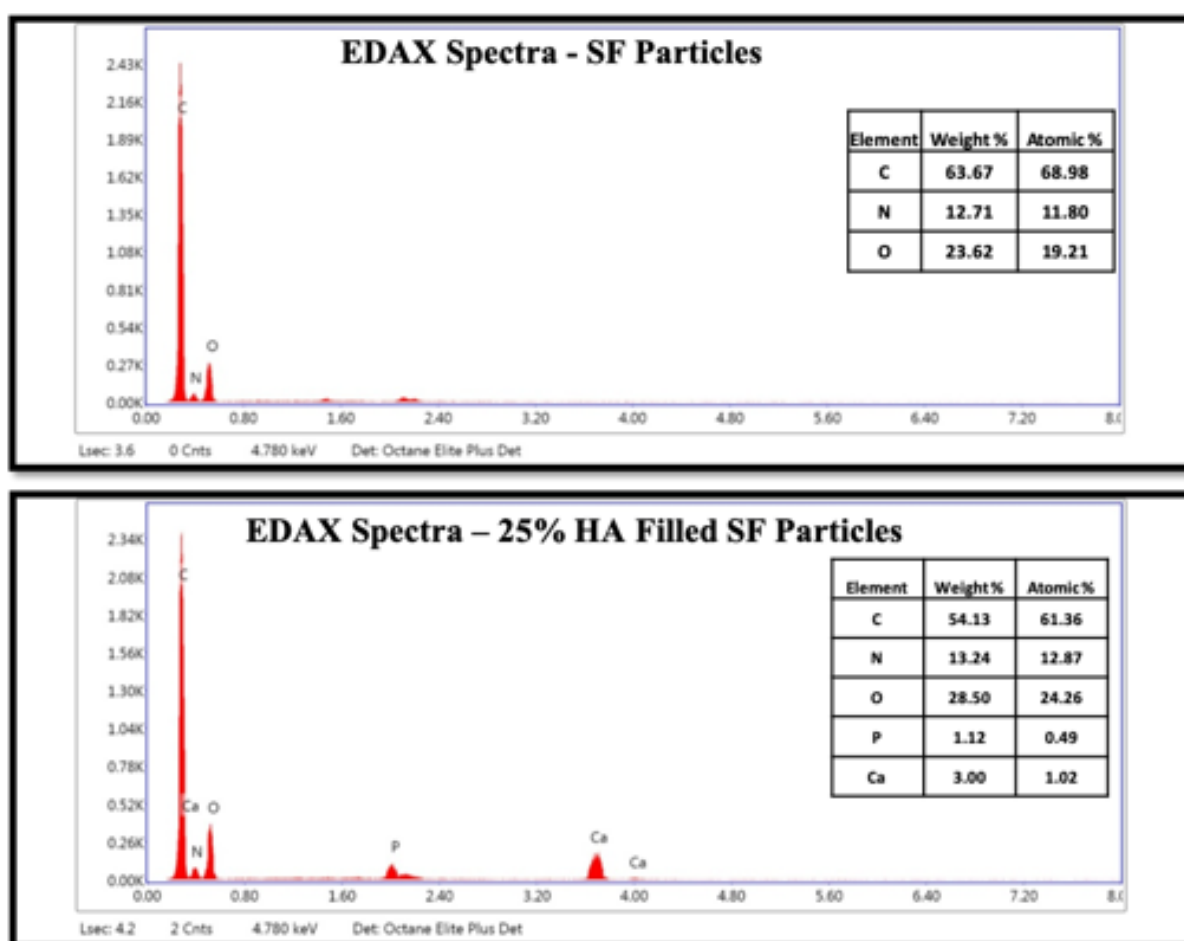
The surface of the biomaterial plays a crucial role in cellular adhesion and thereafter differentiation. The surface morphology of developed microparticles and 3D scaffolds was analyzed by using SEM (**Figure 4-6**). Fold-like microarchitecture is a characteristic of



**Figure 4-6** SEM analysis of SF micro-particles with and without bio-ceramic. Figure 3a-3e has a 200 $\mu$ m scale and represent particle sphericity and evenly distributed bioceramics in bioceramics filled particle. Figure 3f-3j has a 500 $\mu$ m scale and represent scaffold morphology with pores between the particle joints. Figure 3k-3o were shown at a 50 $\mu$ m scale and representing the tight adhesion of two particles with each other in a scaffold.

methanol treated SF microparticles as shown in the earlier publication.<sup>15</sup> We observed increased surface roughness with increased concentration of HA and CaS (**Figure 4-3a to 4-3e** respectively). SEM micrograph of SF, SF-25/50% HA and SF-25/50% CaS

scaffolds showed monodispersed microparticles arranged in hexagonal packing structure (**Figure 4-3f to 4-3j**). Clear adhesion between adjacent microparticles was visible in the electron micrograph of 3D scaffolds. (**Figure 4-3k to 4-3o**). Elemental mapping using energy dispersive spectroscopy (EDX) analysis also confirmed the incorporation of bioceramics in SF microparticles that are depicted in **Figure 4-7**. The presence of C, N, and O indicates the presence of SF-protein. The presence of Ca and P in SF-25/50% HA sample confirm the incorporation of HA and the presence of Ca and S in SF-25/50% CaS samples confirm the incorporation of CaS. SEM analysis of all three types of scaffolds also showed pore size  $>100\mu\text{m}$ .



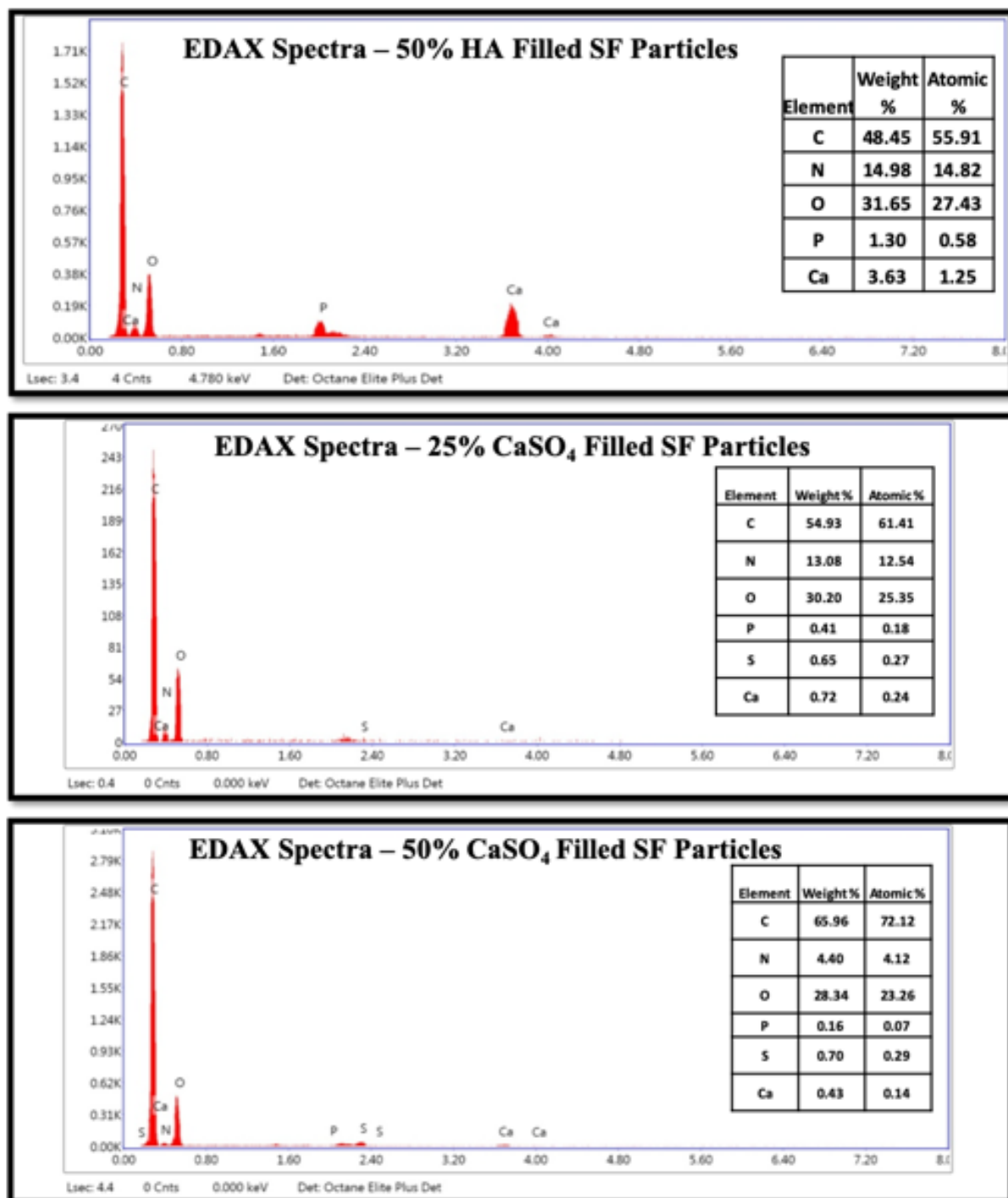


**Figure 4-7** EDX spectra of SF and bioceramics filled microparticles

#### 4.4.5 Thermogravimetric analysis (TGA)

Thermogravimetric analysis was used to quantify the amount of filler present in the micro-particles and this data is summarized in **Figure 4-8**. SF microparticles



completely degrade at  $\sim 700^\circ\text{C}$  indicated by 0% weight retention at  $T > 700^\circ\text{C}$ . SF-25% HA microparticles showed an average of 19.9% weight retention while SF-50% HA microparticles showed 29.1% weight retention at temperatures  $> 700^\circ\text{C}$  till  $900^\circ\text{C}$ . Similarly, SF-25% CaS microparticles displayed average 16.7% weight retention while SF-50% CaS microparticles showed 28.3% weight retention at temperatures  $> 700^\circ\text{C}$ . Percent weight retention of all microparticles at 700, 800 and  $900^\circ\text{C}$  are tabulated in **Table 4-3**. This indicates that after the incorporation of 50% of bioceramics, only  $\sim 30\%$  loading of filler is actually achieved in the microparticle. Further experimentation was, therefore, carried out with SF microparticles with 50% filler loading.

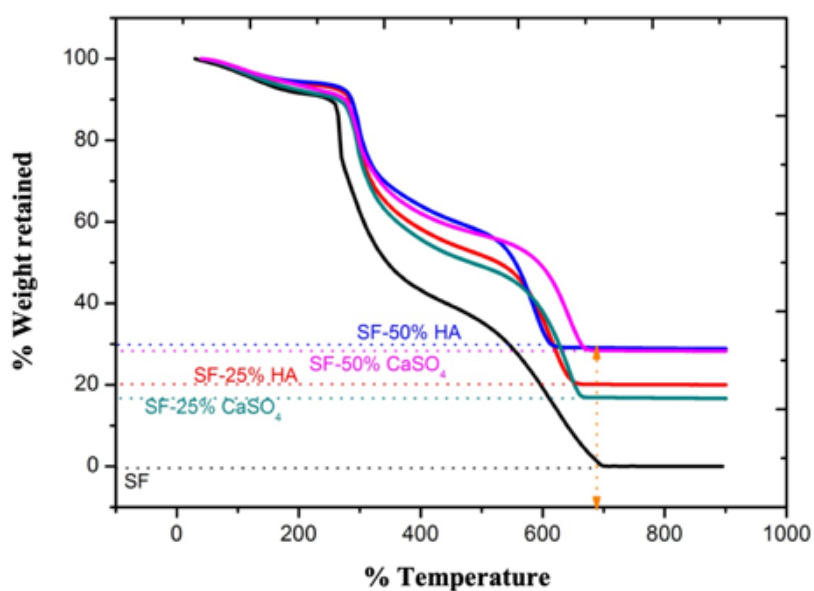


**Figure 4-8** Thermogravimetric analysis of SF, SF-25% HA, SF-50% HA, SF-25% CaS and SF-50% CaS micro-particles. TGA analysis was performed from  $25^\circ\text{C}$  to  $900^\circ\text{C}$  at a heating rate of  $10^\circ\text{C}/\text{min}$  in an air atmosphere using a TGA Q5000 machine

	SF	SF-25%HA	SF-25%CaSO <sub>4</sub>	SF-50%CaSO <sub>4</sub>	SF-50% HA

Temp.	Wt (%)	Wt (%)	Wt (%)	Wt (%)	Wt (%)
700	0	20.0	16.8	28.4	29.1
800	0	20.0	16.7	28.3	28.9
900	0	19.9	16.6	28.2	28.8
Avg Wt %	0	19.9	16.7	28.3	28.9

**Table 4-3** TGA analysis: remaining weight percent at different temperatures of SF and bioceramics filled microparticles

#### 4.4.6 Mechanical Properties of microparticles

Mechanical properties of microparticles were tested by using a nanoindentation test and reported as Young's modulus (**Figure 4-9a**). SF microparticles showed Young's modulus  $\sim 3$  GPa whereas Young's modulus of SF-50% HA and SF-50% CaS was  $\sim 8$  GPa and  $\sim 5.3$  GPa respectively. These results indicate that the blending of bioceramics (HA/CaS) with SF improved the mechanical properties of microparticles when compared with pure SF microparticles (one-way ANOVA,  $p = 2.7 \times 10^{-6}$ ).

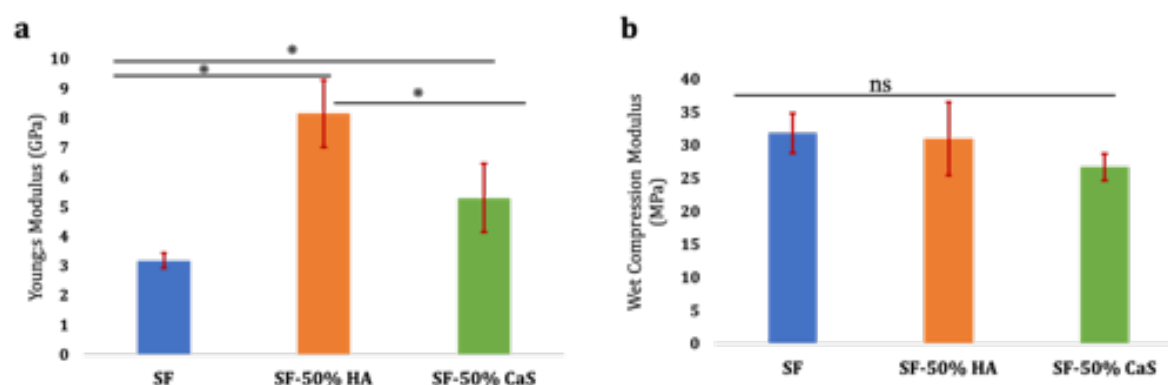


**Figure 4-9** (a) Nanoindentation: SF, SF-50% HA and SF-50% CaS particles Data represented as average Young's Modulus (GPa)  $\pm$  Std. Dev. ( $n=3$ )  $*p<0.05$ . (b) Wet compression modulus: bulk mechanical properties of SF, SF-50% HA and SF-50% CaS scaffolds, Data represented as average compression modulus  $\pm$  Std. Dev. ns: Not significant difference.

#### 4.4.7 Mechanical properties of 3D scaffolds

Bulk mechanical properties of SF, SF-50% HA and SF-50% CaS 3D scaffolds were tested and the compression modulus has been shown in **Figure 4-9b**. The SF scaffold has a compression modulus of  $\sim 31$ MPa. The SF-50% HA and SF-50% CaS scaffolds also exhibited a comparable compression modulus indicating that the addition of bioceramics did not significantly influence the bulk mechanical properties of the scaffold.

#### **4.4.8 Surface wettability of 3D scaffolds**

Surface wettability or hydrophobic/hydrophilic characteristics significantly influence cell attachment on the biomaterial. In order to assess the effect of the incorporation of bioceramics in SF on hydrophobicity/surface wettability, contact angle measurement was performed by the sessile drop method (**Figure 4-10**). SF scaffold exhibited an instantaneous contact angle of  $107 \pm 4$ , which over a time frame of 5 minutes came down to  $101 \pm 6$  indicating a hydrophobic surface (**Figure 4-10**). SF-50% HA scaffold gave an initial contact angle of  $90 \pm 7$  that was lower than the initial contact angle of SF scaffold ( $p = 0.026$ ) and further decreased to  $82 \pm 6$  with time. On the other hand, the initial contact angle of SF-50% CaS scaffold was  $75 \pm 5$ , which is also significantly lower than the initial contact angle of SF scaffold ( $p = 2.3 \times 10^{-5}$ ). Results from the data mentioned in **Figure 4-10** confirmed that bioceramics lower the hydrophobicity of SF. Thus, CaS was found to significantly lower the contact angle and improve the wettability of the scaffold.

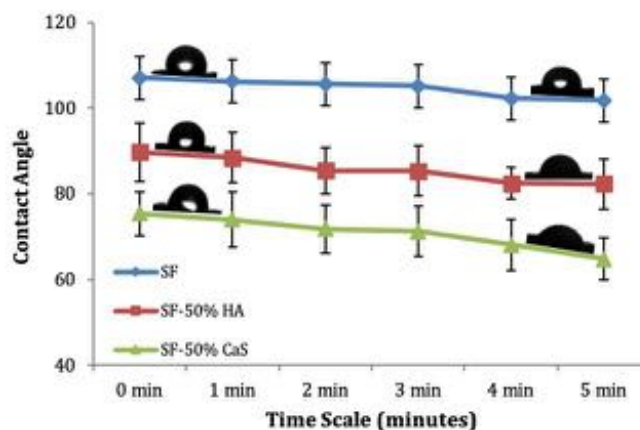


**Figure 4-10** Surface wettability of 3D scaffolds. Surface wettability of 3D scaffolds of SF, SF-50% HA and SF-50% CaS was analyzed by measuring the contact angle. Data represented as average contact angle  $\pm$  Std. Dev. ( $n=3$ )

#### 4.4.9 Bioerosion in proteolytic environment

SF, SF-50% HA and SF-50% CaS scaffolds were treated with protease XIV. The physical appearance of the enzyme-treated scaffolds is summarised in **Figure 4-11**. An average percent weight loss with respect to the initial weight of scaffolds is represented in **Figure 4-12**. On day 7, pure SF scaffolds exhibited 8% weight loss while SF-50% HA scaffolds showed only 0.6% weight loss. On other hand SF-50% CaS scaffolds showed significantly higher % weight loss (11%) compared to SF-50% HA ( $p = 2.41 \times 10^{-11}$ ). SF-50% HA scaffolds showed 3.4% weight loss by day 14 ( $p = 0.003$ ) and 10% by day 28 ( $p = 7.9 \times 10^{-11}$ ), which was significantly higher than day 7. In the case of SF-50% CaS scaffold, 25% weight loss on day 28 was significantly different than the 17% weight loss on day 14 ( $p = 7.0 \times 10^{-9}$ ).

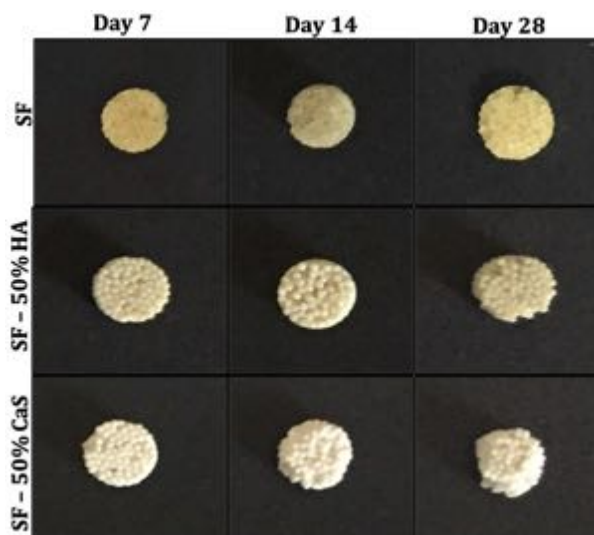


**Figure 4-11** Physical appearance of protease XIV enzyme-treated SF, SF-50% HA and SF-50% CaS scaffolds

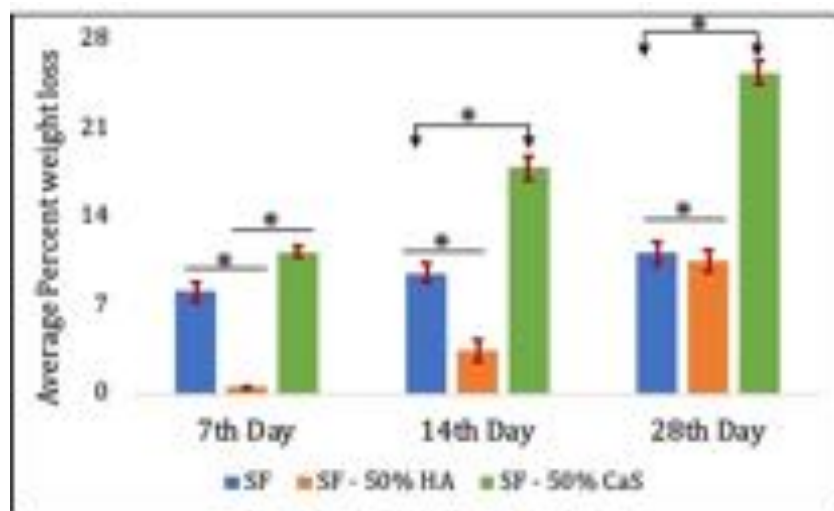


**Figure 4-12** In-vitro bio-erosion in the proteolytic environment. SF, SF-50%HA and SF-50% at different time points day 7, day 14 and day 28. Data represented as an average weight loss  $\pm$  std. dev. (n=3) \*p<0.05

#### 4.4.10 In-vitro cytotoxicity (MTT assay) assay

This test is the first step towards ensuring the application of biomaterial in tissue engineering. Therefore, to analyze cytotoxicity of developed with or without bioceramics filled microparticles based 3D scaffolds, MTT assay was performed as a prerequisite. More than 80% cell viability with both the types of direct and indirect MTT assay (**Figure 4-13**) confirmed non cytotoxic nature of the developed scaffolds.

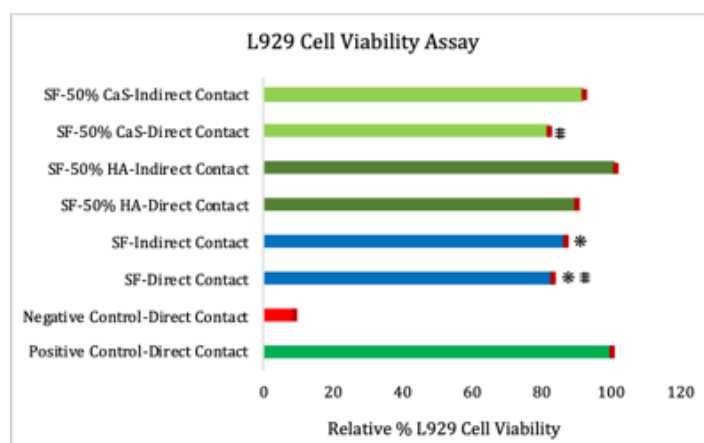


**Figure 4-13** In-vitro L929 cell viability assay (MTT assay) on SF, SF-50% HA and SF-50% CaS scaffolds. \* # Significantly not different ( $p > 0.05$ ). Others are significantly different ( $p < 0.05$ )

#### 4.4.11 Quantitative hMSCs proliferation (Picogreen dsDNA Assay)

PicoGreen dsDNA assay is an ultra-sensitive fluorescent DNA stain based kit for quantitating double-stranded DNA (dsDNA). hMSCs proliferation on SF, SF-50% HA and SF-50% CaS scaffolds were further confirmed by the quantitative PicoGreen assay and the results are summarized in **Figure 4-14a**. All three types of scaffolds supported hMSCs adhesion and proliferation. The incorporation of CaS and HA did not show a difference in hMSCs adhesion and proliferation. On day 7, pure SF scaffold showed 9.5 ng/mL DNA which was significantly increased

12.2ng/mL on 14th day ( $p = 0.002$ ) and 15.0ng/mL on 28th day ( $p = 1.7 \times 10^{-7}$ ). In the case of SF-50% HA, the initial 8.7ng/mL DNA on 7th day was not significantly increased on day 14 but rose up to 14.3ng/mL on day 28 (7th and 28th day,  $p = 1.04 \times 10^{-6}$  and 14th and 28th day,  $p = 0.003$ ). On the other hand, in SF-50% CaS scaffold, hMSCs significantly proliferate as the function of all three time points (7th and 14th day,  $p = 0.0004$ ; 14th and 28th day,  $p = 0.03$ ; 7th and 14th day,  $p = 6.99 \times 10^{-7}$ ).

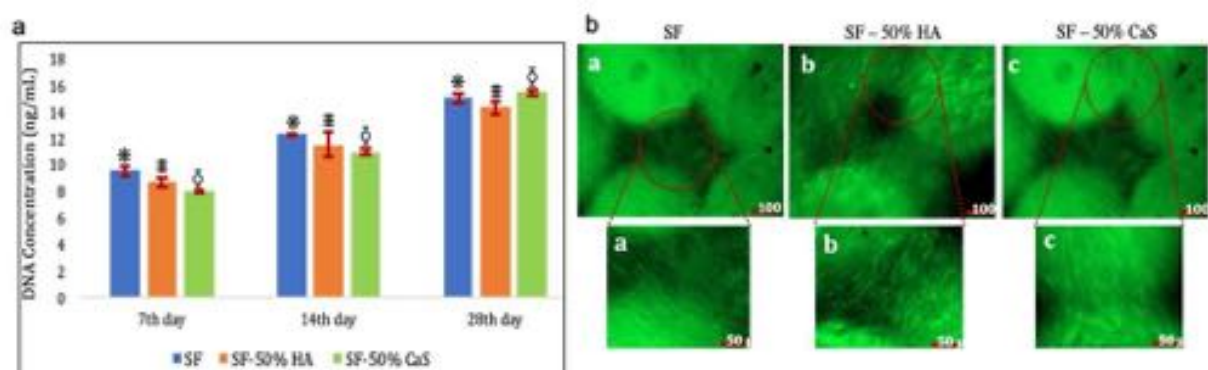


**Figure 4-14** hMSCs cell growth. (a) PicoGreen assay: dsDNA concentration was measured using Quant-iT PicoGreen dsDNA kit at day 7, day 14 and day 28-time points. Data represented as DNA concentration (ng/ml)  $\pm$  Std. Dev. ( $n=3$ ).  $*p < 0.05$ . (b) Actin staining: Morphology of hMSCs seeded on SF, SF-50% HA and SF-50% CaS scaffolds were observed by actin-cytoskeleton at the end of day 28 of culture.

#### 4.4.12 Actin cytoskeleton staining

F-actin cytoskeleton staining was visualized with Alexa Fluor 488 phalloidin and epifluorescence micrographs of F-actin were taken on day 28 (**Figure 4-14b**). In accordance with our proliferation data, we observed the well-expanded cell morphology of hMSCs. hMSCs expansion was seen throughout the microparticle surface and also in between the microparticles. No visible difference in cell cytoskeleton among different types of scaffolds was observed. The data overall suggested that the developed scaffolds do not impart any toxic effects and support hMSCs adhesion and proliferation.

### 4.4.13 Detection of osteoblast differentiation markers

Ability of scaffolds to support hMSCs differentiation into mature osteoblasts was evaluated by measuring expression of different markers such as ALP , BMP-2 and Osteocalcin (OCN).

#### **4.4.13.1 Expression of alkaline phosphatase (ALP)**

The activity of ALP was measured by colorimetric assay on the 7<sup>th</sup>,14<sup>th</sup> and 28<sup>th</sup> days. ALP activity was calculated using a standard calibration curve (**Figure 4-1**) as per the manufacturer's instruction. Calculated ALP activity is presented in **Figure 4-15a**. Detectable ALP activity was observed on day 7 in SF, SF-50% HA and SF-50% CaS scaffolds. From the data, it is observed that SF and SF-50% CaS supports hMSCs osteogenic differentiation equally on the 7<sup>th</sup> and 14<sup>th</sup> day, however, decreased activity was observed in SF-50% CaS as compared to SF. On the 14<sup>th</sup> day of the experiment, increased ALP activity in SF-50% HA with respect to the 7<sup>th</sup> day was observed and remained constant till the 28<sup>th</sup> day. In conclusion, the highest ALP activity was observed to increase in SF scaffold starting from 7<sup>th</sup> day to 28<sup>th</sup> day, while SF-50% HA started significant differentiation of hMSCs after 7<sup>th</sup> day and remained constant till 28<sup>th</sup> day.



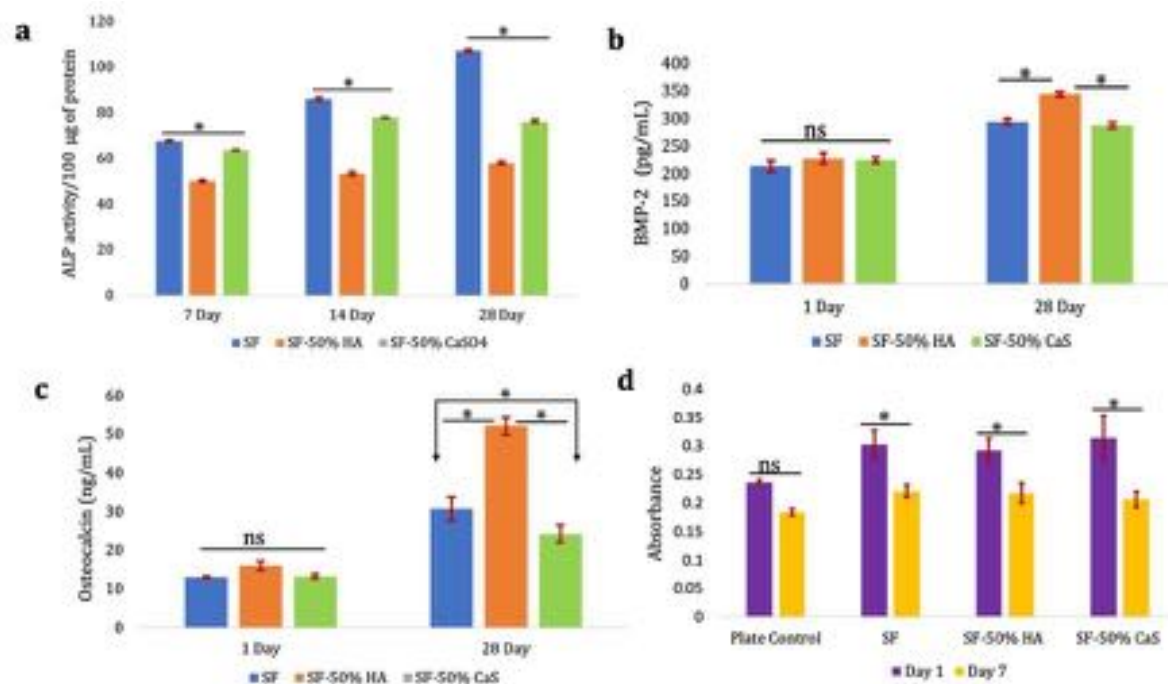


**Figure 4-15** Osteogenic differentiation and inflammatory response. (a) ALP activity was measured from conditioned media collected at day 7, day 14 and day 28. ALP activity was normalized with the total protein loaded and expressed as ALP activity / 100µg of protein. (b) BMP-2 expression was estimated from conditioned media on day 1 and day 28 using ELISA. (c) Expression of osteocalcin was also estimated by ELISA from conditioned media on day 1 and day 28. (d) Inflammatory reaction against the SF, SF-50% HA and SF-50% CaS by estimating expression level of TNF- $\alpha$ . Data represented as Average  $\pm$  Std. Dev. (n=3). ns= not significant difference. \* p < 0.05.

#### **4.4.13.2 Expression of BMP-2 and osteocalcin**

The family of BMPs play a vital role in the development of new bone tissue and osteoblast differentiation. BMP-2 levels were measured using ELISA assay. All three types of scaffolds exhibited BMP-2 expression (**Figure 4-15b**) on day 1, however by day 28 SF-50% HA showed the highest BMP-2 levels compared to SF (p = 0.002) and SF-CaS. Among SF and SF-50% CaS, no significant difference was seen in BMP-2 expression was observed on day 28.

Osteocalcin - a late osteogenic marker was estimated by using ELISA assay. As per the manufacturer's instruction (Standard curve; **Figure 4-3**). Osteocalcin expression levels are presented in **Figure 4-15c**. Under the osteogenic stimulus, hMSCs cultured on all three scaffolds showed similar expression levels of detectable osteocalcin levels on day 1 ( $p > 0.05$ ). Although hMSCs cultured on all scaffolds showed a time-dependent increase in OCN levels, by day 28. SF-50% CaS showed statistically significant, high OCN levels as compared to SF alone and SF-HA scaffolds. ( $p = 3.0 \times 10^{-12}$ ).

#### **4.4.14 Detection of Inflammatory response**

THP-1 cells were used to assess inflammatory response induced by SF, SF-50% HA and SF-50% CaS scaffolds. Untreated THP-1 cells (plate control) were considered as a negative control and TNF-alpha expression levels are represented in **Figure 4-15d**.

Relative to plate control cells, on day 1 elevated absorbance was detected in SF, SF-50% HA and SF-50% CaS scaffolds. As a function of time on day 7, the level of TNF- $\alpha$  significantly decreased with respect to day 1 ( $p = 0.02$ ) for all three types of scaffolds and as a result decrease in absorbance was observed, which was similar to non-treated control cells. The non-significant difference of TNF- $\alpha$  between control cells and all three types of scaffolds indicates that neither scaffolds stimulate an inflammatory response. This implies that filled/unfilled scaffolds are biocompatible and there is a reduced risk of failure after implantation due to immune rejection. However, further both *in-vitro* and *in-vivo* studies would be required to evaluate the immunogenic potential of these scaffolds upon implantation.

## **4.5 Discussion**

Bone defects / cavities and non-unions are the most frequently encountered problems in modern reconstructive orthopaedic surgery and here use of bone void filler is a promising option. Bone tissue engineering is, therefore, an active area of research.<sup>16,17</sup> One of the most important elements of BTE is the design of a biocompatible scaffold that provides appropriate mechanical support with optimum pore size and interconnected porosity. Porosity was calculated by measuring the weight and volume of individual cylindrical scaffolds. The densities used for calculation were silk fibroin = 1.35 gm/cm<sup>3</sup>; calcium sulphate = 2.32 gm/cm<sup>3</sup>; hydroxyapatite = 3.16 gm/cm<sup>3</sup>. These properties must be over and above the property of osteo-regeneration. The scaffold must also have appropriate and controlled bioerosion rates and also the flexibility to incorporate functional biomolecules for osteoinductivity.<sup>18,19</sup>

Synthetic bone void fillers, which are currently used in surgery include ceramics such as hydroxyapatite, calcium sulfate, tricalcium phosphate and/or their blends/composites with synthetic or natural polymers. SF – a natural biopolymer, has been extensively explored in the recent past for BTE. It has also been blended with other polymers and ceramics for BTE applications.<sup>20,21</sup> Our group has more recently also demonstrated the promise of silk microparticle based scaffolds in BTE.<sup>13</sup> Further, we have also shown that osteogenic differentiation ability of these scaffolds can be enhanced by simple surface coating of scaffolds with collagen and chitosan, which are natural bio-polymers. The objective of this work was to understand the effect of filler loading on the osteogenic potential of SF microparticle scaffolds. The scaffolds were thoroughly characterised for their morphological, chemical and mechanical properties and the study unfolds crucial insights into the linkage between these properties and the osteogenic potential of SF as a scaffolding material in BTE.

This study demonstrated a simple and reproducible protocol to develop composite scaffolds of SF either with HA or CaS. HA is a most stable bioceramics that has chemical similarities to natural bone. HA is also osteoconductive and has low immunogenicity.<sup>22</sup> CaS is another biocompatible, bioresorbable ceramic. CaS is also known to be hydrophilic as compared to SF and HA.<sup>23,24</sup> The uniform loading of the fillers into the micro-particles was confirmed using spectroscopic techniques such as FTIR and EDS. FTIR analysis also further confirmed that there was no significant change in secondary protein conformation upon addition of fillers. TGA analysis corroborated that the maximum loading of fillers was ~30% by weight of SF. Microscopic images confirmed that the surface of these ceramic filled microparticles is different from the surface of pure SF microparticle. The ceramic fillers are uniformly distributed throughout the surface of the microparticle. This implies that the surface would have a mixture of functional groups that the cells would interact with. The presence of these ceramic fillers on the surface of the microparticle also increases the surface roughness of the microparticles. This change in chemical and physical properties of the microparticle surface, also affects the hydrophilicity of the scaffold, with the CaS-filled microparticles being most hydrophilic.

Bone is the highest load bearing tissue in the body. The mechanical strength of cancellous bone varies from 10MPa to 30GPa depending on the anatomical site in the body and the race, ethnicity, gender and age of the patient.<sup>25</sup> Therefore, it is necessary to characterize the mechanical properties of the scaffold. The bulk modulus of developed scaffolds (**Figure 4-9b**) shows a comparable modulus for filled and unfilled SF scaffolds. This is due to the fact that the bulk porosity of the scaffold plays a significant role as compared to the filler loading. This has also been reported for other microparticle scaffolds. It may also be noted here that the SF-50% CaS scaffold has slightly higher bulk porosity and correspondingly a slightly

lower compression modulus. The compression modulus is a bulk property but an individual cell would interact with the surface of a single microparticle.

Therefore, it is necessary to characterise the mechanical properties of the individual microparticle. The measurement of this local modulus of the microparticles was done using nano-indentation. It was surprising to see a Young's modulus > 2GPa for all our scaffolds, with the SF-50% HA microparticle showing the highest modulus. The fillers, therefore, do reinforce the SF matrix and improve the modulus of the filled microparticles.

SF bioresorb in the body over a time duration varying from few months to few years, depending on the SF protein. Here, we demonstrate that in spite of having similar protein conformation, the rate of bioerosion can be tuned by incorporation of different bioceramics (**Figure 4-12**). The rate of bioerosion is fastest in CaS filled scaffolds and is lowest in HA filled scaffolds while pure SF microparticles have an intermediate rate of bioerosion. HA and CaS both have good biocompatibility and osteoinductivity but are limited by its bioresorption rate. HA bioresorb at an extremely slow rate resulting in new bone forming primarily around the filler.<sup>26,27</sup> CaS bioresorbs within few months of implantation, not providing enough time for the new bone to form.<sup>28</sup> Rate of new bone formation also depends on the age of the patient and the anatomical site. It also depends on the physical well-being of the patient. For example, the rate of new bone formation in a child is extremely high while it can be uncannily slow for an osteoporotic patient. Thus, here we propose a system that allows a clinician to pick and choose the appropriate bone void filler depending on the patient needs and the clinical condition.

Addition of filler to microparticle based biomaterial has no significant effect on cell growth, observed in qualitative cell growth analysis and quantitative cell assay are also in line with the report by Kucharska et al.<sup>29</sup>

Also, during adult bone remodelling and repair, the stem cells differentiate into an osteoblastic lineage upon receiving appropriate signals from the biomaterial. There are multiple osteogenic markers of the osteoblast that appear in the surroundings during the differentiation process at different time and have also been well documented with respect to each stage of the path way.<sup>30,31</sup> Osteogenic potential of SF, SF-50% HA and SF-50% CaS were evaluated by measuring the osteogenic markers ALP, osteocalcin. Among the family of BMPs, BMP-2 plays a crucial role in osteogenesis<sup>32</sup> and it has also been reported that mRNAs of BMP-2 are expressed only later in osteogenesis.<sup>33</sup> We measured BMP-2 concentration on 28<sup>th</sup> day. In the osteogenic differentiation process, days 1-14 are known as the initial level while days 14 - 28 is reported as a later phase of the process. ALP level is significantly increased in SF and SF- 50% CaS on 7<sup>th</sup> day. This confirms early differentiation in these scaffolds, which was significantly decreased on 28<sup>th</sup> day. SF-50% HA induced hMSCs differentiation after 7<sup>th</sup> day. On the day 28, we observed a decreased ALP level in all three scaffolds indicating successful differentiation of hMSCs into osteoblast. SF-50% HA performs better at later stages of differentiation and this is further validated by the significantly high level of osteocalcin and BMP-2 with respect to SF and SF-50% CaS. Also, significantly increased secretion of both osteocalcin and BMP-2 on 28<sup>th</sup> day as compare to day 1 in all three types of scaffolds, indicates that although the signalling pathways (early and late) maybe different for various scaffolds, each of the scaffold, does support differentiation of hMSCs into osteogenic lineage.

Innate immunity - a first line of defence system is non-specific reactions, which involves immune recognition by responding to foreign material and activation of monocytes that results in the rejection of foreign material.<sup>34</sup> Toll like receptors (TLRs) are present on the surface of monocytes and activation of TLRs results in the secretion of IL1b, IL6 and TNF pro-inflammatory cytokines.<sup>35</sup> Herein, we observed that even after long incubation time (7 days) with THP-1 cells, the

scaffolds did not trigger macrophage response indicating the non-immunogenic nature of SF.<sup>36</sup>

During the bone development, there are several signalling cascades involved such as BMP/TGF $\beta$ , WNT, Notch, FGF, IGF and PDGF. It has been demonstrated that without supplementation of dexamethasone, SF results in osteogenic differentiation of BMSCs by activating WNT/ $\beta$ -catenin signalling. Calcium ions are known to activate NOTCH cascade – a osteogenic regulator along with ERK/MPK signalling pathway<sup>37-39</sup> and this might be the reason that SF-50% CaS scaffold secretes osteogenic marker in early phase of differentiation process. On the other hand, HA is known for the triggering of ERK/MAPK, FGF and NOTCH signalling<sup>6</sup> which results in the steady significant performance of SF-50% HA scaffolds in later phase of osteogenic differentiation. It has been also documented that mechanical stiffness is also responsible in the activation of ERK/MAPK cascade. SF itself has the ability to trigger osteogenic signalling. However, co-activation of more than one signalling cascade to achieve hMSCs differentiation into osteogenic lineage might also prove to be a promising strategy for bone void fillers especially in clinical settings.<sup>40,41</sup>

## 4.6 Conclusions

We report here the potential of 3D silk fibroin microparticle scaffolds with and without bioceramics (HA and CaS) for osteo-regeneration applications. The physico-chemical and mechanical characterization of these filled/unfilled microparticles showed that the particles are monodisperse, have appropriate surface texture and roughness for cell attachment and the SF protein has a predominant beta sheet conformation. We also demonstrated incorporation of bioceramics ~30% by weight of microparticles. Interestingly, the addition of fillers

did not alter the bulk mechanical properties of the scaffold. However, the Young's modulus measured using a nano-indentation experiment confirmed a two and three fold increase for the SF-50% CaS and SF-50% HA scaffolds respectively. The 3D scaffolds prepared using these microparticles also exhibit tuneable rates of bioerosion, where the SF-CaS scaffold exhibited the fastest rate of bioerosion and the SF-HA scaffold had the slowest rate. The scaffolds are non-cytotoxic and non-immunogenic. SF-50% CaS support the early stage differentiation of stem cells as compared to SF-50% HA scaffolds, which predominantly increase differentiation at late stage. Thus, we would like to conclude that addition of fillers to SF microparticles provides an easy methodology to tune the performance of the scaffold in BTE with an exceptional control on the mechanical, bioresorption and osteo-regenerative properties.

## 4.7 References

- (1) Fernandez de Grado, G.; Keller, L.; Idoux-Gillet, Y.; Wagner, Q.; Musset, A. M.; Benkirane-Jessel, N.; Bornert, F.; Offner, D. Bone Substitutes: A Review of Their Characteristics, Clinical Use, and Perspectives for Large Bone Defects Management. *J. Tissue Eng.* **2018**, *9*. <https://doi.org/10.1177/2041731418776819>.
- (2) Carson, J. S.; Bostrom, M. P. G. Synthetic Bone Scaffolds and Fracture Repair. *Injury* **2007**, *38* (SUPPL. 1). <https://doi.org/10.1016/j.injury.2007.02.008>.
- (3) Gao, C.; Deng, Y.; Feng, P.; Mao, Z.; Li, P.; Yang, B.; Deng, J.; Cao, Y.; Shuai, C.; Peng, S. Current Progress in Bioactive Ceramic Scaffolds for Bone Repair and Regeneration. *Int. J. Mol. Sci.* **2014**, *15* (3), 4714–4732. <https://doi.org/10.3390/ijms15034714>.
- (4) Stefan Zwingenberger, Christophe Nich, Roberto D. Valladares, Zhenyu Yao, Maik Stiehler, and S. B. G. Recommendations and Considerations for the Use



- of Biologics in Orthopedic Surgery. **2012**, 26 (4), 245–256. <https://doi.org/10.2165/11631680-000000000-00000.Recommendations>.
- (5) Midha, S.; Murab, S.; Ghosh, S. Osteogenic Signaling on Silk-Based Matrices. *Biomaterials* **2016**, 97, 133–153. <https://doi.org/10.1016/j.biomaterials.2016.04.020>.
- (6) Mottaghitlab, F.; Hosseinkhani, H.; Shokrgozar, M.; Mao, C.; Yang, M.; Farokhi, M. Silk as a Potential Candidate for Bone Tissue Engineering. *J. Control. release* **2015**, 215, 112–128.
- (7) Huang, W.; Ling, S.; Li, C.; Omenetto, F. G.; Kaplan, D. L. Chem Soc Rev Generated Using Bio-Nanotechnology. **2018**, 6486–6504. <https://doi.org/10.1039/c8cs00187a>.
- (8) Kasoju, N.; Bora, U. Silk Fibroin in Tissue Engineering. *Adv. Healthc. Mater.* **2012**, 1 (4), 393–412. <https://doi.org/10.1002/adhm.201200097>.
- (9) Kundu, B.; Rajkhowa, R.; Kundu, S. C.; Wang, X. Silk Fibroin Biomaterials for Tissue Regenerations ☆. *Adv. Drug Deliv. Rev.* **2013**, 65 (4), 457–470. <https://doi.org/10.1016/j.addr.2012.09.043>.
- (10) Das, S.; Pati, D.; Tiwari, N.; Nisal, A.; Sen Gupta, S. Synthesis of Silk Fibroin-Glycopolyptide Conjugates and Their Recognition with Lectin. *Biomacromolecules* **2012**, 13 (11), 3695–3702. <https://doi.org/10.1021/bm301170u>.
- (11) Sofia, S.; McCarthy, M. B.; Gronowicz, G.; Kaplan, D. L. Functionalized Silk-Based Biomaterials for Bone Formation. *J. Biomed. Mater. Res.* **2001**, 54 (1), 139–148. [https://doi.org/10.1002/1097-4636\(200101\)54:1<139::AID-JBM17>3.0.CO;2-7](https://doi.org/10.1002/1097-4636(200101)54:1<139::AID-JBM17>3.0.CO;2-7).
- (12) Hayden R. S.; Vollrath M.; Kaplan D. L. NIH Public Access. **2014**, 10 (1), 1–17. <https://doi.org/10.1016/j.actbio.2013.09.028.Effects>.
- (13) Parekh, N.; Hushye, C.; Warunkar, S.; Gupta, S. Sen; Nisal, A. RSC Advances In Vitro Study of Novel Microparticle Based Silk. *RSC Adv.* **2017**, 7, 26551–

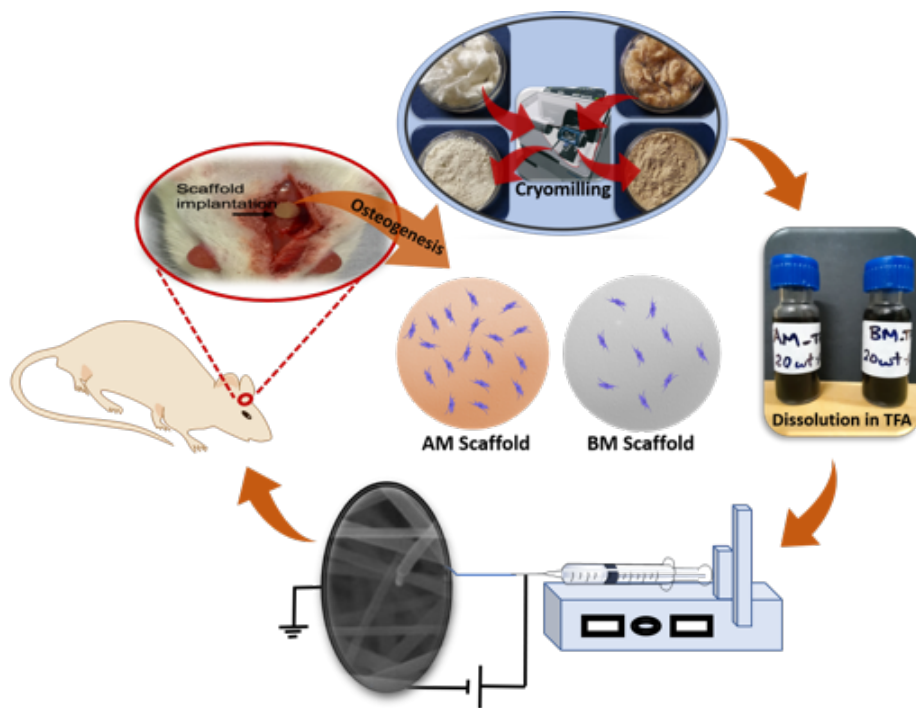
26558. <https://doi.org/10.1039/C7RA03288A>.
- (14) Nisal, A.; Sayyad, R.; Dhavale, P.; Khude, B.; Deshpande, R. Silk Fibroin Micro-Particle Scaffolds with Superior Compression Modulus and Slow Bioresorption for Effective Bone Regeneration. **2018**, No. April, 1–10. <https://doi.org/10.1038/s41598-018-25643-x>.
- (15) Mandal, B. B.; Grinberg, A.; Seok, E.; Panilaitis, B.; Kaplan, D. L. High-Strength Silk Protein Scaffolds for Bone Repair. *Pnas* **2012**, *109* (20), 7699–7704. <https://doi.org/10.1073/pnas.1119474109>.
- (16) Ak, F.; Oztoprak, Z.; Karakutuk, I.; Okay, O. Macroporous Silk Fibroin Cryogels. *Biomacromolecules* **2013**, *14* (3), 719–727. <https://doi.org/10.1021/bm3018033>.
- (17) Yetiskin, B.; Akinci, C.; Okay, O. Cryogelation within Cryogels : Silk Fibroin Scaffolds with Single-, Double- and Triple-Network Structures. *Polymer (Guildf)*. **2017**, *128*, 47–56. <https://doi.org/10.1016/j.polymer.2017.09.023>.
- (18) Journal, A. I.; Bölgen, N.; Korkusuz, P.; Vargel, İ.; Kılıç, E.; Güzel, E.; Uçkan, D.; Pişkin, E. Stem Cell Suspension Injected HEMA-Lactate- Dextran Cryogels for Regeneration of Critical Sized Bone Defects Stem Cell Suspension Injected HEMA-Lactate-Dextran Cryogels for Regeneration of Critical Sized Bone Defects. **2014**, *1401*. <https://doi.org/10.3109/21691401.2013.775578>.
- (19) Raia, N. R.; Partlow, B. P.; McGill, M.; Kimmerling, E. P.; Ghezzi, E.; Kaplan, D. L. Enzymatically Crosslinked Silk-Hyaluronic Acid Hydrogels. *Biomaterials* **2017**. <https://doi.org/10.1016/j.biomaterials.2017.03.046>.
- (20) Jo, Y. Y.; Kim, S. G.; Kwon, K. J.; Kweon, H. Y.; Chae, W. S.; Yang, W. G.; Lee, E. Y.; Seok, H. Silk Fibroin-Alginate-Hydroxyapatite Composite Particles in Bone Tissue Engineering Applications in Vivo. *Int. J. Mol. Sci.* **2017**, *18* (4). <https://doi.org/10.3390/ijms18040858>.
- (21) Shen, Y.; Yang, S.; Liu, J.; Xu, H.; Shi, Z.; Lin, Z.; Ying, X.; Guo, P.; Lin, T.; Yan, S.; Huang, Q.; Peng, L. Engineering Scaffolds Integrated with Calcium Sulfate and Oyster Shell for Enhanced Bone Tissue Regeneration. *Appl. Mater.*

- Interfaces* **2014**, *6*, 12177–12188. <https://doi.org/10.1021/am501448t>.
- (22) Farokhi, M.; Mottaghitlab, F.; Samani, S.; Shokrgozar, M. A.; Kundu, S. C.; Reis, R. L.; Fatahi, Y.; Kaplan, D. L. Silk Fibroin/Hydroxyapatite Composites for Bone Tissue Engineering. *Biotechnol. Adv.* **2018**, *36* (1), 68–91. <https://doi.org/10.1016/j.biotechadv.2017.10.001>.
- (23) Thomas, M. V.; Puleo, D. A. Calcium Sulfate: Properties and Clinical Applications. *J. Biomed. Mater. Res. - Part B Appl. Biomater.* **2009**, *88* (2), 597–610. <https://doi.org/10.1002/jbm.b.31269>.
- (24) Pecora, G.; De Leonardis, D.; Ibrahim, N.; Bovi, M.; Cornelini, R. The Use of Calcium Sulphate in the Surgical Treatment of a “through and through” Periradicular Lesion. *Int. Endod. J.* **2001**, *34* (3), 189–197. <https://doi.org/10.1046/j.1365-2591.2001.00369.x>.
- (25) Henkel, J.; Woodruff, M. A.; Epari, D. R.; Steck, R.; Glatt, V.; Dickinson, I. C.; Choong, F. M.; Schuetz, M. A.; Hutmacher, D. W. Bone Regeneration Based on Tissue Engineering Conceptions – A 21st Century Perspective. **2013**, 216–248. <https://doi.org/10.4248/BR201303002>.
- (26) Kim, M. H.; Kim, B. S.; Lee, J.; Cho, D.; Kwon, O. H.; Park, W. H. Silk Fibroin/Hydroxyapatite Composite Hydrogel Induced by Gamma-Ray Irradiation for Bone Tissue Engineering. *Biomater. Res.* **2017**, *21* (1), 1–9. <https://doi.org/10.1186/s40824-017-0098-2>.
- (27) Krishnamurithy, G.; Science, M.; Medicine, C. C. A Review on Hydroxyapatite-Based Scaffolds As a Potential Bone Graft Substitute for Bone Tissue Engineering Applications. *Jumec* **2013**, *16* (2), 1–6.
- (28) Wang, P.; Pi, B.; Wang, J. N.; Zhu, X. S.; Yang, H. L. Preparation and Properties of Calcium Sulfate Bone Cement Incorporated with Silk Fibroin and Sema3A-Loaded Chitosan Microspheres. **2015**, *9* (1), 51–65. <https://doi.org/10.1007/s11706-015-0278-8>.
- (29) Kucharska, M.; Walenko, K.; Lewandowska-Szumieł, M.; Brynk, T.; Jaroszewicz, J.; Ciach, T. Chitosan and Composite Microsphere-Based

- Scaffold for Bone Tissue Engineering: Evaluation of Tricalcium Phosphate Content Influence on Physical and Biological Properties. *J. Mater. Sci. Mater. Med.* **2015**, 26 (3). <https://doi.org/10.1007/s10856-015-5464-9>.
- (30) Aubin, J. E. Regulation of Osteoblast Formation and Function. *Reviews in Endocrine and Metabolic Disorders.* 2001, pp 81–94. <https://doi.org/10.1023/A:1010011209064>.
- (31) Rutkovskiy, A.; Stensløykken, K.-O.; Vaage, I. J. Osteoblast Differentiation at a Glance. *Med. Sci. Monit. Basic Res.* **2016**, 22, 95–106. <https://doi.org/10.12659/msmbr.901142>.
- (32) Canalis, E.; Economides, A. N.; Gazzerro, E. Bone Morphogenetic Proteins, Their Antagonists, and the Skeleton. *Endocr. Rev.* **2003**, 24 (2), 218–235. <https://doi.org/10.1210/er.2002-0023>.
- (33) Huang, Z.; Nelson, E. R.; Smith, R. L.; Goodman, S. B. The Sequential Expression Profiles of Growth Factors from Osteroprogenitors to Osteoblasts in Vitro. *Tissue Eng.* **2007**, 13 (9), 2311–2320. <https://doi.org/10.1089/ten.2006.0423>.
- (34) Maumita Bhattacharjee, Elke Schultz-Thater, Emanuele Trella, Sylvie Miot , Sanskrita Das, Marko Loparic , Alok R. Ray, Ivan Martin, Giulio C. Spagnoli, S. G. The Role of 3D Structure and Protein Conformation on the Innate and Adaptive Immune Responses to Silk-Based Biomaterials. *Biomaterials* **2013**, 34, 8161–8171.
- (35) GregoryH.Altman, FrankDiaz, CarolineJakuba, TaraCalabro, RebeccaL.Horan, JingsongChen, HelenLu, JohnRichmond, D. K. Silk-Based Biomaterials. *Biomaterials* **2003**, 24, 401–416.
- (36) Matteo Santin Antonella Motta Giuliano Freddi Mario Cannas. In Vitro Evaluation of the Inflammatory Potential of the Silk Fibroin. *J. Biomed. Mater. Res.* **1999**, 46 (3).
- (37) Leila Ghorbanian, Rahmatollah Emadi, Seyed Mohammad Razavi, Heungsoo Shin, A. T. Fabrication and Characterization of Novel Diopside/Silk Fibroin

- Nanocomposite Scaffolds for Potential Application in Maxillofacial Bone Regeneration. *Int. J. Biol. Macromol.* **2013**, *58*, 275–280.
- (38) S. Khoshniat, A. Bourguine, M. Julien, M. Petit, P. Pilet, T. Rouillon, et al. Phosphate-Dependent Stimulation of MGP and OPN Expression in Osteoblasts via the ERK1/2 Pathway Is Modulated by Calcium. *Bone* **2011**, *48* (4), 894–902.
- (39) Dvorak, M. M.; Siddiqua, A.; Ward, D. T.; Carter, D. H.; Dallas, S. L.; Nemeth, E. F.; Riccardi, D. Physiological Changes in Extracellular Calcium Concentration Directly Control Osteoblast Function in the Absence of Calciotropic Hormones. *Proc. Natl. Acad. Sci. U. S. A.* **2004**, *101* (14), 5140–5145. <https://doi.org/10.1073/pnas.0306141101>.
- (40) C.B. Khatiwala, P.D. Kim, S.R. Peyton, A. J. P. ECM Compliance Regulates Osteogenesis by Influencing MAPK Signaling Downstream of RhoA and ROCK. *J. Bone Miner. Res.* **2009**, *24* (5), 886–898.
- (41) Shih, Y. R. V.; Tseng, K. F.; Lai, H. Y.; Lin, C. H.; Lee, O. K. Matrix Stiffness Regulation of Integrin-Mediated Mechanotransduction during Osteogenic Differentiation of Human Mesenchymal Stem Cells. *J. Bone Miner. Res.* **2011**, *26* (4), 730–738. <https://doi.org/10.1002/jbmr.278>.

# Chapter 5 Development of non-mulberry electrospun scaffold



This chapter is adapted from the following submitted and under review manuscript to “The International Journal of Biological Macromolecules”

“Superior processability of *Antheraea mylitta* silk with cryo-milling: performance in bone tissue regeneration”, **Nimisha Parekh\***, Bijosh C K, Kartiki Kane, Alaka Panicker, Anuya A. Nisal\*, Pralhad Wangikar and Sachin Agawane,

## 5.1 Abstract

Non-mulberry silk polymers have a promising future in biomedical applications. However, the dissolution of non-mulberry silk fiber is still a challenge and this poor processability has limited the use of this material. Here, we report a unique protocol to process the *Antheraea mylitta* (AM) silk fiber. We have shown that the cryo-milling of silk fiber reduces the beta sheet content by more than 10% and results in an SF powder that completely dissolves in routine solvents like trifluoroacetic acid (TFA) within few hours to form highly concentrated solutions (~20wt%). Further, these solutions can be processed using conventional processing techniques such as electrospinning to form 3D scaffolds. *Bombyx mori* (BM) silk was used as a control sample in the study. *In-vitro* studies were also performed to monitor cell adhesion and proliferation and hMSCs differentiation into osteogenic lineage. Finally, the osteogenic potential of the scaffolds was also evaluated by a 4-week implantation study in rat calvarial model. The *in-vitro* and *in-vivo* results show that the processing techniques do not affect the biocompatibility of the material and the AM scaffolds support bone regeneration. Our results, thus, show that cryo-milling facilitates enhanced processability of non-mulberry silk and therefore expands its potential in biomedical applications.

This Chapter begins with Section 5.2, which describes a literature review by discussing the use of non-mulberry silk as a biomaterial and the difficulty in processing the SF solution from silk fiber. Section 5.3 focuses on the materials and experimental protocols used in the study. Section 5.4 summarises the results followed by a discussion in Section 5.5. Section 5.6 concludes Chapter 5 and Section 5.7 compiles references used in this study.

## 5.2 Literature Review

In bone, non-union multisite/craniofacial fractures need a non-load bearing external bone void filler. Various materials like ceramics, natural/synthetic polymers and different blends are explored as either in the form of film/electrospun mats to treat the bone cracks or craniofacial defects.<sup>1-5</sup>

SF has been recognized as a promising material for BTE from many decades due to its versatile biochemical and biomechanical properties.<sup>6,7</sup> Mulberry silk of silkworm *Bombyx mori* (BM) has been extensively explored for biomedical applications because of its known aqueous processability.<sup>3</sup> However, the transformation of non-mulberry silk from being a textile commodity to biomaterials is relatively new and exciting.<sup>8,9</sup>

Non-mulberry silk has an inherent RGD motif, which helps cell attachment, cell proliferation and differentiation.<sup>10-13</sup> Non-mulberry silk also contains higher alanine amino acid that results in higher beta-sheet conformation and reduces the ability to process this silk.<sup>14,15</sup> This is why most reported literature on non-mulberry silk uses silk extracted directly from the silkworm's silk gland.<sup>16-18</sup> Different types of non-mulberry silks are used as biomaterials such as *Antheraea mylitta* and *Antheraea pernyi* and *Antheraea assamensis*.<sup>9,19</sup> This work focuses on *Antheraea mylitta* (AM) silk. There are a few reports, where Lithium bromide, a chaotropic salt, is used to make a solution from the silk fiber of AM.<sup>8,20-25</sup> However, this process results in an SF solution with low concentration. The dissolution



process is also tedious and typically requires 12h to prepare a solution in LiBr to produce a 0.8mg/mL concentration solution.<sup>12</sup> In another study, the authors have reported the use of 1-Butyl-3-Methylimidazolium Acetate (BMIAC) to process the AM fibers.<sup>26</sup> Here, too, the authors reported that the protocol involves more than one day to obtain silk fibroin in solution form. To overcome these limitations and to address the challenge of AM fiber processing, herein, we have for the first time developed a protocol to prepare a highly concentrated SF solution and have demonstrated that this solution can be further used to prepare scaffolds for biomedical applications.

Here, we report a protocol to prepare AM silk solution from the cryo-milled AM fibers by using trifluoroacetic acid (TFA) as the solvent. Prior to dissolution, the cryo-milled powder was characterised using various spectroscopic and microscopic techniques. The electrospinning technique was used to form scaffolds with the concentrated silk solutions. These scaffolds were later evaluated for their application in bone tissue engineering through *in-vitro* and *in-vivo* studies. BM silk was used as a control for all the studies.

## **5.3 Experimental Section – Materials and Methods**

### **5.3.1 Materials**

AM silk fibers were purchased from farmers, Tandipara, Birbhum Dist., West Bengal, and BM silk fibers were procured from Central Sericultural Research & Training Institute (CSRTI), Mysore. Sodium Bicarbonate ( $\text{NaHCO}_3$ )

(#1.93237.0521), and Methanol (CH<sub>3</sub>OH) (#1.06007.2500) were purchased from Merck. Trifluoroacetic acid (TFA) (#T6508), was procured from Sigma Aldrich. IMDM (cat#12440-046), RPMI (cat#A10491-01), fetal bovine serum (FBS) (cat#10082-147), FBS for hMSCs (cat#12662-011), Alamar blue (cat#1987309), MTT (cat#M6494), StemPro osteogenic differentiation kit (cat# A1007201), ELISA kits for detection of BMP-2 (cat#EHBMP2), osteocalcin (cat# BMS2020INST), TNF- $\alpha$  (cat# BMS223-4) were purchased from Invitrogen. ALP detection kit (cat# ab83369) was procured from Abcam. hMSCs (cat#PT-2501) were purchased from Lonza and revived and stored as per suppliers' instructions. For all experiments using hMSC's, cells from passage number 3 were used. THP-1 cell line was purchased from National Centre for Cell Sciences, Pune.

### **5.3.2 Degumming of silk**

Silk fibers were degummed to remove sericin. A previously reported protocol for BM fibers was used for both AM and BM.<sup>27</sup> Briefly, the silk fibers were boiled in 0.5wt/v% NaHCO<sub>3</sub> solution for 30mins and this process was repeated 3 times for AM and 2 times for BM. These fibers were then washed thoroughly with DI water to remove residues and dried at 60°C for 48h.

### **5.3.3 Cryomilling of AM and BM fiber, dissolution and its characterization**

1.

Degummed silk fibers were chopped into small pieces less than 1cm and filled to half volume of a 50ml grinding jar of the CryoMill (Retsch GmbH, Germany)

consisting of a 2.5cm stainless steel grinding ball. The CryoMill was programmed for various cycles at a cycle time of 9 minutes at a frequency of 20/s with the controlled flow of liquid nitrogen to get fine powder of silk fibers. The digital images of the AM and BM fiber prior to cryo-milling and the powder obtained post cryo-milling are shown in **Figure 5-1**.



**Figure 5-1** Degummed fiber and cryomilled powder of BM and AM

### 5.3.4 AM and BM dissolution

The cryomilled AM and BM fibers were dissolved in TFA in different weight percentages and the dissolution times were studied. A similar dissolution experiment was also parallelly performed on the SF fibers to understand the effect of cryo-milling on dissolution.

### 5.3.5 FTIR analysis

FTIR measurements and deconvolution of Amide I band, between 1600-1700  $\text{cm}^{-1}$  were done as per the protocol mentioned in Chapter 4, Section 4.3.

### 5.3.6 XRD analysis

The crystalline structure analysis of the degummed fiber and its cryomilled powder of both AM and BM silk were performed on a powder X-ray diffractometer, Rigaku with Ni-filtered Cu-K $\alpha$  radiation. The voltage and current of the X-ray source were 40kV and 20mA, respectively. The wavelength  $\lambda$  was 0.15406 nm. The samples were mounted on glass frames and scanned from 2° to 50° (2 $\theta$ ) at a speed of 10°/min.

### 5.3.7 Preparation of scaffolds

A 20wt/v % solution of AM and BM cryomilled powder in TFA was used to prepare the scaffolds using electrospinning technique. Electrospinning (E-spin Nano) was performed at a flow rate of 0.3ml/h in a 5ml syringe under 20 kV voltage field, and the distance between needle tip and grounded target was 16cm. The electrospun fibers were collected on the aluminium foil and kept at room temperature overnight. The scaffolds were annealed with methanol vapor for 48h followed by washing with DI water upto 2h on an orbital shaker. At the end of washing, scaffolds were dried at 60°C for 6h.

### 5.3.8 Electron microscopy analysis

The morphology of the electrospun fibers and cryomilled powders was observed under a field emission scanning electron microscope (FE-SEM) (Nova NanoSem

450) at 18kV accelerated voltage and 5mm working distance. Prior to SEM imaging, samples were made conductive by sputter coating them with a 5nm thick gold coating. Representative images were captured at suitable magnification.

### **5.3.9 *In-vitro* cytotoxicity (MTT assay) assay:**

MTT assay was performed to study cytotoxicity of developed scaffolds by using L929 fibroblast cell line as per protocol mention in Nisal et.al, 2018.

### **5.3.10 *In-vitro* cell adhesion (seeding) assay**

Cell seeding efficiency of MG63 cells on the electrospun AM and BM scaffolds was analyzed by the trypan blue cell counting method. MG-63 cells were maintained in DMEM+10% FBS. MG-63 cells with a density of  $2 \times 10^4$  cells per scaffold were seeded in 100mL of complete media on AM and BM scaffolds along with plate control. The plate was incubated at 37°C for specific time points. At each time point, cells were trypsinized and cell count was taken by using the Neubauer chamber. Cell adherence percentage was calculated by using the following equation: % adherence =  $A_{\text{test}} / A_{\text{control}} * 100\%$ . (A test is the adherence of the cells to the sample and A control is the adherence of cells to control wells without sample)

### **5.3.11 hMSCs proliferation assay (Alamar Blue Assay)**

*In-vitro* cell proliferation was qualitatively analyzed using alamar blue dye (resazurin-based reagent) based assay on 7<sup>th</sup>, 14<sup>th</sup> and 28<sup>th</sup> day in both normal growth media (NGM) (IMDM+10% hMSCs FBS) and osteogenic media (OstM). Sterilized AM and BM scaffolds were placed in a 24 well flat-bottomed non-

adherent cell culture plate and seeded with hMSCs at a density of  $5 \times 10^3$  cells per scaffold in 50 $\mu$ L of complete media (IMDM + 10% hMSCs-FBS). The cells were allowed to settle for 15 minutes at 37°C, 5% CO<sub>2</sub> atmosphere. Additional 250 $\mu$ L media was added to the tissue culture plate, which was then incubated at 37°C for 28 days in a 5% CO<sub>2</sub> atmosphere. Media was replenished after every 48h. At each time point, growth media was replaced with a 10% alamar blue solution, followed by the 6h incubation at 37°C with 5% CO<sub>2</sub>. Developed colour was recorded in terms of absorbance at 570nm, using 600nm as a reference wavelength. Normalized final values were reported as a function of cell proliferation.

### **5.3.12 hMSCs differentiation into osteogenic lineage**

Sterilized AM and BM scaffolds were placed in a 24 well flat-bottomed non-adherent cell culture plate and seeded with hMSCs at a density of  $1 \times 10^4$  cells per scaffold in 50 $\mu$ L of complete media (IMDM + 10% hMSCs-FBS). The cells were allowed to settle for 15 minutes at 37°C, 5% CO<sub>2</sub> atmosphere. Additional 250 $\mu$ L media was added to the tissue culture plate, which was then incubated at 37°C for 28 days in a 5% CO<sub>2</sub> atmosphere. The next day, normal growth media was removed and osteogenic differentiation media was added. Fresh osteogenic media was replenished after every 48h. Secreted expression levels of ALP, BMP-2 and Osteocalcin (OCN) markers were measured to monitor the osteogenic potential of AM and BM scaffolds. Spent media was collected on each time point and stored at -80°C for marker analysis.

### **5.3.12.1 Alkaline phosphatase (ALP) expression**

ALP colorimetric assay was used to measure the enzyme activity as per our previous reports.<sup>28,29</sup> In brief, 80 $\mu$ L of an appropriately diluted sample was mixed with 50 $\mu$ L of pNPP (5mM) solution and incubated at 25°C for an hour in the dark. After incubation 20 $\mu$ L of stop solution was added to stop the enzyme activity. Absorbance of developed color was recorded at 405 nm and value was calculated from the developed calibration curve (**Figure 5-2**). In the same samples, total protein was also measured by Bradford assay and ALP activity normalized with total protein is reported here.

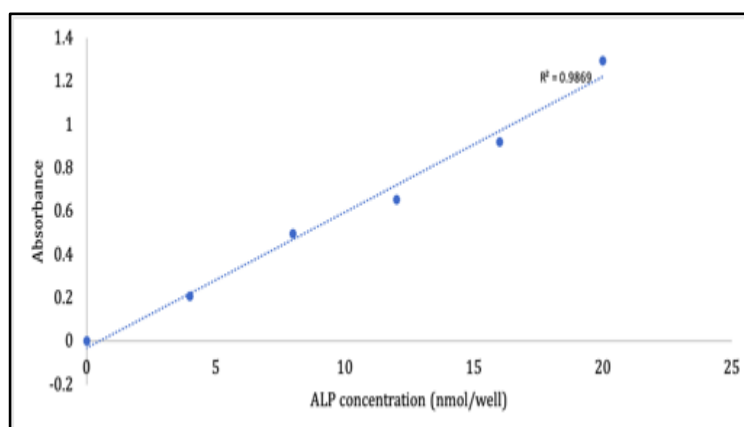


**Figure 5-2** Calibration curve for ALP estimation

### **5.3.12.2 BMP-2 and OCN expression**

Expressions of both BMP-2 and OCN were analyzed by using standard ELISA technique on day 1 and day 28. Spent media was used as a sample. The individual calibration curve **Figure 5-3** for BMP-2 and **Figure 5-4** for OCN were developed and from that expression of BMP-2 and OCN were obtained and plotted.

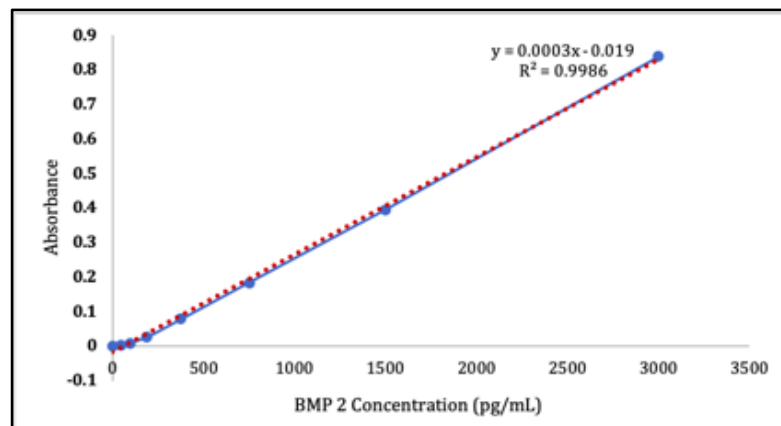


**Figure 5-3** Calibration curve for BMP-2 estimation

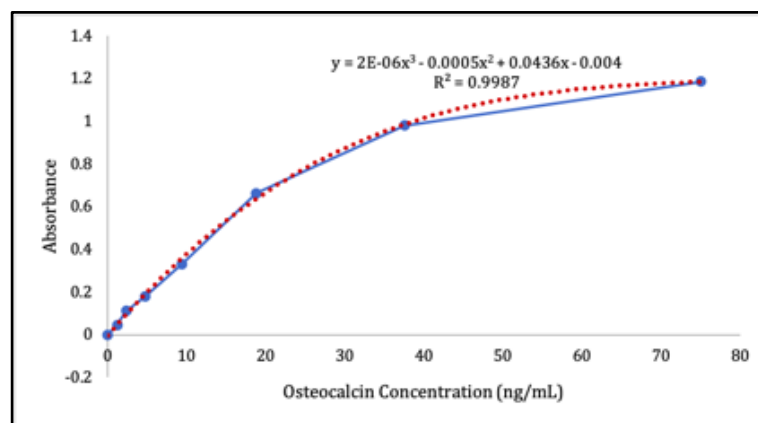


**Figure 5-4** Calibration curve for osteocalcin estimation

### 5.3.13 Detection of extracellular calcium deposition

Calcium deposition, as a result of osteogenic differentiation, was measured at the end of the 28<sup>th</sup> day by using Alizarin red S staining. In brief, hMSCs cells were seeded on sterile AM and BM scaffolds at a density of  $1 \times 10^4$  cells per scaffold in 50 $\mu$ L of complete media. The cells were allowed to be settled for 15 minutes at 37°C with 5% CO<sub>2</sub>. The additional 250 $\mu$ L media was added and the cell culture plate was incubated at 37°C with 5% CO<sub>2</sub> for 28 days. On the day after seeding, the



media was replaced with osteogenic differentiation media. Fresh osteogenic media was replenished after every 48h. On the 28<sup>th</sup> day, scaffolds were fixed with 4% formaldehyde at room temperature for 10 minutes. Scaffolds were washed with PBS after fixation and then stained with 2% Alizarin Red solution for 20 minutes at room temperature. After staining, the scaffolds were washed with DI water until no staining colour was observed in washing water. Deposited calcium was observed under a bright field by Axio Observer Z1 from Carl Zeiss. Deposited calcium was extracted by using 0.5mL 10% acetic acid for 30 minutes at room temperature followed by 10 minutes at 85°C. Solution was centrifuged at 14000 rpm for 15 minutes and absorbance of collected supernatant was measured at 405 nm. In this experiment, scaffolds without cells were taken as background control.

#### **5.3.14 *In- vitro* inflammatory response (TNF- $\alpha$ )**

Level of TNF- $\alpha$  indicates occurrence of immune reaction at material and tissue interface. Inflammatory reactions against the developed AM and BM scaffolds were analyzed by evaluating the expression of TNF- $\alpha$  with THP-1 (human monocytic cell line) cells.  $8 \times 10^3$  cells per scaffold per well were cultured in 1ml of complete media and incubated at 37°C in 5% CO<sub>2</sub> atmosphere for up to 7 days. Media was changed after every 48h and spent media was collected on day 1 and day 7, which was used to measure the expression levels of TNF- $\alpha$  by using a standard ELISA kit. Two independent experiments with duplicates reading in each set were taken at 450 nm and results are reported in terms of average absorbance.

### 5.3.15 Rat calvarial defect model for *in vivo* new bone regeneration

The osteogenic potential of AM and BM scaffolds were also studied *in vivo*. This study was performed in order to evaluate any inflammatory response that could have been generated due to the scaffold. For this study, rat calvarial defect was considered a model defect. The animal experiment was performed at PRADO, Preclinical Research and Development Organization, Pvt., Ltd, with prior approval of the Institutional Animal Ethics Committee (IAEC) (Protocol No. IAEC-20-080). All procedures of this study were in accordance with the guidelines set by the Committee for the Purpose of Control and Supervision of Experiments on Animals (CPCSEA) as published in The Gazette of India, December 15, 1998. (CPCSEA Reg No. 1723/PO/RcBiBt/S/13/CPCSEA). A total of 15 female Sprague Dawley rats with the bodyweight range of 200-350 gm was divided equally into three groups (5 animals per group). Group 1 – empty defect, Group 2 – BM scaffold and Group 3 – AM scaffold. For creating calvarial defects (**Figure 5-5**), animals were anaesthetized (Ketamine-90mg/kg and Xylazine 10mg/kg) and a ~15mm incision was made to the skin. A 4mm defect, as shown in Figure 4, was created in the calvarial bone using 1- 2mm drill bits. Calvarial defect in group one was left empty. Also, in group 2, a BM scaffold was placed, while group 3 used AM scaffold. The skin was sutured using a non-absorbable suture and post-operative care of the surgical site was taken for 10 days, including injections of analgesic (meloxicam 1mg/kg). At 4 weeks of treatment, animals were euthanized using an overdose of CO<sub>2</sub>. Calvarial bone tissues were collected in 10% neutral buffered formalin for further histopathological evaluation as explained below.

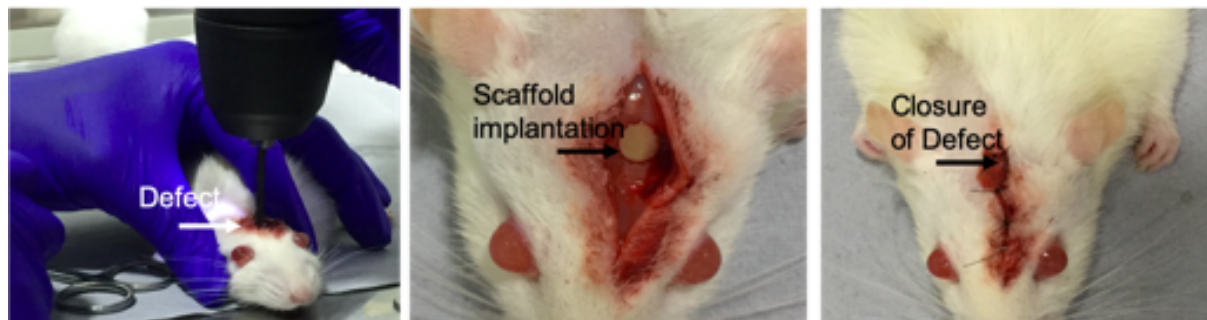


**Figure 5-5** Brief overview of the creation of calvarial defect, scaffold implantation and closure of the defect

### 5.3.16 Histopathology

After 24h of fixation, tissues were decalcified, processed routinely and later embedded in paraffin. After 24h of fixation, tissues were decalcified, processed routinely and embedded in paraffin. The sections of 3-5 $\mu$ m thickness were cut (SLEE CUT 5062 Microtome, Model: SLEE/ CUT5062). All sections were stained with haematoxylin and eosin stain (H&E) and Masson's trichrome stain by using standard protocol to evaluate the morphology of newly developed bone. Masson's trichrome is a commonly used staining method in bone histology and newly formed bone is typically seen in blue colour. Histological changes related to new bone formation were observed under Labomed/LX300 microscope equipped with an objective lens of 10X & 40X with an eyepiece magnification of 10X.

### 5.3.17 Statistical analysis

One way and two-way analysis of variance (ANOVA) with Tukey's post-hoc test by using Past 3 software was used for all statistical analysis. A value of  $P < 0.05$  was considered statistically significant. All data are presented as mean  $\pm$  SD (n=3).

## 5.4 Results

The application of non-mulberry silk in the biomedical field has been limited due to the poor processability of this material vis-à-vis mulberry silk. In this work, we have shown that the cryo-milling of silk fibers enhances the solubility of the AM and BM fibers in routine solvents like TFA. The solutions, so obtained, can be processed using conventional techniques such as electrospinning to make 3D scaffolds that show promise in BTE. The next section highlights the key results obtained after microscopic and spectroscopic characterization of the powders obtained post-cryo-milling.

### 5.4.1 Cryomilling of AM and BM fiber, dissolution and its characterization

The degummed silk fibers were cryomilled as per the protocol described in Section 5.3.3 and the characterization was performed after every cycle of cryomilling. FTIR spectroscopy was used to study the effect of cryo-milling on the conformation of silk fibroin protein. The amide I peak in the IR spectra, observed in the 1580-1620 $\text{cm}^{-1}$ , was deconvoluted to understand the predominant secondary conformation of SF. The spectra of AM and BM fibers and their cryomilled powders are shown in **Figures 5-6**.

**Figure 5-6a** shows the complete spectra for the AM and BM fibers and cryomilled powders. **Figure 5-6b** highlights the area of interest i.e. the Amide I and Amide II peaks. Degummed silk fibers of AM and BM show characteristic peaks in 1510 $\text{cm}^{-1}$  for Amide-II and 1618 $\text{cm}^{-1}$  for Amide I. This indicates that the predominant conformation of the protein is beta sheet structures. However, the Amide I peak

shifts to a higher wavenumber for the cryo-milled powders, implying that the random coil content in the sample has been increased.

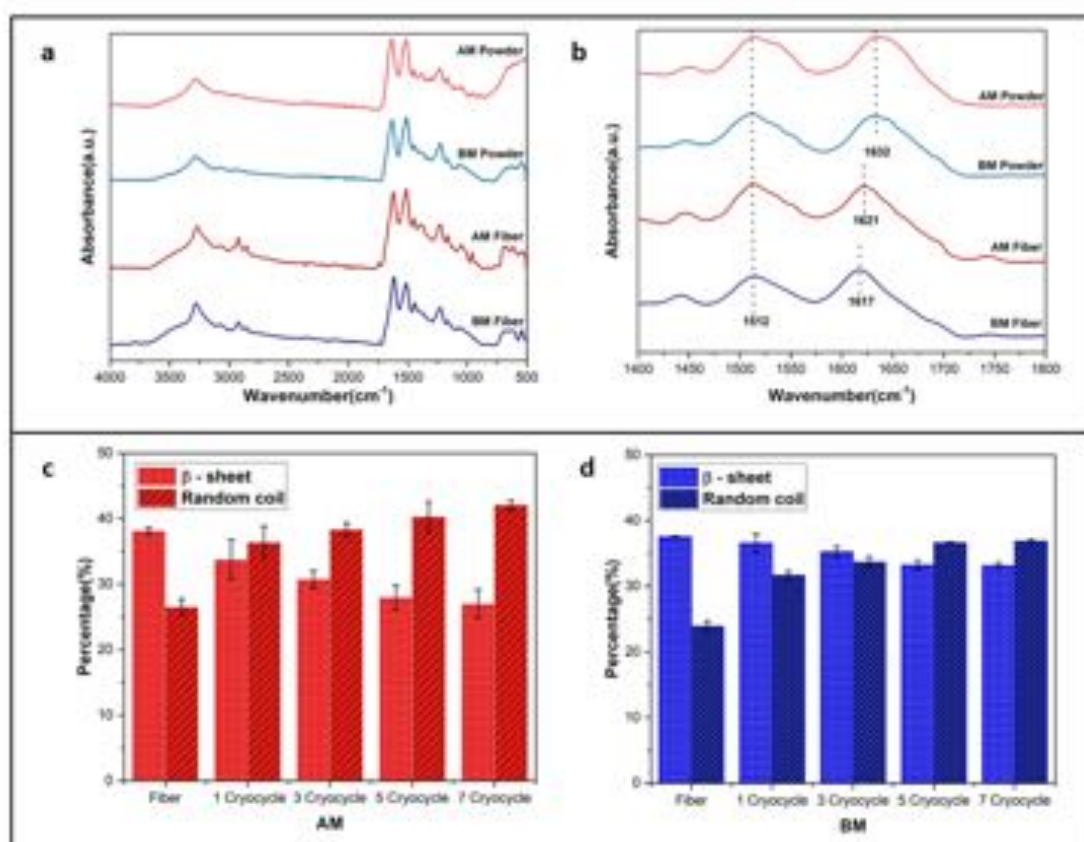


**Figure 5-6** Secondary structure analysis of AM and BM. a. FTIR spectra of AM, BM fiber and powder, b. FTIR Spectra from 1400-1800 cm<sup>-1</sup>, c & d β-sheet and random coil % in AM and BM respectively

The C=O stretch of the Amide I peak in region 1700-1600 cm<sup>-1</sup> was deconvoluted to gain further insights on protein conformation. This data has been summarized in **Figure 5-6c** for AM and **Figure 5-6d** for BM. AM fiber shows a β-sheet content of 38 % and random coil content of 26 % while the BM fiber shows 37% and 24% respectively. On cryo-milling, after one cryo cycle, the β-sheet content changed to 34% and 37% for AM and BM powder respectively.

On further increase in the number of cryo-cycles, the powders show a lower  $\beta$ -sheet content and higher random coil or amorphous content, i.e. after three cryocycles the  $\beta$ -sheet content decreased to 31% and 35% respectively for AM and BM powder. Meanwhile, amorphous content increased from 37% to 38% and 32% to 34%. When cryomilled for a longer duration, i.e. after completion of 5 cryo-cycles,  $\beta$ -sheet content decreased to 28% and 33%, for AM and BM powder. Correspondingly, the random coil or amorphous content increased to 40% and 36% in AM and BM respectively. Thus, the FTIR result provides evidence that the cryo-milling technique does alter the secondary structure of silk protein and it improves the random coil conformation. When the number of cycles was further increased to 7, there was no significant change in the  $\beta$ -sheet and random coil content as compared to 5 cryo-cycles. Thus, further experiments were done on cryo-milled powders prepared using 5 cycles.

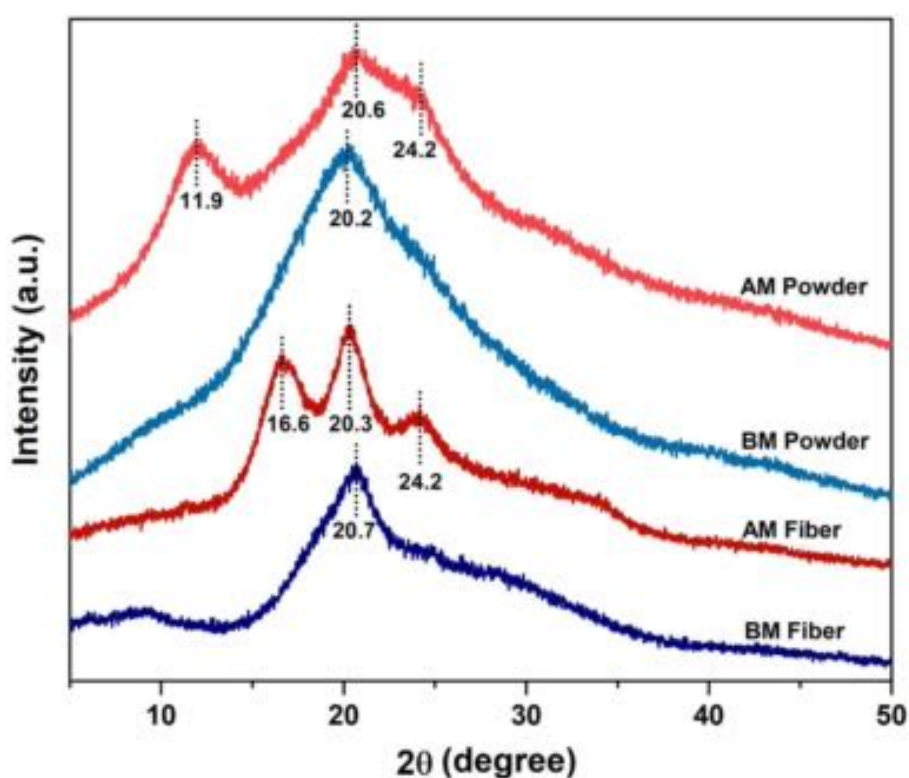


**Figure 5-7** X-ray Diffraction studies of AM and BM - fiber and powder

To corroborate the FTIR data and validate the secondary structure transition of the protein, XRD was used as a complementary tool. XRD data of BM, AM fiber and respective cryo-milled powders is presented in **Figure 5-7**. The BM fiber showed a strong diffraction peak at  $20.7^\circ$ , while the AM fiber showed two peaks at  $16.6^\circ$  and  $20.3^\circ$ . These peaks represent silk II or the crystalline conformation of SF. The BM and AM powders show broader diffraction peaks that indicate an enhancement of amorphous nature. AM powder also shows a peak at  $11.9^\circ$ , which corresponds to silk I conformation. These results provide evidence that cryomilling techniques enhance the amorphous nature of the material. XRD results proved that cryomilling causes a substantial decrease in  $\beta$ -sheet and an associated increase in random coil, which agrees with the FTIR data of cryomilled powder.

The morphology of cryo-milled powders was analyzed using SEM (**Figure 5-8**). As can be seen from **Figure 5-8**, the powders consist of irregularly shaped particles that also exhibited a tendency to form aggregates. The particle size for both the AM and BM powders and agglomerates was found to be in the range of 1-10  $\mu\text{m}$ .

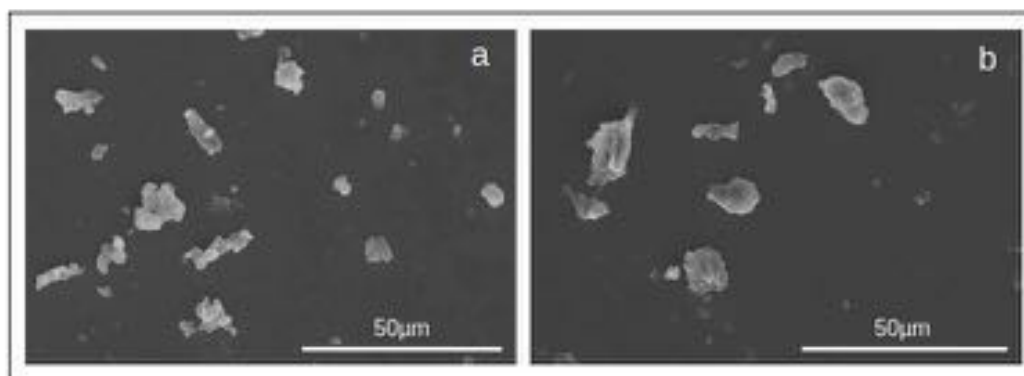


**Figure 5-8** SEM of cryomilled (a) AM and (b) BM powder

Further, the cryo-milled AM and BM powders were used to prepare solutions in TFA and the data are summarized in **Figure 5-9**. The dissolution was monitored visually every 15 minutes and the dissolution time was recorded when no fraction of undissolved material could be observed in the experimental vial. The dissolution time of fiber and powders of both AM and BM were found to be drastically different. For a 1 wt% solution, the AM fiber took around 3h for complete dissolution and BM took around 2h, while the powder dissolved in less than 10 mins for both. As the concentrations of the solutions were varied, the dissolution times were also affected. When the concentrations were increased to 15 wt%, the fibers of both AM and BM did not dissolve completely (**Figure 5-10**), hence further concentrations were not studied. However, for the cryo-milled powders, even 20wt% solutions could be prepared in a reasonable time frame (**Figure 5-11**). For 20 wt% solutions, it took 6h for AM and 5.4h for BM. Hence it was observed that the cryomilling significantly reduced the dissolution time of both AM and BM fibers.

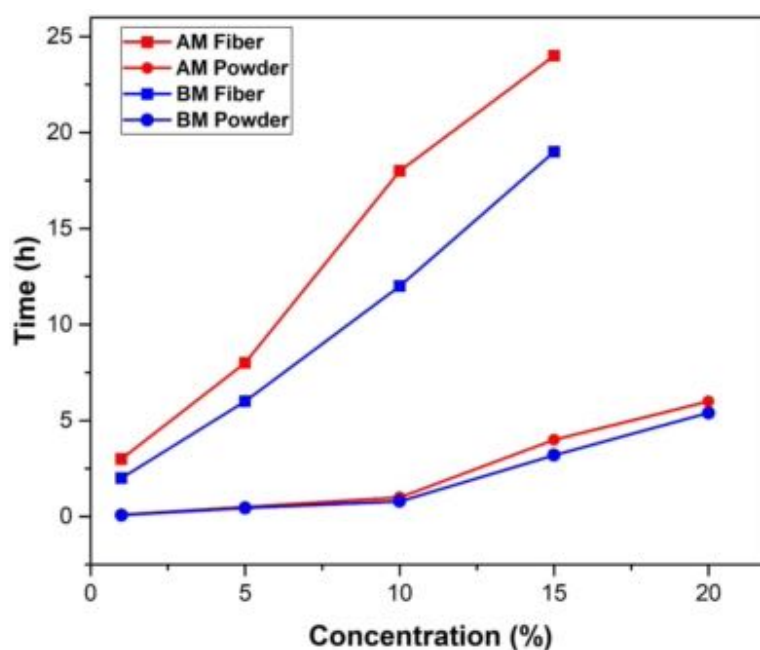


**Figure 5-9** Dissolution of silk fiber and its cryomilled form in TFA



The 20wt% SF-TFA solution, prepared by dissolving the cryo-milled AM and BM powder, was used to prepare scaffolds. Electro-spinning was chosen as the method to prepare scaffolds. This method has been used widely for scaffold preparation because of its good porosity and pore inter-connectivity, which results in good cell proliferation.<sup>30,31</sup> The non-woven electrospun mats have also been used as

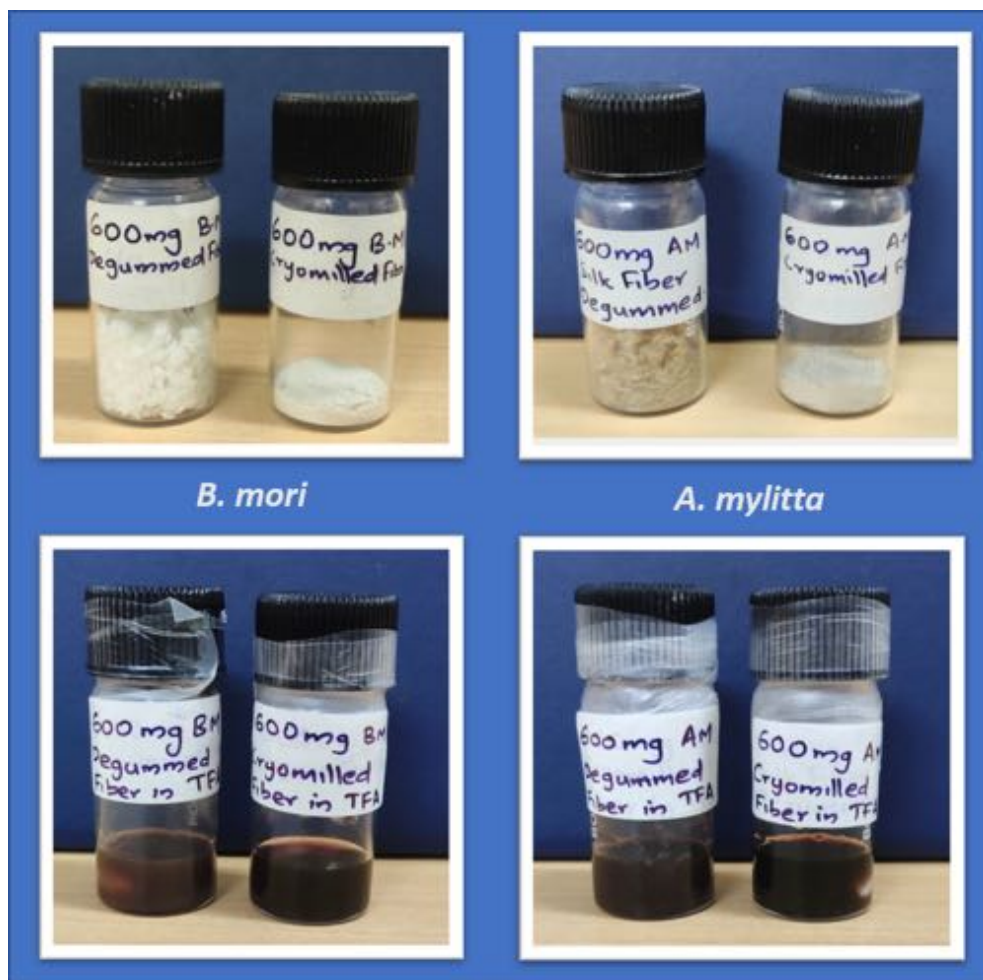


**Figure 5-10** Solution of AM and BM fiber and cryomilled powder in TFA



**Figure 5-11** 20 wt % AM and BM cryomilled powder in TFA

scaffolds by several groups in BTE. The parameters for electrospinning were optimized by studying the ability of the solution to form a continuous thread. Further, scanning electron microscopy was used as a tool to determine the optimum parameters for producing a uniform non-woven electro-spun mat for AM and BM solutions. It was found that at 20kV voltage, 0.3mm/s flow rate and 16 cm collector-tip distance, the non-woven mats had the required characteristics. The SEM images for both AM and BM electrospun mats are shown in **Figures 5-12a & 5-12b**. The non-woven mats had a similar morphology and AM showed electrospun nanofibers with diameter in the range of  $167 \pm 49\text{nm}$  while BM showed  $136 \pm 30\text{nm}$ . The electrospun mat had randomly arranged fibers, which created good pore sizes and pore interconnectivity as is seen from the SEM images. The mats were annealed to induce  $\beta$ -sheet formation. **Figure 5-12c & 5-12d** show the morphology of the electrospun mat after the annealing treatment. The annealing treatment results in fusing of fibers in multiple locations. This observation is in accordance with previous literature.<sup>25</sup> The non-woven

electrospun AM and BM mats were then further used to study their performance for BTE using both *in-vitro* and *in-vivo* techniques.

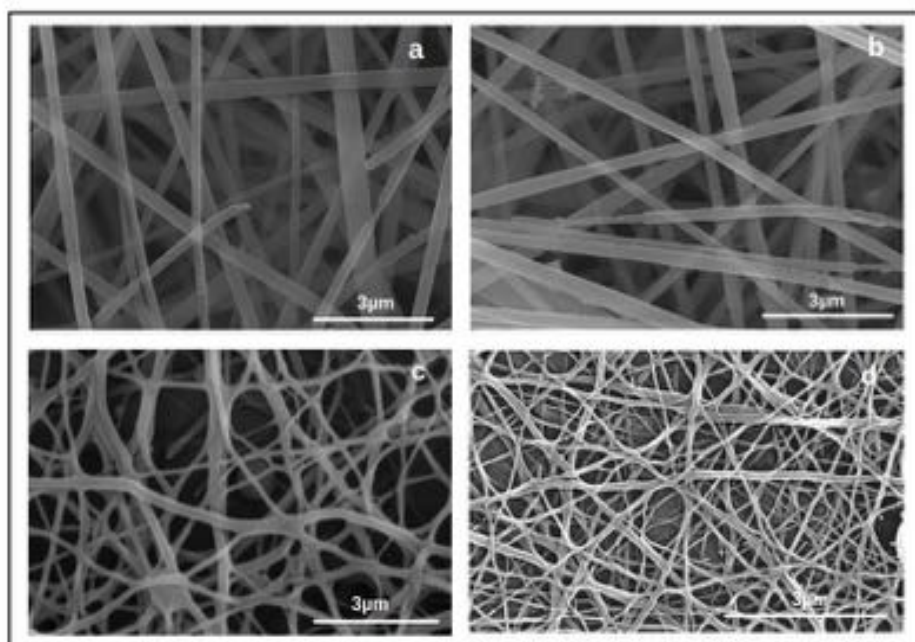


**Figure 5-12** SEM images of electrospun scaffolds from (a) AM before annealing, (b) BM before annealing, (c) AM after annealing and (d) BM after annealing

### 5.4.2 *In-vitro* cytotoxicity assay

As a prerequisite of biomaterial's application, cytotoxicity of the developed AM and BM scaffold's were analyzed by using standard MTT assay. No clinical significant difference between AM and BM scaffolds and more than 90% cell viability as observed in **Figure 5-13** confirmed non cytotoxicity of electrospun AM and BM scaffolds.

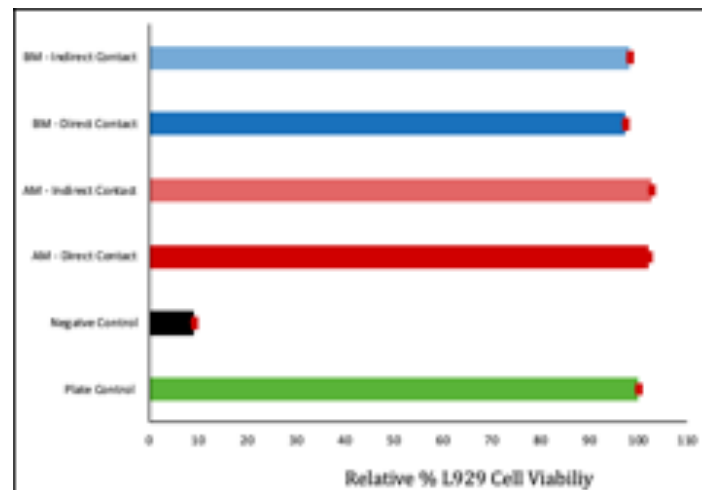


**Figure 5-13** In-vitro L929 cell viability was analyzed by MTT assay on AM and BM scaffolds. Data are represented by average cell viability with respect to plate control  $\pm$  Std. Dev. ( $n=3$ )

### 5.4.3 In-vitro cell adhesion assay

Relative Percent MG63 cell seeding efficiency was checked for both AM and BM scaffolds and data is represented in **Figure 5-14**. No significant difference was seen between AM and BM scaffolds. This shows that both scaffolds support the attachment of MG63 cells onto them.

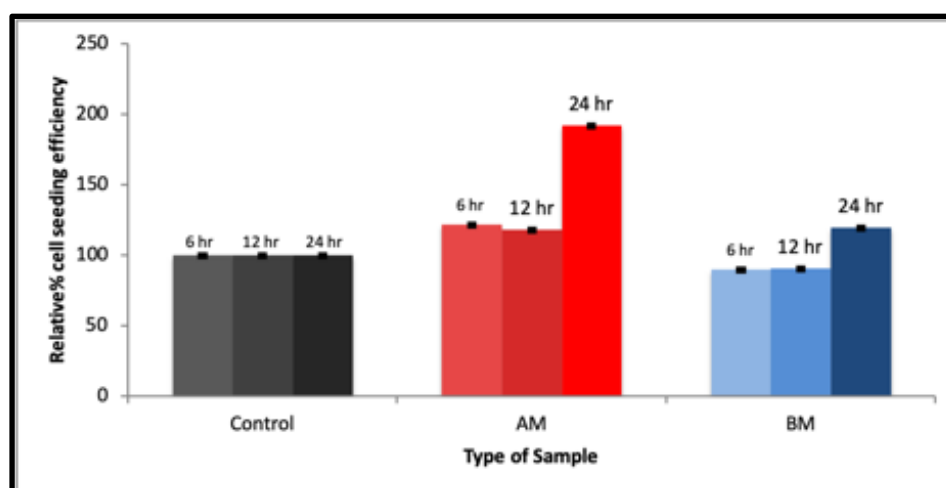


**Figure 5-14** Relative percent MG63 cell seeding efficiency for AM and BM scaffolds

#### 5.4.4 hMSCs proliferation assay (Alamar Blue Assay)

Adhesion and proliferation of hMSCs cells on AM and BM scaffolds was monitored in both normal growth media and osteogenic media on day 7, 14 and 28. **Figure 5-15a** represents the cell growth in normal growth media. There was no significant difference between AM and BM on day 7 and day 14. However, on day 28, higher cell proliferation was observed in AM scaffold in comparison to BM, which was also found to be statistically significant ( $p=0.006$ ). In the AM scaffold, 7th day growth was found to be significantly different than 14th day ( $p=5.5e^{-4}$ ) and 28th day ( $p=2.6e^{-6}$ ) and 14th day cell proliferation was also significantly different than 28th day ( $p=0.008$ ). Similarly, for the BM scaffold, 7th day cell proliferation was significantly different than 14th day ( $p=2.7e^{-4}$ ) and 28th day ( $p=3.1e^{-4}$ ) but there was no significant difference between 14th and 28th day.

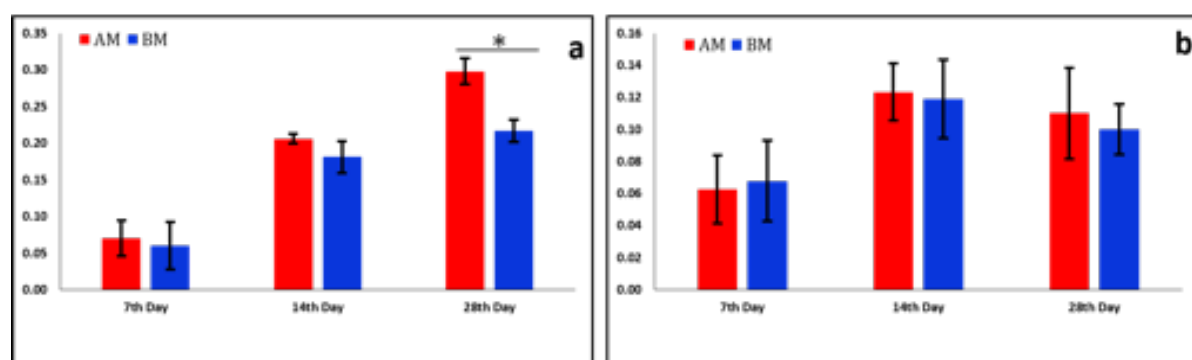


**Figure 5-15** In-vitro hMSCs cell proliferation: Data represented as average normalized factor  $\pm$  std. dev. ( $n=3$ ).  $*p < 0.05$ . a) Alamar blue assay in normal cell growth media. b) Alamar blue assay in osteogenic differentiation media

As the cells commit to an osteogenic lineage, their ability to proliferate decreases and they convert to mature osteoblast and finally to osteocytes.<sup>32</sup> Therefore, to

monitor cell steadiness in the growth phase during cell differentiation, cell proliferation was also monitored in osteogenic differentiation media and results are plotted in **Figure 5-15b**. Cells were found to be proliferating from day 7 to day 14, but there was no further cell proliferation after day 14 and hence no significant growth was observed between 14 to 28 in both AM and BM scaffolds.

#### 5.4.5 hMSCs differentiation into osteogenic lineage

hMSCs differentiation was monitored by measuring osteogenic markers from early to late stage of cell differentiation. Upon differentiation of hMSCs to osteogenic lineage, up regulation of genes results in the expression of specific markers<sup>33-35</sup>. Here, the spent media from *in-vitro* cell culture experiments was analyzed to detect the presence of specific osteogenic markers ALP, BMP-2, OCN. ALP which is an early-to-mid stage osteogenic marker. ALP activity was normalized with the total protein content of the cells and the data is presented in **Figure 5-15a**. It was observed that the ALP secretion significantly increased as the experiment progressed over time (7<sup>th</sup>-28<sup>th</sup> day, AM  $p=0.000003$  and 14<sup>th</sup>-28<sup>th</sup> day, AM  $p=0.00001$ ). In the case of BM also, a significant difference in ALP expression was observed at different time points (7<sup>th</sup>-28<sup>th</sup> day BM  $p=0.01$  and 14<sup>th</sup>-28<sup>th</sup> day  $p=0.02$ ). Both AM and BM scaffolds support ALP expression but the data on day 28 ( $p=0.0002$ ) shows that the expression of ALP for AM scaffolds is significantly higher as compared to BM scaffolds. **Figures 5-15b and 5-15c** depict the expression of OCN and BMP2 markers. OCN is a late marker of the osteogenic differentiation process while BMP2 plays a crucial role throughout the new bone development process. As can be seen from the result, AM induced higher expression of OCN ( $p=0.009$ ) and BMP-2 ( $p=0.001$ ) than the BM scaffold.

Bone tissue regeneration culminates with the formation of a mineralized matrix. Calcium deposition was visualized by alizarin red S staining (**Figure 5-17**). The dye was extracted by using acetic acid and the data is presented in **Figure 5-16d**. From the results, a significant difference ( $p=0.006$ ) between AM and BM was clearly observed indicating that AM supports higher mineralization.

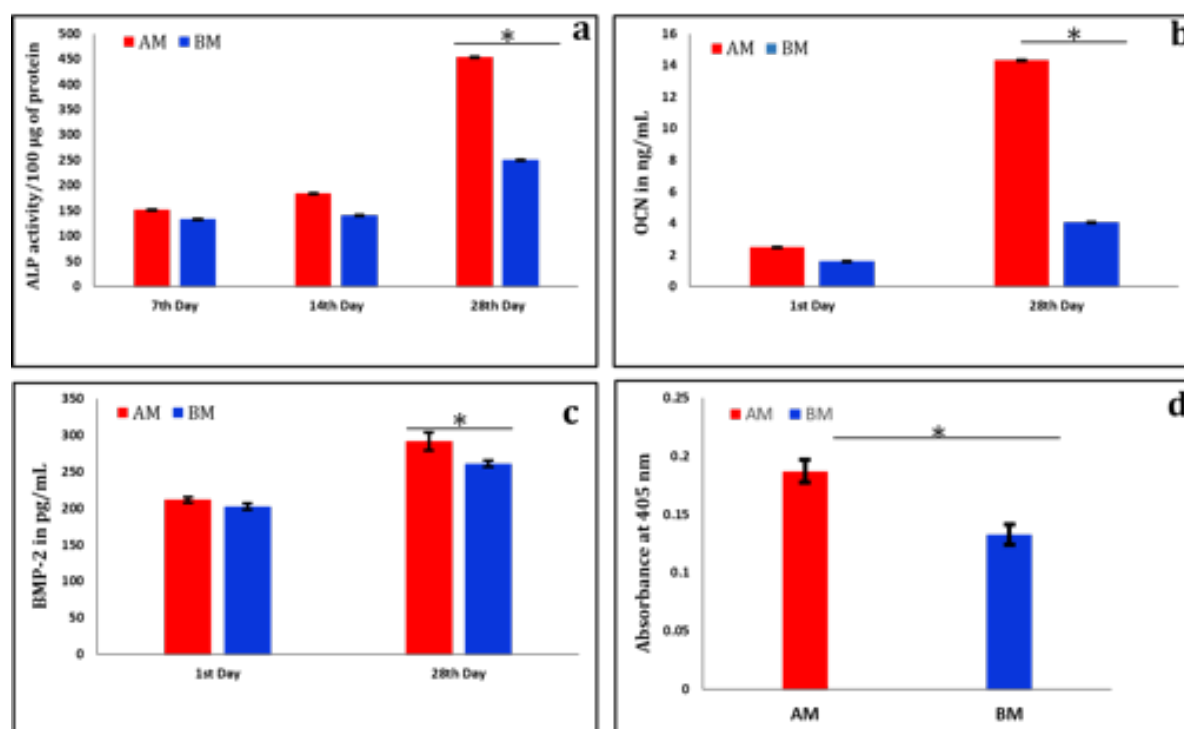


**Figure 5-16** Osteogenic potential by estimating expression of alkaline phosphatase (ALP) activity, bone morphogenic protein-2 (BMP-2) and Osteocalcin levels (OCN). (a) ALP activity was normalized with the total protein loaded and expressed as ALP activity / 100µg of protein. (b) Expression of OCN were represented as average OCN (ng/ml)  $\pm$  std. dev. ( $n=3$ ) (c) BMP-2 expression was represented as average BMP-2 (pg/ml)  $\pm$  std. dev. ( $n=3$ ) (d) BMP-2 expression was represented as average BMP-2 (pg/ml)  $\pm$  std. dev. ( $n=3$ ) \* $p<0.05$ . (d) Quantification of calcium deposition: calcium deposition by alizarin red S staining which was extracted by using acetic acid at the end of 28 days by measuring the absorbance at 405nm

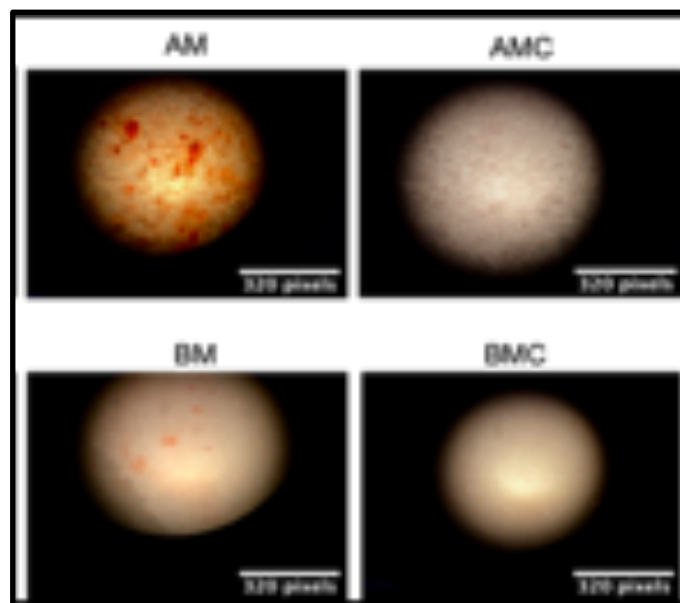


**Figure 5-17**  $Ca^{2+}$  deposition stained by Alizarin Red S staining at the end of 28 days

#### 5.4.6 *In-vitro* inflammatory response (TNF- $\alpha$ )

Further, we also did a preliminary evaluation to understand the immune response to both AM and BM scaffolds. THP-1 cell line was used in order to check the activity of TNF- $\alpha$  cytokine. Lipopolysaccharide (LPS) was used as a positive control. From the results (**Figure 5-18**), positive control showed a remarkably high TNF- $\alpha$  activity as compared to negative control. From the results (**Figure 5-18**), there is no significant difference observed between AM and BM on both the time points. LPS showed a remarkably high TNF- $\alpha$  activity as compared to PC supporting the validity of the experiment. On day 7, there is a significant low level of TNF- $\alpha$  expression observed for both AM and BM scaffolds with respect to LPS. This data shows both AM and BM are non-inflammatory. On day 1, AM and BM both showed



decreased TNF- $\alpha$  activity as compared to LPS. But a significant difference is observed only between AM and LPS ( $p=0.04$ ).

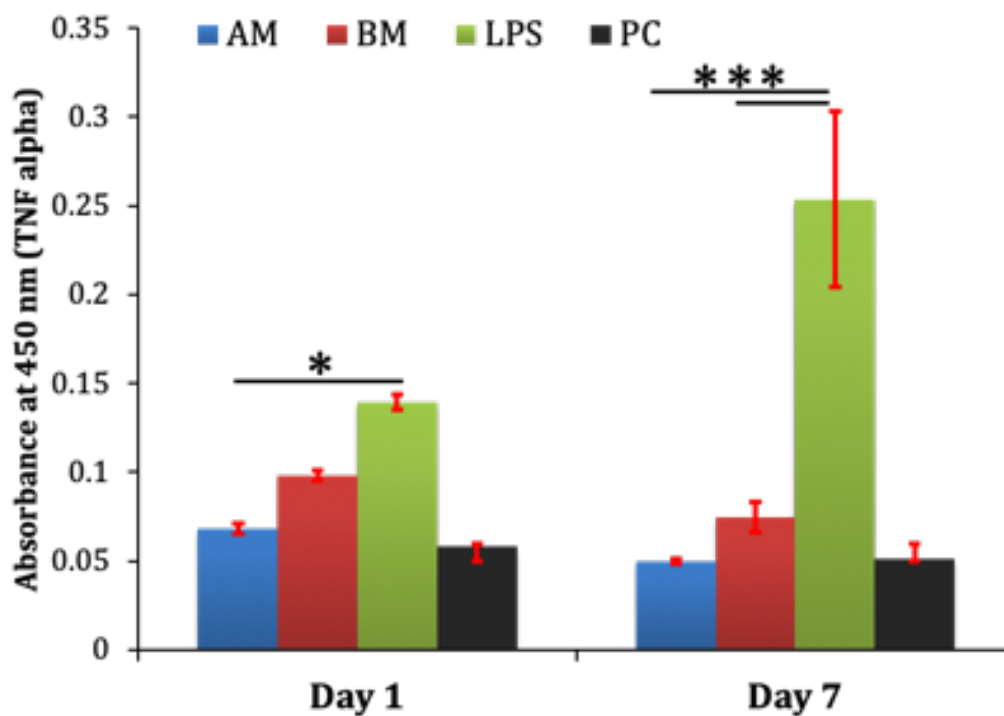


**Figure 5-18** TNF- $\alpha$  activity. Data represented as average  $\pm$  std. dev. ( $n=2$ ) \* $p < 0.05$

#### 5.4.7 Rat calvarial defect model for *in-vivo* new bone regeneration

The calvarial defect model in a rat was used to evaluate *in-vivo* new bone formation. Cross sectional H&E stained sections are represented in **Figure 5-19A**. Compared with empty defects, the AM and BM scaffolds showed better regeneration of bone. From the histological images, it was clear that AM and BM both support new bone formation as compared to empty defects. However, thin fibrous connective tissue is more visible in BM treated scaffold, which is negligible

in case of AM scaffold upon implantation. Higher mineralization of bone was seen in the AM scaffold group as visible by Masson's trichrome stain (**Figure 5-19B**) and this confirmed the enhanced osteo-regenerative ability and bone repair process in AM scaffolds.

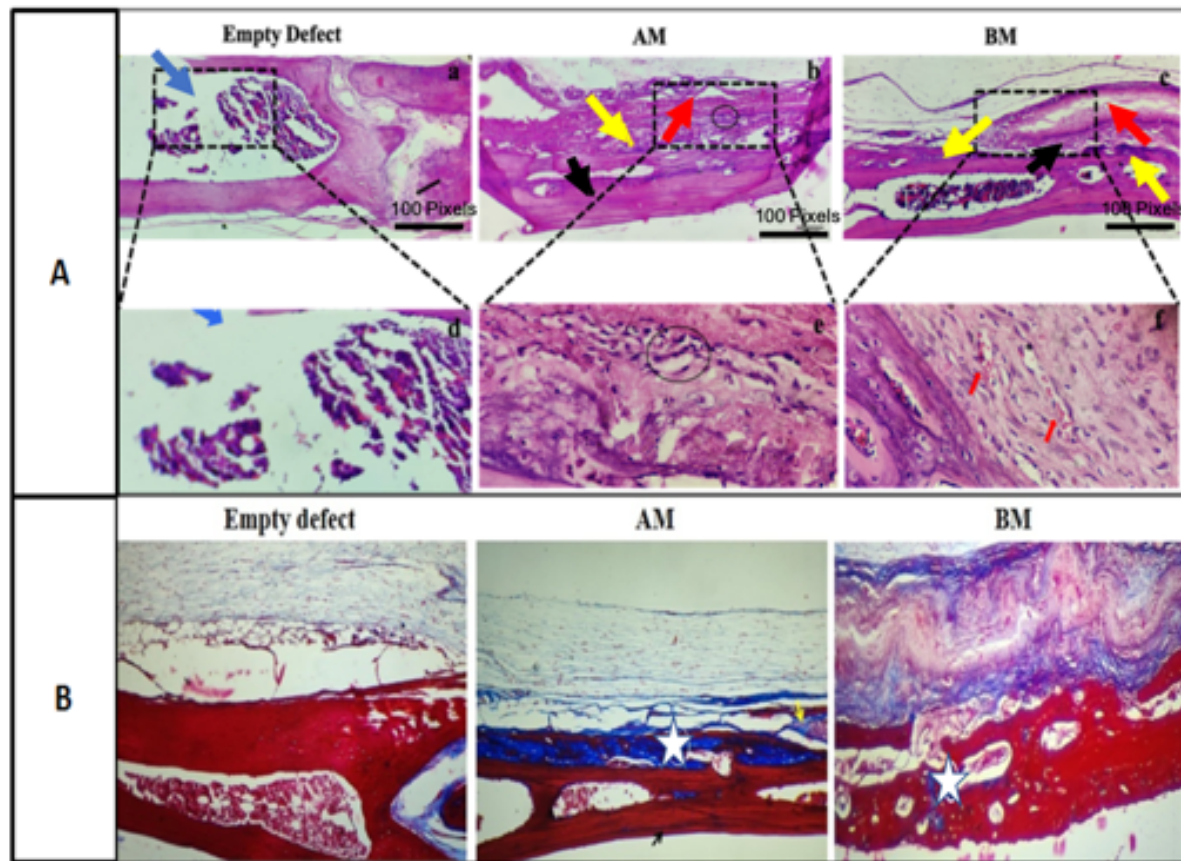


**Figure 5-19** Rat calvarial defect model for in-vivo new bone regeneration. Fig 4A: standard H&E staining. Black arrow: old bone; Yellow arrow: new bone formation; Blue arrow: fibrous tissue formation; Red arrow: scaffold. Fig 4B: Masson trichrome staining. White star: mineralized bone; Yellow arrow: fibrous tissue

## 5.5 Discussion

SF has been widely reported for load-bearing and non-load bearing bone tissue engineering applications.<sup>36-40</sup> Non-mulberry SF from *A.mylitta* has a high amount of alanine resulting in distinct crystalline morphology, and this highly crystalline content results in limited processability of this material.<sup>14</sup> Silk fiber dissolution with the help of chaotropic reagent such as lithium bromide (LiBr) or with Ajisawa mixture and DMAc/LiBr are reported for BM fibers. But these methods have been found to be ineffective for AM. This limited processability has reduced the use of this biomaterial in various regenerative medicine and tissue engineering applications.

To overcome the challenges in processability of AM fibers, in this work we have shown that cryo-milling can be used as a process to enhance the solubility of AM fibers into routine solvents like TFA. Both AM and BM fibers were degummed, chopped into small pieces and cryomilled. The cryomilling technique resulted in a powder with a typical size range of 1-10 microns. (**Figure 5-7**). FTIR spectroscopy and XRD analysis confirmed that cryo-milling results in an increase in the amorphous and random coil content in the SF and reduces the percentage of beta sheets. Further, the study also showed that TFA is an effective solvent for the cryo-milled powder.

The study also demonstrated that the cryo-milled powder can be used to prepare SF solutions with concentrations as high as 20wt%. Preparation of AM solutions in TFA at high concentrations using degummed AM fibers has been a challenge. Small amount of fiber is generally left behind in the solution as undissolved

material, which must be filtered off and hence the exact concentration cannot be obtained. Cryomilling of the degummed fiber, results in a powdered material, which can be easily dissolved even at 20% concentration within 6h. Similar trends were also seen in BM fiber and powder. The dissolved AM and BM were then made into scaffolds by electrospinning technique.

Electrospinning was desired over other techniques of scaffold making since it produces scaffolds with good pore sizes and pore interconnectivity suitable for cell growth. To induce the  $\beta$ - sheet formation after electrospinning, the scaffolds were treated with methanol vapour.

The scaffolds prepared using this technique were first tested for cytotoxicity using L929 fibroblasts cells, as per the standard reported protocols. Results from **Figure 5-13** showed more than 90% cell viability in both AM and BM scaffolds. It has been well documented that the presence of RGD, a cell adhesive peptide sequence in AM could be responsible for enhanced cell attachment.<sup>11</sup> To verify whether RGD supported more cell adhesion, we performed cell adhesion study by using MG-63 cells on AM and BM scaffolds up to 24h by using standard trypan blue cell counting protocol. Higher cell attachment on the AM scaffold than BM (**Figure 5-14**) confirmed that the RGD sequence present in AM plays an important role for cell adhesion. Further *in-vitro* biocompatibility of AM and BM was studied by observing hMSCs cell growth in both normal growth media and osteogenic media upto 28 days. Cells were growing in NGM on both AM and BM scaffolds throughout the time span. On BM scaffolds, cell growth on 7<sup>th</sup>, 14<sup>th</sup> and 28<sup>th</sup> days was consistent with the earlier reports and no significant difference found between AM and BM upto 14 days. However, more cell growth was observed on the 28th day in AM than BM. The cell growth pattern at different time points among AM and BM

individually are reported in **Figure 5-20**. These results are in a line with the earlier reports that showed biological behaviour between BM and AM silk.<sup>12,38</sup>

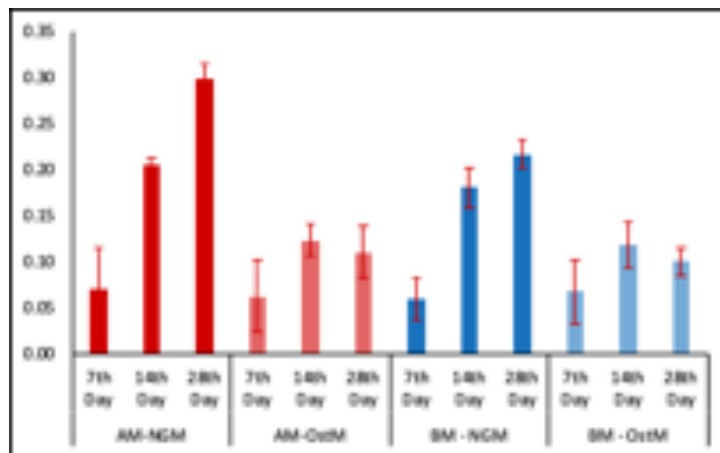


**Figure 5-20** In-vitro hMSCs cell growth in normal growth media (NGM) and osteogenic media (OstM). Data are represented by average cell viability with respect to plate control  $\pm$  Std. Dev. ( $n=3$ )

As cells start differentiating into particular cell lineage further cell growth does not occur and this is observed in the hMSCs growth data (**Figure 5-15**) in OstM where cell were growing from day 7 to 14 but saturation occurred as they started differentiation into osteogenic lineage and hence no further cell growth was observed on 28th day.<sup>33,35</sup> This result supports cell differentiation. hMSCs differentiation into osteogenic lineage were confirmed by estimating early (ALP), middle (BMP-2) and late (OCN) stage osteogenic markers. Increased expression of secreted marker with the timespan (**Figure 5-16**) confirmed both AM and BM support hMSCs differentiation. However, in all the markers significant differences between AM and BM were observed at a later stage, which is also in accordance with previously published reports. This finding also supports the data of more cell attachment in AM scaffold with enhanced osteogenic differentiation at later stages.

Significant differences between AM and BM were further confirmed by calcium mineralization stained by Alizarin Red S staining method. On the 28th day, calcium mineralization was visibly higher in AM than BM (**Figure 5-17**), which was confirmed by calcium quantification (**Figure 5-16d**).

Non-immunogenic behaviour of developed AM and BM scaffolds was also evaluated by studying *in-vitro* TNF alpha expression and confirmed by *in-vivo* implantation of both the scaffolds in rat calvarial critical size defect. Figure 10 showed *in-vitro* TNF-alpha expression. Both AM and BM scaffolds showed considerably lower expression than the positive control LPS confirming the biocompatibility of both (AM and BM) the types of scaffolds.

Non-mulberry silk has more hydrophilicity, better tensile properties and presence of cell adhesive peptide sequence. These parameters enhance its performance in tissue engineering application, which is thoroughly studied by *in-vitro* cell culture data and further confirmed by *in-vivo* implantation in rat critical sized calvarial defect (**Figure 5-19**). In bone related biomedical application, *in-vivo* research with animal models has been a preferred experimental system and more specifically rodent models, have been extensively used. Among different types of defects, the calvarial defect model has found great application in basic and applied research as this resourceful model allows biomaterials evaluation and bone tissue engineering approaches within a non-load-bearing orthotopic site with excellent reproducibility.<sup>41,42</sup> Thus, the calvarial defect model in a rat was used to evaluate *in-vivo* new bone formation ability of newly developed AM and BM scaffold. Both, H & E and Masson's Trichrome staining data confirm that BM and AM both support new bone regeneration *in-vitro* and *in-vivo*. However, AM does exhibit enhanced osteogenic potential as compared to BM and this data is in agreement with, previous reports.<sup>9,11,19,40,43</sup>

## 5.6 Conclusions

In conclusion, a unique protocol for AM fiber dissolution was successfully established to prepare biocompatible electrospun scaffolds. Detailed characterization proved that the cryomilling technique significantly decreased beta sheet content in the fiber. This reduced beta sheet content enabled the preparation of highly concentrated SF solutions. Also, a detailed step by step *in-vitro* and *in-vivo* biological experiments demonstrated successful application of AM and BM scaffolds towards bone tissue engineering. Furthermore, we observed no significant *in-vitro* proinflammatory secretion of cytokine TNF- $\alpha$  when exposed to AM and BM scaffolds. Thus, these properties position both AM and BM electrospun scaffold as a potential platform for bone tissue-engineering efforts. However, AM performed better with respect to BM in both *in-vitro* and *in-vivo* studies.

## 5.7 References

- (1) Melke, J.; Midha, S.; Ghosh, S.; Ito, K.; Hofmann, S. Silk Fibroin as Biomaterial for Bone Tissue Engineering. *Acta Biomater.* **2015**, *31*, 1–16. <https://doi.org/10.1016/j.actbio.2015.09.005>.
- (2) Kundu, B.; Rajkhowa, R.; Kundu, S. C.; Wang, X. Silk Fibroin Biomaterials for Tissue Regenerations ☆. *Adv. Drug Deliv. Rev.* **2013**, *65* (4), 457–470.

- <https://doi.org/10.1016/j.addr.2012.09.043>.
- (3) Mottaghtalab, F.; Hosseinkhani, H.; Shokrgozar, M.; Mao, C.; Yang, M.; Farokhi, M. Silk as a Potential Candidate for Bone Tissue Engineering. *J. Control. release* **2015**, *215*, 112–128.
- (4) Bhattacharjee, P.; Kundu, B.; Naskar, D.; Kim, H. W.; Maiti, T. K.; Bhattacharya, D.; Kundu, S. C. Silk Scaffolds in Bone Tissue Engineering: An Overview. *Acta Biomater.* **2017**, *63*, 1–17. <https://doi.org/10.1016/j.actbio.2017.09.027>.
- (5) Vidal, L.; Kamplaitner, C.; Brennan, M.; Hoornaert, A.; Layrolle, P. Reconstruction of Large Skeletal Defects: Current Clinical Therapeutic Strategies and Future Directions Using 3D Printing. *Front. Bioeng. Biotechnol.* **2020**, *8* (February). <https://doi.org/10.3389/fbioe.2020.00061>.
- (6) Collins, A. M.; Skaer, N. J. V; Gheysens, T.; Knight, D.; Bertram, C.; Roach, H. I.; Oreffo, R. O. C.; Von-Aulock, S.; Baris, T.; Skinner, J.; Mann, S. Bone-like Resorbable Silk-Based Scaffolds for Load-Bearing Osteoregenerative Applications. *Adv. Mater.* **2009**, *21* (1), 75–78. <https://doi.org/10.1002/adma.200802239>.
- (7) Kasoju, N.; Bora, U. Silk Fibroin in Tissue Engineering. *Adv. Healthc. Mater.* **2012**, *1* (4), 393–412. <https://doi.org/10.1002/adhm.201200097>.
- (8) Singh, B. N.; Pramanik, K. Tissue and Cell Fabrication and Evaluation of Non-Mulberry Silk Fibroin Reinforced Chitosan Based Porous Composite Scaffold for Cartilage Tissue Engineering. **2018**, *55* (October), 83–90. <https://doi.org/10.1016/j.tice.2018.10.003>.
- (9) Darshan, G. H.; Kong, D.; Gautrot, J.; Vootla, S. Physico-Chemical Characterization of Antheraea Mylitta Silk Mats for Wound Healing Applications. *Sci. Rep.* **2017**, *7* (1), 1–11. <https://doi.org/10.1038/s41598-017-10531-7>.



- (10) Fazal, N.; Latief, N. Bombyx Mori Derived Scaffolds and Their Use in Cartilage Regeneration: A Systematic Review. *Osteoarthr. Cartil.* **2018**, *26* (12), 1583–1594. <https://doi.org/10.1016/j.joca.2018.07.009>.
- (11) Naskar, D.; Nayak, S.; Dey, T.; Kundu, S. C. Non-Mulberry Silk Fibroin Influence Osteogenesis and Osteoblast-Macrophage Cross Talk on Titanium Based Surface. *Sci. Rep.* **2014**, *4*, 4745. <https://doi.org/10.1038/srep04745>.
- (12) Acharya, C.; Ghosh, S. K.; Kundu, S. C. Silk Fibroin Film from Non-Mulberry Tropical Tasar Silkworms: A Novel Substrate for in Vitro Fibroblast Culture. *Acta Biomater.* **2009**, *5* (1), 429–437. <https://doi.org/10.1016/j.actbio.2008.07.003>.
- (13) Behera, S.; Naskar, D.; Sapru, S.; Bhattacharjee, P.; Dey, T.; Ghosh, A. K.; Mandal, M.; Kundu, S. C. Hydroxyapatite Reinforced Inherent RGD Containing Silk Fibroin Composite Scaffolds: Promising Platform for Bone Tissue Engineering. *Nanomedicine Nanotechnology, Biol. Med.* **2017**, *13* (5), 1745–1759. <https://doi.org/10.1016/j.nano.2017.02.016>.
- (14) Andiappan, M.; Kumari, T.; Sundaramoorthy, S.; Meiyazhagan, G.; Manoharan, P.; Venkataraman, G. Comparison of Eri and Tasar Silk Fibroin Scaffolds for Biomedical Applications. *Prog. Biomater.* **2016**, *5* (2), 81–91. <https://doi.org/10.1007/s40204-016-0047-5>.
- (15) Sen, K.; Babu K, M. Studies on Indian Silk. I. Macrocharacterization and Analysis of Amino Acid Composition. *J. Appl. Polym. Sci.* **2004**, *92* (2), 1080–1097. <https://doi.org/10.1002/app.13609>.
- (16) Konwarh, R.; Bhunia, B. K.; Mandal, B. B. Opportunities and Challenges in Exploring Indian Non-Mulberry Silk for Biomedical Applications. *Proc. Indian Natl. Sci. Acad.* **2017**, *83* (1), 85–101. <https://doi.org/10.16943/ptinsa/2017/41288>.

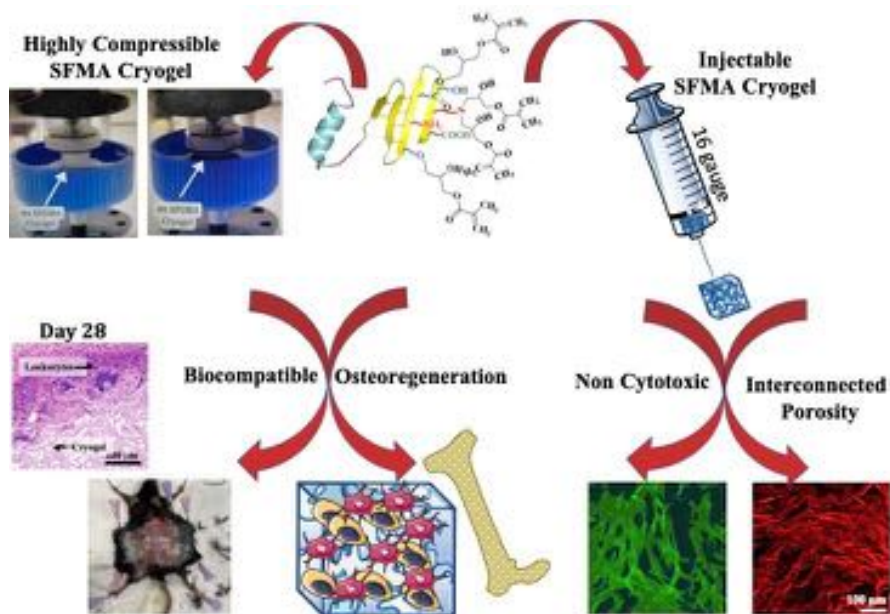
- (17) Gupta, P.; Adhikary, M.; M, J. C.; Kumar, M.; Bhardwaj, N.; Mandal, B. B. Biomimetic, Osteoconductive Non-Mulberry Silk Fiber Reinforced Tricomposite Scaffolds for Bone Tissue Engineering. *ACS Appl. Mater. Interfaces* **2016**, *8* (45), 30797–30810. <https://doi.org/10.1021/acsami.6b11366>.
- (18) Mandal, B. B.; Kundu, S. C. Non-Mulberry Silk Gland Fibroin Protein 3-D Scaffold for Enhanced Differentiation of Human Mesenchymal Stem Cells into Osteocytes. *Acta Biomater.* **2009**, *5* (7), 2579–2590. <https://doi.org/10.1016/j.actbio.2009.02.033>.
- (19) Singh, Y. P.; Moses, J. C.; Bhunia, B. K.; Nandi, S. K.; Mandal, B. B. Hierarchically Structured Seamless Silk Scaffolds for Osteochondral Interface Tissue Engineering. *J. Mater. Chem. B* **2018**, *6* (36), 5671–5688. <https://doi.org/10.1039/c8tb01344f>.
- (20) Rockwood, D. N.; Gil, E. S.; Park, S. H.; Kluge, J. A.; Grayson, W.; Bhumiratana, S.; Rajkhowa, R.; Wang, X.; Kim, S. J.; Vunjak-Novakovic, G.; Kaplan, D. L. Ingrowth of Human Mesenchymal Stem Cells into Porous Silk Particle Reinforced Silk Composite Scaffolds: An in Vitro Study. *Acta Biomater.* **2011**, *7* (1), 144–151. <https://doi.org/10.1016/j.actbio.2010.07.020>.
- (21) Zhang, Y.; Ni, M.; Zhang, M.; Ratner, B. Calcium Phosphate – Chitosan Composite Scaffolds for Bone Tissue Engineering. *Tissue Eng.* **2003**, *9* (2), 337–345.
- (22) Liu, Q.; Wang, F.; Gu, Z.; Ma, Q.; Hu, X. Exploring the Structural Transformation Mechanism of Chinese and Thailand Silk Fibroin Fibers and Formic-Acid Fabricated Silk Films. <https://doi.org/10.3390/ijms19113309>.
- (23) Phillips, D. M.; Drummy, L. F.; Conrady, D. G.; Fox, D. M.; Naik, R. R.; Stone, M. O.; Trulove, P. C.; Long, H. C. De; Mantz, R. A. Dissolution and Regeneration of

- Bombyx Mori Silk Fibroin Using Ionic Liquids. **2004**, No. 10, 14350–14351.
- (24) Zheng, Z.; Guo, S.; Liu, Y.; Wu, J.; Li, G.; Liu, M.; Wang, X.; Kaplan, D. Lithium-Free Processing of Silk Fibroin. **2016**, 31 (3), 450–463. <https://doi.org/10.1177/0885328216653259>.
- (25) Chen, J.; Chen, S.; Lai, G. Preparation and Characterization of Biomimetic Silk Fibroin / Chitosan Composite Nanofibers by Electrospinning for Osteoblasts Culture. **2012**, 1–11.
- (26) Silva, S. S.; Popa, E. G.; Gomes, M. E.; Oliveira, M. B.; Nayak, S.; Subia, B.; Mano, J. F.; Kundu, S. C.; Reis, R. L. Acta Biomaterialia Silk Hydrogels from Non-Mulberry and Mulberry Silkworm Cocoons Processed with Ionic Liquids. *Acta Biomater.* **2013**, 9 (11), 8972–8982. <https://doi.org/10.1016/j.actbio.2013.06.044>.
- (27) Nisal, A.; Sayyad, R.; Dhavale, P.; Khude, B.; Deshpande, R. Silk Fibroin Micro-Particle Scaffolds with Superior Compression Modulus and Slow Bioresorption for Effective Bone Regeneration. **2018**, No. April, 1–10. <https://doi.org/10.1038/s41598-018-25643-x>.
- (28) Parekh, N.; Hushye, C.; Warunkar, S.; Gupta, S. Sen; Nisal, A. RSC Advances In Vitro Study of Novel Microparticle Based Silk. *RSC Adv.* **2017**, 7, 26551–26558. <https://doi.org/10.1039/C7RA03288A>.
- (29) Parekh, N. A.; Deshpande, R. V.; Shukla, S. G.; Nisal, A. A. Silk Fibroin 3D Microparticle Scaffolds with Bioactive Ceramics: Chemical, Mechanical, and Osteoregenerative Characteristics. *Adv. Eng. Mater.* **2020**, 2000458, 1–11. <https://doi.org/10.1002/adem.202000458>.
- (30) Wilk, S. Advances in Fabricating the Electrospun Biopolymer-Based Biomaterials. **2021**.

- (31) Agarwal, S.; Wendorff, J. H.; Greiner, A. Use of Electrospinning Technique for Biomedical Applications. *Polymer (Guildf)*. **2008**, *49* (26), 5603–5621. <https://doi.org/10.1016/j.polymer.2008.09.014>.
- (32) Aubin, J. E. Regulation of Osteoblast Formation and Function. *Reviews in Endocrine and Metabolic Disorders*. 2001, pp 81–94. <https://doi.org/10.1023/A:1010011209064>.
- (33) 2012 - McNamara - Osteogenic Markar.Pdf.
- (34) Deshpande, R.; Shukla, S. Silk Fibroin and Ceramic Scaffolds : Comparative in Vitro Studies for Bone Regeneration. **2021**, No. March, 1–12. <https://doi.org/10.1002/btm2.10221>.
- (35) Wei Huang, Shuying Yang, Jianzhong Shao, and Y.-P. L. Signaling and Transcriptional Regulation in Osteoblast Commitment and Differentiation. *Front Biosci* **2013**, *12*, 3068–3092. <https://doi.org/10.1038/jid.2014.371>.
- (36) Mandal, B. B.; Grinberg, A.; Seok, E.; Panilaitis, B.; Kaplan, D. L. High-Strength Silk Protein Scaffolds for Bone Repair. *Pnas* **2012**, *109* (20), 7699–7704. <https://doi.org/10.1073/pnas.1119474109>.
- (37) Yetiskin, B.; Akinci, C.; Okay, O. Cryogelation within Cryogels : Silk Fibroin Scaffolds with Single- , Double- and Triple-Network Structures. *Polymer (Guildf)*. **2017**, *128*, 47–56. <https://doi.org/10.1016/j.polymer.2017.09.023>.
- (38) Mao, Z.; Bi, X.; Ye, F.; Shu, X.; Sun, L.; Guan, J.; Ritchie, R. O.; Wu, S. Controlled Cryogelation and Catalytic Cross-Linking Yields Highly Elastic and Robust Silk Fibroin Scaffolds. **2020**. <https://doi.org/10.1021/acsbiomaterials.0c00752>.
- (39) Mandal, B. B.; Kundu, S. C. Biomaterials Osteogenic and Adipogenic Differentiation of Rat Bone Marrow Cells on Non-Mulberry and Mulberry

- Silk Gland Fibroin 3D Scaffolds. *Biomaterials* **2009**, *30* (28), 5019–5030. <https://doi.org/10.1016/j.biomaterials.2009.05.064>.
- (40) Sahu, N.; Baligar, P.; Midha, S.; Kundu, B.; Bhattacharjee, M.; Mukherjee, S.; Mukherjee, S.; Maushart, F.; Das, S. Nonmulberry Silk Fibroin Scaffold Shows Superior Osteoconductivity Than Mulberry Silk Fibroin in Calvarial Bone Regeneration. **2015**, 1709–1721. <https://doi.org/10.1002/adhm.201500283>.
- (41) Gomes, P. S.; Fernandes, M. H. Rodent Models in Bone-Related Research: The Relevance of Calvarial Defects in the Assessment of Bone Regeneration Strategies. *Lab. Anim.* **2011**, *45* (1), 14–24. <https://doi.org/10.1258/la.2010.010085>.
- (42) Spicer, P. P.; Kretlow, J. D.; Young, S.; Jansen, J. A.; Kasper, F. K.; Mikos, A. G. Evaluation of Bone Regeneration Using the Rat Critical Size Calvarial Defect. *Nat. Protoc.* **2012**, *7* (10), 1918–1929. <https://doi.org/10.1038/nprot.2012.113>.
- (43) Silva, S. S.; Mano, J. F.; Reis, R. L. Potential Applications of Natural Origin Polymer-Based Systems in Soft Tissue Regeneration. *Crit. Rev. Biotechnol.* **2010**, *30* (3), 200–221. <https://doi.org/10.3109/07388551.2010.505561>.

# Chapter 6 Development of mulberry and non-mulberry silk fibroin-based injectable scaffold



This chapter work has been done as a part of my Fulbright-Nehru Doctoral Research Fellowship in Bioengineering for the year 2020-2021 at Northeastern University, Boston, USA (This manuscript is under preparation)

## 6.1 Abstract

Bone injuries such as craniofacial fractures are commonly treated with invasive open surgeries. Ideally, these traditional clinical practices should be performed with minimally invasive strategies to help minimise surgery time, reduce recovery time and improve outcomes. The purpose of this work was to engineer injectable and biomimetic silk fibroin-based injectable cryogels as three-dimensional scaffolds for osteoregenerative applications. To this end, bioabsorbable mulberry silk fibroin (SF), a naturally delivered, biocompatible, and fibrous protein with excellent mechanical properties, was first chemically modified with methacrylated residues. Next, silk-based cryogels were prepared at -20°C using methacrylated SF (SFMA) and then fully characterized to assess their physicochemical properties. SFMA-based cryogels exhibited remarkable physical properties as they can sustain a high degree of compression - up to 99% of their volume. These cryogels also exhibit shape memory properties, and can be successfully injected through a small-bore hypodermic needle. *In-vitro* studies with human dermal fibroblasts showed that silk-based cryogels are cytocompatible and promoted cell-matrix interactions. However, cryogels containing RGD or blended with NMS displayed more elongated cells along the polymer network. Furthermore, these cryogels did not trigger an activation of primary murine bone marrow-derived dendritic cells, suggesting a low risk of inflammation in the host, which was confirmed by a histological analysis of cryogels when subcutaneously injected in mice for 28 days. Finally, these cryogels also supported controlled cell differentiation, promoted the osteogenic phenotype in human mesenchymal stem cells, which is a critical step toward using these constructs in bone tissue repair and regeneration.

This Chapter begins with Section 6.2, which describes a literature review highlighting the advantage of injectable biomaterials and processing difficulty with SF to make it flexible for injection. Section 6.3 focuses on the methodology used to produce chemically modified SF and its physico-chemical characterization. Section 6.4 discusses the results followed by a discussion in 6.5. Section 6.6 concludes Chapter 6 and the references have been summarized in Section 6.7.

## 6.2 Literature Review

In the current years, worldwide, there have been dramatic lifestyle changes, increased accidents, trauma, bone fractures, and diseases.<sup>1-3</sup> Although bone has a natural healing property without scar tissue formation, bone traumas suffer from compromised bone healing and reintegration.<sup>4</sup> Tissue engineering with the help of a 3D scaffold system is the modern therapeutic option for BTE that has also overcome the limitations like dual surgery, long surgery time and donor site morbidity associated with the 'autografts – grafting a bone from the patient's own body that is considered as the 'gold standard' for an orthopaedic surgeon.<sup>5-7</sup>

In bone, non-union/long bone fractures or multisite/craniofacial fractures need an external bone void filler. This biomaterial should not only provide support, but it should also be biocompatible, osteoconductive, osteoinductive, biodegradable with appropriate mechanical properties so that the biomaterial will be integrated with natural ECM of bone to develop new bone tissue without generating the extended immunogenic response.<sup>8</sup> Various materials like metals, ceramics, natural/synthetic polymers and different blends are explored as either in the implantable or injectable form of biomaterial to treat different types of bone



defects.<sup>9,10</sup> Traditional clinical practice can be transformed into non-invasive injectable therapeutics that helps to minimize surgery time, join hands in the increasing demands in regenerative<sup>11</sup> and intellectual medicine toward selected clinical bone defects. Various polymers and bioceramics are reported as injectable regimens to treat bone defects.<sup>12,13</sup>

SF is one of the highly explored natural biopolymer, which is approved by the United States Food and Drug Administration (US-FDA).<sup>14,15</sup> Inherent structural, mechanical strength with an osteoconductive property makes SF one of the foremost biomaterial for BTE.<sup>16-20</sup> Based on the types of origin, SF having unique structural properties<sup>21</sup> where it can form beta sheets (crystalline structure) from alpha-helical structure (random coil arrangements) with various chemical crosslinking or physical treatments that favour the development of a rigid load-bearing 3D scaffold system while giving the challenge to formulate a 3D injectable scaffold for BTE.<sup>22,23</sup> SF based conventional injectable hydrogels<sup>24</sup> with or without crosslinking agents are reported for BTE however, the use of conventional hydrogels is limited by poor mechanical performance that can be enhanced by blending with different ceramics/polymers.<sup>25</sup>

Cryogel – a class of hydrogel, is an advanced biomaterial with a unique interconnected porous 3D architecture.<sup>26</sup> An ever-growing body of literature demonstrates their applicability in the realm of tissue engineering as extracellular matrix analogue scaffolds.<sup>27,28</sup> Cryogels are produced by controlled freezing, which results in a highly interconnected porous polymer network. Cryogelation is a simple method that avoids utilizing porogens or using aggressive and toxic solvents to achieve a porous structure. Cryogels are formed at temperatures below the solvent's freezing point (e.g., water), where we can avoid concerns such as

toxicity of organic solvents. Porogen removal is achieved by simply holding the cryogel at temperatures above the solvent freezing point.<sup>29</sup>

Furthermore, various parameters can be easily fine-tuned to customize cryogels for their intended use.<sup>30</sup> Okay *et al.* have developed SF based cryogels by using chemical cross-linker to achieve a higher modulus comparable to cancellous bone. However, all these reported cryogels are stiff and are implantable cryogels.<sup>31-35</sup> To date, there is no report available for SF-based injectable cryogel scaffolds for BTE application.

The RGD (Arg-Gly-Asp) peptide is an integrin recognition motif found in fibronectin and one of the most extensively studied cell adhesion peptides in various TE applications. Non-mulberry silk has an inherent RGD motif, which helps cell attachment, cell proliferation and differentiation.<sup>36-38</sup>

In this work, we engineered for the first time injectable SF-based cryogels from methacrylated silk fibroin (SFMA). These cryogels were prepared by crosslinking methacrylated SF (SFMA) at subzero temperatures. To improve cell-adhesion properties, SFMA-based cryogels either contained RGD motif, an extensively studied cell adhesion peptide, or were blended with RGD-containing non-mulberry silk fiber from *Antheraea mylitta* (NMS). All developed cryogels were investigated for their syringe injectability, shape memory features, pore size, pore connectivity, swelling ratio, enzymatic degradation, mechanical properties, and compressibility. Cryogels were also tested for their cytocompatibility by using human dermal fibroblasts (hDFs) and murine bone marrow-derived dendritic cells (BMDCs) and biocompatibility by subcutaneous injection of cryogel in mice model. Lastly, cryogels were evaluated for their osteogenic potential by inducing osteogenic differentiation of human mesenchymal stem cells (hMSCs).

## 6.3 Experimental Section – Materials and Methods

### 6.3.1 Materials

Mulberry silk fibers were purchased from Central Sericultural Research & Training Institute (CSRTI), Mysore and *Antheraea mylitta* non-mulberry silk fiber (NMS) were purchased from farmers, Tandipara, Birbhum Dist., West Bengal. Sodium Bicarbonate ( $\text{NaHCO}_3$ ) (#1.93237.0521), Lithium bromide (LiBr) (cat#213225), Dialysis tube (D9652), Protease XIV (cat#P5147) enzyme, glycidyl methacrylate (GMA) (151238), triethylamine (TEA) (T0886) and Bone morphogenic protein-2 (BMP-2) (RAB0028-1KT), Far-red fixable dead cell staining from ViaQuant™, Genecopoeia, Rockville, MD, USA, 4% Paraformaldehyde solution, Triton X, DAPI were procured from Sigma Aldrich. DMEM (12320-032), IMDM (cat#12440-046), fetal bovine serum (FBS) (cat#10082-147), FBS for hMSCs (cat#12662-011), Alamar blue (cat#1987309), StemPro osteogenic differentiation kit (cat# A1007201), TNF- $\alpha$  (cat# BMS223-4), Osteocalcin (OCN) (BMS2020INST) and 2-mercaptoethanol from Fisher Scientific. Human Dermal Fibroblast (HDF) and Human Mesenchymal Stem Cells (hMSCs) were generous gifts from Prof. Dai's lab at NEU, Boston, USA. Alkaline phosphatase (ALP) (NC9885130), penicillin and streptomycin bought from Fisher Scientific, Hampton, NH, USA, Alexa Fluor 488-phalloidin from Cell Signalling Technology, Danvers, MA, USA, C57Bl/6 mice- eight-week-old purchased from The Jackson Laboratory, Bar Harbor, ME, USA, GM-CSF from Genscript, Piscataway, NJ, USA.

### 6.3.2 Synthesis of methacrylated silk fibroin (SFMA)

SF solution using LiBr was prepared as per the earlier reported protocol.<sup>39</sup> In brief, *B. mori* cocoons were boiled in 0.5 w/v% of NaHCO<sub>3</sub> solution for 30 minutes each for sericin removal twice. SF fiber was washed thoroughly with DI water a minimum of three times and was vacuum dried for 48h at 60°C. The fiber was then dissolved in 9.3M LiBr solution at 60°C for 4h. At the end of 4h, the solution was allowed to cool down at room temperature (RT). In the SF-LiBr solution, GMA and TEA were added (2.5g SF + 31g GMA + 15.5g TEA) and stirred at 300rpm at RT to prepare methacrylated SF (SFGMA). At the end of the 48h reaction time, a solution was dialyzed extensively against DI water for 48h by changing the water three times in a day. The SF-GMA solution was centrifuged at high speed at the end of dialysis for 45 minutes. The collected supernatant was lyophilized at -55°C for 4 days to obtain a chemically modified SFGMA sponge stored at -80°C till further use. Rhodamine-labelled SFMA was synthesized as per previous report.<sup>30</sup> Briefly, SFMA (1g) was dissolved in a 10 mL sodium bicarbonate buffer (NaHCO<sub>3</sub>, pH 8.5). 10 mg NHS-Rhodamine from ThermoFisher was subsequently added to the SFMA solution while stirring overnight at RT. After an overnight reaction, the Rhodamine-labeled SFMA was freeze-dried at -80°C overnight, followed by lyophilization for two days. The final product was then stored at -20°C until further use.

### 6.3.3 Chemical Characterization of SFMA

Chemical functionalization of silk fibroin with a methyl group with a degree of methacrylation was calculated using proton nuclear resonance (<sup>1</sup>H NMR) Spectroscopy. 3% (w/v) SFGMA and pure SF solution were prepared using D<sub>2</sub>O as

a solvent. NMR spectra were obtained with 15 Hz sample spinning, 45° tip angle with 10s recycle delay, for 256 scans at RT in Varian Inova-500 MHz NMR spectrometer. The degree of methacrylation was calculated as per the reported method where signals raised from lysine amino acids present in SF are used for calculation.<sup>40</sup> Signals produced in the range of 6.9-7.5ppm from aromatic amino acids were used to normalise the spectrum. Lysine peak at 2.8-2.95ppm was integrated into pure SF and SFGM NMR spectra. The degree of methacrylation was calculated using equation 1:

$$\text{Degree of Methacrylation} = \left(1 - \frac{\text{Integrated lysine peak of SFGMA}}{\text{Integrated lysine peak of Pure SF}}\right) * 100 \text{Eqn. 1}$$

Incorporation of the methyl group in modified silk and its effect on beta-sheet was further studied by using FTIR from Perkin Elmer coupled with Golden Gate Diamond ATR at 4 cm<sup>-1</sup> resolution, and 32 scans were recorded in the range of 1400 to 1800 cm<sup>-1</sup>. The amide I peak obtained in the spectral range of 1580 to 1720 cm<sup>-1</sup> was deconvoluted and used to analyze fibroin protein's secondary structure (beta-sheet). Peakfit v4.1 software was used to calculate the crystallinity index.

Change in the viscosity after chemical modification has been measured by using spindle CPE-42 in DV-II+ Pro viscometer from Brookfield for both pure SF and SFMA.

### **6.3.4 Cryomilling of non-mulberry silk fiber (NMS)**

Cryomilled *A. mylitta* SF fibers were obtained as mentioned in Chapter 5, section 5.3.3.

### **6.3.5 Preparation of SFMA and SFMA with NMS/MPA/APR Cryogels**

Redox-induced free radical polymerization mechanism in aqueous solution at sub-zero temperature was used to prepare cryogels. 8% (w/v) SFGAM solution was prepared by using DI water. Different combination that includes 0.5% (v/v), 1% (v/v) NMS and 0.5 % (w/v) MPA/APR were mixed with SFMA solution to prepare cryogels in the presence of 1.12% (w/v) APS and 0.56% (w/v) TEMED. Precooled polymer solution was immediately poured into teflon mould and transferred to a freezer at a preset sub-zero -20°C temperature. Polymeric solution with initiator system was allowed to cryo-polymerize for 16-18h at -20°C. The resulting cryogel was thawed at RT and washed with deionized water. Different sizes [4mm (l) x 4mm (w) x 1mm (h), 8 mm (d) x 6 mm (h), 17mm (d) x 1mm (h)] of cryogels were synthesized for different types of characterization and to evaluate its biological performance.

### **6.3.6 Injectability Test**

4mm × 4mm × 1mm cuboid-shaped cryogels from different concentrations of SFMA and SFMA with NMS/MPA were prepared and suspended in 0.2mL of phosphate buffered saline (PBS) to test for syringe-injectability by using a 16-gauge needle. In brief, cryogels were positioned on the aperture of the needle, followed by forcing them through the needle by using PBS. The videos were taken using a Pro 12MP camera system.

### **6.3.7 Physical Characterization of Cryogels**

For mechanical properties, 6mm height x 8mm diameter cylindrical-shaped cryogels were fabricated and compressed between two parallel plates on a TA Instruments Electroforce 3200 universal mechanical testing platform. To reduce slippage, water-resistant sandpaper was attached to both platens. To maintain an *in vivo*-like environment, the cryogels were submerged in PBS. Ten successive cycles were recorded with a strain rate of 10% per minute on each sample. Compressive strain (mm) and load (N) were measured at the 8th cycle. A stress/strain curve was developed, and moduli were calculated by obtaining the tangent of the slope of the linear region.

The conventional gravimetric method was used to calculate the swelling ratio. Cryogels were allowed to swell in PBS for 24h followed by recording their wet weight. These cryogels were then washed with DI water, freeze-dried and used to record the dry weight. The swelling ratio ( $Q_M$ ) was calculated by dividing the weight of fully swollen cryogel by the weight of freeze-dried cryogel.

Pore interconnectivity of cryogels was obtained by cryogel immersion in PBS for 24h to record wet weight. A kimwipe was gently applied on the surface of the cryogel to remove the free water and record its partially dehydrated weight. The degree of pore interconnectivity was calculated based on the amount of water wicked away divided by the initial total amount of water.

For scanning electron microscopy (SEM), freeze-dried cryogels (dimensions: 4mm × 4mm × 1mm) were prepared and mounted on the sample holder using carbon tape followed by sputter-coating with platinum/palladium. Cryogels were then imaged using secondary electron detection on a Hitachi S-4800 scanning electron microscope (Hitachi High-Technology Corporation, Tokyo, Japan). *In-vitro* bioerosion study in the proteolytic environment was conducted using protease XIV enzyme. Developed cryogels were incubated in the enzymatic solution

(1Unit/mL) at 37°C for 14 days with time points of day 7 and day 14. Freshly prepared enzyme solutions were filter-sterilised and replenished after every 48h. On day 7 and 14, cryogels were washed with PBS, freeze-dried, and weighed.

### **6.3.8 *In-vitro* cell adhesion efficiency**

Human Dermal Fibroblasts (HDF) were cultured in Dulbecco's Modified Eagles Medium (DMEM) supplemented with 10% (v/v) Fetal Bovine Serum (FBS), 100 µg/mL penicillin and 100 µg/mL streptomycin at standard culture condition (37°C, 5% CO<sub>2</sub>). For sterilization, 4mm × 4mm × 1mm cryogels were treated with 70% ethanol for 15 min, followed by washing with sterile water several times. Before seeding, cryogels were mechanically compressed on sterile gauze to remove water under sterile conditions. 20 µl of cell suspension containing 2 × 10<sup>5</sup> cells in a complete culture medium were dropwise added on top of each cuboid-shaped cryogel and incubated for 2h. The cell-loaded cryogels were supplemented with 1mL of fresh media and incubated at 37°C, 5% CO<sub>2</sub> atmosphere. At the end of 24h, cryogels were transferred into another plate and an Alamar blue assay was performed as mentioned in section 5.3.11. Simultaneously, a calibration curve was prepared by using a known number of HDF cells by Alamar blue assay at the end of 24h.

### **6.3.9 *In-vitro* cell viability and cytoskeleton staining**

HDF cells are cultured and loaded on cryogel as mentioned in above Section 6.3.8. The cell-loaded cryogels were supplemented with 1mL of fresh media and incubated at 37°C, 5% CO<sub>2</sub> atmosphere. Cell viability was determined via a fixable dead cell assay for day 1 and 3. At each time point, cells loaded on cryogels were



treated with a far-red fixable dead cell staining according to manufacturer's instructions, followed by fixation with 4% paraformaldehyde solution for 15 min at RT and washed with PBS three times. Before microscopy, cells were permeabilized with PBS supplemented with 0.1% (v/v) Triton X-100 for 5 min, then stained with DAPI and Alexa Fluor 488-phalloidin according to manufacturer's protocols. Confocal microscopy images were acquired using a Leica TCS SP5 X WLL Confocal Microscope (Buffalo Grove, IL, USA) and analyzed using ImageJ software (Version 1.52e, Bethesda, MD, USA). For each cryogel, five representative sections were analyzed. As mentioned above, cell viability was analyzed with a direct contact method where HDF cells were seeded on cryogels. On desired time points (Day 1 and 3), 10% (v/v) Alamar blue solution was added and incubated for 6h at 37°C, 5% CO<sub>2</sub> atmosphere. At the end of incubation, fluorescence was measured at 590nm. Relative percent cell viability was calculated by using plate control.

### **6.3.10 hMSCs proliferation assay and cytoskeleton staining**

*In-vitro* hMSCs proliferation was performed using Alamar blue dye-based assay on day 7, 14 and 28 in growth media (IMDM + 10% hMSCs FBS). Ethanol-treated cryogels were placed in a 24 well flat-bottomed tissue culture plate. hMSCs at a density of  $5 \times 10^4$  cells per cryogel in 20 $\mu$ l of growth media. The cells were allowed to settle for 2h at 37°C, 5% CO<sub>2</sub> atmosphere. Additional 500 $\mu$ l media was added to the tissue culture plate and incubated for 28 days. Fresh growth media was replenished after every 48h. At the desired time points, growth media was replaced with a 10% Alamar blue solution and incubated for 6h at 37°C with 5%

CO<sub>2</sub>. At the end of incubation, fluorescence was measured at 590 nm and the increase in emission was recorded to calculate the cell proliferation function.

### **6.3.11 hMSCs differentiation into osteogenic lineage**

Ability of cryogel to support osteogenesis was evaluated by using hMSCs. Ethanol (70% v/v) sterilized cryogels were kept in a 24 well flat-bottomed tissue culture treated plate. hMSCs at the density of  $5 \times 10^4$  cells per cryogel were seeded in 20 $\mu$ L of growth media. The cells were allowed to settle for 2h at 37°C, 5% CO<sub>2</sub> atmosphere. An additional 500 $\mu$ L media was added to the tissue culture plate, then incubated at 37°C for 24h in a 5% CO<sub>2</sub> atmosphere. The next day, growth media was removed, and the osteogenic differentiation media was added. Fresh osteogenic media was replenished after every 48h. Spent media was collected at each time point and stored at -80°C for marker analysis. Expression levels of alkaline phosphatase (ALP), bone morphogenic protein (BMP-2), osteocalcin (OCN) and calcium deposition were measured to evaluate the osteogenic potential of developed cryogels.

ALP enzyme activity is measured by colorimetric assay, while expression level of both BMP-2 and OCN were analyzed using ELISA as per the protocol provided by the manufacturer by using spent media as a sample. The individual calibration curve for each marker was developed, and expression of ALP, BMP-2 and OCN were obtained. In the same samples, total protein was also measured using nanodrop, which was used to normalize the determined individual concentration of osteogenic markers. At the end of day 28, calcium deposition was measured by using Alizarin Red S staining. Cryogels were fixed with 4% paraformaldehyde at room temperature (RT) for 10 minutes followed by PBS washing, and then stained with 2% Alizarin Red S solution for 20 minutes. After staining, the scaffolds were

washed thoroughly with deionized water (DI). The deposited calcium was observed under an optical microscope (Carl Zeiss). Further, the deposited calcium was extracted using 0.5 mL of 10% acetic acid for 30 minutes at RT and then incubated at 85°C for 10 minutes. The solution was centrifuged at 14000 rpm for 15 minutes, and then the supernatant was collected to measure its absorbance at 405 nm.

### **6.3.12 Generation of BMDCs and *in vitro* dendritic cell (DC) activation assay**

Eight-week-old female C57BL/6J mice were housed according to NIH guidelines. All animal experiments were performed by NIH recommendations and approved by the DLAM ethics committee at Northeastern University. BMDCs were extracted from C57BL/6 tibia and femur bone marrow as previously described<sup>41</sup> and cultured for 8-10 days in RPMI 1640 media supplemented with 10% (v/v) heat-inactivated FBS, 100U/mL penicillin, 100µg/mL streptomycin, 50µM 2-mercaptoethanol and 20ng/mL murine GM-CSF. To evaluate DC activation, BMDCs were cultured with SFMA, RGD-containing SFMA, SFMA + 0.5%NMS, SFMA + 1% NMS cryogels (dimensions: 4mm × 4mm × 1mm) in complete culture medium for one day. Cells treated with LPS (200ng/mL) were used as positive control whereas cells with media alone were used as negative control. BMDC activation was evaluated by flow cytometry (Attune NxT Flow Cytometer, ThermoFisher Scientific, Waltham, MA, USA) using the following fluorescent antibodies (ThermoFisher Scientific, Waltham, MA, USA and Biolegend, San Diego, CA, USA): eBioscience™ Fixable Viability Dye eFluor™ 506, anti-mouse CD11c (N418,

hamster IgG, APC), anti-mouse MHC II (M5/114.15.2, Rat IgG2b, APC-Cy7), anti-mouse CD86 (GL1, rat IgG2a, BV421), and anti-mouse CD317 (927, rat IgG2b PE).

### **6.3.13 *In-vivo* biocompatibility assessment**

Cuboid shaped SFGMA, SFGMA+1%NMS and SFGMA+RGD cryogels (4mm × 4mm, × 1mm) were fabricated using free-radical polymerization. Next, the cryogels were sterilized in 70% ethanol for 15 minutes and washed twice with sterile PBS. Sterile cryogels were suspended in sterile PBS (0.2mL) followed by syringe-injection through 16-gauge hypodermic needle in both dorsal flanks of eight-week- old female C57BL/6J mice (n=3; The Jackson Laboratory, Bar Harbor, ME, USA). After 3 days and 28 days, mice were euthanized, and cryogels were explanted with the surrounding tissue. Explanted cryogels were fixed in 4% paraformaldehyde (PFA), embedded in paraffin, to obtain a section of 5µm thickness. The slices were stained using haematoxylin and eosin (H&E) and Masson's trichrome (MT) for histological analysis.

### **6.3.14 Statistical analysis**

In the present study, all data are presented as mean ± standard deviation (SD). One-way and two-way analysis of variance (ANOVA) with Tukey's post-hoc test was performed using the Past three software and GraphPad to analyze significant differences among and within the groups. A value of  $p < 0.05$  was considered statistically significant.

## 6.4 Results

### 6.4.1 Synthesis and characterization of SFMA

SF is known to have intermediate hydrophilicity and as a prerequisite for cryogel formation, SF was chemically modified with a methacrylation reaction using GMA. As per **Figure 6-1A**, SF was degummed, dissolved in LiBr and modified with GMA in the presence of TEA. GMA reaction majorly involved ring-opening polymerization reaction. Specifically, SF can be modified with GMA that incorporate methacryloyl as a functional group. Possible SF sites for methacryloyl modification include amine (mainly a side group of a lysine residue), hydroxyl, and carboxyl groups (**Figure 6-1B**).

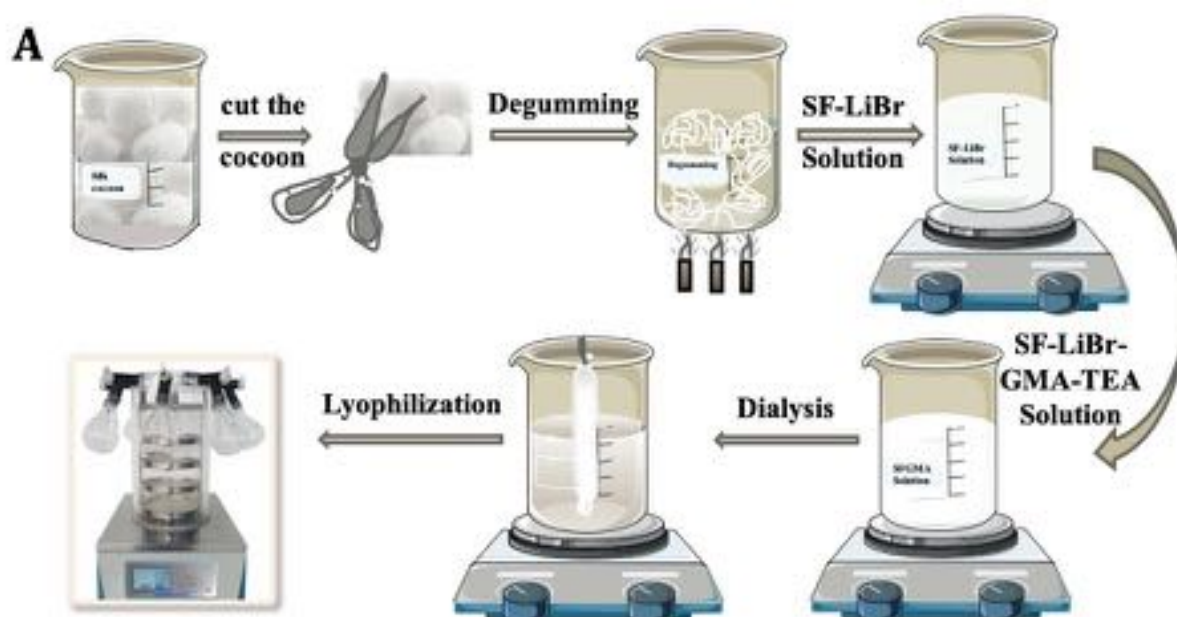


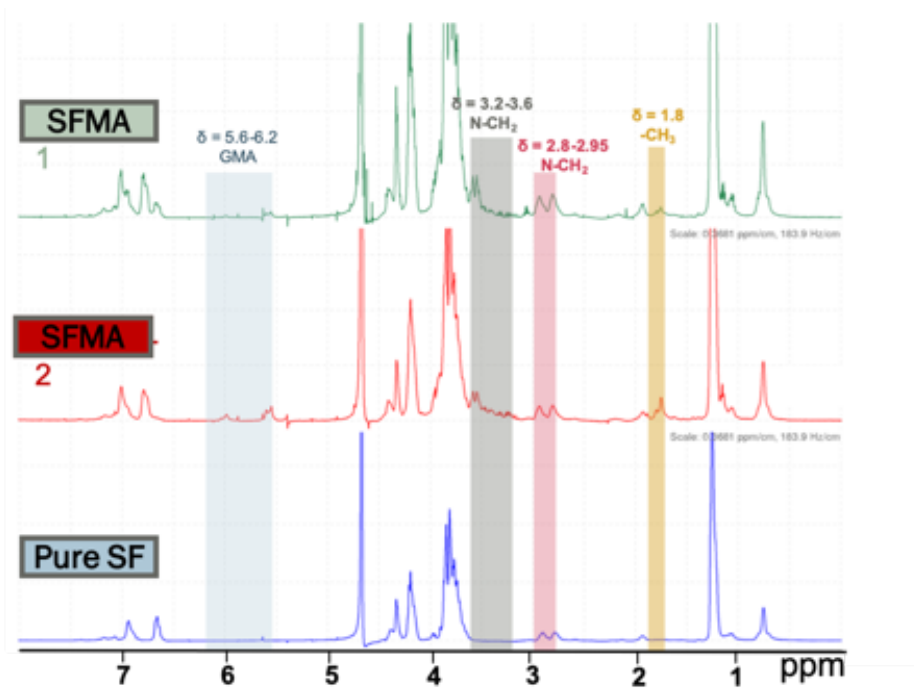


**Figure 6-1** Schematic for the fabrication of SFMA A) fabrication of chemically modified SF with GMA; a. degumming of SF b. Washing of degummed SF fibers DI water; c. Dissolution of SF into 9.3M Lithium Bromide solution; d. Addition of GMA and TEA; e. Dialysis with Dialysis with DI water; f. lyophilization; g. lyophilized SFMA. B) Incorporation of functional methacrylate groups into SF by epoxide ring-opening polymerization reaction and a possible site for the modification includes -NH<sub>2</sub>, -OH and -COOH.<sup>42</sup>

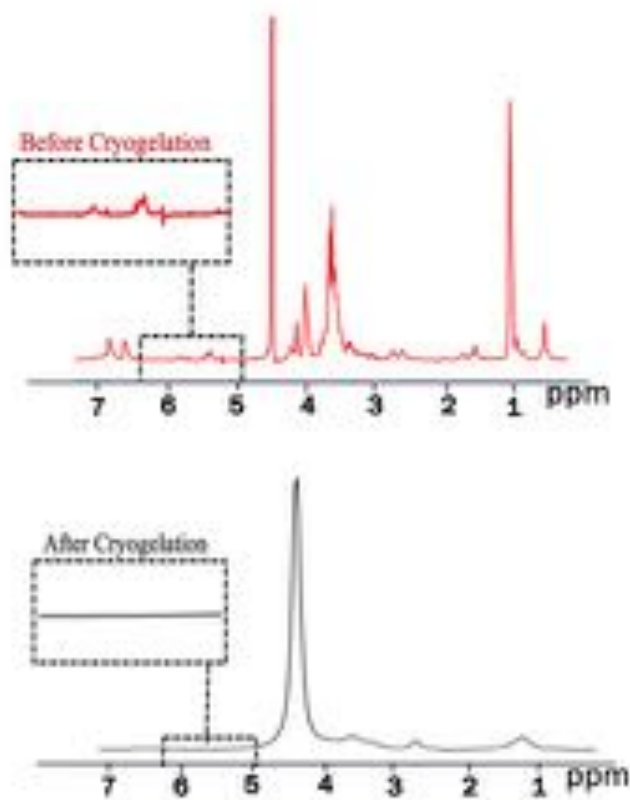
<sup>1</sup>H NMR technique was used to confirm the methacrylation of SF. Detection of signature peaks of the methacrylate vinyl group at  $\delta = 6.2\text{--}5.6$  ppm and the methyl group of GMA at  $\delta = 1.8$  ppm in SFMA confirms incorporation of the methyl group in SF. Peaks in  $\delta = 6.2\text{--}5.6$  ppm were increasing with a two days reaction (SFMA-2 in **Figure 6-2A**) as compared to the one-day reaction of SF with GMA (SFMA-1 in **Figure 6-2A**). The decrease of the lysine methylene signal in SFMA at  $\delta = 2.9$  ppm indicated modification of the lysine residues in SF resulting in methacrylation of 14% in SFMA-2 and 10% in SFMA-1. Additionally, hydrogen neighbouring the C–N bond resulting in peaks at  $\delta=3.2\text{--}3.6$  in SFMA confirms successful chemical modification of SF. Upon cryogelation, the methylene peaks disappeared, suggesting total consumption of the reactive pendant methacrylate groups in methacrylated SF as shown in **Figure 6-2B**.

Fourier-transform infrared spectroscopy (FTIR) was used to further confirm the modification of SF with GMA through the presence of GMA and SF related peaks in FTIR spectra depicted in **Figure 6-2C**. Both pure SF and SFMA spectra show signature peaks for Amide I (1648), Amide II (1527) and Amide III (1249). An alcohol group stretching is observed at  $1238\text{cm}^{-1}$  and can be attributed to the opening of the GMA epoxy group. Other small confirmatory changes were detected at  $951$  and  $1165\text{cm}^{-1}$  representing the GMA reaction with SF. The C=O stretch of the Amide I peak in region  $1700 - 1600\text{cm}^{-1}$  was deconvoluted to confirm the protein conformation in methacrylated SF. **Figure 6-2D** shows a significant decrease in  $\beta$ -sheet content in SFMA compared to pure SF, further supporting the incorporation of methyl groups in SF upon GMA reaction. Viscosity of the SFMA and pure SF was plotted in **Figure 6-2E** and significantly decreased viscosity was obtained with SFMA. This data is in alignment with the reduction in beta sheet content observed in FTIR spectra for the SFMA sample. Reduced intermolecular beta sheets are known to contribute to reduction in viscosity due to decrease in intermolecular physical cross-links. The SFMA solution and SF solutions were used for further experimentation to form cryogels.

**A**



**B**





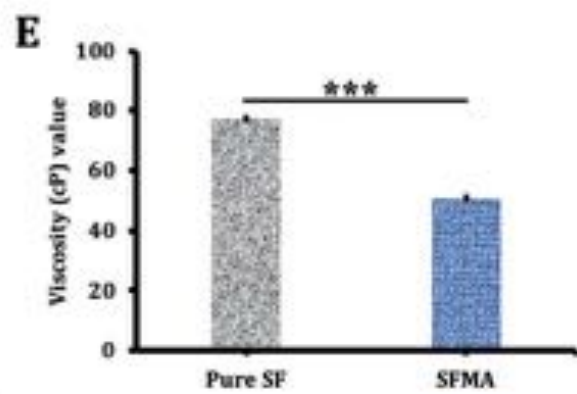
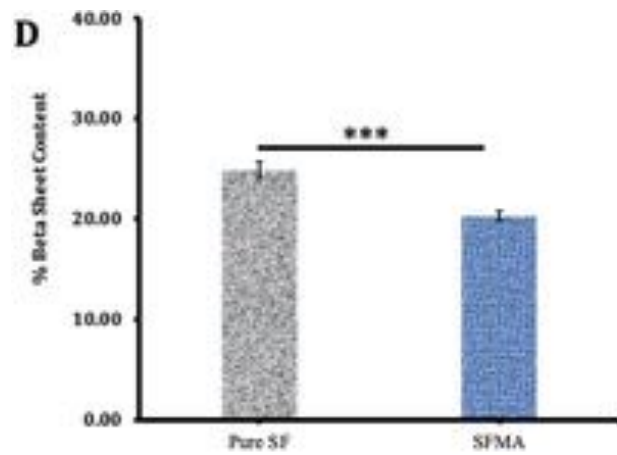
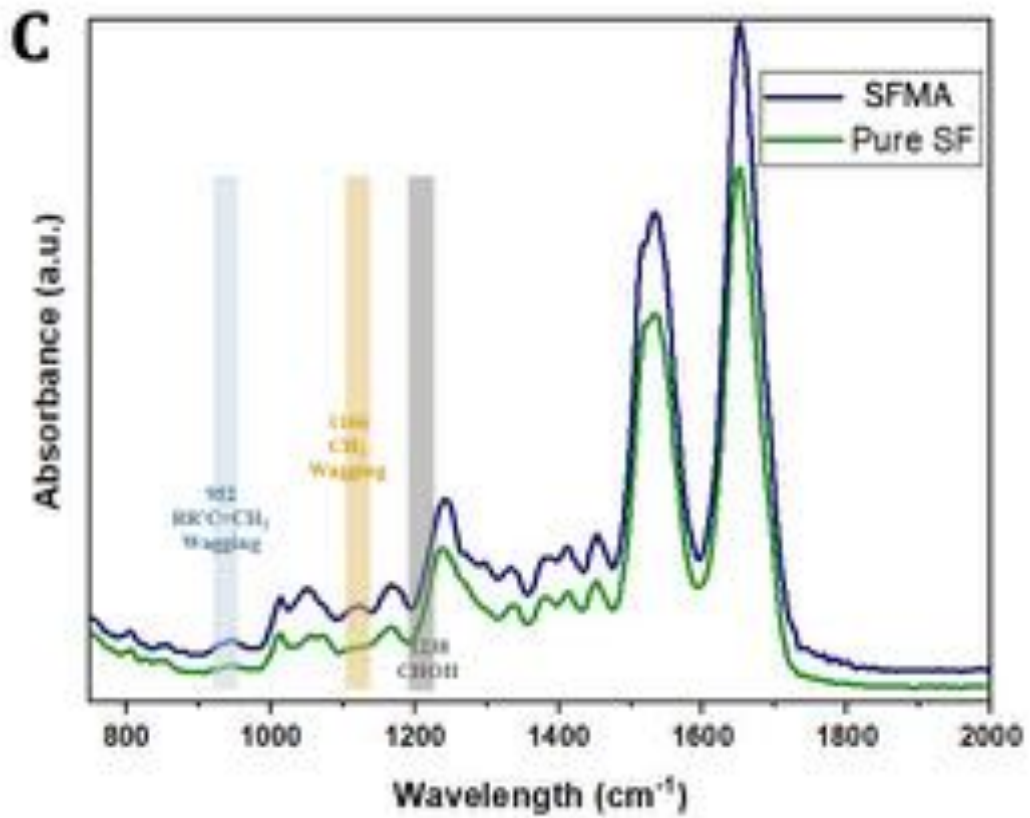


**Figure 6-2** Chemical characterization of SFMA by  $^1\text{H}$  NMR and FTIR: A)  $^1\text{H}$  NMR spectra of pure SF and SFMA in  $\text{D}_2\text{O}$ , 1d reaction between GMA and SF is indicated by SFMA 1 while 2d reaction by SFMA 2. B)  $^1\text{H}$  NMR spectra of SFMA before and after cryogelation. C) FTIR spectra of pure SF, SFMA. D) Beta sheet percentage in pure SF and SFMA and E) Viscosity measurement of pure SF and SFMA.

## 6.4.2 Preparation of SFMA-based Cryogels

All cryogels were fabricated at  $-20^\circ\text{C}$  by using an initiator system. During cryopolymerization, polymer solutions were surrounded by ice crystals resulting from most of the water content in the polymer solution (Figure 6.3). The principle behind the cryogel formation is free radical cryo-polymerization for 16-18h resulting in interconnected porous cryogel structure after thawing at RT. These cryogels were washed and annealed with 70% ethanol for 15 min. The resulting 3D cryogels are syringe injectable by using a 16-gauge needle. Injectability videos for SFMA, SFMA+0.5% NMS, SFMA+1% NMS and SFMA+0.5% MPA are available as video 4, 5, 6 respectively in the [link](#) given here.

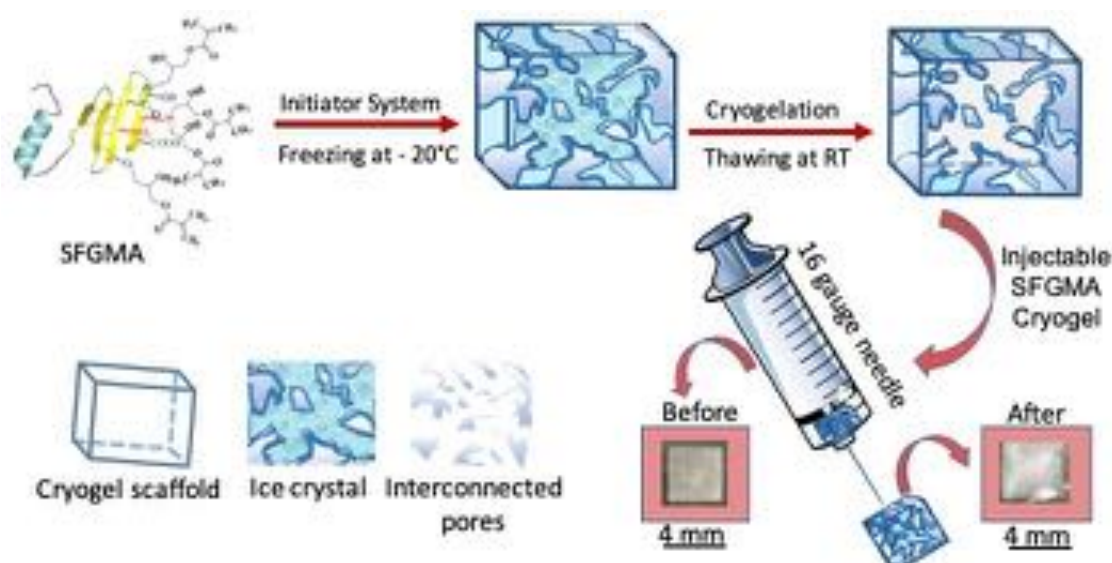


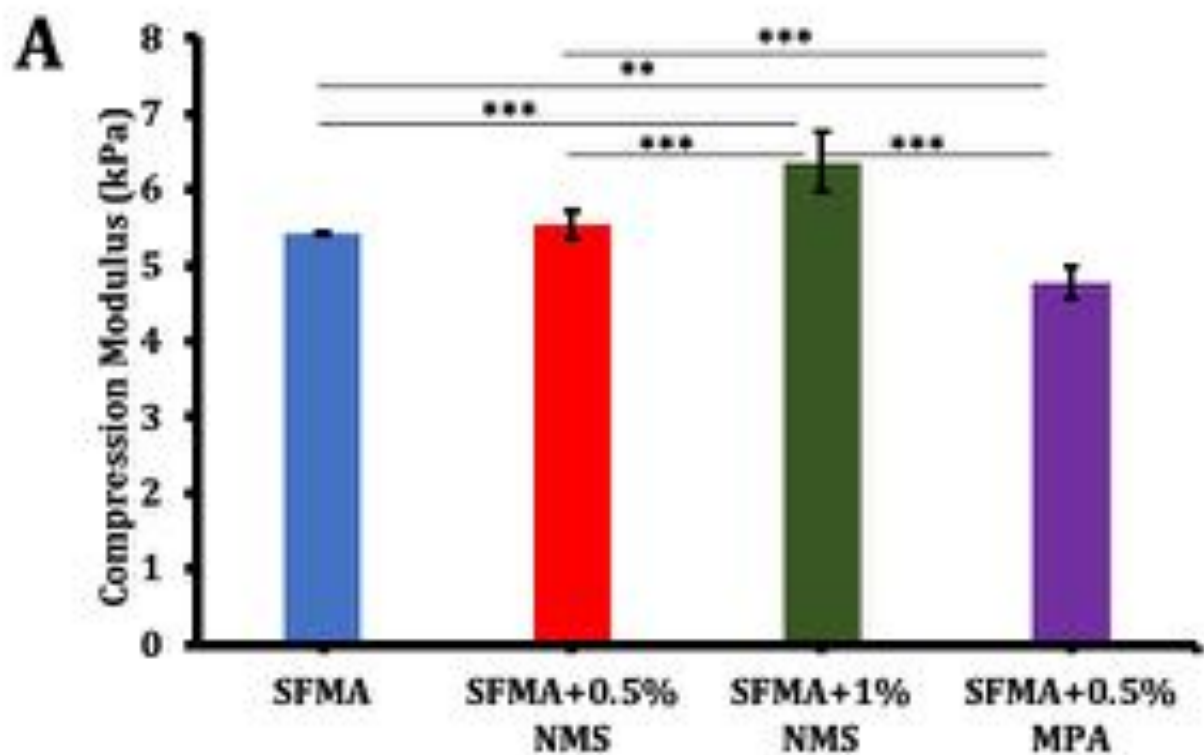
**Figure 6-3** Procedure for the fabrication of SFMA. Injectable SFMA cryogel by using TEMED and APS as an initiator system at  $-20^{\circ}\text{C}$  for 16-18h

### 6.4.3 Physical Characterization of SFMA-based Cryogels

Mechanical properties of developed cryogels were tested and the compression modulus of the cryogels were then calculated. Ten successive compression cycles were performed on each cryogel ( $n=5$ ), and modulus was calculated on the 8<sup>th</sup> cycle (**Figure 6-4**). Compression modulus of the SFMA cryogel is 5.4kPa. Addition of 1% NMS (SFMA+1% NMS) resulted in a statistically significant increase in compression modulus to 6.4kPa. However, the addition of MPA slightly decreased the modulus to 4.7kPa. There is no significant modulus difference observed between SFMA and SFMA+0.5% NMS (modulus 5.5kPa). Thus, the overall modulus of SFMA cryogels falls within 5-7kPa.

The cryogels were also found to exhibit excellent shape memory properties. The cryogels could be completely compressed to >99% strain and also showed

excellent recovery after removal of compressive load. This recovery of the cryogels has been shown in Figure B, C, D E. Although the cryogels exhibit a hysteresis between loading and unloading cycle, no significant change in loading and unloading cycle was observed for 10 different cycles. This excellent elastic recovery of cryogel was further studied for 100 cycles. In the video [attached here](#), it can be observed that SFMA is compressed for more than 100 cycles without any visible mechanical damages, depicting the superior physical properties of SFMA-based cryogels for injectable BTE applications.



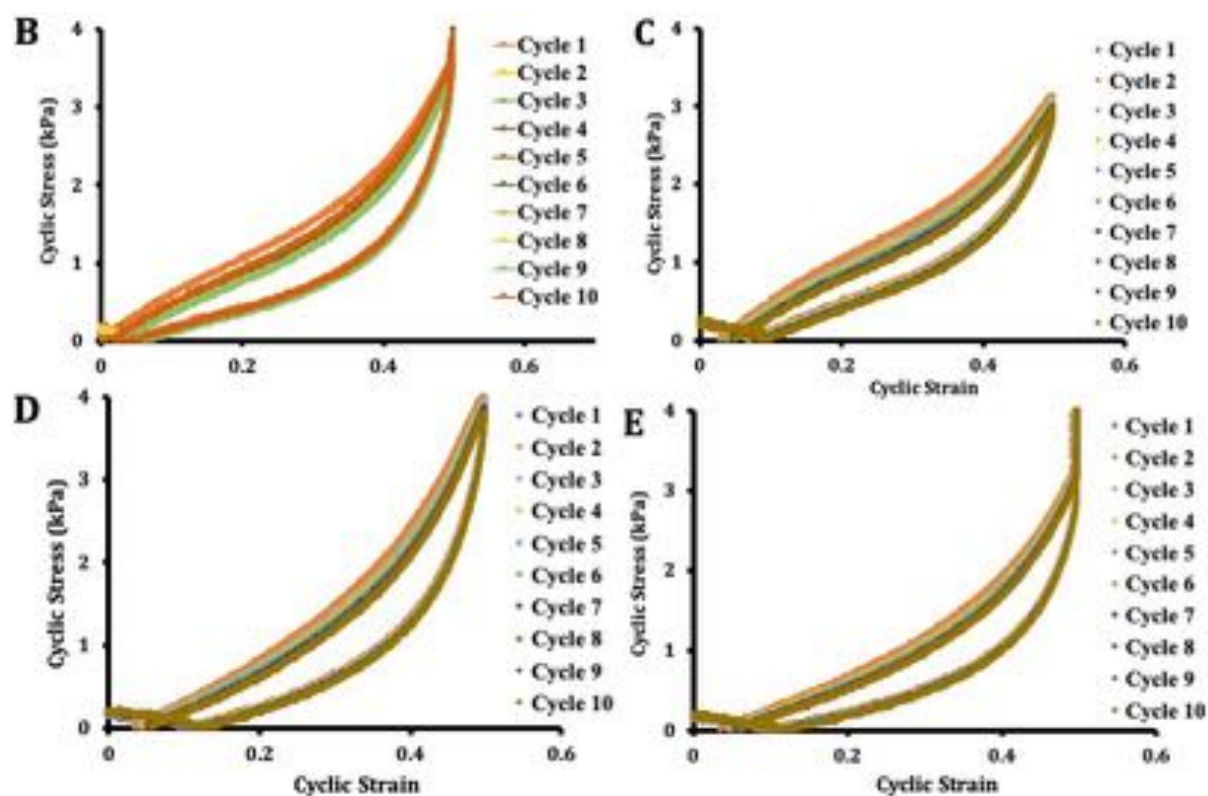


**Figure 6-4** Mechanical characterization of SFMA-based cryogels: A) Comparative compression modulus of SFMA Cryogels. B) 10 compressive cycles of SFMA. C) 10 compressive cycles of SFMA + 0.5% NMS. D) 10 compressive cycles of SFMA + 1% NMS. E) 10 compressive cycles of SFMA + 0.5% MPA. Values represent mean and SD ( $n = 5$ ). Data were analysed using two-way analysis of variance (ANOVA) ( $* p < 0.05$ )

Cryogels, which were developed from rhodamine labelled SF, were used to visualise the polymer wall structure visible in **Figure 6-5A**. Average pore size of cryogels were in the range of 45 – 55 $\mu\text{m}$  and is shown in **Figure 6-5B**. Higher pore size was observed in SFMA with 0.5% MPA cryogel. All cryogels showed  $\sim 70\%$  well-interconnected porosity (**Figure 6-5C**). As shown in **Figure 6-5D**, the highest swelling ratio ( $Q_M$  21-22) was observed with SFMA and SFMA+0.5% MPA, which showed a slight decrease after addition of NMS.

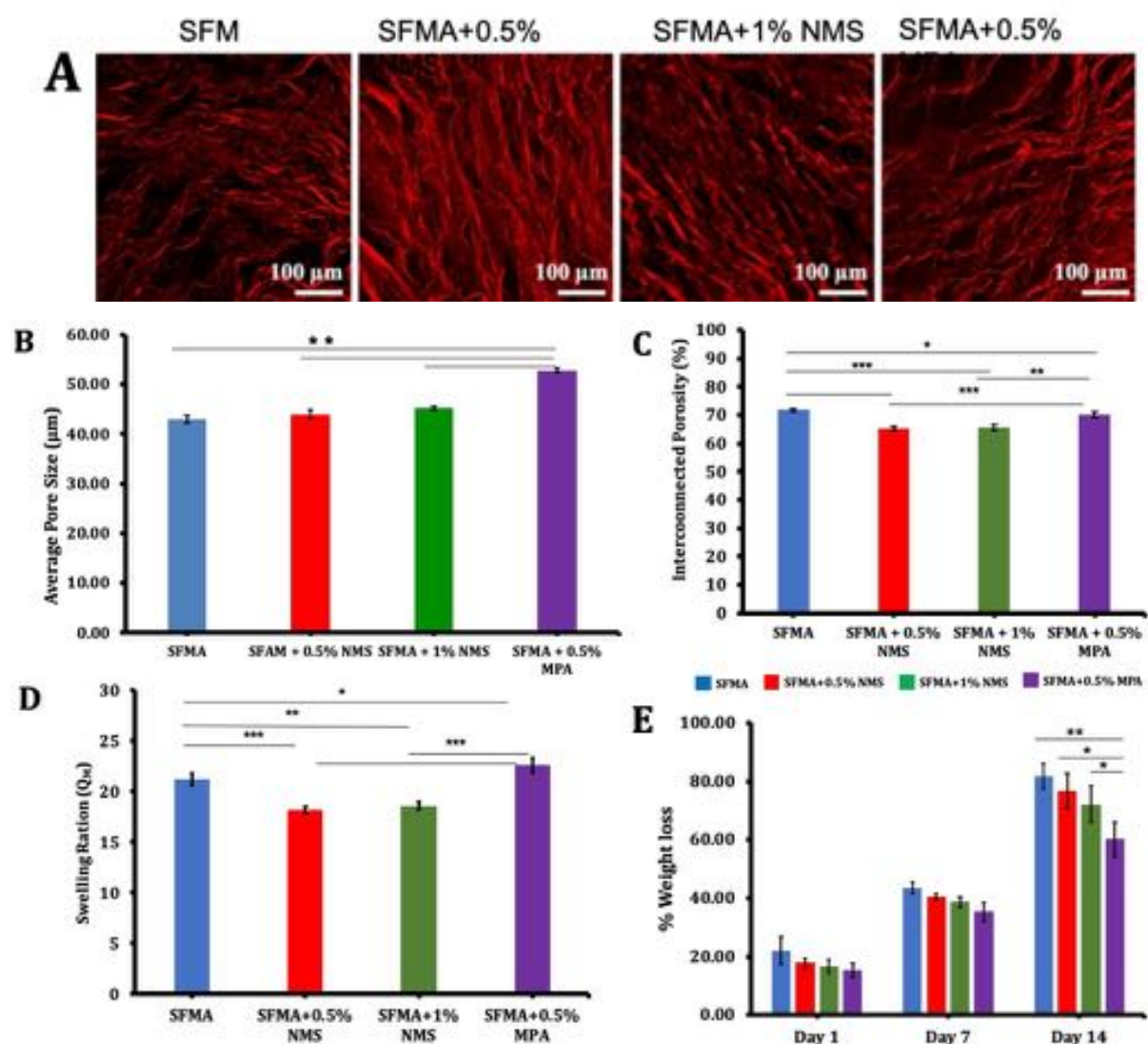


**Figure 6-5** Physical characterization of SFMA cryogels: A) Cryogel polymer wall staining B) Average pore size C) Pore interconnectivity D) Swelling Ratio E) *in-vitro* enzymatic degradation of cryogels. Values represent mean and SD ( $n = 5$ ). Data were analysed using one-way/two-way analysis of variance (ANOVA) (\*  $p < 0.05$ )

The blending of NMS/MPA also affects the *in-vitro* degradation profile (**Figure 6-5E**). Enhanced weight loss (~80%) was observed at day 14 with SFMA cryogel. Microfiber of non-mulberry silk has higher alanine content that provides a more crystalline structure that helps in delayed degradation of SFMA. The slowest



weight loss was observed with SFMA+0.5% MPA, which would be contributed by PEG polymer's physical and chemical properties.

#### 6.4.4 *In-vitro* cell adhesion efficiency

Cell adhesive efficiency of cryogels were tested by Alamar blue assay and results are depicted in the **Figure 6-6**. More than 70% cells were able to adhere to all cryogels. Also, significantly higher number of cells were found to be attached to SFMA containing 1% NMS and 0.5% APR.

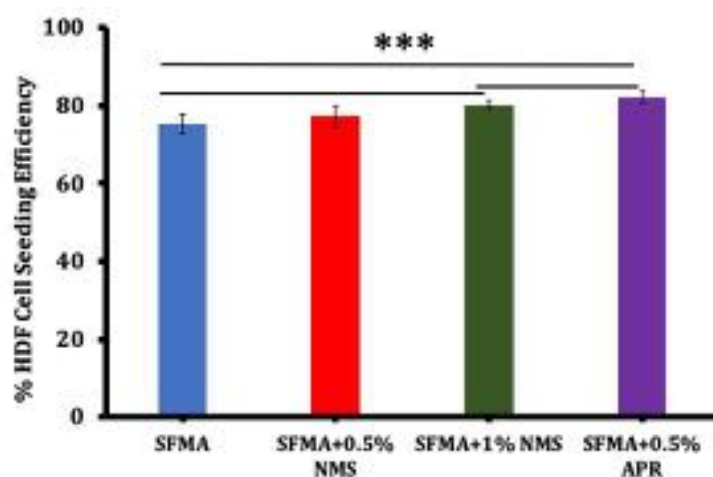


**Figure 6-6** Cell seeding efficiency of cryogels: HDF cells adhere to cryogels after 24h. Values represent mean and SD ( $n = 5$ ). Data were analyzed using one-way/two-way analysis of variance (ANOVA) ( $* p < 0.05$ )

#### 6.4.5 *In-vitro* HDF cell viability and cytoskeleton staining

Cell viability is a prerequisite for TE application, and therefore, HDF cell viability was evaluated using Alamar blue assay. HDF cells were seeded on the cryogels, and the fraction of viable cells were assessed on day 1 and 3. **Figure 6-7A** shows

~80% cell viability for all cryogels and hence confirms the non-cytotoxic behaviour of all the developed cryogels. **Figure 6-7B** suggests that cells are growing homogeneously across all SFMA-based cryogels from day 1 to 3. However, more cells in elongated morphology are observed in NMS- and RGD-containing SFMA-based cryogels. This result agrees with previous reports, where intrinsic RGD sequence within non-mulberry silk has shown to promote cell attachment and proliferation.

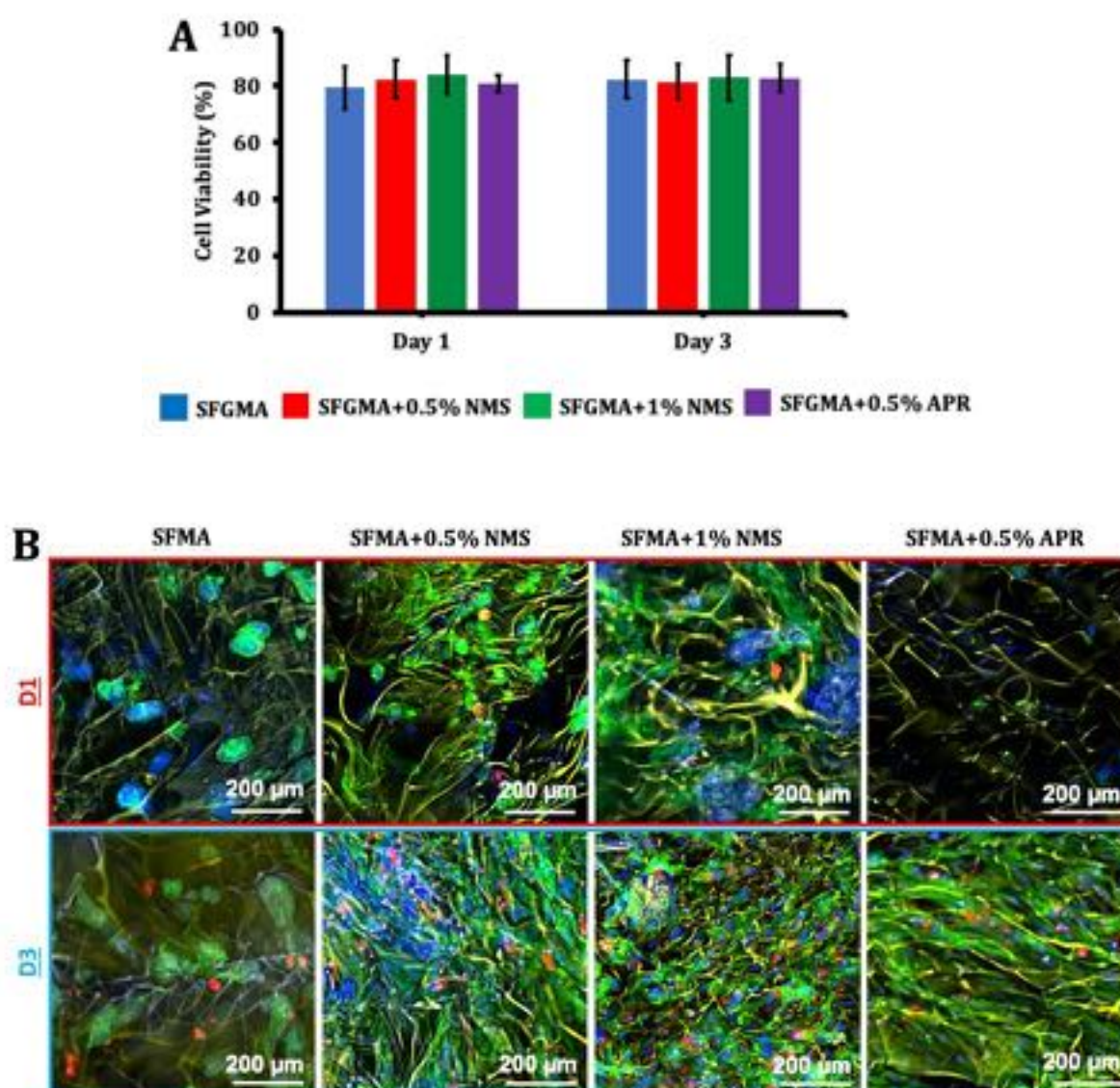


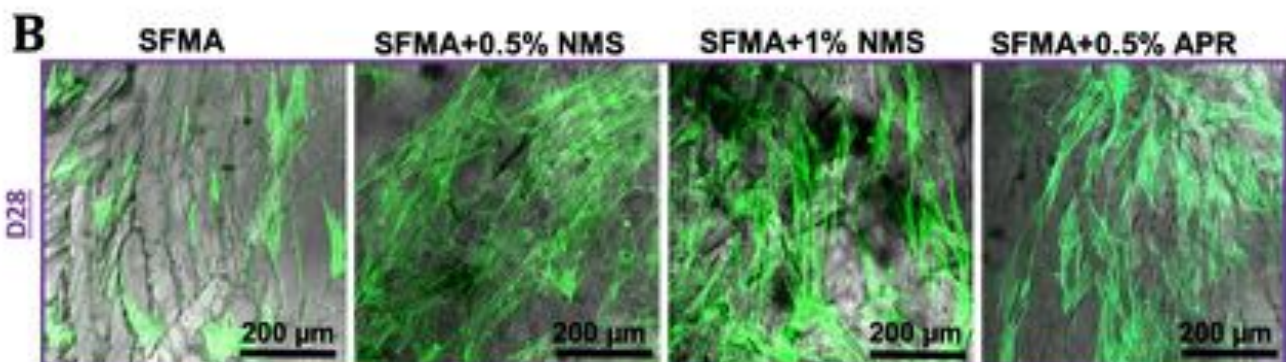
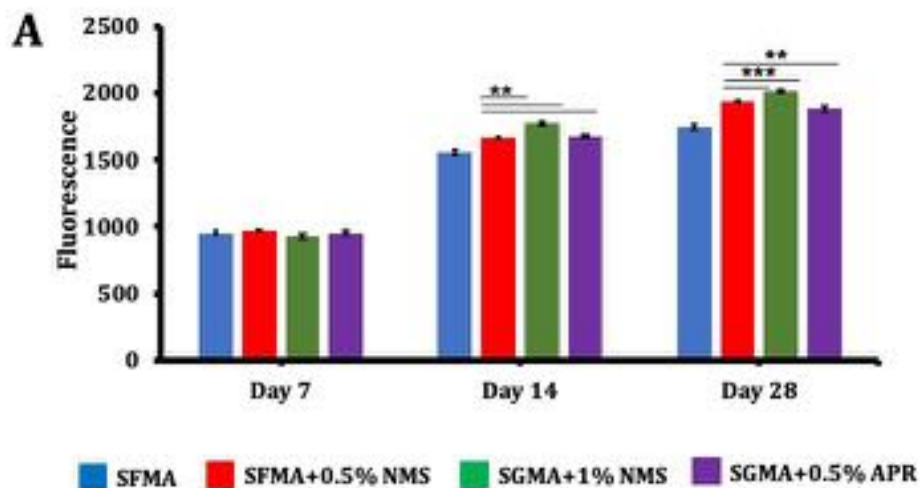
**Figure 6-7** (A) Viability of HDFn on the cryogels after day 1 and 3 incubation period. B) Confocal images of HDFn cells cultured on cryogels. The polymer walls of cryogels are



labelled with Rhodamine (red), cell nuclei with DAPI (blue), dead cells with far-red fixable dead cell staining (yellow), and cytoskeleton with Alexa Fluor 488-phalloidin (green). All cryogels were fabricated at  $-20\text{ }^{\circ}\text{C}$  and values represent mean and SD ( $n = 5$ ).

### 6.4.6 hMSCs proliferation assay and cytoskeleton staining

hMSCs proliferation was analyzed using an Alamar blue assay. The cells were seeded on cryogels and the cell growth was assessed on day 7, 14 and 28. From the results, no significant difference was observed between the group of cryogels on 7d.



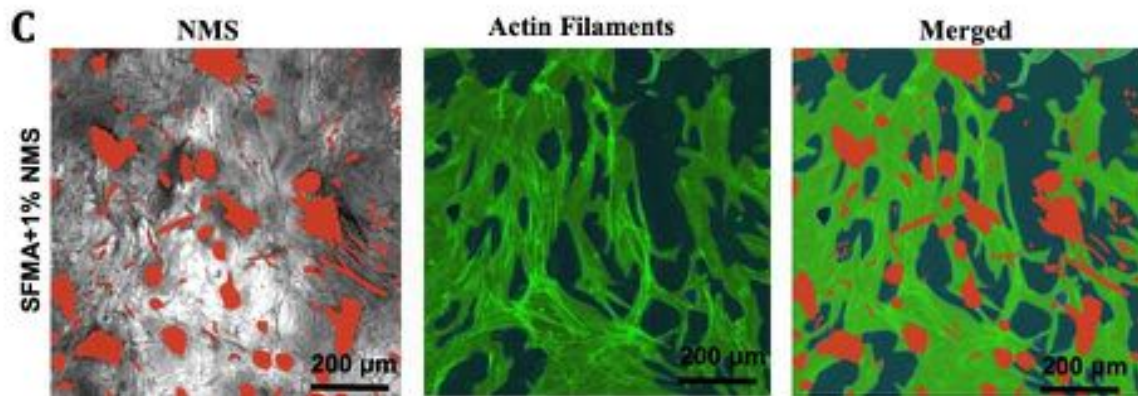


**Figure 6-8** *In-vitro* hMSCs human mesenchymal stem cells grown in complete growth media: (A) Alamar blue assay at day 7, 14 and 28 on cryogels seeded with hMSCs. B) Confocal images of actin cytoskeleton - stained with Alexa Fluor 488-phalloidin (green). C) SFMA+1% NMS cryogel was artificially coloured in red while actin filaments appeared in green.

Cells grew in all cryogels with time and on day 28<sup>th</sup>, a statistically significant number of cells were observed in SFMA cryogels containing NMS/APR than the SFMA cryogel. These results suggest that the cell attachment and proliferation ability of silk can be improved by providing cell anchoring moieties such as the RGD motif.

F-actin cytoskeleton staining further provides insight, visualized with Alexa Fluor 488 phalloidin, and fluorescence images were captured at day 28 (**Figure 6-8B**). Well expanded cells are seen on all types of cryogel. However, more cells were observed with SFMA cryogels containing NMS/APR than the only SFMA cryogel. Interestingly, we also observed that cells form a network along with the polymer wall direction in SFMA cryogels. This network can be visualized in **Figure 6-8B**. Also in some cases it was found that cells formed a bridge in SFMA+NMS cryogels, wherever NMS fibre groups were present, which is depicted in **Figure 6-8C**.

#### 6.4.7 hMSCs differentiation into osteogenic lineage

Cryogels' potential to differentiate hMSCs into osteogenic lineage was monitored by measuring osteogenic markers from early to late stage of cell differentiation. As hMSCs start to become osteogenic lineage, up-regulation of genes results in the expression of specific markers. In the present study, the spent media from *in-vitro* cell culture experiments was collected at different time points and analyzed for the presence of specific osteogenic markers. An early-to-mid stage osteogenic marker alkaline phosphatase (ALP) was normalized with the total protein content of the cells and presented in **Figure 6-8A**. It was observed that the ALP secretion significantly increased in all cryogels as the experiment progressed over time (7<sup>th</sup>-28<sup>th</sup> day). ALP activity observed in SFMA and SFMA+0.5% NMS cryogels were similar while SFMA+1% NMS and SFMA+APR potential to differentiate hMSCs to osteoblasts were identical; however, it was significantly higher than SFMA and SFMA+0.5%NMS cryogels. Therefore, enhanced osteogenic potential can be achieved with 1%NMS/0.5% APR incorporation in SFMA cryogels.

**Figure 6-8B** depicts the expression of OCN, a late marker of the osteogenic differentiation process. In contrast, **Figure 6-8C** depict the expression of the BMP2 marker. This crucial factor plays a vital role throughout the new bone development process and is also responsible for the directional differentiation of hMSCs. A similar trend to the ALP result was also observed for both OCN and BMP-2; significantly enhanced expression of OCN and BMP-2 were observed with 1%NMS/0.5% APR incorporated SFMA than the only SFMA or with 0.5% NMS cryogels.

The development of new bone tissue is reflected in forming a mineralized matrix. Alizarin red S staining represented the calcium deposition (**Figure 6-8E**). The Alizarin stained calcium deposition was extracted using acetic acid, and the data is presented in **Figure 6-8D**. More calcium deposition was observed with SFMA cryogels with 1%NMS/0.5% APR than the only SFMA or 0.5% NMS cryogels.

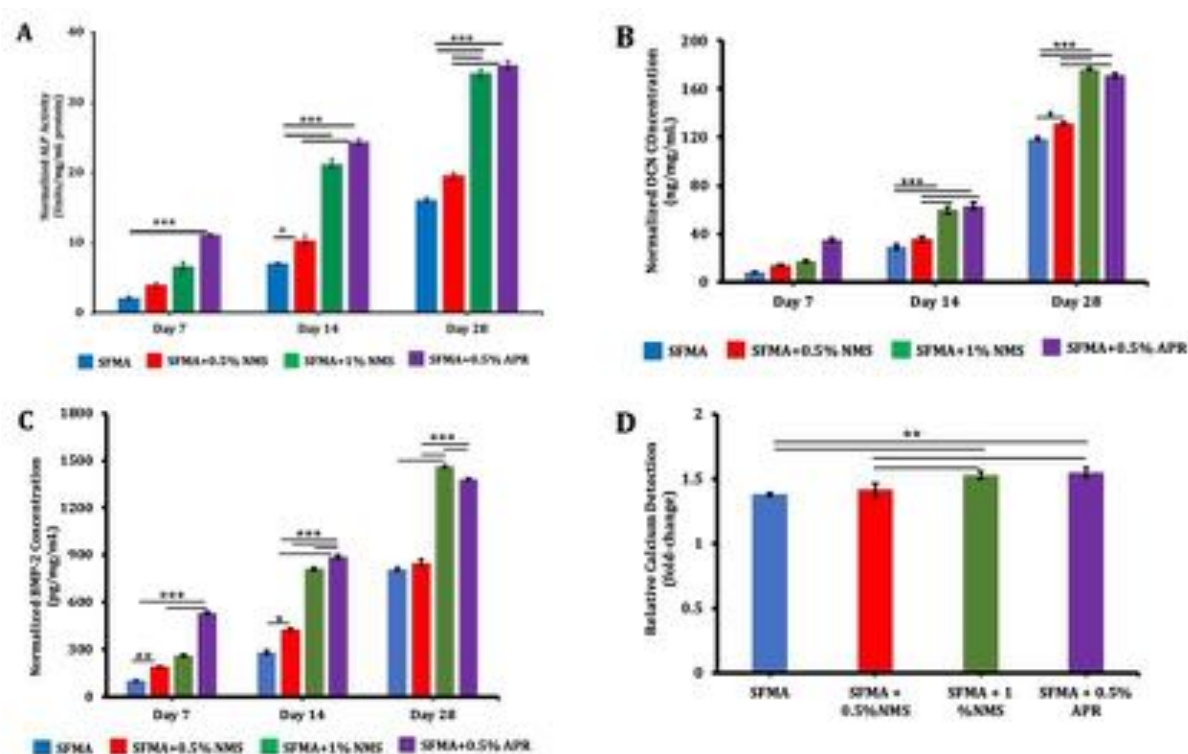
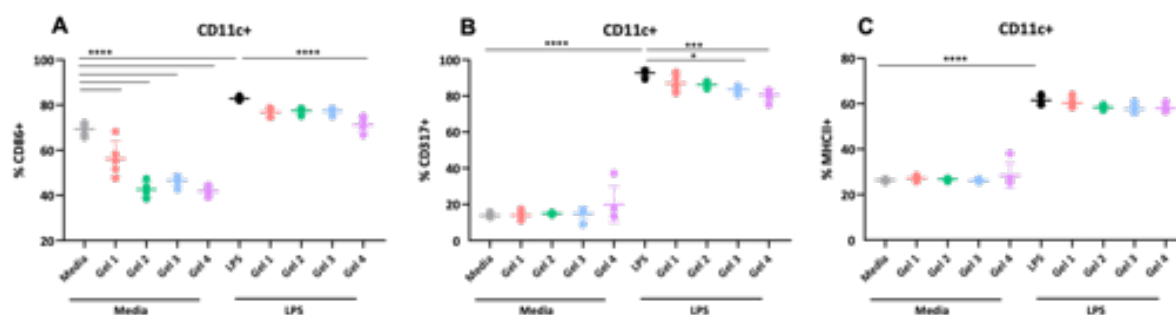


**Figure 6-9** Osteogenic potential by estimating expression of alkaline phosphatase (ALP) activity, Osteocalcin levels (OCN), bone morphogenic protein-2 (BMP-2) and Calcium extraction: A) ALP activity was normalized with the total protein loaded and expressed as Units/mg/mL of protein B) Expression of osteocalcin estimated by ELISA. OCN level was normalized with the total protein loaded and expressed as ng/mg/mL of protein C) BMP-2 expression was estimated using ELISA. BMP-2 activity was normalized with the total protein loaded and expressed as pg/mg/mL of protein D) Quantification of calcium deposition: calcium deposition by alizarin red S staining, which was extracted at the end of 28 day. Values represent mean, and SD ( $n = 5$ ), and data were analyzed using ANOVA ( $* p < 0.05$ ).

#### 6.4.8 *In-vitro* bone marrow-derived dendritic cells (BMDCs) activation assay

BMDCs play a critical role in priming adaptive immune responses. They are known to secrete various proinflammatory cytokines upon maturation and present different activation markers as a function of immune responses. BMDCs were analyzed to evaluate the immunogenicity of the developed SFMA, SFMA+0.5%NMS, SFMA+1%NMS and SFMA+0.5% APR cryogels *in-vitro*.



After a 24h culture with the cryogels, the fraction of activated CD11c+CD86+ CD11c+CD317+ and CD11c+MHCII+ BMDCs were detected by immunostaining in conjunction with flow cytometry. This assay includes the negative control (media alone) and positive control (LPS) along with cryogels (**Figure 6-9**). From the data, it has been proved that all the developed formulations of SFMA cryogels did not activate BMDCs *in-vitro* but downregulated CD86 expression. All the developed formulations of SFMA cryogels seem to have an anti-inflammatory effect on LPS treated BMDCs as observed by downregulation of activation markers such as CD80, CD86, and CD317. However, the addition of NMS and APR seems to slightly increase the downregulation of activation markers compared to SFMA gels alone, thereby demonstrating a more pronounced anti-inflammatory activity.

### 6.4.9 *In-vivo* biocompatibility assessment

Finally, the immunological response of the SFMA and its combination cryogels were examined in a mouse model. SFMA, SFMA+1%NMS and SFMA+0.5% APR cryogels were subcutaneously injected into the backs of C57BL/6 mice. Further, the cryogels were explanted on day 3 and 28 subsequently stained with hematoxylin and eosin (H&E) (**Figure 6-11A**) and Masson's trichrome (MT) stain for histological analysis (**Figure 6-11B**). We assessed the cellular infiltration into



cryogels as well as their integration within the surrounding tissues. Overall, across the three silk-based cryogels tested, cryogels were surrounded by a thin capsule of fibrin and induced a minimal infiltration of leukocytes (e.g., neutrophils and macrophages). It is worth noting that the cellular infiltration was slightly more observable at the periphery of the cryogels with nearly no cells at the core. Consistent with their high degree of cytocompatibility and minimal *in-vitro* DC activation, these silk-based cryogels indicate minimal host inflammatory responses in mice.

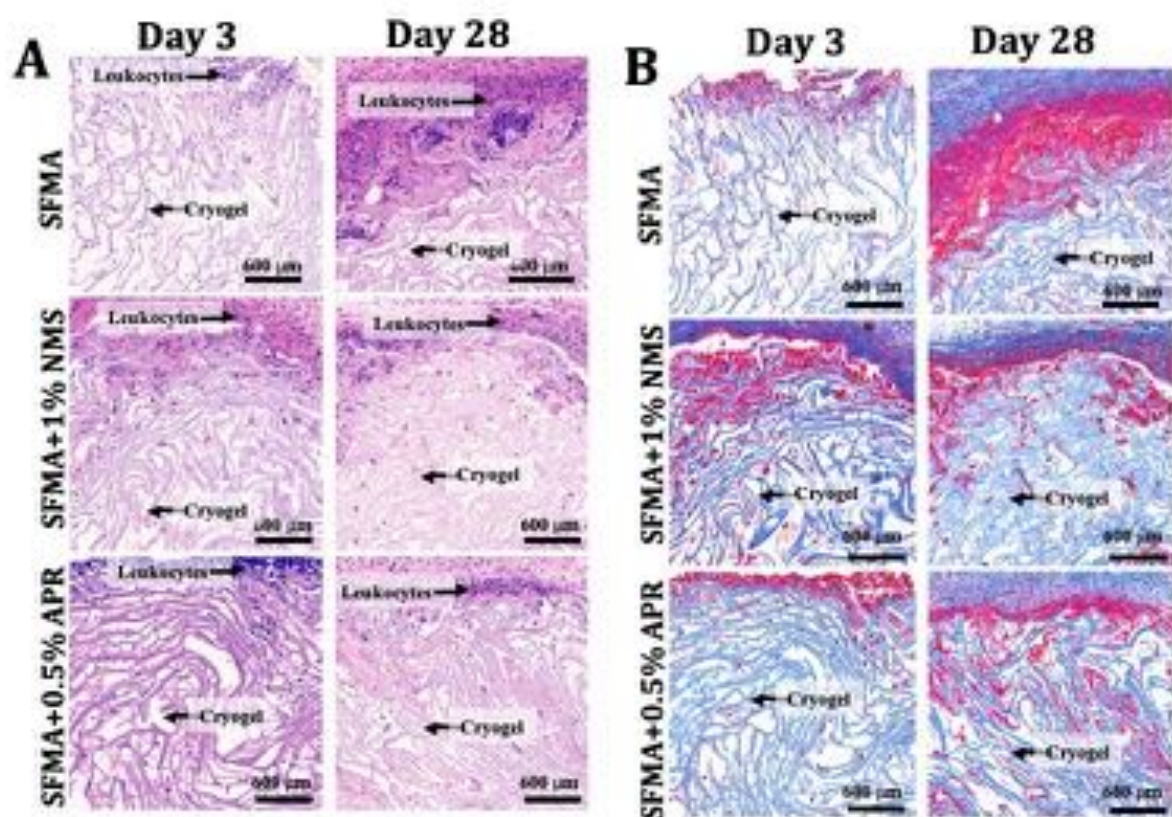


**Figure 6-11** *In-vivo* biocompatibility assessment. H&E staining of SFMA cryogel (dimension: 4mm x 4mm x 1mm) scaffold sections explanted on day 3 and 28 following subcutaneous injections in the dorsal flanks of C57BL/6 mice: (A) H&E staining highlights the macroporous polymeric network of cryogels, infiltrated leukocytes (dark blue dots), fibrin formation (purple), and surrounding tissues (cryogel-free) (B) Masson's trichrome staining. Images are representative of  $n = 5$  samples per condition.

## 6.5 Discussion

Bone is a 3D porous tissue with interconnected pores. Successful bone tissue regeneration depends on a 3D scaffold system with optimum porosity with interconnected pores that can pass nutrition and help remove metabolic waste. The scaffold cannot work only to fill the damaged part in bone defects but is also compatible with the ECM of the host tissue. In addition, the scaffold must be biodegradable at an appropriate rate within the host tissue with minimum immune response. An injectable cryogel – shape-memory scaffold with interconnected porosity would be the successful form of modern bone tissue engineering application suitable for multisite bone fracture, bone cracks, a craniofacial defect where open surgery can be avoided.

In this present report, we have developed first-time injectable cryogels for bone tissue regeneration application by using SF as a polymer. SF is a natural, biocompatible, FDA-approved, degradable polymer for bone tissue engineering. SF is hydrophobic in nature, and to enhance its processability SF has been methacrylated<sup>43,44</sup> for various TE applications for use in methods like 3D bioprinting etc.<sup>40</sup> A prerequisite for cryogel formation is aqueous solution preparation and to accommodate hydrophilicity, SF was induced by methacrylation reaction by using GMA. SFMA was characterized to confirm the incorporation of methyl groups in SF that significantly lower the beta-sheets content in the SF (**Figure 6-2D**). This chemical modification in SF contributed to reducing the viscosity of SF significantly (**Figure 6-2E**). The shape memory is the most critical parameter of the cryogel. To achieve it, different concentrations like 4%, 8% and 12% of SFMA cryogels were prepared and tested for its injectability as per Video 1, 2 and 3 respectively. Injectability videos were available on this [link](#). Based on the observations, 4% SFMA cryogel has a good swelling ratio and

interconnected porosity; however, it is unable to swell and take its original shape after injecting. This is because methacrylation of SF results in the reduction of the beta-sheet in SF.

On the other hand, 12% SFMA cryogel is compact and its injection required considerable force to push with a syringe to pass through a needle, resulting in torn cryogel after injection. 8% SFMA cryogel fulfilled all the required properties and was used in a subsequent study. Non-mulberry silk (NMS) is known for its inherent mechanical strength because of its higher alanine content and specifically, NMS from *A. mylitta* possesses a natural RGD peptide sequence, which helps cells to adhere and proliferate. Synthetic RGD peptide coupled with PEG polymer was used as a control to evaluate NMS performance. Based on injectability criteria, 8% SFMA, 8% SFMA+0.5% NMS, 8% SFMA+1% NMS and 8%SFMA+0.5% MPA/APR were selected for these studies, where MPA is used for chemical/physical characterization while APR for biological assays.

SF itself is a mechanically robust polymer. However, methacrylation induced hydrophilicity lowered the beta-sheets required to make SF cryogels injectable. The aqueous processability of NMS is a pretty challenging task because of more crystallinity in its structure.<sup>21</sup> Hence, most TE application with NMS uses its aqueous form directly extracted from the silk worm's larval stage from the silk gland. Here, we tried to take advantage of fiber reinforcement strategy, and hence cryomilled powder of NMS was mixed in SFMA to make combination cryogels. High young's modulus in SFMA with 1% NMS confirmed reinforcement strategy. After ten cycles of compression, we observed that cryogels recovered back to their original shape (**Figure 6-4**) without any deformation, which inspired us to evaluate its compressive property by increasing the number of compression cycles. Though SFMA cryogels modulus is in the kPa range, it has excellent elasticity, making it a more appropriate candidate for BTE as it can withstand



multiple bending within the bone. Larger cryogels could be injected through a catheter for large bone defects. Also, several small cryogels could be injected all at once via a syringe. The addition of NMS further helped lower the proteolytic degradation of SFMA that provided options to clinicians to tune biomaterial's degradation rate as per the physical/clinical scenario.

The addition of NMS and APR have a significant impact on the biological performance of SFMA cryogel. HDF cells are more attached on SFMA+1% NMS and SFMA+0.5% APR cryogels after 24h (**Figure 6-6**), and more viable, elongated HDFn cells (**Figure 6-7**) further confirm the RGD help in cell behaviour which is in line with published reports.<sup>45</sup> The use of hMSCs with a scaffold system has been proven an impactful model to study TE/BTE applications.<sup>46-49</sup> The effect of NMS and APR was also reflected in osteogenesis, where SFMA cryogels in BTE were further enhanced with it. In addition, all cryogels did not activate BMDCs in *in-vitro*, however, the addition of NMS and APR shows an anti-inflammatory effect. Kaplan et al. showed non-inflammatory behaviour of conventional hydrogel upon subcutaneous injection in mice model and in a similar line SF based cryogels reported in this study also induce minimal immune cells infiltration upon injection in mice making it biocompatible biomaterial.

## 6.6 Conclusions

This study successfully fabricated cryogels from mulberry silk fibroin (SFMA) that is injectable with a hypodermic 16-gauge needle. Additionally, we obtained an exciting and promising outcome of this study by developing highly compressible cryogels, which are biodegradable. Combining mulberry silk and non-mulberry silk fibroin enhances the physical and mechanical properties of SFMA cryogels and significantly improves its osteogenic potential *in-vitro*. A critical aspect of a

biomaterial is the inflammatory reaction. The combination cryogels activate the BMDCs, showing an anti-inflammatory effect with non-mulberry silk. Further biocompatibility was supported by an *in-vivo* study in the mice model. In conclusion, all the data make the silk fibroin based injectable cryogels a potential biomaterial for osteoregenerative application.

## 6.7 References

- (1) Vidal, L.; Kampleitner, C.; Brennan, M.; Hoornaert, A.; Layrolle, P. Reconstruction of Large Skeletal Defects: Current Clinical Therapeutic Strategies and Future Directions Using 3D Printing. *Front. Bioeng. Biotechnol.* **2020**, *8* (February). <https://doi.org/10.3389/fbioe.2020.00061>.
- (2) Henkel, J.; Woodruff, M. A.; Epari, D. R.; Steck, R.; Glatt, V.; Dickinson, I. C.; Choong, F. M.; Schuetz, M. A.; Hutmacher, D. W. Bone Regeneration Based on Tissue Engineering Conceptions – A 21st Century Perspective. **2013**, 216–248. <https://doi.org/10.4248/BR201303002>.
- (3) Wu, A.-M.; Bisignano, C.; James, S. L.; Abady, G. G.; Abedi, A.; Abu-Gharbieh, E.; Alhassan, R. K.; Alipour, V.; Arabloo, J.; Asaad, M.; Asmare, W. N.; Awedew, A. F.; Banach, M.; Banerjee, S. K.; Bijani, A.; Birhanu, T. T. M.; Bolla, S. R.; Cámara, L. A.; Chang, J.-C.; Cho, D. Y.; Chung, M. T.; Couto, R. A. S.; Dai, X.; Dandona, L.; Dandona, R.; Farzadfar, F.; Filip, I.; Fischer, F.; Fomenkov, A. A.; Gill, T. K.; Gupta, B.; Haagsma, J. A.; Haj-Mirzaian, A.; Hamidi, S.; Hay, S. I.; Ilic, I. M.; Ilic, M. D.; Ivers, R. Q.; Jürisson, M.; Kalhor, R.; Kanchan, T.; Kavetsky, T.; Khalilov, R.; Khan, E. A.; Khan, M.; Kneib, C. J.; Krishnamoorthy, V.; Kumar, G. A.; Kumar, N.; Lalloo, R.; Lasrado, S.; Lim, S. S.; Liu, Z.; Manafi, A.; Manafi, N.; Menezes, R. G.; Meretoja, T. J.; Miazgowski, B.; Miller, T. R.; Mohammad, Y.; Mohammadian-Hafshejani, A.; Mokdad, A. H.; Murray, C. J. L.; Naderi, M.;

- Naimzada, M. D.; Nayak, V. C.; Nguyen, C. T.; Nikbakhsh, R.; Olagunju, A. T.; Otstavnov, N.; Otstavnov, S. S.; Padubidri, J. R.; Pereira, J.; Pham, H. Q.; Pinheiro, M.; Polinder, S.; Pourchamani, H.; Rabiee, N.; Radfar, A.; Rahman, M. H. U.; Rawaf, D. L.; Rawaf, S.; Saeb, M. R.; Samy, A. M.; Sanchez Riera, L.; Schwebel, D. C.; Shahabi, S.; Shaikh, M. A.; Soheili, A.; Tabarés-Seisdedos, R.; Tovani-Palone, M. R.; Tran, B. X.; Travillian, R. S.; Valdez, P. R.; Vasankari, T. J.; Velazquez, D. Z.; Venketasubramanian, N.; Vu, G. T.; Zhang, Z.-J.; Vos, T. Global, Regional, and National Burden of Bone Fractures in 204 Countries and Territories, 1990–2019: A Systematic Analysis from the Global Burden of Disease Study 2019. *Lancet Heal. Longev.* **2021**, *2* (9), e580–e592. [https://doi.org/10.1016/s2666-7568\(21\)00172-0](https://doi.org/10.1016/s2666-7568(21)00172-0).
- (4) Willems, N. M. B. K.; Langenbach, G. E. J.; Everts, V.; Zentner, A. The Microstructural and Biomechanical Development of the Condylar Bone: A Review. *Eur. J. Orthod.* **2014**, *36* (4), 479–485. <https://doi.org/10.1093/ejo/cjt093>.
- (5) Hao, Z.; Song, Z.; Huang, J.; Huang, K.; Panetta, A.; Gu, Z.; Wu, J. The Scaffold Microenvironment for Stem Cell Based Bone Tissue Engineering. *Biomater. Sci.* **2017**, *5* (8), 1382–1392. <https://doi.org/10.1039/c7bm00146k>.
- (6) Nikolova, M. P.; Chavali, M. S. Recent Advances in Biomaterials for 3D Scaffolds: A Review. *Bioact. Mater.* **2019**, *4* (August), 271–292. <https://doi.org/10.1016/j.bioactmat.2019.10.005>.
- (7) Mödinger, Y.; Teixeira, G. Q.; Neidlinger-Wilke, C.; Ignatius, A. Role of the Complement System in the Response to Orthopedic Biomaterials. *Int. J. Mol. Sci.* **2018**, *19* (11). <https://doi.org/10.3390/ijms19113367>.
- (8) Zeeshan Sheikh, Shariq Najeeb, Zohaib Khurshid, Vivek Verma, H. R. and M. G. Biodegradable Materials for Bone Repair and Tissue Engineering Applications. **2015**, 5744–5794. <https://doi.org/10.3390/ma8095273>.

- (9) Qu, H.; Fu, H.; Han, Z.; Sun, Y. Biomaterials for Bone Tissue Engineering Scaffolds: A Review. *RSC Adv.* **2019**, *9* (45), 26252–26262. <https://doi.org/10.1039/c9ra05214c>.
- (10) Koons, G. L.; Diba, M.; Mikos, A. G. Materials Design for Bone-Tissue Engineering. *Nat. Rev. Mater.* **2020**, *5* (8), 584–603. <https://doi.org/10.1038/s41578-020-0204-2>.
- (11) Zhou, H.; Liang, C.; Wei, Z.; Bai, Y.; Bhaduri, S. B.; Webster, T. J.; Bian, L.; Yang, L. Injectable Biomaterials for Translational Medicine. *Mater. Today* **2019**, *28* (September), 81–97. <https://doi.org/10.1016/j.mattod.2019.04.020>.
- (12) Peter, S. J.; Kim, P.; Yasko, A. W.; Yaszemski, M. J.; Mikos, A. G. Crosslinking Characteristics of an Injectable Poly ( Propylene Fumarate )/ <sup>h</sup> -Tricalcium Phosphate Paste and Mechanical Properties of the Crosslinked Composite for Use as a Biodegradable Bone Cement. **1998**.
- (13) Liu, M.; Zeng, X.; Ma, C.; Yi, H.; Ali, Z.; Mou, X.; Li, S.; Deng, Y.; He, N. Injectable Hydrogels for Cartilage and Bone Tissue Engineering. **2017**, No. November 2016. <https://doi.org/10.1038/boneres.2017.14>.
- (14) Bandyopadhyay, A.; Chowdhury, S. K.; Dey, S.; Moses, J. C.; Mandal, B. B. Silk : A Promising Biomaterial Opening New Vistas REVIEW. *J. Indian Inst. Sci.* **2019**, *99* (3), 445–487. <https://doi.org/10.1007/s41745-019-00114-y>.
- (15) Kochhar, D.; Debari, M. K.; Abbott, R. D.; Abbott, R. D. The Materiobiology of Silk : Exploring the Biophysical Influence of Silk Biomaterials on Directing Cellular Behaviors. **2021**, *9* (June), 1–11. <https://doi.org/10.3389/fbioe.2021.697981>.
- (16) Midha, S.; Murab, S.; Ghosh, S. Osteogenic Signaling on Silk-Based Matrices. *Biomaterials* **2016**, *97*, 133–153. <https://doi.org/10.1016/j.biomaterials.2016.04.020>.

- (17) Ribeiro, V. P.; Pina, S.; Costa, J. B.; Cengiz, I. F.; García-Fernández, L.; Fernández-Gutiérrez, M. D. M.; Paiva, O. C.; Oliveira, A. L.; San-Román, J.; Oliveira, J. M.; Reis, R. L. Enzymatically Cross-Linked Silk Fibroin-Based Hierarchical Scaffolds for Osteochondral Regeneration. *ACS Appl. Mater. Interfaces* **2019**, *11* (4), 3781–3799. <https://doi.org/10.1021/acsami.8b21259>.
- (18) Deshpande, R.; Shukla, S.; Kale, A.; Deshmukh, N.; Nisal, A.; Venugopalan, P. Silk Fibroin Microparticle Scaffold for Use in Bone Void Filling: Safety and Efficacy Studies. *ACS Biomater. Sci. Eng.* **2022**, *8* (3), 1226–1238. <https://doi.org/10.1021/acsbiomaterials.1c01103>.
- (19) Parekh, N.; Hushye, C.; Warunkar, S.; Gupta, S. Sen; Nisal, A. RSC Advances In Vitro Study of Novel Microparticle Based Silk. *RSC Adv.* **2017**, *7*, 26551–26558. <https://doi.org/10.1039/C7RA03288A>.
- (20) Parekh, N. A.; Deshpande, R. V.; Shukla, S. G.; Nisal, A. A. Silk Fibroin 3D Microparticle Scaffolds with Bioactive Ceramics: Chemical, Mechanical, and Osteoregenerative Characteristics. *Adv. Eng. Mater.* **2020**, *2000458*, 1–11. <https://doi.org/10.1002/adem.202000458>.
- (21) Guo, C.; Zhang, J.; Jordan, J. S.; Wang, X.; Henning, R. W.; Yarger, J. L. Structural Comparison of Various Silkworm Silks: An Insight into the Structure-Property Relationship Structural Comparison of Various Silkworm Silks : An Insight into the Structure-Property Relationship. **2018**. <https://doi.org/10.1021/acs.biomac.7b01687>.
- (22) Murphy, A. R.; Kaplan, D. L. Biomedical Applications of Chemically-Modified Silk Fibroin. *J. Mater. Chem.* **2009**, *19* (36), 6443–6450. <https://doi.org/10.1039/b905802h>.
- (23) Collins, A. M.; Skaer, N. J. V; Gheysens, T.; Knight, D.; Bertram, C.; Roach, H. I.; Oreffo, R. O. C.; Von-Aulock, S.; Baris, T.; Skinner, J.; Mann, S. Bone-like

- Resorbable Silk-Based Scaffolds for Load-Bearing Osteoregenerative Applications. *Adv. Mater.* **2009**, *21* (1), 75–78. <https://doi.org/10.1002/adma.200802239>.
- (24) Roohaniesfahani, I.; Wang, J.; No, Y. J.; de Candia, C.; Miao, X.; Lu, Z.; Shi, J.; Kaplan, D. L.; Jiang, X.; Zreiqat, H. Modulatory Effect of Simultaneously Released Magnesium, Strontium, and Silicon Ions on Injectable Silk Hydrogels for Bone Regeneration. *Mater. Sci. Eng. C* **2019**, *94* (December 2017), 976–987. <https://doi.org/10.1016/j.msec.2018.10.053>.
- (25) Raia, N. R.; Partlow, B. P.; McGill, M.; Kimmerling, E. P.; Ghezzi, E.; Kaplan, D. L. Enzymatically Crosslinked Silk-Hyaluronic Acid Hydrogels. *Biomaterials* **2017**. <https://doi.org/10.1016/j.biomaterials.2017.03.046>.
- (26) Razavi, M.; Qiao, Y.; Thakor, A. S. Three-Dimensional Cryogels for Biomedical Applications. **2019**, No. August, 2736–2755. <https://doi.org/10.1002/jbm.a.36777>.
- (27) Memic, A.; Colombani, T.; Eggermont, L. J.; Rezaeeyazdi, M.; Steingold, J.; Rogers, Z. J.; Navare, K. J.; Mohammed, H. S. Latest Advances in Cryogel Technology for Biomedical Applications. **2019**, *1800114*, 1–45. <https://doi.org/10.1002/adtp.201800114>.
- (28) Hixon, K. R.; Lu, T.; Sell, S. A. Acta Biomaterialia Review Article A Comprehensive Review of Cryogels and Their Roles in Tissue Engineering Applications. *Acta Biomater.* **2017**, *62*, 29–41. <https://doi.org/10.1016/j.actbio.2017.08.033>.
- (29) Eggermont, L. J.; Rogers, Z. J.; Bencherif, S. A.; Colombani, T.; Memic, A. Injectable Cryogels for Biomedical Applications. *Trends Biotechnol.* **2020**, *38* (4), 418–431. <https://doi.org/10.1016/j.tibtech.2019.09.008>.
- (30) Rezaeeyazdi, M.; Colombani, T.; Memic, A.; Bencherif, S. A. Injectable Hyaluronic Acid-Co-Gelatin Cryogels for Tissue-Engineering Applications.

- Materials (Basel)*. **2018**, *11* (8), 23–25.  
<https://doi.org/10.3390/ma11081374>.
- (31) Ak, F.; Oztoprak, Z.; Karakutuk, I.; Okay, O. Macroporous Silk Fibroin Cryogels. *Biomacromolecules* **2013**, *14* (3), 719–727.  
<https://doi.org/10.1021/bm3018033>.
- (32) Yetiskin, B.; Akinci, C.; Okay, O. Cryogelation within Cryogels : Silk Fibroin Scaffolds with Single-, Double- and Triple-Network Structures. *Polymer (Guildf)*. **2017**, *128*, 47–56. <https://doi.org/10.1016/j.polymer.2017.09.023>.
- (33) Yetiskin, B.; Okay, O. International Journal of Biological Macromolecules High-Strength and Self-Recoverable Silk Fibroin Cryogels with Anisotropic Swelling and Mechanical Properties. *Int. J. Biol. Macromol.* **2018**, No. xxxx.  
<https://doi.org/10.1016/j.ijbiomac.2018.09.087>.
- (34) Vishaka GV, Rathore MS, Chandrashekhraiah M, H. N. and S. R. Studies on Silk as a Suture in Medical Science Studies on Silk as a Suture in Medical Science. **2019**, No. September 2020.
- (35) Mao, Z.; Bi, X.; Ye, F.; Shu, X.; Sun, L.; Guan, J.; Ritchie, R. O.; Wu, S. Controlled Cryogelation and Catalytic Cross-Linking Yields Highly Elastic and Robust Silk Fibroin Scaffolds. **2020**.  
<https://doi.org/10.1021/acsbiomaterials.0c00752>.
- (36) Acharya, C.; Ghosh, S. K.; Kundu, S. C. Silk Fibroin Film from Non-Mulberry Tropical Tasar Silkworms: A Novel Substrate for in Vitro Fibroblast Culture. *Acta Biomater.* **2009**, *5* (1), 429–437.  
<https://doi.org/10.1016/j.actbio.2008.07.003>.
- (37) Andiappan, M.; Kumari, T.; Sundaramoorthy, S.; Meiyazhagan, G.; Manoharan, P.; Venkataraman, G. Comparison of Eri and Tasar Silk Fibroin Scaffolds for Biomedical Applications. *Prog. Biomater.* **2016**, *5* (2), 81–91.  
<https://doi.org/10.1007/s40204-016-0047-5>.

- (38) Behera, S.; Naskar, D.; Sapru, S.; Bhattacharjee, P.; Dey, T.; Ghosh, A. K.; Mandal, M.; Kundu, S. C. Hydroxyapatite Reinforced Inherent RGD Containing Silk Fibroin Composite Scaffolds: Promising Platform for Bone Tissue Engineering. *Nanomedicine Nanotechnology, Biol. Med.* **2017**, *13* (5), 1745–1759. <https://doi.org/10.1016/j.nano.2017.02.016>.
- (39) Nisal, A.; Sayyad, R.; Dhavale, P.; Khude, B.; Deshpande, R. Silk Fibroin Micro-Particle Scaffolds with Superior Compression Modulus and Slow Bioresorption for Effective Bone Regeneration. **2018**, No. April, 1–10. <https://doi.org/10.1038/s41598-018-25643-x>.
- (40) Kim, S. H.; Yeon, Y. K.; Lee, J. M.; Chao, J. R.; Lee, Y. J.; Seo, Y. B.; Sultan, T.; Lee, O. J.; Lee, J. S.; Yoon, S.; Hong, I.; Khang, G.; Lee, S. J.; Yoo, J. J.; Park, C. H. Precisely Printable and Biocompatible Silk Fibroin Bioink for Digital Light Processing 3D Printing. *Nat. Commun.* **2018**. <https://doi.org/10.1038/s41467-018-03759-y>.
- (41) Bencherif, S. A.; Sands, R. W.; Ali, O. A.; Li, W. A.; Lewin, S. A.; Braschler, T. M.; Shih, T.; Verbeke, C. S.; Bhatta, D.; Dranoff, G.; Mooney, D. J. Injectable Cryogel-Based Whole-Cell Cancer Vaccines. **2015**, No. May. <https://doi.org/10.1038/ncomms8556>.
- (42) Reis, A. V.; Fajardo, R.; Schuquel, I. T. A.; Guilherme, M. R.; Rubira, A. F.; Muniz, E. C. Reaction of Glycidyl Methacrylate at the Hydroxyl and Carboxylic Groups of Poly ( Vinyl Alcohol ) and Poly ( Acrylic Acid ): Is This Reaction Mechanism Still Unclear ? **2009**, 3750–3757.
- (43) Tsukada, M.; Yamamoto, T.; Nakabayashi, N. Grafting of Methyl Methacrylate onto Silk Fibers Initiated by Tri-n-Butylborane. *J. Appl. Polym. Sci.* **1991**, *43*, 2115–2121.
- (44) Taktak, F.; Ögen, Y. Pure and Applied Chemistry Preparation and Characterization of Novel Silk Fibroin / 2- ( N , N-Dimethylamino ) Ethyl



- Methacrylate Based Composite Hydrogels with Enhanced Mechanical Properties for Controlled Release of Cefixime. **2017**, 1325. <https://doi.org/10.1080/10601325.2017.1320750>.
- (45) Alipour, M.; Mahmoudi, R.; Bardania, H.; Baneshi, M. Recent Progress in Biomedical Applications of RGD-Based Ligand: From Precise Cancer Theranostics to Biomaterial Engineering: A Systematic Review. **2020**, No. September 2019, 839–850. <https://doi.org/10.1002/jbm.a.36862>.
- (46) Moses, J. C.; Nandi, S. K.; Mandal, B. B. Multifunctional Cell Instructive Silk-Bioactive Glass Composite Reinforced Scaffolds Toward Osteoinductive, Proangiogenic, and Resorbable Bone Grafts. *Adv. Healthc. Mater.* **2018**, 7 (10). <https://doi.org/10.1002/adhm.201701418>.
- (47) Arthur, A.; Zannettino, A.; Gronthos, S. The Therapeutic Applications of Multipotential Mesenchymal/Stromal Stem Cells in Skeletal Tissue Repair. *J. Cell. Physiol.* **2009**, 218 (2), 237–245. <https://doi.org/10.1002/jcp.21592>.
- (48) Bianco, P.; Robey, P. G. 35102181. **2001**, 414 (November).
- (49) Sundelacruz, S.; Kaplan, D. L. D. L. Stem Cell- and Scaffold-Based Tissue Engineering Approached to Osteochondral Regenerative Medicine. *Semin. Cell Dev. Biol.* **2009**, 20 (6), 646–655. <https://doi.org/10.1016/j.semcd.2009.03.017>.

# Chapter 7 Conclusions and Future Work

## 7.1 Summary and Conclusions

This dissertation describes development of different 3D scaffold systems by using natural silk fibroin as a polymer (both mulberry and non-mulberry silk). All differently developed scaffolds were fully characterized by using various techniques like SEM, FTIR, TGA, contact angle, etc. The mechanical properties of the scaffold, such as compression modulus and Young's modulus, were also measured. Further, the degradation profile of the scaffold was also studied *in-vitro* by using protease enzymes. The biological properties were evaluated by looking at cell viability, cell proliferation and cell morphology. Finally, the developed scaffolds were assessed for its ability to differentiate primary cells or hMSCs into bone forming cells (osteogenic lineage) by measuring concentration of ALP, OCN, BMP-2, and calcium mineralization. Estimation of secreted cytokine and dendritic cell activation markers was used to evaluate the immunological response against the developed silk fibroin scaffolds.

**Chapter 1** provides a brief introduction to tissue engineering and use of silk as a biomaterial. This chapter also discusses the motivation of this dissertation and outlines the objective of the thesis. This chapter also provides an overview of the organisation of dissertation.

**Chapter 2** begins with a brief literature survey for the bone as a tissue. It further discusses advancements in bone tissue regeneration, bone graft substitutes and their limitations. Silk fibroin's physical, chemical and structural properties have also been discussed, followed by an overview of potential of silk in tissue regeneration applications. The chapter concludes by describing the motivation and objectives of the present thesis.

**Chapter 3** describes a surface coating strategy for microparticle-based silk fibroin scaffold. In this work, microparticles from silk fibroin have been formulated and fused by using regenerated silk solution to make a load bearing 3D microparticle based SF scaffold with appropriate pore size, porosity with pore interconnectivity, good mechanical strength and tuneable bioresorption. Further, *in-vitro* studies demonstrating cell adhesion, proliferation and differentiation of MG-63 osteoblast-like cell line were also performed. In addition, the surface of these scaffolds was also modified using two biopolymers - Type I collagen and chitosan. The findings of this study show that although the SF scaffold does support *in-vitro* cell attachment, proliferation and differentiation, this performance can be further enhanced using the surface coating approach. Also, the ALP activity and bone mineralisation were superior in the chitosan modified scaffolds.

**Chapter 4** describes the formation of bioceramics filled microparticles from silk fibroin. The focus of the work in this chapter is the fabrication of silk fibroin (SF) 3D microparticle scaffolds with the addition of hydroxyapatite (HA) and calcium sulfate (CaS) as bioceramics. Physicochemical characterization shows ~30% filler loading by TGA analysis, ~ 40% optimum porosity with >100 µm pore size from SEM data observed for filled/unfilled scaffolds. There is a three-fold increase in Young's Modulus in the case of SF-HA, while a two-fold increase for SF-CaS, as observed by nano-indentation studies. Bioerosion study results show early

bioerosion with SF-CaS scaffold while prolonged bioerosion with SF-HA scaffold. *In-vitro* osteo-regenerative potential was analyzed using hMSCs ability to differentiate into osteogenic lineage by estimating ALP, BMP-2 and OCN. SF-CaS supports the early stage differentiation as compared to SF-50%HA scaffolds, which predominantly support late stage differentiation. The expression of TNF- $\alpha$ , suggests a reduced risk of immune rejection. Therefore, the work described in this chapter concludes that although SF scaffolds support bone tissue regeneration, the choice of bioceramics enhances the applicability in various clinical scenarios by providing a controlled rate of bioerosion, tuneable speed of osteo-regeneration and improved load-bearing capacities.

**Chapter 5** describes the processing protocol to obtain a highly concentrated silk fibroin solution from the fiber of *A. Mylitta* silkworm in TFA by using cryomilling technique. This study showed that the cryo-milling of silk fiber reduces the beta sheet content by more than 10% and resultant SF powder completely dissolves in trifluoroacetic acid (TFA) within 6 hours to form ~20wt% concentrated solutions. Further, this solution can be processed using electrospinning to form 3D scaffolds. As a control, *Bombyx mori* (BM) silk was used in the study. *In-vitro* studies were also performed to observe cell adhesion and proliferation rate along with hMSCs differentiation into osteogenic lineage. Finally, *in-vivo* osteogenic potential of the AM and BM scaffolds was evaluated by using rat calvarial model for the period of 4-week implantation. The processing techniques do not affect the biocompatibility of the material and the AM scaffolds support bone regeneration. Thus, the results in this study showed that cryo-milling facilitates enhanced processability of non-mulberry silk and therefore expands its potential in biomedical applications.

**Chapter 6** describes development of mulberry and non-mulberry silk fibroin based injectable cryogel scaffold. To achieve that, the methacrylated group was incorporated into mulberry silk fibroin using the epoxide ring-opening

polymerization method by using glycidyl methacrylic acid. Individual methacrylated silk fibroin (SFGMA) and SFGMA combined with either non-mulberry silk fiber (NMS) or Methoxy/RGD PEG acrylate were developed in this study. Developed cryogels were fully characterized by using various physicochemical techniques. *In-vitro* HDF cell viability and cytoskeleton studies showed that all cryogels support cell adhesion and proliferation. However, cells are more elongated on cryogels loaded with NMS and MPA. *In-vitro* differentiation of hMSCs to osteogenic cell lineage was analyzed by estimating ALP, BMP-2, OCN and calcium deposition. Further, cryogels had a non-inflammatory effect on bone marrow-derived dendritic cell activation *in-vitro*. In addition, NMS and MPA loaded cryogels also showed an anti-inflammatory effect, supported by the 28 day study in *in-vivo* injection in mice model. Hence this work concludes that the fabrication of methacrylated silk fibroin based injectable cryogels have promising future in osteo-regenerative applications.

## 7.2 Scope of Future Work

Successful BTE application can be achieved by a multi-tasking approach as it depends on multi factors like age, physical and clinical conditions of patients as well it also depends on the type of fracture. Here, the work presented in this thesis tried to address the wide range of bone defects by providing a choice of biomaterial as per the clinical scenario that include (a) critical size long bone defect by designing load bearing implantable SF microparticle scaffolds decorated surface with coating or use of bioceramics as a filler and (b) multisite/craniofacial/calvarial defects that can be addressed by electrospun mats or injectable SF cryogel. However, there are few bone diseases that require great attention for their treatment by using advanced therapies.

Osteoporosis is one of the structural bone defects/diseases. Over 200 million people have osteoporosis and the incidence rate increases with age. Over 70% of those over age 80 are affected. One in 3 females and 1 in 5 males over the age of 50 will have an osteoporotic fracture.<sup>1</sup> Alendronate sodium – a bisphosphonate drug by oral route is the first choice for the treatment of osteoporosis.<sup>2,3</sup> Low bioavailability of about 1% and about 50% absorption are the disadvantages of oral route of drug administration. Hence, localized and controlled delivery of alendronate is beneficial as it will improve the efficacy by targeting the site of action.<sup>4</sup>

Recent advances in the development of scaffold based drug delivery systems have been viewed as potential alternatives, due to sustained drug release at targeted sites.<sup>5</sup> Ideally, augmentation of osteoporotic fractures with osteoconductive bone grafts reduces the occurrence of secondary fracture by releasing the incorporated drug and also provides a scaffold for ingrowth of new bone at the bone defected site. In the last two decades, there have been several reports on the use of silk fibroin as a biomaterial generated for tissue engineering applications. The chemical and biological properties of silk fibroin provide an advantage to modulate its design as per the required application.

SF can be used as a vehicle for the delivery of alendronate drug.<sup>6</sup> The unique mechanical property, non-cytotoxic nature, and ability of SF can support the differentiation of mesenchymal stem cells along the osteogenic lineage and help in faster new bone formation and release of alendronate drug helps to treat osteoporosis. Thus, proposed SF-alendronate combination provides a dual advantage as a treatment for osteoporosis and as a platform for new bone tissue regeneration.<sup>7,8</sup>

## 7.2.1 Formation of SF scaffold with/without Alendronate drug

To support this proposed work, we have primarily developed alendronate loaded microparticle-based SF scaffold by dropping SF solution into liquid nitrogen (LN<sub>2</sub>) and a conventional freeze-dried scaffold. Both these scaffolds were evaluated for drug release in the *in-vitro* model by using MG-63 cells. SF scaffold formation method is described in **Figure 7-1**.

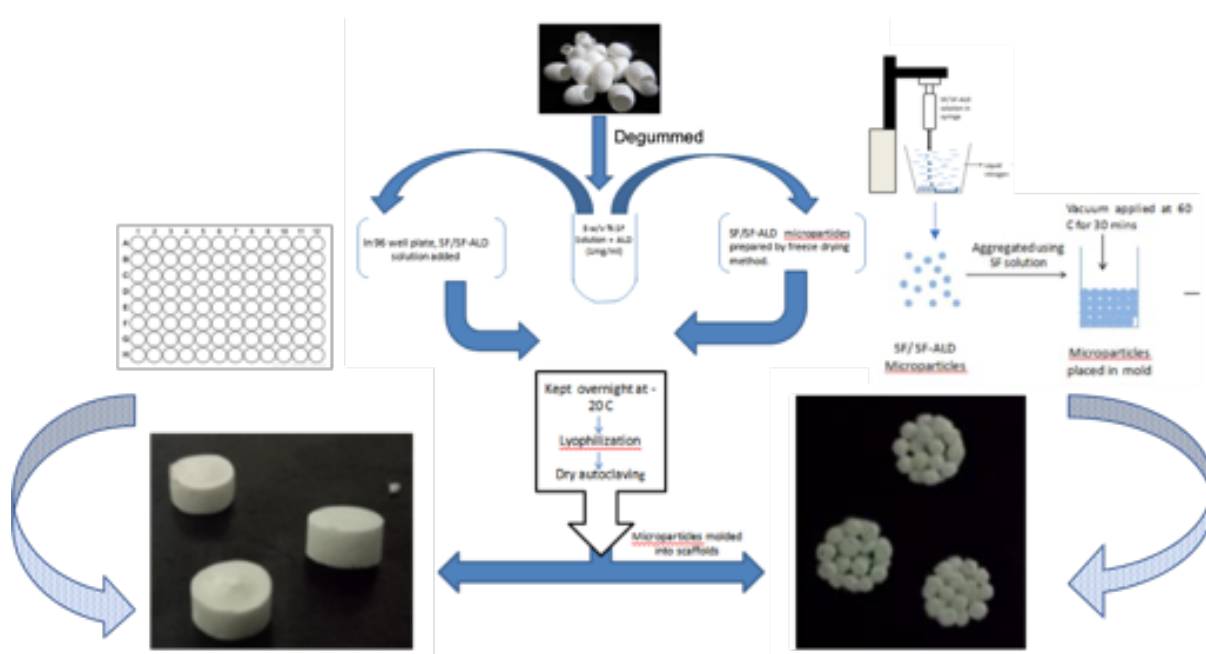


**Figure 7-1** Schematic for the formation of SF microparticle/freeze dried scaffolds with/without alendronate drug loading. Freeze dried SF Scaffold (FD-SF); alendronate drug loaded SF scaffold (FD-SF+Ald); Microparticle SF Scaffold (M-SF) and alendronate drug loaded SF scaffold (FD-SF+Ald); Microparticle SF Scaffold (M-SF) and alendronate drug loaded microparticle SF scaffold (M-SF+Ald)

## 7.2.2 Primary cell culture study

MG-63 is an osteosarcoma cell line and *in-vitro* cell proliferation was analysed by using alamar blue assay, a dye-resazurin-based reagent to observe the release effect of alendronate. Autoclaved sterilized FD-SF, FD-SF+Ald, M-SF, M-SF+Ald scaffolds were placed in a 96 well flat bottomed non-adherent cell culture plate and MG-63 cells were seeded on the scaffolds at a density of  $5 \times 10^4$  cells per scaffold in complete media. The cells were allowed to be settled for 5–7 minutes at 37°C with 5% CO<sub>2</sub>. The additional 90  $\mu$ L of media for cells was then added and the cell culture plate was incubated at 37°C with 5% CO<sub>2</sub> for up to 7 days. Cell proliferation was analyzed on the 3rd, 5<sup>th</sup> and 7<sup>th</sup> day. During the experiment, fresh growth media was changed after every 48h. The results obtained are plotted in **Figure 7-2**.

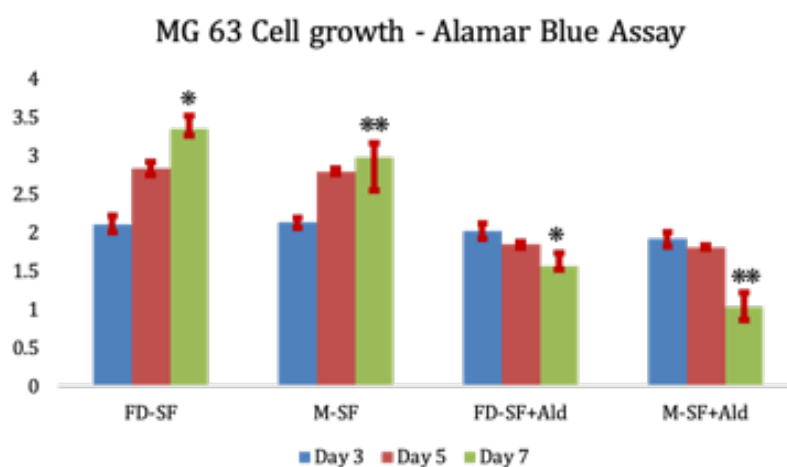


**Figure 7-2** *In-vitro* MG-63 cell growth on FD-SF, FD-SF+Ald, M-SF and M-SF+Ald scaffolds up to 7 days

Significant decrease in cell growth on FD-SF+Ald scaffold with respect to without drug loaded FD-SF was observed on day 7 ( $p = 4.36 \times 10^{-12}$ ). Similar trend also was observed in microparticle based SF scaffold. Alendronate loaded M-SF+Ald



showed significant decrease in MG-63 cell growth as compared to the M-SF scaffold (without drug) on day 7 ( $p = 7.2 \times 10^{-13}$ ). MG-63 cells are the osteogenic sarcoma (OSA) cells and have potential for osteogenic differentiation.<sup>9</sup> The mechanism of action of Ald occurs by reducing prenylation of proteins essential for normal cellular function. Observed reduction in cell growth of MG-63 in both the form of drug loaded SF scaffolds (FD-SF+Ald and M-SF+Ald) gave confirmation of loading and release of alendronate drug from the SF scaffolds and it is in line with the report that states, BPs are responsible for the decrease in cell proliferation along with induction of apoptosis in human OSA cells.<sup>10</sup>

### 7.2.3 Future advance study

This primary study concludes successful loading and release of drug from the SF microparticle scaffold. In future, SF can provide a platform for Alendronate delivery in osteoporotic patients.<sup>11</sup> However, detailed physico-chemical characterization and extensive cell culture studies to show effectiveness on the growth of osteoblast and osteoclast simultaneously by using the co-culture model will help in the development of novel drug delivery platform in BTE.

## 7.3 References

- (1) Li, D.; Chen, K.; Duan, L.; Fu, T.; Li, J.; Mu, Z.; Wang, S.; Zou, Q.; Chen, L.; Feng, Y.; Li, Y.; Zhang, H.; Wang, H.; Chen, T.; Ji, P. Strontium Ranelate Incorporated Enzyme-Cross-Linked Gelatin Nanoparticle/Silk Fibroin Aerogel for Osteogenesis in OVX-Induced Osteoporosis. *ACS Biomater. Sci. Eng.* **2019**, *5* (3), 1440–1451. <https://doi.org/10.1021/acsbmaterials.8b01298>.

- (2) Kawata, T.; Tenjou, K.; Tokimasa, C.; Fujita, T.; Kaku, M.; Matsuki, A.; Kohno, S.; Tsutsui, K.; Ohtani, J.; Motokawa, M.; Shigekawa, M.; Tohma, Y.; Tanne, K. Effect of Alendronate on Osteoclast Differentiation and Bone Volume in Transplanted Bone. *Exp. Anim.* **2004**, *53* (1), 47–51. <https://doi.org/10.1538/expanim.53.47>.
- (3) D'Amelio, P.; Grimaldi, A.; Cristofaro, M. A.; Ravazzoli, M.; Molinatti, P. A.; Pescarmona, G. P.; Isaia, G. C. Alendronate Reduces Osteoclast Precursors in Osteoporosis. *Osteoporos. Int.* **2010**, *21* (10), 1741–1750. <https://doi.org/10.1007/s00198-009-1129-1>.
- (4) Lewiecki, E. M. Bisphosphonates for the Treatment of Osteoporosis: Insights for Clinicians. *Ther. Adv. Chronic Dis.* **2010**, *1* (3), 115–128. <https://doi.org/10.1177/2040622310374783>.
- (5) Ferracini, R.; Martínez Herreros, I.; Russo, A.; Casalini, T.; Rossi, F.; Perale, G. Scaffolds as Structural Tools for Bone-Targeted Drug Delivery. *Pharmaceutics* **2018**, *10* (3), 1–26. <https://doi.org/10.3390/pharmaceutics10030122>.
- (6) Hayden R. S.; Vollrath M.; Kaplan D. L. Effects of Clodronate and Alendronate on Osteoclast and Osteoblast Co-Cultures on Silk-Hydroxyapatite Films. **2014**, *10* (1), 1–17. <https://doi.org/10.1016/j.actbio.2013.09.028.Effects>.
- (7) Vasikaran, S. D. Bisphosphonates: An Overview with Special Reference to Alendronate. *Ann. Clin. Biochem.* **2001**, *38* (6), 608–623. <https://doi.org/10.1258/0004563011901037>.
- (8) Ma, S.; Goh, E. L.; Jin, A.; Bhattacharya, R.; Boughton, O. R.; Patel, B.; Karunaratne, A.; Vo, N. T.; Atwood, R.; Cobb, J. P.; Hansen, U.; Abel, R. L. Long-Term Effects of Bisphosphonate Therapy: Perforations, Microcracks and Mechanical Properties. *Sci. Rep.* **2017**, *7* (March). <https://doi.org/10.1038/srep43399>.
- (9) Xiong, Y.; Yang, H. J.; Feng, J.; Shi, Z. L.; Wu, L. D. Effects of Alendronate on the Proliferation and Osteogenic Differentiation of MG-63 Cells. *J. Int. Med. Res.*

- 2009**, 37 (2), 407–416. <https://doi.org/10.1177/147323000903700216>.
- (10) Poirier, V. J.; Huelsmeyer, M. K.; Kurzman, I. D.; Thamm, D. H.; Vail, D. M. The Bisphosphonates Alendronate and Zoledronate Are Inhibitors of Canine and Human Osteosarcoma Cell Growth in Vitro. *Vet. Comp. Oncol.* **2003**, 1 (4), 207–215. <https://doi.org/10.1111/j.1476-5810.2003.00026.x>.
- (11) Kweon, H.; Shin, S. H.; Chon, J.-W.; Lee, K.-G.; Jo, Y.-Y.; , Ji Young Yoon , Yoo-Kyoung Park, J.-Y. J.; Kim, J.-H.; Shin, and B.-S. Effects of Silk Fibroin Hydrolysate on Bone Metabolism in Ovariectomized Rats. *Int. J. Indust. Entomol.* **2015**, 30 (1), 17–25.

---

## ABSTRACT

---

**Name of the Student: Nimisha Parekh**

**Registration No. :10BB17A26048**

**Faculty of Study: Biological Sciences**

**Year of Submission: 2022**

**AcSIR academic centre/CSIR Lab: CSIR-NCL**

**Name of the Supervisor (s): Dr. Anuya Nisal**

**Title of the thesis: Performance Enhancing Strategies For Silk Fibroin Based 3D Biomaterial For Bone Tissue Engineering**

---

Every year millions of people suffer tissue/organ loss or failure. Tissue/Organ transplantation or the use of biodegradable implants are promising solutions for repair or replacement of tissues/organs. The drawback of transplantation is immunological response from the patient's body. This can be overcome by tissue engineering/regeneration that applies the principles of engineering and life sciences towards the development of biological substitutes that help to restore the lost tissues/organs. The primary challenge in BTE includes development of three-dimensional (3D) scaffolds, which can also promote cell adhesion, proliferation, differentiation, resulting in superior healing of bone defects. Thus, success of the regenerative process depends on the understanding of the mechanism at the interface between cells and the biomaterials used for implants. Several biomaterials have been reported for BTE but none of them match the performance of an autograft. SF has emerged as a promising biomaterial over the last two decades. In the mulberry SF based scaffold system, in spite of the various developments there is scope for further improvement in scaffold formulations. In case of non-mulberry silk, transformation from being a textile commodity to biomaterials is relatively new and exciting as it has an inherent RGD motif, which helps cell attachment, cell proliferation and differentiation. However, non-mulberry silk contains higher alanine content that results in a material with increased beta sheet content. This higher crystallinity prevents dissolution of the silk into any conventional solvents and hence limits the ability to process non-mulberry silk into various scaffolds. As a general rule for tissue engineering, implant should be fabricated from materials that do not have the potential to elicit immunological or clinically detectable primary or secondary foreign body reactions in parallel to the formation of new tissue *in vivo*. Thus, this thesis aims to design different strategies to develop and modify 3D silk fibroin (both mulberry and non-mulberry silk) based biomaterials towards BTE applications. Newly developed biomaterial was fully characterized physically and chemically by using various techniques like SEM, FTIR, TGA, contact angle, etc. The mechanical properties of the scaffold such as compression modulus and Young's modulus were also measured. Further, the *in-vitro* enzymatic degradation of the scaffolds was also studied. The biological properties of the scaffolds were evaluated by studying cell viability, cell proliferation and cell morphology. Finally, the developed scaffolds were assessed for their potential to differentiate primary cells or hMSCs into an osteogenic lineage by measuring the differentiating markers (ALP, OCN, BMP-2, calcium mineralization) and examined for their immunological response.

Following mentioned specific objectives (strategies) are included in the thesis.

1. Surface coating with biopolymers on micro-particle-based SF scaffold
2. Incorporation of bio-ceramics into SF micro-particle-based scaffold
3. Development of non-mulberry silk electrospun scaffold
4. Development of mulberry and non-mulberry SF based injectable scaffold

---

1) List of publications

1. **Nimisha Parekh\***, Chandani Hushye, Saniya Warunkar, Sayam Sen Gupta and Anuya Nisal\*, In-vitro study of novel microparticle based Silk Fibroin scaffold with osteoblast-like cells for load-bearing osteo-regenerative applications, RSC Advances, 2017, 7, 26551 – 26558.
2. **Nimisha A. Parekh\***, Rucha V. Deshpande, Swati G. Shukla, and Anuya A. Nisal\*, “Silk Fibroin 3D Microparticle Scaffolds with Bioactive Ceramics: Chemical, Mechanical, and Osteoregenerative Characteristics”, Adv. Eng. Mater. 2020, DOI: 10.1002/adem.202000458

2) List of Papers with abstract presented (oral/poster) at national/international conferences/seminars with complete details.

1. **Nimisha Parekh**, Swarali Joshi, Anuya Nisal\*, “**Silk Fibroin 3D scaffolds for bone tissue engineering with a focus on osteoporotic defects**”, Conference Proceedings, World Biomaterial Congress, 2020, special symposium Biomaterials for tissue engineering applications (WBC2020-1126)
2. **Nimisha Parekh\***, Swati Shukla and Anuya Nisal\*, “**Silk fibroin composite microparticles with bioactive ceramics towards**

---

**development of biological scaffolds with enhanced osteoregenerative properties”, NCL Science Day 2019**


3. **Nimisha Parekh\***, Swati Shukla, Sayam Sen Gupta and Anuya Nisal, **“Silk fibroin composite microparticles with bioactive ceramics towards development of biological scaffolds with enhanced osteoregenerative properties”, MACRO-2018, December 2018.**
4. **Parekh, Anuya Nisal\***, **“Performance enhancing strategies for micro-particle based silk fibroin 3D scaffolds for bone tissue engineering”, Annual Students Conference National Chemical Laboratory – Research Foundation, 2018.**
5. **Nimisha Parekh**, Anuya Nisal\*, Sayam Sen Gupta, B.L.V. Prasad, **“Modified Silk Fibroin based 3D Scaffolds for Bone Tissue Engineering”, MACRO-2017.**

3) A copy of all SCI publication(s), emanating from the thesis



Cite this: *RSC Adv.*, 2017, 7, 26551

# *In vitro* study of novel microparticle based silk fibroin scaffold with osteoblast-like cells for load-bearing osteo-regenerative applications†

Nimisha Parekh,<sup>\*a</sup> Chandni Hushye,<sup>b</sup> Saniya Warunkar,<sup>b</sup> Sayam Sen Gupta <sup>c</sup> and Anuya Nisal <sup>\*a</sup>

Silk Fibroin (SF) is today considered to be one of the most favorable materials for bone tissue engineering. We have prepared novel SF microparticle based 3D scaffolds, with appropriate pore size, pore interconnectivity and porosity, excellent mechanical properties and tunable bioresorption, while retaining the inherent biocompatibility of SF. These properties make them ideal candidates for osteoregenerative applications. Here, we report the *in vitro* cell viability, cell adhesion and proliferation with osteoblastic differentiation of MG 63 osteoblast-like cell line on these scaffolds. In addition, we have also modified the surface of these scaffolds using collagen type I and chitosan biopolymers. Our results show that although the SF scaffold does support *in vitro* cell attachment, proliferation and differentiation, this performance can be further enhanced using the surface coating approach. Also, the ALP activity and bone mineralization was found to be particularly superior in the chitosan modified scaffolds.

Received 21st March 2017

Accepted 12th May 2017

DOI: 10.1039/c7ra03288a

rsc.li/rsc-advances

## Introduction

Bone tissue engineering (BTE) has emerged as a promising method for accelerated healing of damaged bone tissues.<sup>1</sup> BTE involves use of a three-dimensional scaffold that provides the support for cell attachment and natural tissue formation, thus mimicking the natural extracellular matrix. There are, therefore, stringent requirements on the properties of the scaffold that can be used in BTE. The ideal scaffold should have a three-dimensional architecture with optimum pore size and pore volume for efficient diffusion and/or migration of nutrients and cells. Secondly, it must have appropriate mechanical strength to provide structural rigidity and support. Thirdly, the scaffold must give the proper chemical, biological and morphological clues that will enable in the efficient functioning of the cells for formation of new tissue.<sup>2-4</sup> The main challenge, therefore, lies in the development of a functionalizable biocompatible 3D scaffold that can promote cell adhesion by specific cell–matrix interactions.

Calcium phosphate and bioresorbable bioactive glass-based micro-porous ceramic scaffolds have been extensively explored for use in BTE.<sup>5</sup> However, they are limited by their brittleness. In contrast, variety of natural and synthetic polymeric 3D scaffolds

have been extensively explored for BTE and they exhibit better biocompatibility and mechanical properties.<sup>3,4,6</sup> However, polymer-based matrices typically do not possess the mechanical properties of ceramics and rapidly degrade *in vivo*. Thus they remain nondurable for load bearing applications required in BTE. Recently, a lot of interest is focused on composite materials, which attempt to combine advantages of both polymers and ceramics. However, a 3D scaffold composed of 100% biopolymer having the properties of composite materials is desirable.

In this context, from the last two decades, silk fibroin (SF) has emerged as a promising material for BTE on account of its excellent biocompatibility, tuneable bioresorption, easy processibility and thermo-mechanical stability.<sup>1,7-9</sup> SF-scaffolds have shown to induce bone formation, stimulate osteogenic differentiation of human mesenchymal stem cells,<sup>10-13</sup> and support tissue vascularisation in *in vitro* models of BTE.<sup>14-16</sup> SF can be produced in large commercial quantities with control on quality. It allows easy chemical modification<sup>17</sup> that is required to obtain required functionality and can also be processed into 3D materials such as hydrogels, sponges, fibers, microspheres, and electrospun fiber mats.<sup>1,18-22</sup> The unique mechanical properties and tunable bioresorption rate of these 3D scaffolds allows attachment, proliferation and differentiation of mesenchymal stem cells along the osteogenic lineage for BTE. The efficacy of these 3D scaffolds from SF gets enhanced when they are surface functionalized with integrin binding RGD motifs, collagen, chitosan, gelatin and growth factors like transforming growth factor- $\beta$  (TGF- $\beta$ ), VEG-F and bone morphogenic protein (BMPs).<sup>23-25</sup> However, the main limitation of the scaffolds

<sup>a</sup>Polymer Science and Engineering Dept., National Chemical Laboratory, Homi Bhabha Road, Pune – 411008, India. E-mail: n.parekh@ncl.res.in; aa.nisal@ncl.res.in

<sup>b</sup>Department of Zoology, Poona College, Camp, Pune – 411001, India

<sup>c</sup>Department of Chemical Sciences, Indian Institute of Science and Educational Research, Mohanpur – 741246, Kolkata, India

† Electronic supplementary information (ESI) available: Comparative data of scaffolds and comparative image of cell morphology. See DOI: 10.1039/c7ra03288a

discussed above is that they are mostly soft in nature and do not have high load bearing capacity which is essential for BTE. Recently, high strength SF scaffold for BTE which possess high load bearing ability, has been reported by a few groups.<sup>26–28</sup> Ak *et al.* have described a novel method of cryo-gelation using a cross-linker molecule.<sup>27</sup> Also, Mandal *et al.* have described scaffolds prepared using salt leaching and reinforced with SF microfibers.<sup>26</sup> We have recently developed novel processing protocols to produce unique 3D scaffolds of silk fibroin using SF micro-particles.<sup>29,30</sup> Here, the SF micro-particles are produced by collection of drops of SF solution in a methanol bath. These micro-particles are then fused together using a dilute solution of SF in water. This novel protocol has then been used to produce 3D scaffolds with excellent mechanical properties (dry compression modulus 10–100 MPa, wet compression modulus of 25 MPa), which is one of the main prerequisite for BTE and a property that is lacking in almost all SF based scaffold. The bulk porosity in scaffolds is in the range of 40–60% and the pore sizes are of the order of 50–500  $\mu\text{m}$ . It has been well documented that microparticle based scaffolds have improved pore interconnectivity and better control on pore size and porosity.<sup>31</sup> The conformation of SF protein in the microparticle can be controlled, which implies that the bioresorption of the scaffold can be tuned. In addition to these advantages, the methodology of scaffold fabrication is flexible enough to incorporate various functionalities such as growth factors, fillers and drug molecules amongst others. These properties make this scaffold unique for BTE in comparison to other scaffolds recently reported. (ESI Fig. S1,† for a comparison of properties with other load bearing SF-scaffolds).

In this paper, we explore the *in vitro* cell morphology, cell viability, cell adhesion and proliferation with osteoblastic differentiation of MG 63 osteoblast-like cell line on these scaffolds containing 100% SF and having high mechanical strengths. In addition, we report a simple method to enhance the performance of this SF-scaffold for BTE by surface coating of the scaffolds with collagen type I and chitosan biopolymers. Collagen, a dominant component of the ECM in the bone tissue, is known to favour cell adhesion and provide the right chemical cues for osteogenic differentiation.<sup>32–34</sup> Chitosan on the other hand, is known for its inherent osteogenic potential and has been a well-documented biopolymer for BTE.<sup>35–39</sup> We show the *in vitro* cell viability, cell adhesion and proliferation with osteoblastic differentiation of MG 63 osteoblast-like cells in this collagen (Coll-SF)/chitosan (CS-SF) coated SF scaffolds and compare their performance to the uncoated SF-scaffolds.

## Materials and methods

### SF-scaffold preparation

SF-scaffold has been prepared as per the protocol mentioned in our patent applications.<sup>29,30</sup> In brief, 4 mL syringe was filled with the SF-HFIP solution. A syringe pump with an infusion rate of 1 mL min<sup>-1</sup> was used and the drops of SF-HFIP solution were collected in a stirred methanol coagulant bath. The particles so formed were kept in methanol bath for 3 h. Fresh methanol was then replenished after 3 h and the particles were further

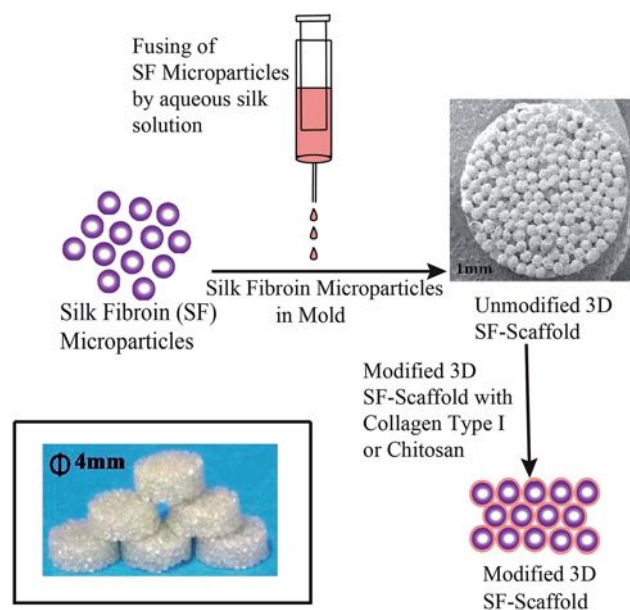


Fig. 1 Schematic representation of SF-scaffold preparation and surface modification.

incubated in methanol for 12 h. The micro-particles were allowed to air dry and the 3D SF-scaffold was prepared by fusing these SF micro-particles in a cylindrical mold using aqueous SF solution as shown in Fig. 1.

### Surface modification

**For collagen.** 1 mg mL<sup>-1</sup> sterile collagen solution (Sigma) was diluted 10 times using sterile DI water. A SF-scaffold was kept in the well of a 96 well plate. 100  $\mu\text{L}$  of the collagen solution prepared was added to each well and incubated at room temperature for 12 h. The remaining solution was then pipetted out and the scaffold was dried at 4  $^{\circ}\text{C}$  for 12 h. The scaffold was stored at 4  $^{\circ}\text{C}$  until further use.

**For chitosan.** 1 wt% chitosan (Sigma) solution was prepared in 0.05 M acetic acid. 100  $\mu\text{L}$  of this chitosan solution was added per scaffold to the SF-scaffold and kept at 60  $^{\circ}\text{C}$  for 20 minutes in an oven to obtain dry CS-SF scaffold.

### Surface characterisation by scanning electron microscopy

The uncoated as well as coated SF scaffolds were observed for surface features using a Scanning Electron Microscope (SEM). The samples were sputter coated with 5 nm gold (Au) coating using a Polaron SC 6420 sputter coater prior to SEM imaging. Image was captured on a Quanta 200 3D SEM equipped with a tungsten filament gun, operating at WD 10.6 mm and 20 kV. Images of representative areas at suitable magnification were captured.

### Cell culture

MG63 human osteoblast-like cells were purchased from National Centre for Cell Science (NCCS), Pune, Maharashtra, India. Cells were maintained in DMEM (Gibco) with 10% FBS (Gibco).



### Cell viability

**Trypan blue assay.** MG 63 cells were maintained in complete media containing DMEM with 10% FBS. Before seeding the cells, scaffolds were incubated in complete media at 37 °C with 5% CO<sub>2</sub> for 12 h.  $5 \times 10^4$  cells per scaffold in 100  $\mu$ L of complete media were seeded on SF, Coll-SF and CS-SF scaffolds. Cells were trypsinized and counted on the 1<sup>st</sup>, 3<sup>rd</sup>, 5<sup>th</sup> and 7<sup>th</sup> day in Neubauer chamber by using standard trypan blue method.

**Live/dead assay.** MG 63 cells were seeded on SF, Coll-SF, CS-SF scaffolds at a density of  $5 \times 10^4$  in DMEM containing 10% FBS. Cells were incubated at 37 °C with 5% CO<sub>2</sub> upto 7 days. During incubation, on the 1<sup>st</sup>, 3<sup>rd</sup>, 5<sup>th</sup> and 7<sup>th</sup> day, cells were stained with live/dead staining solution that comprises of 10  $\mu$ L of 7.5 mM propidium iodide and 1  $\mu$ L of 0.67 mM acridine orange (both stock were prepared in PBS) in 1 mL of DMEM containing 10% FBS. Cells were incubated at 37 °C with 5% CO<sub>2</sub> for ~25 minutes. Later, cells were washed two times with PBS and images were captured by epi-fluorescence microscopy using Axio Observer Z1 Carl Zeiss Microscope.

### Cell proliferation

Cell proliferation was determined by MTT (3-(4,5-dimethylthiazol-2-yl)-2,5-diphenyltetrazolium bromide) assay. Before seeding the cells, SF, Coll-SF and CS-SF scaffolds were incubated in complete media at 37 °C with 5% CO<sub>2</sub> for 12 h. MG 63 cells were seeded in a flat-bottomed non-adhesive 96-well plate at a density of  $5 \times 10^4$  cells per scaffold in 100  $\mu$ L of complete media. The plate was incubated at 37 °C with 5% CO<sub>2</sub> for 24 h. During incubation, on the 1<sup>st</sup>, 3<sup>rd</sup>, 5<sup>th</sup> and 7<sup>th</sup> day, the media was replaced with filter sterilized MTT (0.45 mg mL<sup>-1</sup>) prepared in DMEM containing 10% FBS and further incubated for 4 h at 37 °C with 5% CO<sub>2</sub>. MTT reagent was replaced by DMSO 100  $\mu$ L per well and kept at 37 °C with 5% CO<sub>2</sub> for 20–25 minutes. Addition of DMSO dissolves the formazan crystals formed by reaction of sample with MTT and the developed color was measured at 550 nm using a microtitre plate reader (Multiskan EX, Thermo Scientific). Each absorbance was taken to be the mean of triplicate measurements.

### Cell morphology by actin cytoskeleton staining

MG 63 cells were seeded on SF, Coll-SF, CS-SF scaffolds at a density of  $5 \times 10^4$  in DMEM containing 10% FBS. Cells were incubated at 37 °C with 5% CO<sub>2</sub> up to 7 days. During incubation, on the 3<sup>rd</sup>, 5<sup>th</sup> and 7<sup>th</sup> day, actin cytoskeleton staining was performed using the following protocol: scaffolds were washed with PBS followed by the cell fixation with 4% paraformaldehyde for 15 minutes at room temperature. The cells were later washed with PBS two times and 0.1% Triton X-100 (Sigma-Aldrich) for 5 minutes. The cells were again subjected to PBS washing two times and incubated with 5% BSA for 20 minutes at room temperature to avoid non-specific binding. Actin filaments were stained by 1 : 100 dilution of alexafluor 488 phalloidin (Thermo Fisher Scientific) prepared in PBS and incubated for 30 minutes in dark at room temperature. Cell's nucleus was counter stained with DAPI at 300 nM concentration for 4 minutes at room temperature and washed with PBS.

Images were captured by epi-fluorescence microscopy using Axio Observer Z1 Carl Zeiss Microscope.

### Osteogenic differentiation by alkaline phosphatase (ALP) assay

Alkaline phosphatase (ALP) activity was assayed using colorimetric ALP kit (Abcam, U.K.). Briefly, MG 63 cells were seeded on a SF, Coll-SF, CS-SF scaffolds at a density of  $5 \times 10^4$  cells per scaffold in 10  $\mu$ L of complete media. The cells were allowed to be settled for 5–7 minutes at 37 °C with 5% CO<sub>2</sub>. The additional 90  $\mu$ L media for cells was then added and the cell culture plate was then incubated at 37 °C with 5% CO<sub>2</sub> for 7 days. On the second day of the experiment, seeding media was replaced with osteogenic differentiation media (Invitrogen). During incubation, on the 3<sup>rd</sup>, 5<sup>th</sup> and 7<sup>th</sup> day, spent media from cell seeded scaffolds was collected and 80  $\mu$ L of the spent media was incubated with 50  $\mu$ L of *p*-nitrophenyl phosphate (5 mM) solution at room temperature for 1 h in the dark. At the end of the incubation, enzyme activity was stopped by adding 20  $\mu$ L of stop solution. Simultaneously, standard curve was plotted (ESI Fig. S2†) as per manufacturer's instruction. The amount of *p*-nitro-phenol produced was measured by measuring absorbance at 405 nm.

### Extracellular mineral (Ca<sup>+2</sup>) deposition and quantification

Mineralized calcium deposition at the end of 7<sup>th</sup> day was analyzed with Alizarin Red S staining. In brief, MG 63 cells were seeded on a SF, Coll-SF, CS-SF scaffolds at a density of  $5 \times 10^4$  cells per scaffold in 10  $\mu$ L of complete media. The cells were allowed to be settled for 5–7 minutes at 37 °C with 5% CO<sub>2</sub>. The additional 90  $\mu$ L media for cells was then added and the cell culture plate was then incubated at 37 °C with 5% CO<sub>2</sub> for 7 days. On the day after seeding, the media was replaced with osteogenic differentiation media (Invitrogen). On 7<sup>th</sup> day, scaffolds were fixed with 4% formaldehyde at room temperature for 10 min. They were later washed with PBS and then stained with 2% Alizarin Red (Sigma) solution for 20 minutes at room temperature. After staining, the scaffolds were washed two times with DI water. Calcium deposition was observed under bright field by Axio Observer Z1 from Carl Zeiss.

Ca deposition was further confirmed by quantifying the total calcium content.<sup>23,40</sup> In brief, at the end of 7<sup>th</sup> day, scaffolds were washed with PBS and the deposited calcium was extracted with 0.5 mL of 5% trichloroacetic acid for 30 minutes. At the end of incubation, Ca was quantified using *O*-cresolphthalein complexone colorimetric assay (Sigma).

The developed color for scaffolds seeded with cells were measured at 575 nm and the absorbance at 575 nm for scaffolds that were not seeded with cells was subtracted to quantify the Ca content. Standard calibration curve was prepared as per manufacturer instructions (ESI Fig. S3†).

## Results and discussion

### 3D microparticle SF-scaffold

Silk fibroin based scaffolds have been prepared using a variety of methods like lyophilisation, salt leaching, electrospinning,

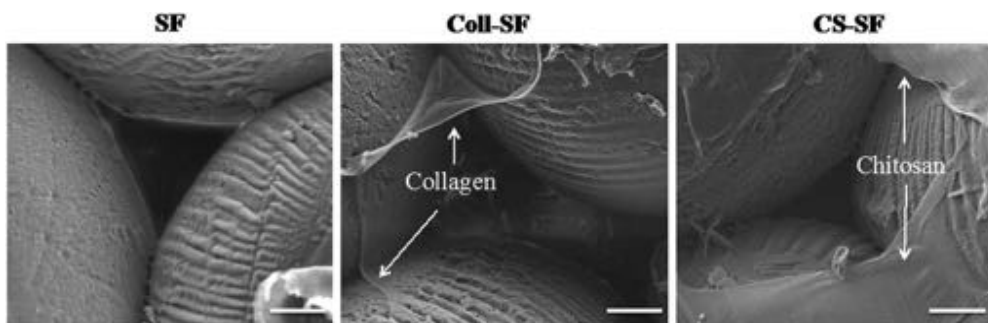


Fig. 2 SEM images of SF, Coll-SF and CS-SF and all images were at the scale bar is 50  $\mu\text{m}$ .

ice crystal templating, *etc.* These materials have shown promise in BTE applications. In this report, we use 3D microparticle SF-scaffold which was prepared using a methodology developed in our laboratory. Preliminary studies on the physical properties of this 3D microparticle SF-scaffold (such as mechanical integrity, pore size and pore volume and rate of bioresorption) match the requirements for a scaffold in BTE (ESI Fig. S1†).

However, the hydrophobic nature of SF results in limited cell-biomaterial interaction. We have introduced surface modification of the SF-scaffold to further improve cell adhesion and proliferation. Our process involves coating the surface of this microparticle scaffold using collagen type I and chitosan – biopolymers that are known to enhance cell adhesion and proliferation. The method involved incubating the SF-scaffolds with the biopolymer and allowing them to anneal and coat the surface. The morphological features of surface coating were studied using Scanning Electron Microscopy (SEM). Fig. 2 shows the SEM images of SF scaffold (SF) and surface modified scaffolds treated with collagen (Coll-SF) and chitosan (CS-SF). The SEM images of SF scaffold (Fig. 2) display mono-disperse micro-particles packed together in hexagonal packing. The surface of SF micro-particles shows presence of dried SF solution used to fuse these particles together. The interparticle pore sizes are clearly visible and are of the order of 100  $\mu\text{m}$ . The collagen modified SF scaffold shows presence of additional material domains dispersed throughout the surface (Fig. 2). These could be attributed to the collagen coating. Similar material domains were also observed in the chitosan treated scaffold (Fig. 2). It has been found that a minimum pore size of 30 microns is necessary for effective cell migration and colonization.<sup>41</sup> As can be seen in the Fig. 2, the method used for coating here does not alter the pore size of the scaffold. This implies that the surface modification technique is not expected to inhibit transport of nutrients and waste diffusion or cell migration in the scaffold.

### Cell viability and proliferation studies

The uncoated and coated SF scaffolds were evaluated using *in vitro* cell culture studies. MG-63 cells, was chosen for this study as it has a high proliferation rate. *In vitro* studies performed in a 7 day experiment are therefore sufficient to provide reliable and sensitive information on performance of this material as a possible scaffold for BTE.<sup>42–44</sup> Cell viability of MG 63 is

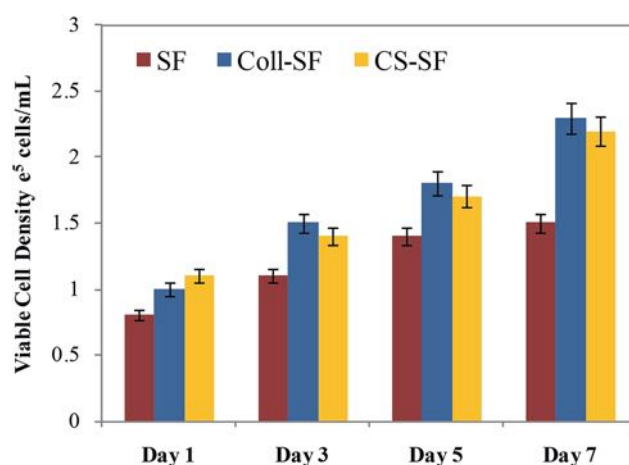


Fig. 3 Viable MG 63 cell density counted by trypan blue dye exclusion method (data are represented as the mean  $\pm$  SD of two independent experiments).

prerequisites for further application of any developed material and hence it was quantitatively assayed by using trypan blue dye exclusion method and qualitatively by performing live/dead imaging using AO and PI stains. Fig. 3 shows the viable cell count on the 1<sup>st</sup>, 3<sup>rd</sup>, 5<sup>th</sup> and 7<sup>th</sup> day after seeding the MG 63 on SF, Coll-SF and CS-SF scaffolds and it shows that SF scaffold does support attachment of the MG63 cells.

Also, as the experiment progresses the number of viable cells on the SF-scaffold increases. However, coating or surface modifying the scaffolds resulted in increased number of viable cells. On a given day of the experiment, the Coll-SF scaffolds and CS-scaffolds have a higher number of viable cells as compared to the uncoated SF scaffold. However, viability of the cells on the Coll-SF and CS-SF scaffold is comparable and no significant differences between these two scaffolds were observed here.

The trends observed in cell viability were further corroborated using live-dead assay. Fig. 4 shows the individual channel images of AO and PI on the 1<sup>st</sup>, 3<sup>rd</sup>, 5<sup>th</sup> and 7<sup>th</sup> day after seeding the MG 63 on SF, Coll-SF and CS-SF scaffold. For the SF-scaffold, MG 63 cells did adhere and found to be live to the micro-particle surface. Also, there were increased number of viable cells visible as the days progressed. Insignificant or no red coloured spots in these images indicate absence of dead cells on these scaffolds.

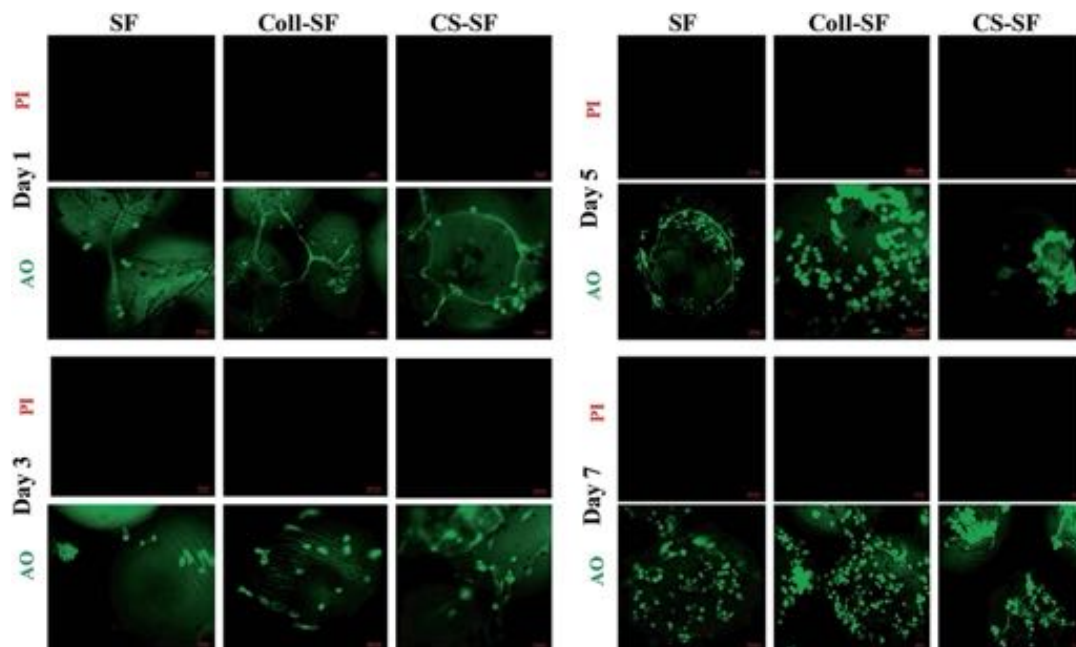


Fig. 4 Epi-fluorescence images of live (green) and dead (red) MG 63 cells grown on SF, Coll-SF and CS-SF. All images were taken at same exposure time and scale bar is 50  $\mu\text{m}$ .

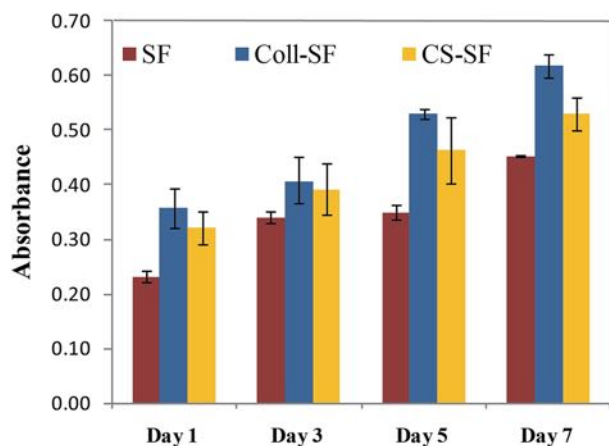


Fig. 5 Cell proliferation assay (MTT assay) of MG 63 cultured on SF, Coll-SF and CS-SF till 7 days. Data are presented as the mean  $\pm$  SD of two independent experiments.

Also, the number of live cells observed for modified scaffolds is always higher as compared to the uncoated SF scaffold. The living cell with elongated and spread morphology was most clearly visible on the Coll-SF scaffold as compared to the other two scaffolds used in the study (ESI Fig. S4<sup>†</sup>). Interestingly, as the experiment progressed, cells formed clumps on CS-SF scaffold.

This clumping was not observed in the SF or Coll-SF scaffold. It has been reported that degree of acetylation of chitosan is responsible for the clustering of cells.<sup>41</sup> In our study, 15–25% acetylated chitosan was used to modify the surface and our observations are in accordance with the literature reports.<sup>35,41</sup>

Cell proliferation was analyzed by using MTT assay. As can be seen in Fig. 5, all three scaffolds do support proliferation of the cells. Increased absorbance as a result of proliferation of viable cells were observed with both surface modified scaffolds as compare to unmodified SF scaffold. These results are in-line with those observed in trypan blue and live-dead assay experiments. The viable cell count nearly doubled on the 7<sup>th</sup> day after incubation. Similar trends in cell proliferation were also observed for the Coll-SF and CS-SF scaffolds.

#### Cell morphology by actin cytoskeleton staining

Cellular morphology was evaluated by F-actin cytoskeleton staining with alexafluor 488 phalloidin. Fig. 6 shows the actin cytoskeleton of MG 63 grown on SF, Coll-SF and CS-SF scaffolds. From the images, the significant cell growth with clear morphology of cells with respect to all three scaffolds is clearly visible. More elongated cell morphology with increased number of cells was visible with Coll-SF as compare to SF and CS-SF. Also, for the CS-SF scaffolds, we did observe spreading out of some cells, but the predominant morphology was spherical (ESI Fig. S5<sup>†</sup>). This variation in morphology of the cells can be attributed to the spread in degree of acetylation in the chitosan used for experimentation. Both the results are in accordance with MTT and live/dead assay results.

In short, data obtained from trypan blue dye extraction method, live/dead assay, actin cytoskeleton staining and cell proliferation assayed by MTT (Fig. 3–6) showed improved performance of the biopolymer coated scaffolds towards cell viability, proliferation and adhesion with retained cell morphology. This is in line with several reports where collagen and chitosan has been shown to improve cell adhesion and



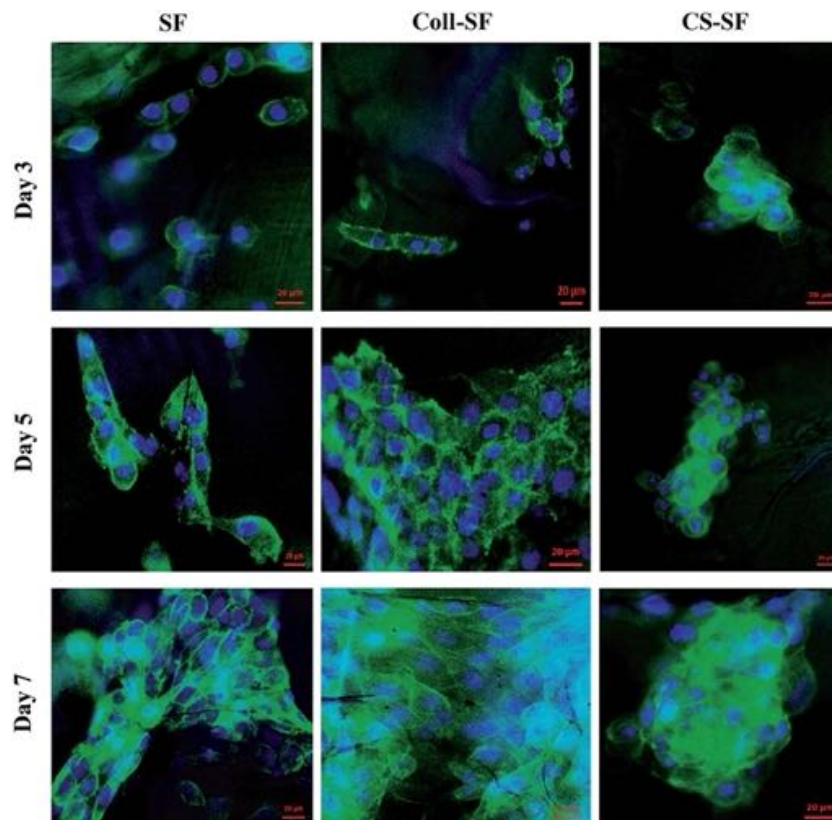


Fig. 6 Actin cytoskeleton staining of MG63 cells with alexafluor phalloidin 488 and nucleus were counter stained with DAPI. Scale bar is 20  $\mu\text{m}$ .

proliferation. Collagen type I is the dominant component of the ECM in a bone tissue and hence provides the right chemical cues for cell recognition. The integrins present on the cell surface are known to recognize the triple helix structure of collagen. Also, it has been acknowledged that collagen plays an important role in cytoskeleton reorganization and signal transduction, which in turn regulates the cell adhesion and proliferation.<sup>46</sup> Chitosan has been used in BTE and is shown to induce proliferation of osteoblast cells. The chemical structure of chitosan is similar to glycosaminoglycans (GAGs), which is an important component in ECM. This has been cited as one of the possible reasons for improved adhesion of cells to chitosan.<sup>39</sup> Our observations support this literature.

### Osteogenic differentiation

Bone is a mineralized connective tissue, which is continuously bioresorbed and neoformed. The formation of new bone tissue requires commitment from the cells towards the osteogenic lineage. The osteoblasts are responsible for synthesis of the bone matrix and as the cells proliferate it shows higher ALP activity and mineral deposition. Thus, in addition to cell adhesion and proliferation, understanding the functioning of cells is also of prime importance in BTE. In this study, we used ALP activity and calcium deposition to monitor osteogenic differentiation of MG 63 cells on unmodified and modified scaffolds.

ALP is an initial marker for the osteogenic differentiation process and is secreted into the ECM, playing a crucial role in bone ECM mineralization.

In our study Fig. 7, we detected measurable ALP activity with all three scaffolds and within the standard calibration curve (ESI Fig. S3†). The ALP activity was evident on day 3 for the SF scaffold and was found to be significantly enhanced on day 7. For the Coll-SF scaffold too, a similar increased ALP activity was observed for day 7. On 3<sup>rd</sup> and 7<sup>th</sup> day, the ALP activity between the three types

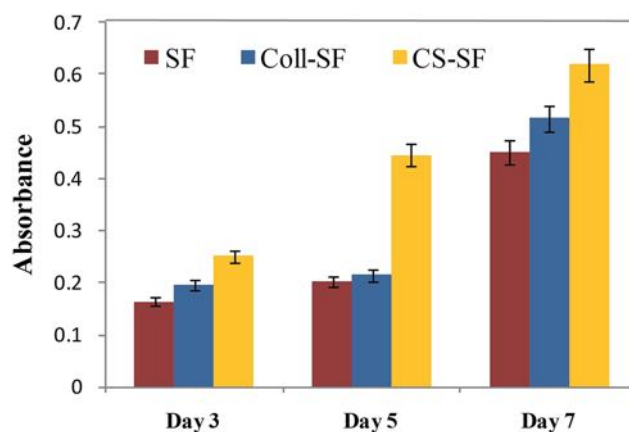


Fig. 7 ALP assay- MG 63 cells cultured on SF, Coll-SF and CS-SF till 7 days. Absorbance was taken at 405 nm and data are presented as the mean  $\pm$  SD of two independent experiments.

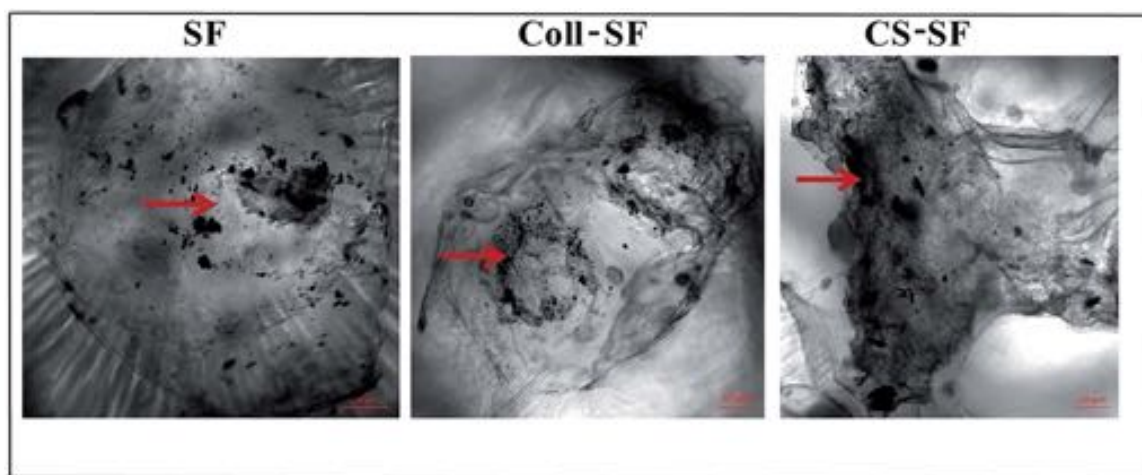


Fig. 8 Calcium depositions by alizarin red S staining. Arrow indicates deposited calcium nodules. All bright field images were taken at same exposure time and scale bar is 50  $\mu\text{m}$ .

of scaffold studied were comparable, with CS-SF scaffold showing the highest ALP activity. However, on the 5<sup>th</sup> day, the ALP activity in the CS-SF scaffold was significantly higher than the other two scaffolds studied. Here, the absorbance for CS-SF scaffold was nearly double that of SF and Coll-SF scaffold.

Presence of ALP enzyme is the predetermining early marker as the cells started to differentiate into osteogenic lineage. Throughout the assay, we got higher ALP activity with CS-SF scaffold. The invigorating effect of chitosan on osteogenesis has been extensively reported<sup>45,46</sup> however the exact mechanism of this osteogenic behavior is unknown. One of the possible reasons that have been discussed is the cationic charge on chitosan.<sup>47</sup> Also, it has been suggested that high molecular weight (>10 kDa) of chitosan results in improved osteogenic behaviour of MG63 cells. The molecular weight of chitosan used here is 190–310 kDa and thus our observations are in sync with literature.<sup>46,48,49</sup>

Alizarin red S staining was used to detect *in vitro* extracellular mineral (calcium) deposition as a result of osteoblastic differentiation initiation process. After the 7<sup>th</sup> day of seeding the MG 63 cells, calcium deposited nodules were detected on all three scaffold Fig. 8. Amount of deposition was not significantly different in SF scaffold and Coll-SF scaffold.

This deposition has been considerably increased as a part of differentiation process with the CS-SF scaffold as is evident in the images. For the Coll-SF scaffolds, Ca deposition is slightly higher than the SF and this improvement can be attributed to the GER sequence in collagen, which acts as an integrin binding site.<sup>1,50</sup> Also, our ALP activity assay shows moderately increased ALP activity with Coll-SF as compare to SF on 7<sup>th</sup> day but considerable difference has been noticed with CS-SF. Further, the total amount of Ca deposition was quantified by using *O*-cresolphthalein complexone colorimetric assay (ESI Fig. S6<sup>†</sup>). Higher Ca content was observed with CS-SF scaffolds as compared to SF and Coll-SF scaffolds. These results are in accordance with the alizarin red S staining studies.

## Conclusions

We report here *in vitro* cell behavior of osteoblast-like cells on novel SF microparticle scaffolds for applications in load-bearing osteo-regenerative applications. Additionally, we have modified the surface of these scaffolds using natural biopolymers – collagen type I and chitosan. Our results suggest that SF microparticle scaffold does support cell attachment, proliferation and differentiation of cells. This behavior can be further enhanced by coating the surface of these scaffolds with collagen type I and chitosan biopolymers. Although the cell attachment, viability and morphology were found to be superior in collagen modified scaffolds, the osteogenic differentiation is better in chitosan-modified scaffolds. The efficacy of these scaffolds for load bearing bone tissue engineering application *in vivo* is currently underway.

## Acknowledgements

The authors acknowledge BiolMed Innovations Pvt. Ltd. for providing SF micro-particles and SF scaffolds as per the Materials Transfer Agreement signed between BiolMed Innovations and CSIR-National Chemical Laboratory, Pune. We also thank Mr Abhijit Shete for providing help in sample preparation for Scanning Electron Microscopy. We acknowledge Dr Mujeeb-Shaikh from Poona College for supporting the project. Also, this work was funded through the CSIR 12th Five Year Plan Project CSC0134.

## References

- 1 J. Melke, S. Midha, S. Ghosh, K. Ito and S. Hofmann, *Acta Biomater.*, 2015, **31**, 1–16.
- 2 X. Le, G. E. J. Poinern, N. Ali, C. M. Berry and D. Fawcett, *Int. J. Biomater.*, 2013, **2013**, 1–16.
- 3 X. Liu and P. X. Ma, *Ann. Biomed. Eng.*, 2004, **32**, 477–486.
- 4 D. W. Hutmacher, *Biomaterials*, 2000, **21**, 2529–2543.

- 5 S.-J. Ding, C.-K. Wei and M.-H. Lai, *J. Mater. Chem.*, 2011, **21**, 12793–12802.
- 6 E. Sachlos and J. T. Czernuszka, *Eur. Cells Mater.*, 2003, **5**, 29–40.
- 7 N. Kasoju and U. Bora, *Adv. Healthcare Mater.*, 2012, **1**, 393–412.
- 8 L. D. Koh, Y. Cheng, C. P. Teng, Y. W. Khin, X. J. Loh, S. Y. Tee, M. Low, E. Ye, H. D. Yu, Y. W. Zhang and M. Y. Han, *Prog. Polym. Sci.*, 2015, **46**, 86–110.
- 9 A. E. Thurber, F. G. Omenetto and D. L. Kaplan, *Biomaterials*, 2015, **71**, 145–157.
- 10 L. Meinel, O. Betz, R. Fajardo, S. Hofmann, A. Nazarian, E. Cory, M. Hilbe, J. McCool, R. Langer, G. Vunjak-Novakovic, H. P. Merkle, B. Rechenberg, D. L. Kaplan and C. Kirker-Head, *Bone*, 2006, **39**, 922–931.
- 11 S. Saha, B. Kundu, J. Kirkham, D. Wood, S. C. Kundu and X. B. Yang, *PLoS One*, 2013, **8**, 1–10.
- 12 B. Kundu, R. Rajkhowa, S. C. Kundu and X. Wang, *Adv. Drug Delivery Rev.*, 2013, **65**, 457–470.
- 13 P. Gupta, M. Adhikary, M. Christakiran, M. Kumar, N. Bhardwaj and B. B. Mandal, *ACS Appl. Mater. Interfaces*, 2016, **8**, 30797–30810.
- 14 S. Ghanaati, R. E. Unger, M. J. Webber, M. Barbeck, C. Orth, J. A. Kirkpatrick, P. Booms, A. Motta, C. Migliaresi, R. A. Sader and C. J. Kirkpatrick, *Biomaterials*, 2011, **32**, 8150–8160.
- 15 R. E. Unger, A. Sartoris, K. Peters, A. Motta, C. Migliaresi, M. Kunkel, U. Bulnheim, J. Rychly and C. James Kirkpatrick, *Biomaterials*, 2007, **28**, 3965–3976.
- 16 S. Fuchs, X. Jiang, H. Schmidt, E. Dohle, S. Ghanaati, C. Orth, A. Hofmann, A. Motta, C. Migliaresi and C. J. Kirkpatrick, *Biomaterials*, 2009, **30**, 1329–1338.
- 17 S. Das, D. Pati, N. Tiwari, A. Nisal and S. Sen Gupta, *Biomacromolecules*, 2012, **13**, 3695–3702.
- 18 D. L. Kaplan and C. Vepari, *Prog. Polym. Sci.*, 2007, **32**, 991–1007.
- 19 A. Nisal, M. Dhanalakshmi, A. Lele, B. L. V Prasad and J. Bellare, *Proc. 70th Annu. Tech. Conf. Exhib.*, Soc. Plast. Eng., Mumbai, India, 6–7 December 2012, pp. 270–275.
- 20 A. Nisal, C. Kalelkar, J. Bellare and A. Lele, *Rheol. Acta*, 2013, **52**, 833–840.
- 21 P. Dubey, L. Nawale, D. Sarkar, A. Nisal and A. Prabhune, *RSC Adv.*, 2015, **5**, 33955–33962.
- 22 P. Dubey, S. Kumar, V. K. Aswal, S. Ravindranathan, P. R. Rajamohanam, A. Prabhune and A. Nisal, *Biomacromolecules*, 2016, **17**, 3318–3327.
- 23 V. Karageorgiou, M. Tomkins, R. Fajardo, L. Meinel, B. Snyder, K. Wade, J. Chen, V. Vunjak-Novakovic and D. L. Kaplan, *J. Biomed. Mater. Res., Part A*, 2006, **33**, 324–334.
- 24 H. J. Chung and T. G. Park, *Adv. Drug Delivery Rev.*, 2007, **59**, 249–262.
- 25 W. Zhang, C. Zhu, D. Ye, L. Xu, X. Zhang, Q. Wu, X. Zhang, D. L. Kaplan and X. Jiang, *PLoS One*, 2014, **9**, 1–9.
- 26 B. B. Mandal, A. Grinberg, E. Seok, B. Panilaitis and D. L. Kaplan, *Proc. Natl. Acad. Sci. U. S. A.*, 2012, **109**, 7699–7704.
- 27 F. Ak, Z. Oztoprak, I. Karakutuk and O. Okay, *Biomacromolecules*, 2013, **14**, 719–727.
- 28 A. M. Collins, N. J. V Skaer, T. Gheysens, D. Knight, C. Bertram, H. I. Roach, R. O. C. Oreffo, S. Von-Aulock, T. Baris, J. Skinner and S. Mann, *Adv. Mater.*, 2009, **21**, 75–78.
- 29 A. Nisal, P. Venugopalan and N. Sinha, CSIR-National Chemical Laboratory, WO2014125505 A1, 2014, pp. 1–10.
- 30 A. Nisal, P. Venugopalan and B. Khude, CSIR-National Chemical Laboratory, WO2016110873 A1, 2016, pp. 1–9.
- 31 B. Dhandayuthapani, Y. Yoshida, T. Maekawa and D. S. Kumar, *Int. J. Polym. Sci.*, 2011, 290602.
- 32 M. Vandrovcová, T. Douglas, D. Hauk, B. Grössner-Schreiber, J. Wiltfang, L. Bačáková and P. H. Warnke, *Physiological Research*, 2011, **60**, 797–813.
- 33 A. M. Ferreira, P. Gentile, V. Chiono and G. Ciardelli, *Acta Biomater.*, 2012, **8**, 3191–3200.
- 34 M. H. Lee, C. You and K. H. Kim, *Materials*, 2015, **8**, 1150–1161.
- 35 J. Y. Lee, S. H. Nam, S. Y. Im, Y. J. Park, Y. M. Lee, Y. J. Seol, C. P. Chung and S. J. Lee, *J. Controlled Release*, 2002, **78**, 187–197.
- 36 J. Venkatesan and S. K. Kim, *Mar. Drugs*, 2010, **8**, 2252–2266.
- 37 A. R. Costa-Pinto, R. L. Reis and N. M. Neves, *Tissue Eng., Part B*, 2011, **17**, 331–347.
- 38 S. Zeng, L. Liu, Y. Shi, J. Qiu, W. Fang, M. Rong, Z. Guo and W. Gao, *PLoS One*, 2015, **10**, e0128658.
- 39 R. LogithKumar, A. KeshavNarayan, S. Dhivya, A. Chawla, S. Saravanan and N. Selvamurugan, *Carbohydr. Polym.*, 2016, **151**, 172–188.
- 40 C. Li, C. Vepari, H.-J. Jin, H. J. Kim and D. L. Kaplan, *Biomaterials*, 2006, **27**, 3115–3124.
- 41 I. F. Amaral, P. Sampaio and M. A. Barbosa, *J. Biomed. Mater. Res., Part A*, 2006, **76**, 335–346.
- 42 B. Liu, S. Wu, L. Han and C. Zhang, *Int. J. Mol. Med.*, 2015, 1572–1582.
- 43 M. Yang, Y. Shuai, W. He, S. Min and L. Zhu, *Int. J. Mol. Sci.*, 2012, **13**, 7762–7775.
- 44 C. Pautke, M. Schieker, T. Tischer, A. Kolk, P. Neth, W. Mutschler and S. Milz, *Anticancer Res.*, 2004, **24**, 3743–3748.
- 45 Y. Zhang, M. Ni, M. Zhang and B. Ratner, *Tissue Eng.*, 2003, **9**, 337–345.
- 46 A. Fakhry, G. B. Schneider, R. Zaharias and S. Şenel, *Biomaterials*, 2004, **25**, 2075–2079.
- 47 X. Yang, X. Chen and H. Wang, *Biomacromolecules*, 2009, **10**, 2772–2778.
- 48 K. Lee, G. Jin, C. H. Jang, W.-K. Jung and G. Kim, *J. Mater. Chem. B*, 2013, **1**, 5831.
- 49 S. Sundelacruz and D. L. D. L. Kaplan, *Semin. Cell Dev. Biol.*, 2009, **20**, 646–655.
- 50 C. G. Knight, L. F. Morton, D. J. Onley, A. R. Peachey, J. Messent, P. A. Smethurst, S. Danny, R. W. Farndale, J. Michael, C. G. Knight, L. F. Morton, D. J. Onley, A. R. Peachey, A. J. Messent, P. A. Smethurst, D. S. Tuckwell, R. W. Farndale and M. J. Barnes, *J. Biol. Chem.*, 1998, **273**, 33287–33294.

**CORRECTION**

---

# Silk Fibroin 3D Microparticle Scaffolds with Bioactive Ceramics: Chemical, Mechanical, and Osteoregenerative Characteristics

*Nimisha A. Parekh, Rucha V. Deshpande, Swati G. Shukla, and Anuya A. Nisal*

Adv. Eng. Mater. 2020, 22, 2000458

DOI: 10.1002/adem.202000458

In the initially published version of this article the affiliation for N. A. Parekh was wrong.

The correct statement is as follows:

N. A. Parekh

Academy of Scientific and Innovative Research (AcSIR)

Ghaziabad 201002, India

The authors apologize for any inconvenience caused.

---

DOI: 10.1002/adem.202200112





# Silk Fibroin 3D Microparticle Scaffolds with Bioactive Ceramics: Chemical, Mechanical, and Osteoregenerative Characteristics

Nimisha A. Parekh,\* Rucha V. Deshpande, Swati G. Shukla, and Anuya A. Nisal\*

Preparation of 3D scaffolds for bone tissue engineering (BTE) is a challenging task as it requires appropriate pore size and porosities, mechanical properties, and controlled bioerosion rate. The focus of this work is the fabrication of silk fibroin (SF) 3D microparticle scaffolds with the incorporation of hydroxyapatite (HA) and calcium sulfate (CaS) as bioceramics. Physicochemical characterization shows  $\approx 30\%$  filler loading and  $\approx 40\%$  optimum porosity with  $> 100 \mu\text{m}$  pore size for these filled/unfilled scaffolds. Nanoindentation studies show improved Young's modulus at microparticle level with the incorporation of bioceramics. SF-HA scaffolds showed three fold increase in Young's modulus, whereas SF-CaS showed two fold increase. In vitro bioerosion study results in early bioerosion with SF-CaS scaffold, whereas prolonged bioerosion with SF-HA scaffold. In vitro osteoregenerative potential is analyzed by estimating alkaline phosphatase (ALP), bone morphogenetic protein-2 (BMP-2), and osteocalcin (OCN). SF CaS supports early stage differentiation while SF 50% HA predominantly supports late stage. The expression of TNF- $\alpha$  suggests a reduced risk of immune rejection. This work, therefore, concludes that although SF supports bone tissue regeneration, the choice of bioceramic enhances the applicability in various clinical scenarios by providing a controlled bioerosion rate, tunable speed of osteoregeneration, and improved load bearing capacities.

## 1. Introduction

Bone regeneration in large bone cavities presents a major challenge. These bony voids are either filled with an autograft/allograft (patient's own bone from another anatomical location or cadaveric bone, respectively), or synthetic bone graft substitute

called "bone void filler." Autografts are the 'gold standard' for bone grafting, but have inherent limitations of donor site morbidity and limited supply.<sup>[1]</sup> More recently, synthetic ceramics have shown promise for this application of bone void filling because of their chemical similarity to ceramics present in natural bone. Commonly used bioceramics include hydroxyapatite (HA), beta tricalcium phosphate (TCP), and more recently calcium sulfate (CaS). These materials are biocompatible, and support cell adhesion, proliferation, and growth of bone cells. Although these bioceramics are used as bone void fillers, they have certain limitations: they are intrinsically brittle and lack the required mechanical properties. Also, some of them have faster bioresorption rate (e.g., CaS and TCP), whereas others do not completely bioresorb (e.g., HA). In this context, to achieve native bone-like properties, current trend in bone tissue engineering (BTE) is to use a composite of bioceramic and a biocompatible polymer.<sup>[2,3]</sup>

Silk fibroin (SF)—a natural biopolymer—has come up as potential candidate for BTE, owing to its biocompatibility, mechanical properties, tunable biodegradation rate, and ease of processability. The silk from the *Bombyx mori* silkworm, commonly known as a mulberry silkworm, can be produced with good quality in large quantities.<sup>[4–6]</sup> Efficacy of SF-based biomaterials has been proven in various tissue regeneration models.<sup>[7,8]</sup> SF can be easily modulated to obtain required functionality and different forms.<sup>[9,10]</sup> Different SF-based biomaterials including SF films,<sup>[11]</sup> SF-3D scaffold,<sup>[12,13]</sup> and SF-reinforced biomaterials<sup>[14]</sup> have proven to be successful for bone regeneration purpose.

We have earlier reported a method to prepare silk fibroin microparticle scaffolds that have shown a high potential in BTE.<sup>[12]</sup> These SF microparticle scaffolds have excellent mechanical properties, pore interconnectivity, and a superior ability to promote osteoregeneration. The objective of this work was to prepare regenerated silk fibroin (RSF) microparticle scaffolds filled with nano-HA or CaS.<sup>[12,13]</sup> The addition of these fillers would further enhance the mechanical properties of these scaffolds and would thereby contribute toward the osteoregenerative potential. We compare and evaluate the performance of these microparticles and scaffolds vis-à-vis pure SF scaffolds. We have characterized the microparticles and their scaffolds for the

N. A. Parekh, Dr. A. A. Nisal  
Polymer Science and Engineering Department  
National Chemical Laboratory  
Homi Bhabha Road, Pune 411008, India  
E-mail: n.parekh@ncl.res.in; aa.nisal@ncl.res.in

N. A. Parekh  
Academy of Scientific and Innovative Research  
New Delhi 110025, India

Dr. R. V. Deshpande, Dr. S. G. Shukla  
National Chemical Laboratory Innovation Park  
BiolMed Innovations Pvt. Ltd.  
100, Homi Bhabha Road, Pune 411008, India

The ORCID identification number(s) for the author(s) of this article can be found under <https://doi.org/10.1002/adem.202000458>.

DOI: 10.1002/adem.202000458



physicochemical properties using spectroscopic and thermal techniques. We have also characterized the mechanical properties at the microparticle length scale using nanoindentation technique. Furthermore, the bulk compression modulus of the scaffolds was also measured. The scaffolds were evaluated for their potential in supporting bone tissue regeneration through in vitro studies. We monitored the growth and differentiation of human mesenchymal stem cells (hMSCs) on the filled/unfilled scaffolds. We also studied the immune response toward these scaffolds upon exposure to THP-1 cells. We report that addition of bioactive ceramics to microparticle-based SF scaffolds provides the flexibility to prepare bone void fillers with controlled rates of bioerosion and tunable osteoregeneration, while surprisingly it does not alter the bulk mechanical performance of the scaffolds.

## 2. Experimental Section

SF cocoons were purchased from Central Sericultural Research & Training Institute (CSRTI), Mysore; sodium bicarbonate ( $\text{NaHCO}_3$ ) was purchased from Merck (1.93237.0521); lithium bromide (Li-Br) (cat#213225), nano-HA (cat#677418), protease XIV (cat#P5147) enzyme were procured from Sigma-Aldrich; hexafluoroisopropanol (HFIP) was purchased from Gujarat Fluorochemicals Ltd.; and medical grade calcium sulfate was used in the study. All cell culture reagents—IMDM (cat#12440-046), RPMI (cat#A10491-01), fetal bovine serum (FBS) (cat#10082-147), FBS for hMSCs (cat#12662-011), Alamar blue (cat#1987309), MTT (cat#M6494), StemPro osteogenic differentiation kit (cat#A1007201), PicoGreen assay kit (cat#P11496), enzyme-linked immunosorbent assay (ELISA) kits for detection of bone morphogenetic protein-2 (BMP-2) (cat#EHBMP2), osteocalcin (OCN) (cat#BMS2020INST), and TNF- $\alpha$  (cat#BMS223-4)—were purchased from Invitrogen; alkaline phosphatase (ALP) detection kit (cat#ab83369) was procured from Abcam. hMSCs (cat#PT-2501) were purchased from Lonza and revived and stored as per suppliers' specifications. In all experiments on hMSCs, cells from passage number 3 were used. THP-1 cell line was procured from National Centre for Cell Sciences, Pune.

### 2.1. Preparation of Silk Fibroin Microparticles and Scaffolds

Silk fibroin microparticles and scaffolds were prepared as per the protocol described earlier.<sup>[12]</sup> *B. mori* cocoons were boiled in 0.5 w/v% of  $\text{NaHCO}_3$  solution twice for 30 min each for sericin removal. Collected fibroin was vacuum dried at 60 °C followed by dissolution in 9.3 M lithium bromide (LiBr) at 60 °C for 4 h. This solution was dialyzed extensively against water and the centrifuged solution was lyophilized at -55 °C for 6 h to obtain SF sponge. The powder was dissolved in HFIP, and this SF-HFIP solution was mounted on a syringe pump and the drops of SF-HFIP solution were coagulated in a methanol bath. The particles were incubated in methanol bath for 24 h with frequent change in fresh methanol. The microparticles were allowed to air dry and stored at room temperature till further use. Composite microparticles were prepared by adding 25 and 50 wt% HA and/or  $\text{CaSO}_4$  powder with respect to weight of SF in SF-HFIP solution. 3D scaffolds of SF and SF-bioceramics in the form of cylinders of various diameters and heights were prepared using dilute SF solution. Once

microparticles were added to mold, RSF was added on the top of the microparticles, which has been kept at 60 °C under vacuum for 30–45 min. This high temperature resulted in drying of the aqueous silk solution, fusing the microparticles together, and also inducing beta sheet formation in aqueous silk solution. This process results in making the glue water insoluble. These microparticles and 3D scaffolds are further referred to as SF-25% HA, SF-50% HA, SF-25% CaS, and SF-50% CaS, indicating both the type of filler and the filler loading.

### 2.2. Particle Size Determination

Particle size was analyzed using optical microscopy (Carl Zeiss Axio Observer Z1 microscope). Twenty particles were imaged and the diameter was calculated from the obtained area from ZenPro 2012 software from Carl Zeiss.

### 2.3. Confirmation of Secondary Structure in SF and Presence of Bioceramics

All SF and bioceramic-filled SF microparticles were analyzed using Fourier-transform infrared spectroscopy (FTIR) from Perkin Elmer (Spectrum GX) coupled with Golden Gate Diamond ATR at the resolution of 4  $\text{cm}^{-1}$  in the range of 1400–1800  $\text{cm}^{-1}$  and 32 scans were recorded. The amide I peak obtained in the spectral regime of 1580–1720  $\text{cm}^{-1}$  was deconvoluted to analyze the secondary structure of fibroin protein. Peakfit v4.1 software was used to calculate crystallinity index (CI). The CI was measured as per the protocol described in our earlier publication Nisal et al. Briefly, the amide I peak in the 1600–1700  $\text{cm}^{-1}$  region was deconvoluted into 12 peaks using the second derivative method and the CI was calculated as the ratio of areas of peak assigned to beta sheets to the areas of peaks assigned to random coil and alpha helix.

### 2.4. Surface Morphology and Elemental Analysis

Surface of SF microparticles with or without bioceramics was analyzed using a Quanta 200 3D scanning electron microscope (SEM). Prior to imaging, all samples were sputter coated with 5 nm gold coating using a polaron SC6420 sputter coater. Elemental mapping was performed by energy-dispersive X-ray spectroscopy (EDX) analysis by using Leica Stereoscan-440 SEM equipped with a Phoenix EDX attachment.

### 2.5. Thermogravimetric Analysis

Thermogravimetric analysis (TGA) was performed on an accurately weighed sample from 25 to 900 °C at a heating rate of 10 °C  $\text{min}^{-1}$  in air atmosphere using a TGA Q5000 machine from TA instruments.

### 2.6. Mechanical Properties of Microparticles

Mechanical properties of microparticles were analyzed by nanoindentation. Microparticles were mounted in epoxy using cold mounting method followed by gentle cloth diamond polishing before the indentation test. Indentation was performed on SF,

SF-50% HA, and SF-50% CaS particles on a nanoindenter—Bruker Nano Inc., Minneapolis, USA, Model: TI Premier using a Berkovich tip approximately 300 nm diameter. A 10 mN load as a constant parameter was applied and displacement was recorded. Twenty indentations per sample were recorded and an average modulus was calculated.

## 2.7. Mechanical Properties of 3D Scaffolds

Bulk mechanical properties of SF, SF-50% HA, and SF-50% CaS scaffolds (8 mm in diameter and 5 mm in height) were analyzed using Bose Electroforce 3200 Series III machine equipped with a 450 N load cell at compression speed of  $0.005 \text{ mm s}^{-1}$ , a preset load of  $-1 \text{ N}$  and scan time of 40 s. Scaffolds were immersed into deionized (DI) water for about 2 h and then used for compression test. A stress–strain graph was plotted and compression modulus was reported.

## 2.8. Surface Wettability of 3D Scaffolds

Surface wettability of 3D scaffold of SF, SF-50% HA, and SF-50% CaS was analyzed by measuring the contact angle. Stable sessile drop of  $4 \mu\text{L}$  of DI water was used, and the equilibrium contact angle was reported as the average of at least three measurements for each type of sample.

## 2.9. Bioerosion in Proteolytic Environment

In vitro weight loss study was conducted by using protease XIV enzyme. SF, SF-50% HA, and SF-50% CaS scaffolds were incubated in the enzymatic solution ( $2 \text{ U mL}^{-1}$ ) at  $37^\circ\text{C}$  for maximum of 28 days with time points of days 7, 14, and 28. The experiment was performed in triplicates at each time point. Freshly prepared filter sterilized enzymatic solution was replenished after every 48 h. On the 7th, 14th, and 28th day, scaffolds were washed with PBS, dried in vacuum oven at  $60^\circ\text{C}$  overnight, and weighed. Average weight loss was calculated with respect to initial weight of individual scaffold.

## 2.10. Quantitative hMSCs Proliferation (PicoGreen dsDNA Assay)

Sterilized SF, SF-50% HA, and SF-50% CaS scaffolds were placed in a 96-well flat-bottomed nonadherent cell culture plate and hMSCs were seeded. hMSCs were seeded at a density of  $5 \times 10^4$  cells per scaffold in  $10 \mu\text{L}$  of complete media (IMDM + 10% MSCs-FBS). The cells were allowed to settle for 5–7 min at  $37^\circ\text{C}$ , 5%  $\text{CO}_2$  atmosphere. Additional  $90 \mu\text{L}$  media was added to the tissue culture plate, which was then incubated at  $37^\circ\text{C}$  for 28 days in 5%  $\text{CO}_2$  atmosphere. Media was replenished after every 48 h.

In vitro quantitative cell proliferation was analyzed by measuring DNA concentration. Double-stranded DNA (dsDNA) concentration was analyzed on 7th, 14th, and 28th day using Quant-iT PicoGreen dsDNA kit. On the day of analysis, scaffolds were collected and digested in 1 mL of papain solution ( $125 \text{ mg mL}^{-1}$  of papain in 10 mM L-cysteine, 100 mM phosphate, and 10 mM EDTA at pH 6.3) for 16 h at  $60^\circ\text{C}$ . After incubation, samples

were centrifuged at 14 000 rpm for 10 min, and supernatant was collected and stored at  $-80^\circ\text{C}$  for further analysis. DNA contents were measured by using PicoGreen dsDNA assay kit according to manufacturer's protocol. Fluorescence was measured at 535 nm using a multimode detector and concentration of dsDNA was reported in  $\text{ng mL}^{-1}$ .

## 2.11. Cell Morphology by Actin Cytoskeleton Staining

Morphology of hMSCs seeded on SF, SF-50% HA, and SF-50% CaS scaffolds was observed by actin staining of cytoskeleton at the end of 28 days using the protocol described earlier.<sup>[14]</sup> Scaffolds were washed with (1X) PBS and 4% paraformaldehyde was used as a fixative for 15 min at  $25^\circ\text{C}$ . The washing protocol was repeated for 2 times. Cell permeabilization was done using 0.1% Triton X-100 (Sigma-Aldrich) for 5 min followed by a double PBS wash. Cells were incubated with 5% BSA for 20 min at room temperature. Alexa Fluor 488 phalloidin was prepared in PBS 1:100 ratio and incubated for 30 min at room temperature in dark to stain the actin filaments. A 300 nM solution of 4',6-diamidino-2-phenylindole (DAPI) was used as a counter stain for nucleus. Scaffolds were washed again and images were captured on Axio Observer Z1 microscope (Carl Zeiss).

## 2.12. Osteoblast Differentiation on SF, SF-HA, and SF-CaS Scaffolds

Sterilized SF, SF-50% HA, and SF-50% CaS scaffolds were placed in a 96-well tissue culture-treated plate and hMSCs were seeded. Seeding density was kept at  $5 \times 10^4$  cells per scaffold in  $10 \mu\text{L}$  of complete media (IMDM + 10% MSCs-FBS). The plate was kept for 5–7 min at  $37^\circ\text{C}$ , 5%  $\text{CO}_2$  atmosphere followed by addition of  $90 \mu\text{L}$  media and incubated at same temperature for 24 h. Next day, media was removed and osteogenic differentiation media was added. Fresh osteogenic media was replenished after every 48 h. Osteoblast differentiation was analyzed by estimation of levels of ALP, BMP-2, and OCN. On the day of analysis spent culture media was taken out and stored at  $-80^\circ\text{C}$  for marker analysis.

### 2.12.1. Expression of ALP

Activity of ALP was measured by using ALP colorimetric assay as per the protocol mentioned in our previous paper.<sup>[12]</sup> In brief, appropriate diluted sample in total volume of  $80 \mu\text{L}$  was incubated with  $50 \mu\text{L}$  of pNPP (5 mM) solution at  $25^\circ\text{C}$  for an hour in dark. Enzyme activity was stopped by adding  $20 \mu\text{L}$  of stop solution after an hour. Absorbance was recorded at 405 nm. ALP concentration in samples was calculated by using standard calibration graph, which was further normalized with protein concentration.

### 2.12.2. Expression of BMP-2 and OCN

Both BMP-2 and OCN were analyzed on days 1 and 28. On the day of analysis, spent media was collected. Standard ELISA for both the marker was carried out as per manufacturer's

instruction. Individual calibration curve was developed to calculate levels of BMP-2 and OCN expression in samples.

### 2.13. Detection of Inflammatory Response

Inflammatory reaction against the SF, SF-50% HA, and SF-50% CaS was analyzed by estimating expression level of TNF- $\alpha$  in THP-1 (human monocytic cell line) cells.  $8 \times 10^3$  cells per scaffold per well were seeded and cultured in 1 mL complete media and incubated at 37 °C in 5% CO<sub>2</sub> atmosphere up to day 7 and media was changed after every 48 h. On days 1 and 7 spent media was collected and used to calculate expression levels of TNF- $\alpha$  by using standard ELISA kit. Two independent experiments with duplicates reading in each set were taken and results are reported in terms of absorbance.

### 2.14. Statistical Analysis

Statistical analysis was done by using one-way and two-way analysis of variance (ANOVA) with Tukey's post hoc test by using Past 3 software. A value of  $P < 0.05$  was considered statistically significant.

## 3. Results

### 3.1. Preparation of Microparticles and 3D Scaffolds

Five variants of microparticles were prepared and analyzed for particle size, surface morphology, filler content, and protein conformation using various microscopic, spectroscopic, and thermal characterization techniques. The pure SF microparticles were translucent golden brown in color, whereas SF-25/50% HA, and SF-25/50% CaS microparticles were white opaque in appearance. Scaffolds were prepared in two different sizes of 2 mm (h)  $\times$  4 mm (D) and 4 mm (h)  $\times$  8 mm (D) in cylindrical molds. In all experiments, scaffolds of 4 mm (Dia) size were used except mechanical testing where 8 mm (D) sized scaffolds were used.

### 3.2. Particle Size Determination

Figure 1 shows the results of image analysis performed on optical microscopic images. SF microparticles have an average particle size of 0.52 mm. No significant difference in microparticle size was seen after incorporation of 25% HA or CaS. Absolute values of particle diameter are given in Table S1, Supporting Information. Average microparticle size was high in microparticles with 50 wt% of HA (diameter: 0.60 mm) or CaS (diameter: 0.57 mm) as compared with SF microparticles. For monodispersity measurement d90/d10 ratio was calculated by measuring the diameters of 25 particles. The diameter was sorted in an ascending manner. The d90 describes the diameter where 90% of the particles have a smaller particle size and 10% has a larger particle size. Therefore, a ratio closer to 1 indicates that the particles are monodisperse. Notably, all microparticles exhibited a d90/d10 ratio  $\approx 1$ , indicating that the microparticles are monodispersed.

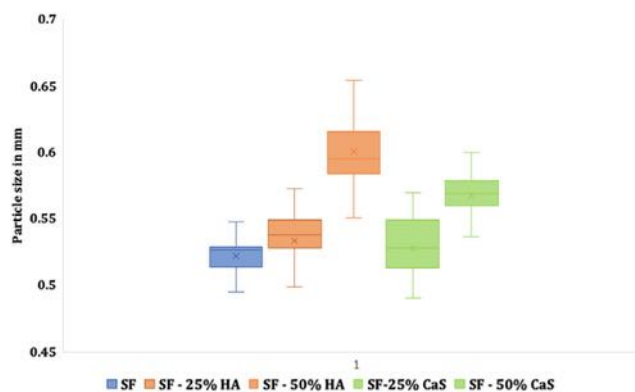


**Figure 1.** Particle size analysis. Particle size distribution of SF, SF-25% HA, SF-50% HA, SF-25% CaS, and SF-50% CaS microparticles was analyzed using optical microscope. Images of at least 20 microparticles were captured by using 10 $\times$  objective and diameter was calculated using ZenPro 2012 software from Carl Zeiss. Data represented as average particle size (mm)  $\pm$  SD.

### 3.3. Confirmation of Secondary Structure in SF and Presence of Bioceramics

Infra-red spectroscopy in the ATR mode was performed to quantify the secondary protein conformation and to verify the presence of incorporated bioceramics. The presence of peak at 1018 cm<sup>-1</sup> in both 25 and 50 wt% SF-HA microparticles confirmed HA incorporation in SF microparticles. Similarly, the presence of peak at 1083 cm<sup>-1</sup> in both 25 wt% and 50 wt% SF-CaS microparticles confirmed successful incorporation of CaS. The Amide I peak observed between 1600 and 1700 cm<sup>-1</sup> was also deconvoluted to evaluate the secondary structure of the SF protein. The ratio of the beta sheets present in the sample to the ratio of random coil and alpha helix structures has been described as a CI. The CI has been tabulated in Supporting Information. As can be seen from the data in Table S2, Supporting Information, addition of various fillers and the quantity of the filler did not have significant effect on the CI. The CI of the material was found to be  $\approx 1.5$ , indicating a predominance of beta sheet conformation in all the microparticles (Figure 2).

### 3.4. Surface Morphology and Elemental Analysis

Surface of the biomaterial plays crucial role in cellular adhesion and thereafter differentiation. Surface morphology of developed microparticles and 3D scaffolds was analyzed by using SEM (Figure 3). Fold-like microarchitecture is a characteristic of methanol-treated SF microparticles as shown in our earlier publication.<sup>[14]</sup> We observed increased surface roughness with increased concentration of HA and CaS (Figure 3a–e, respectively). SEM micrograph of SF, SF-25/50% HA, and SF-25/50% CaS scaffolds showed monodispersed microparticles arranged in hexagonal packing structure (Figure 3f–j). Clear adhesion between adjacent microparticles was visible in electron micrograph of 3D scaffolds (Figure 3k–o). Elemental mapping using EDX analysis also confirmed the incorporation of bioceramics in SF microparticles (Figure S1, Supporting Information).

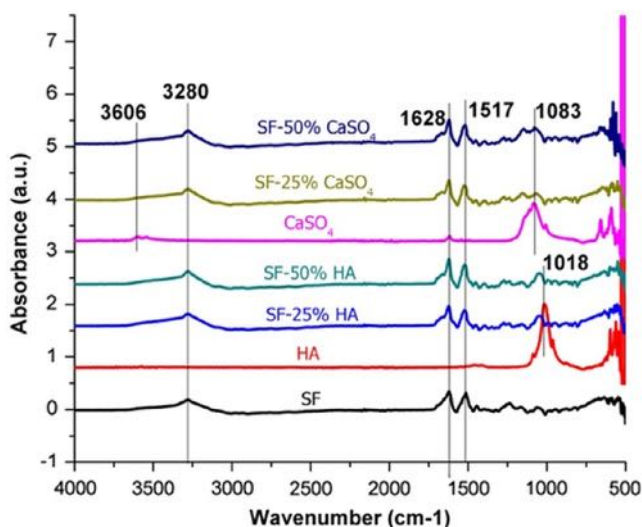


**Figure 2.** Confirmation of secondary structures. SF, SF-25% HA, SF-50% HA, SF-25% CaS, and SF-50% CaS microparticles were analyzed using FTIR-ATR at the resolution of  $4\text{ cm}^{-1}$  in the range of  $1400\text{--}1800\text{ cm}^{-1}$ . Figure shows the FTIR-ATR spectra of SF and SF-bioceramic microparticles. The amide I peak obtained in the spectral regime of  $1580\text{--}1720\text{ cm}^{-1}$  was deconvoluted to analyze the secondary structure of fibron protein.

The presence of C, N, and O indicates the presence of SF protein. The presence of Ca and P in SF-25/50% HA sample confirms the incorporation of HA, and the presence of Ca and S in SF-25/50% CaS samples confirms the incorporation of CaS. SEM analysis of all three types of scaffolds also showed pore size  $>100\text{ }\mu\text{m}$ .

### 3.5. TGA

TGA was used to quantify the amount of filler present in the microparticles, and this data is shown in **Figure 4**. SF microparticle completely degrades at  $\approx 700\text{ }^\circ\text{C}$ , indicating 0% weight retention at  $T > 700\text{ }^\circ\text{C}$  (**Figure 4**). SF-25% HA microparticles showed average 19.9% weight retention, whereas SF-50% HA microparticles showed 29.1% weight retention at temperatures  $>700\text{ }^\circ\text{C}$  till  $900\text{ }^\circ\text{C}$ . Similarly, SF-25% CaS microparticles displayed average 16.7% weight retention, whereas SF-50% CaS microparticles showed 28.3% weight retention at temperatures  $>700\text{ }^\circ\text{C}$ . Percent weight retention of all microparticles at 700, 800, and  $900\text{ }^\circ\text{C}$  is tabulated in Table S4, Supporting Information. This indicates that after incorporation of 50% of bioceramics, only  $\approx 30\%$  loading of filler is actually achieved in the microparticle.

Further experimentation was, therefore, carried out with SF microparticles with 50% filler loading.

### 3.6. Mechanical Properties of Microparticles

Mechanical properties of microparticles were tested by using nanoindentation test and reported as Young's modulus (**Figure 5a**). SF microparticles showed Young's modulus  $\approx 3\text{ GPa}$ , whereas Young's modulus of SF-50% HA and SF-50% CaS was  $\approx 8\text{ GPa}$  and  $\approx 5.3\text{ GPa}$ , respectively. These results indicate that

the blending of bioceramics (HA/CaS) with SF improved mechanical properties of microparticles when compared with pure SF microparticles (one-way ANOVA,  $p = 2.7\text{ e}^{-06}$ ).

### 3.7. Mechanical Properties of 3D Scaffolds

Bulk mechanical properties of SF, SF-50% HA, and SF-50% CaS 3D scaffolds were tested and the compression modulus has been tabulated in **Figure 5b**. The SF scaffold has a compression modulus of  $\approx 31\text{ MPa}$ . The SF-50% HA and SF-50% CaS scaffolds also exhibited a comparable compression modulus, indicating that addition of bioceramics did not significantly influence the bulk mechanical properties of the scaffold.

### 3.8. Surface Wettability of 3D Scaffolds

Surface wettability or hydrophobic/hydrophilic characteristics significantly influence cell attachment on the biomaterial. To assess effect of incorporation of bioceramics in SF on hydrophobicity/surface wettability, contact angle measurement was performed by sessile drop method (**Figure 6**). SF scaffold exhibited an instantaneous contact angle of  $107 \pm 4$ , which eventually came down to  $101 \pm 6$  indicating a hydrophobic surface (**Figure 6**). SF-50% HA scaffold gave initial contact angle  $90 \pm 7$  that was lower than the initial contact angle of SF scaffold ( $p = 0.026$ ) and further decreased to  $82 \pm 6$  with time. On the contrary, initial contact angle of SF-50% CaS scaffold was  $75 \pm 5$ , which is also significantly lower than initial contact angle of SF scaffold ( $p = 2.3\text{ e}^{-5}$ ). Results from the data shown in **Figure 6** confirmed the participation of bioceramics to lower down the hydrophobicity of SF. Thus, CaS was found to significantly lower the contact angle and improve the wettability of the scaffold.

### 3.9. Bioerosion in Proteolytic Environment

SF, SF-50% HA, and SF-50% CaS scaffolds were treated with protease XIV. An average percent weight loss with respect to initial weight of scaffolds is shown in **Figure 7**. On the day 7, pure SF scaffolds exhibited 8% weight loss, whereas SF-50% HA scaffolds showed only 0.6% weight loss. On the contrary, SF-50% CaS scaffolds showed significantly higher % weight loss (11%) compared with SF-50% HA ( $p = 2.41\text{ e}^{-1}$ ). SF-50% HA scaffolds showed 3.4% weight loss by day 14 ( $p = 0.003$ ) and 10% by day 28 ( $p = 7.9\text{ e}^{-1}$ ), which was significantly higher than the day 7. In case of SF-50% CaS scaffold, 25% weight loss on day 28 was significantly different than the 17% weight loss on day 14 ( $p = 7.0\text{ e}^{-9}$ ). Physical appearance of the enzyme-treated scaffolds is summarized in **Figure S2**, Supporting Information. These images of the scaffolds further support the weight loss trends documented earlier.

### 3.10. Quantitative hMSCs Proliferation (PicoGreen dsDNA Assay)

PicoGreen dsDNA assay is an ultrasensitive fluorescent DNA stain-based kit for quantitating dsDNA. hMSCs proliferation on SF, SF-50% HA, and SF-50% CaS scaffolds was further confirmed by the quantitative PicoGreen assay and the results are shown in

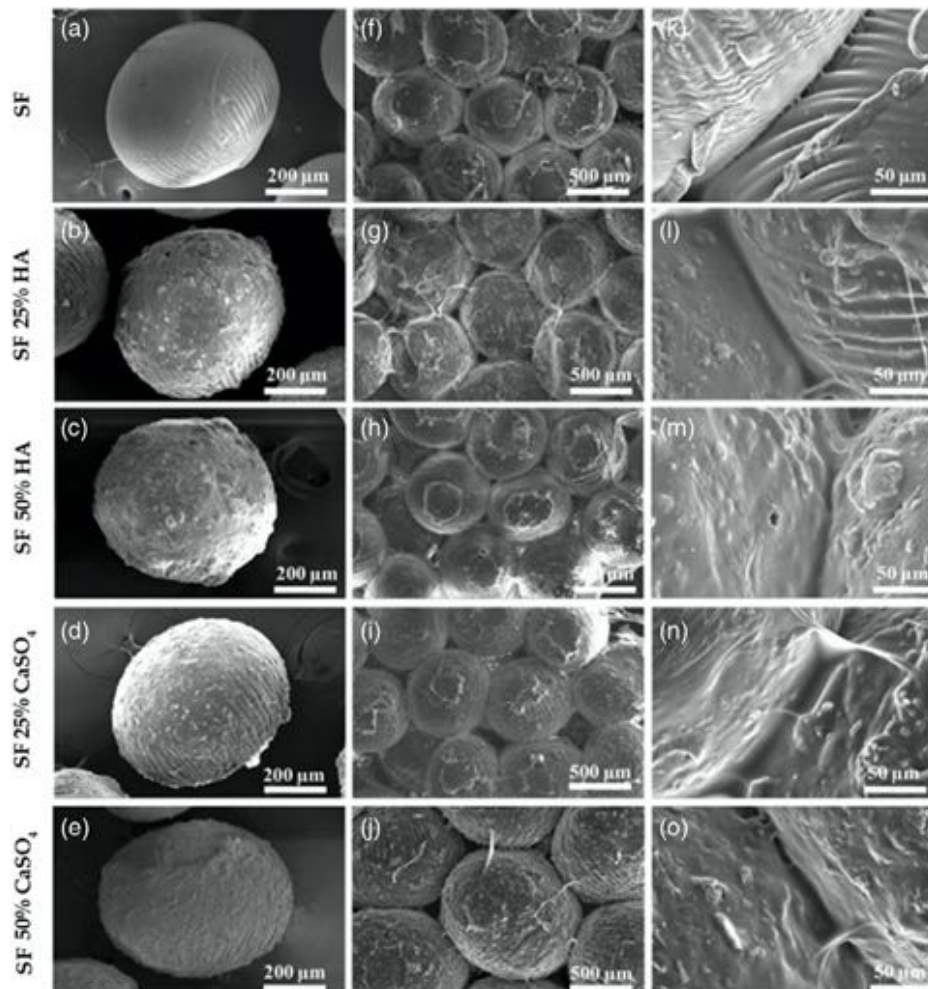


**Figure 3.** SEM analysis of SF microparticles with and without bioceramic. Surface properties of SF microparticles with and without bioceramics were analyzed using Quanta 200 3D SEM. All samples were coated with gold by sputter coating prior to imaging. a–e) 200  $\mu\text{m}$  scale and represent particle sphericity and evenly distributed bioceramics in bioceramics-filled particle. f–j) 500  $\mu\text{m}$  scale and represent scaffold morphology with pores between the particle joints. k–o) 50  $\mu\text{m}$  scale and represent tightly adhesion of two particle with each other in scaffold.

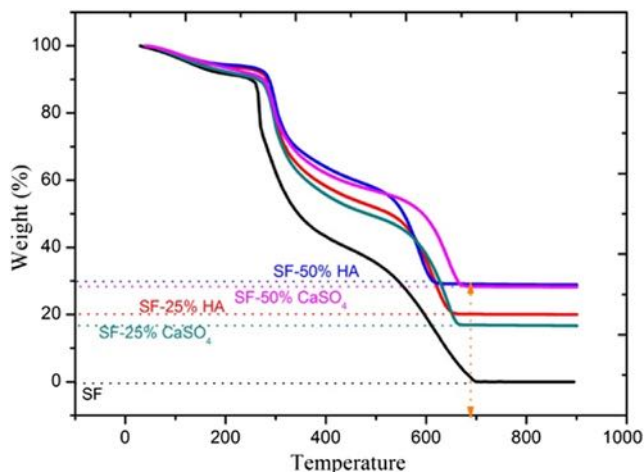


**Figure 4.** TGA. TGA of SF, SF-25% HA, SF-50% HA, SF-25% CaS, and SF-50% CaS microparticles. TGA was performed from 25 to 900  $^{\circ}\text{C}$  at a heating rate of 10  $^{\circ}\text{C min}^{-1}$  in air atmosphere using a TGA Q5000 machine.

**Figure 8a.** All three types of scaffolds supported hMSCs adhesion and proliferation. Results of this assay are in accordance with the Alamar blue assay (Figure S4, Supporting Information). Incorporation of CaS and HA did not show difference in hMSC adhesion and proliferation. On day 7, pure SF scaffold showed 9.5  $\text{ng mL}^{-1}$  DNA which was significantly increased to 12.2  $\text{ng mL}^{-1}$  on 14th day ( $p = 0.002$ ) and 15.0  $\text{ng mL}^{-1}$  on 28th day ( $p = 1.7 \times 10^{-7}$ ). In case of SF-50% HA, initial 8.7  $\text{ng mL}^{-1}$  DNA on 7th day was not significantly increased on day 14, but rose up to 14.3  $\text{ng mL}^{-1}$  on day 28 (7th and 28th day,  $p = 1.04 \times 10^{-6}$  and 14th and 28th day,  $p = 0.003$ ). On the contrary, in SF-50% CaS scaffold, hMSCs significantly proliferate as the function of all three time points (7th and 14th day,  $p = 0.0004$ ; 14th and 28th day,  $p = 0.03$ ; 7th and 28th day,  $p = 6.99 \times 10^{-7}$ ).

### 3.11. Actin Cytoskeleton Staining

F-actin cytoskeleton staining was visualized with Alexa Fluor 488 phalloidin, and epifluorescence micrographs of F-actin were



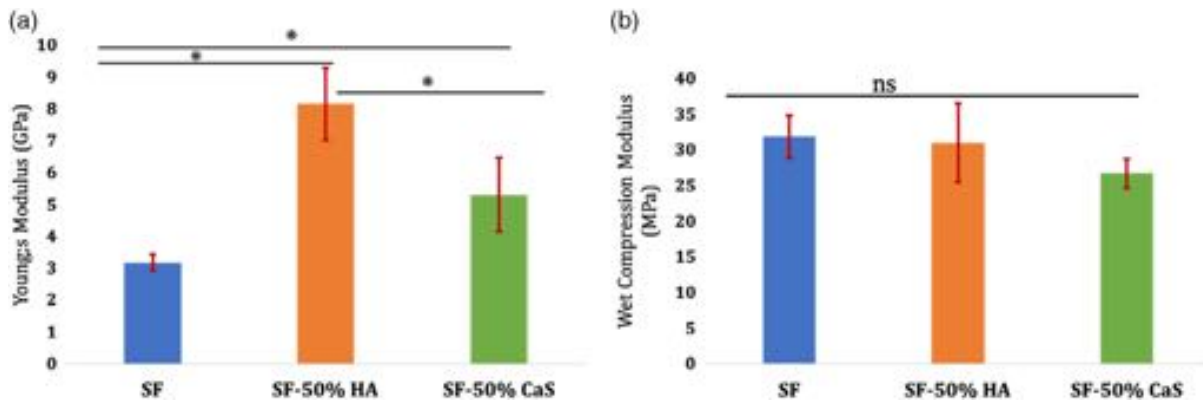


**Figure 5.** Mechanical testing. a) Nanoindentation: mechanical properties of SF, SF-50% HA, and SF-50% CaS particles were analyzed on a nanoindenter (TI Premier using a Berkovich tip  $\approx 300$  nm diameter). A 10 mN load as a constant parameter was applied and displacement was recorded. Data represented as average Young's modulus (GPa)  $\pm$  SD ( $n = 3$ )  $*p < 0.05$ . b) Wet compression modulus: bulk mechanical properties of SF, SF-50% HA, and SF-50% CaS scaffolds (8 mm in diameter and 5 mm in height) were analyzed using Bose Electroforce 3200 Series III machine using 450 N load cell at compression speed of  $0.005 \text{ mm s}^{-1}$ , a preset load of  $-1$  N and scan time of 40 s. Data represented as average compression modulus  $\pm$  SD. NS: not significant difference.

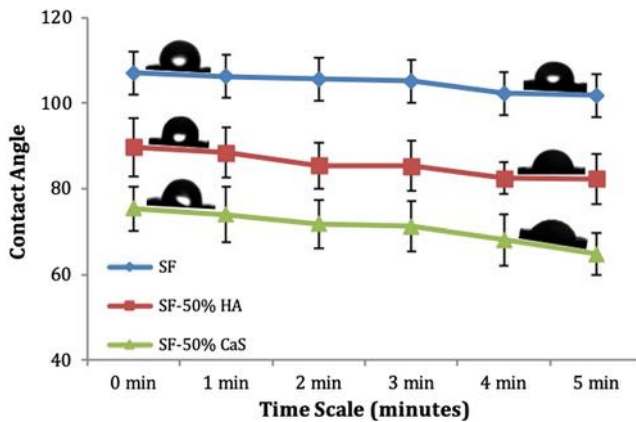


**Figure 6.** Surface wettability of 3D scaffolds. Surface wettability of 3D scaffolds of SF, SF-50% HA, and SF-50% CaS was analyzed by measuring contact angle. Data represented as average contact angle  $\pm$  SD ( $n = 3$ ).

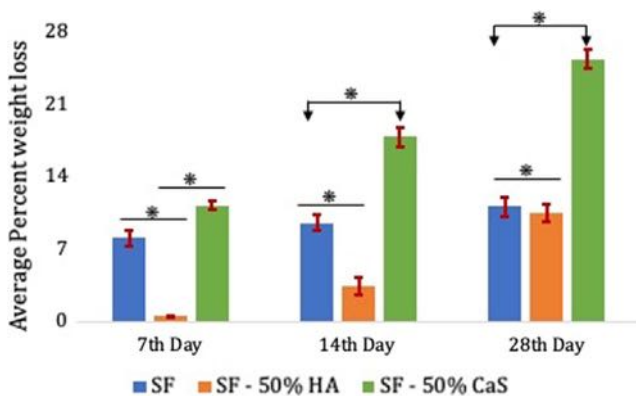


**Figure 7.** In vitro bioerosion in proteolytic environment. SF, SF-50% HA, and SF-50% CaS scaffolds were digested with protease XIV ( $2 \text{ U mL}^{-1}$ ) at  $37^\circ\text{C}$ . The reaction was terminated at different time points: days 7, 14, and 28. Samples were dried in vacuum oven at  $60^\circ\text{C}$  overnight and weighed. Data represented as an average weight loss  $\pm$  SD ( $n = 3$ ),  $*p < 0.05$ .

taken at day 28 (Figure 8b). In accordance with our proliferation data, we observed well-expanded cell morphology of hMSCs. hMSCs expansion were seen throughout the microparticle surface and also in between the microparticles. No visible difference in cell cytoskeleton among different types of scaffolds was observed. The data overall suggested that the developed scaffolds do not impart any toxic effects and support hMSCs adhesion and proliferation.

### 3.12. Detection of Osteoblast Differentiation Markers

Ability of scaffolds to support hMSCs differentiation into mature osteoblasts was evaluated by measuring expression of different markers such as ALP (early marker), BMP-2 (early to late), and OCN (late marker).

#### 3.12.1. Expression of ALP

Activity of ALP was measured by colorimetric assay on the 7th, 14th, and 28th day. ALP activity was calculated using standard calibration curve (Figure S5, Supporting Information) as per manufacturer's instruction. Calculated ALP activity is shown in Figure 9a. Detectable ALP activity was observed on the day 7 in SF, SF-50% HA, and SF-50% CaS scaffolds. From the data, it is observed that SF and SF-50% CaS supports hMSCs osteogenic differentiation equally on 7th and 14th day; however, decreased activity was observed in SF-50% CaS as compared with SF. On the 14th day of experiment, increased ALP activity in SF-50% HA with respect to 7th day was observed and remained constant till 28th day. In conclusion, highest ALP activity was observed in SF scaffold starting from 7th day to 28th day, whereas SF-50% HA started significant differentiation of hMSCs after 7th day and remained constant till 28th day.

#### 3.12.2. Expression of BMP-2 and OCN

Family of BMPs plays a vital in the development of new bone tissue and osteoblast differentiation. BMP-2 levels were

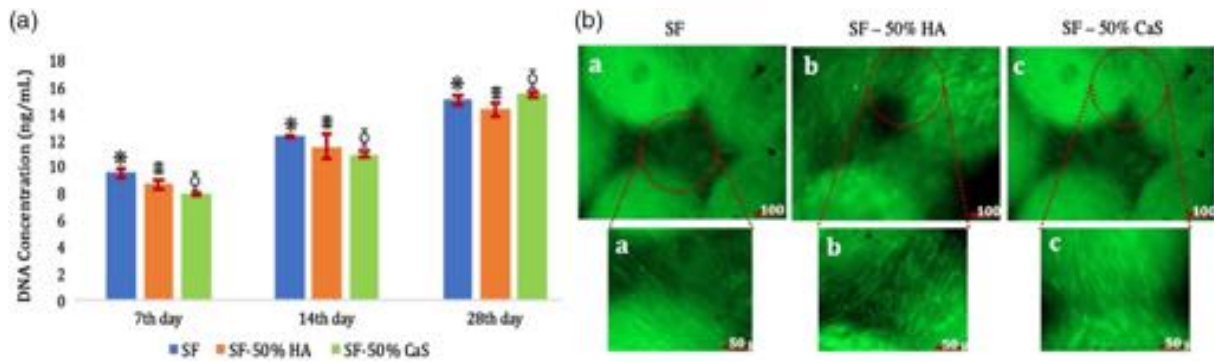


**Figure 8.** hMSCs cell growth. a) PicoGreen assay: hMSCs were seeded on SF, SF-50% HA, and SF-50% CaS scaffolds at a density of  $5 \times 10^4$  cells per scaffold and cultured in IMDM + 10% MSCs-FBS at 37 °C, 5% CO<sub>2</sub> atmosphere. Media was replenished after every 48 h. dsDNA concentration was measured using Quant-iT PicoGreen dsDNA kit at days 7, 14, and 28 time points. Fluorescence was measured at 535 nm using a multimode detector. Data represented as DNA concentration ( $\text{ng mL}^{-1}$ )  $\pm$  SSD ( $n = 3$ ), \* $p < 0.05$ . b) Actin staining: morphology of hMSCs seeded on SF, SF-50% HA, and SF-50% CaS scaffolds was observed by actin cytoskeleton at the end of day 28 of culture. Alexa Fluor 488 tagged phalloidin was used for staining actin filaments. Nucleus was stained with DAPI. Scaffolds were observed and images were captured on Axio Observer Z1 microscope (Carl Zeiss). All images were captured by using 10 $\times$  objective.

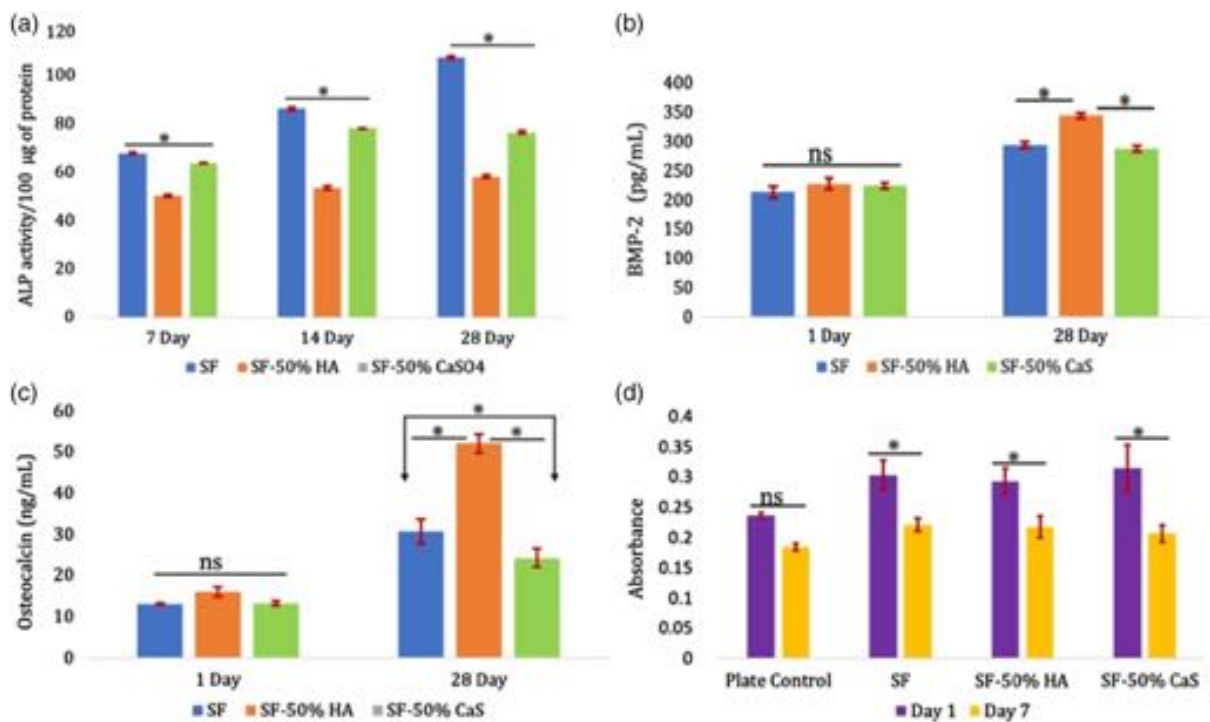


**Figure 9.** Osteogenic differentiation and inflammatory response. hMSCs were seeded on SF, SF-50% HA, and SF-50% CaS scaffolds at a density of  $5 \times 10^4$  cells per scaffold and cultured in osteogenic differentiation media 37 °C, 5% CO<sub>2</sub> atmosphere for days 7, 14, and 28. Osteogenic differentiation media was replenished after every 48 h. Conditioned media was collected at respective time points. Osteogenesis was detected by estimating expression of ALP activity, BMP-2, and OCN levels. a) ALP activity was measured from conditioned media collected at days 7, 14, and 28. ALP activity was normalized with the total protein loaded and expressed as ALP activity/100 µg of protein. Data represented as average  $\pm$  SD ( $n = 3$ ), \* $p < 0.05$ . b) BMP-2 expression was estimated from conditioned media on days 1 and 28 using ELISA. Data represented as average BMP-2 ( $\text{pg mL}^{-1}$ )  $\pm$  SD ( $n = 3$ ), \* $p < 0.05$ . c) Expression of OCN was also estimated by ELISA from conditioned media on days 1 and 28. Data represented as average OCN ( $\text{ng mL}^{-1}$ ) levels  $\pm$  SD ( $n = 3$ ), \* $p < 0.05$ . d) Inflammatory reaction against the SF, SF-50% HA, and SF-50% CaS was analyzed by estimating expression level of TNF- $\alpha$ .  $8 \times 10^3$  THP-1 (human monocytic cell line) cells were seeded on SF scaffolds with and without bioceramic and cultured in RPMI 1640 media and incubated at 37 °C in 5% CO<sub>2</sub> atmosphere for 7 days. Media was replenished after every 48 h. TNF- $\alpha$  levels were estimated at days 1 and 7 using standard ELISA kit. Data represented as average  $\pm$  SD ( $n = 3$ ). NS = not significant difference; \* $p < 0.05$ .

measured using ELISA assay and concentrations were calculated from the standard calibration curve (Figure S6, Supporting Information). All three types of scaffolds exhibited BMP-2 expression (Figure 9b) on day 1; however, by day 28 SF-50% HA showed highest BMP-2 levels compared with SF ( $p = 0.002$ ) and SF-CaS. Among SF and SF-50% CaS, no significant difference was seen in BMP-2 expression, which was observed on day 28.

OCN—a late osteogenic marker—was estimated by using ELISA assay. As per manufacturer's instruction (standard curve; Figure S7, Supporting Information). OCN expression levels are shown in Figure 9c. Under osteogenic stimulus, hMSCs cultured on all three scaffolds showed similar expression levels of detectable OCN levels on day 1 ( $p > 0.05$ ). Although hMSCs cultured on all scaffolds showed time-dependent increase in OCN levels, by day 28. SF-50% CaS showed statistically significant, high OCN levels of as compared with SF alone and SF-HA scaffolds ( $p = 3.0 \times 10^{-2}$ ).

### 3.13. Detection of Inflammatory Response

THP-1 cells were used to assess inflammatory response induced by SF, SF-50% HA, and SF-50% CaS scaffolds. Untreated THP-1 cells (plate control) were considered as a negative control, and TNF- $\alpha$  expression levels are shown in Figure 9d.

Relative to plate control cells, on day 1 elevated absorbance was detected in SF, SF-50% HA, and SF-50% CaS scaffolds. As a function of time on day 7, level of TNF- $\alpha$  significantly decreased with respect to day 1 ( $p = 0.02$ ) for all three types of scaffolds and as a result decrease in absorbance was observed, which was similar to nontreated control cells. Nonsignificant difference of TNF- $\alpha$  between control cells and all three types of scaffolds indicates that neither scaffolds stimulate inflammatory response. This implies that filled/unfilled scaffolds are biocompatible and there is a reduced risk of failure after implantation due to immune rejection. However, further both in vitro and in vivo studies would be required to evaluate the immunogenic potential of these scaffolds upon implantation.

## 4. Discussion

Bone defects/cavities and nonunions are the most frequently encountered problems in modern reconstructive orthopedic surgery and here use of bone void filler is a promising option. Bone tissue engineering is, therefore, an active area of research.<sup>[15,16]</sup> One of the most important elements of BTE is the design of a biocompatible scaffold that provides appropriate mechanical support with optimum pore size and interconnected porosity. Porosity was calculated by measuring the weight and volume of individual cylindrical scaffolds. The densities used for calculation were  $\rho_{\text{silk fibroin}} = 1.35 \text{ gm cm}^{-3}$ ;  $\rho_{\text{calcium sulphate}} = 2.32 \text{ gm cm}^{-3}$ ; and  $\rho_{\text{hydroxyapatite}} = 3.16 \text{ gm cm}^{-3}$ . Calculated porosity was given in Table S3, Supporting Information.

These properties must be over and above the property of osteoregeneration. The scaffold must also have appropriate and controlled bioerosion rates and also the flexibility to incorporate functional biomolecules for osteoinductivity.<sup>[17,18]</sup>

Synthetic bone void fillers, which are currently used in surgery, include ceramics such as HA, CaS, tricalcium phosphate, and/or their blends/composites with synthetic or natural polymers.<sup>[3]</sup> Silk—a natural biopolymer—has been extensively explored in the recent past for BTE. It has also been blended with other polymers and ceramics for BTE applications.<sup>[19,20]</sup> Our group has more recently also demonstrated the promise of silk microparticle-based scaffolds in BTE.<sup>[13]</sup> Furthermore, we have also shown that osteogenic differentiation ability of these scaffolds can be enhanced by simple surface coating of scaffolds with collagen and chitosan, which are natural biopolymers.<sup>[12]</sup> The objective of this work was to understand the effect the filler loading on the osteogenic potential of SF microparticle scaffolds. The scaffolds were thoroughly characterized for their morphological, chemical, and mechanical properties, and the study unfolds crucial insights into the linkage between these properties and the osteogenic potential of SF as a scaffolding material in BTE.

This study demonstrated a simple and reproducible protocol to develop composite scaffolds of SF either with HA or with CaS. HA is a most stable bioceramic that has chemical similarities to natural bone. HA is also osteoconductive and has low immunogenicity.<sup>[21]</sup> CaS is another biocompatible, bioresorbable ceramic. CaS is also known to be hydrophilic as compared with SF and HA.<sup>[22,23]</sup> The uniform loading of the fillers into the microparticles was confirmed using spectroscopic techniques such as FTIR and EDS. FTIR analysis also further confirmed that there was no significant change in secondary protein conformation upon addition of fillers. TGA corroborated that the maximum loading of fillers was  $\approx 30\%$  by weight of SF. Microscopic images confirmed that the surface of these ceramic-filled microparticles is different from the surface of pure SF microparticle. The ceramic fillers are uniformly distributed throughout the surface of the microparticle. This implies that the surface would have a mixture of functional groups that the cells would interact with. The presence of these ceramic fillers on the surface of the microparticle also increases the surface roughness of the microparticles. This change in chemical and physical properties of the microparticle surface also affects the hydrophilicity of the scaffold, with the CaS-filled microparticles being most hydrophilic.

Bone is the highest load bearing tissue in the body. The mechanical strength of cancellous bone varies from 10 MPa to 30 GPa depending on the anatomical site in the body and the race, ethnicity, gender, and age of the patient.<sup>[24]</sup> Therefore, it is necessary to characterize the mechanical properties of the scaffold. The bulk modulus of developed scaffolds (Figure 5b) shows a comparable modulus for filled and unfilled SF scaffolds. This is due to the fact that the bulk porosity of the scaffold plays a significant role as compared with the filler loading. This has also been reported for other microparticle scaffolds.<sup>[6]</sup> It may also be noted here that the SF-50% CaS scaffold has slightly higher bulk porosity and correspondingly a slightly lower compression modulus. The compression modulus is a bulk property, but an individual cell would interact with the surface of a single microparticle.

Therefore, it is necessary to characterize the mechanical properties of the individual microparticle. The measurement of this local modulus of the microparticles was done using nanoindentation. It was surprising to see a Young's modulus  $> 2 \text{ GPa}$  for all our scaffolds, with the SF-50% HA microparticle showing the



highest modulus. The fillers, therefore, do reinforce the SF matrix and improve the modulus of the filled microparticles.

SF bioresorbs in the body over a time duration varying from few months to few years, depending on the SF protein.<sup>[4]</sup> Here, we demonstrate that despite having similar protein conformation, the rate of bioerosion can be tuned by incorporation of different bioceramics (Figure 7). The rate of bioerosion is fastest in CaS-filled scaffolds and is lowest in HA-filled scaffolds, whereas pure SF microparticles have an intermediate rate of bioerosion. HA and CaS both have good biocompatibility and osteoinductivity, but are limited by its bioresorption rate. HA bioresorbs at an extremely slow rate resulting in new bone forming primarily around the filler.<sup>[25,26]</sup> CaS bioresorbs within few months of implantation, not providing enough time for the new bone to form.<sup>[20,27]</sup> Rate of new bone formation also depends on the age of the patient and the anatomical site. It also depends on the physical well-being of the patient. For example, the rate of new bone formation in a child is extremely high, while it can be uncannily slow for an osteoporotic patient. Thus, here we propose a system that allows a clinician to pick and choose the appropriate bone void filler depending on the patient needs and the clinical condition.

Success of developed biomaterials in TE is also dependent on noncytotoxic nature of the biomaterial. We observed >80% cell viability (Figure S3, Supporting Information) for both filled and unfilled SF scaffolds. All SF scaffolds filled or unfilled supported cell growth with equal efficiency as observed from cell proliferation on these scaffolds (Figure S4, Supporting Information) and (Figure 8a). These results are in conjunction with the report by Kucharskya et al.<sup>[28]</sup> As per quantitative and qualitative cell growth analysis, we did not observe any significant difference between biomaterials (Figure S4 and Figure 8a).

Also, during adult bone remodeling and repair, the stem cells differentiate into an osteoblastic lineage upon receiving appropriate signals from the biomaterial. There are multiple osteogenic markers of the osteoblast that appear in the surroundings during the differentiation process at different time and have also been well documented with respect to each stage of the path way.<sup>[29,30]</sup> Osteogenic potential of SF, SF-50% HA, and SF-50% CaS was evaluated by measuring the osteogenic markers ALP and OCN. Among the family of BMPs, BMP-2 plays crucial role in osteogenesis,<sup>[31]</sup> and it has also been reported that mRNAs of BMP-2 are expressed only later in osteogenesis.<sup>[32]</sup> We measured BMP-2 concentration on 28th day. In osteogenic differentiation process, days 1–14 are known as initial level, whereas days 14–28 are reported as a later phase of process.<sup>[32]</sup> ALP level is significantly increased in SF and SF-50% CaS on 7th day. This confirms early differentiation in these scaffolds, which was significantly decreased on 28th day. SF-50% HA induced hMSCs differentiation after 7th day. On the day 28, we observed decreased ALP level in all three scaffolds, indicating successful differentiation of hMSCs into osteoblast. SF-50% HA performs better at later stage of differentiation, and this is further validated by the significantly high level of OCN and BMP-2 with respect to SF and SF-50% CaS. Also, significantly increased secretion of both OCN and BMP-2 on 28th day as compared with day 1 in all three types of scaffolds indicates that although the signaling pathways (early and late) maybe different for various scaffolds, each of the scaffold does support differentiation of hMSCs into osteogenic lineage.

Innate immunity—a first line of defense system—is nonspecific reactions, which involves immune recognition by responding to foreign material and activation of monocytes that results in the rejection of foreign material.<sup>[33]</sup> Toll-like receptors (TLRs) are present on the surface of monocytes and activation of TLRs results in the secretion of IL1b, IL6, and TNF proinflammatory cytokines.<sup>[34]</sup> Herein, we observed that even after long incubation time (7 days) with THP-1 cells, the scaffolds did not trigger macrophage response indicating the nonimmunogenic nature of silk fibroin.<sup>[35]</sup>

During the bone development, there are several signaling cascades involved such as BMP/TGFb, WNT, Notch, FGF, IGF, and PDGF. It has been demonstrated that without supplementation of dexamethasone, SF results in osteogenic differentiation of BMSCs by activating WNT/b-catenin signaling.<sup>[36]</sup> Calcium ions are known to activate NOTCH cascade—a osteogenic regulator along with ERK/MPK signaling pathway<sup>[4,37–39]</sup> and this might be the reason that SF-50% CaS scaffold secretes osteogenic marker in early phase of differentiation process. On the contrary, HA is known for the triggering of ERK/MAPK, FGF, and NOTCH signaling,<sup>[6]</sup> which results in the steady significant performance of SF-50% HA scaffolds in later phase of osteogenic differentiation. It has also been documented that mechanical stiffness is also responsible in the activation of ERK/MAPK cascade.<sup>[40,41]</sup> SF itself has the ability to trigger osteogenic signaling. However, coactivation of more than one signaling cascade to achieve hMSCs differentiation into osteogenic lineage might also prove to be a promising strategy for bone void fillers especially in clinical settings.

## 5. Conclusion

We report here the potential of 3D silk fibroin microparticle scaffolds with and without bioceramics (HA and CaS) for osteoregeneration applications. The physicochemical and mechanical characterization of these filled/unfilled microparticles showed that the particles are monodisperse, have appropriate surface texture and roughness for cell attachment, and the SF protein has a predominant beta sheet conformation. We also demonstrated incorporation of bioceramics ≈30% by weight of microparticles. Interestingly, the addition of fillers did not alter the bulk mechanical properties of the scaffold. However, the Young's modulus measured using a nanoindentation experiment confirmed a two- and threefold increase for the SF50% CaS and SF-50% HA scaffolds, respectively. The 3D scaffolds prepared using these microparticles also exhibit tunable rates of bioerosion, where the SF-CaS scaffold exhibited a fastest rate of bioerosion and the SF-HA scaffold had a slowest rate. The scaffolds are noncytotoxic and nonimmunogenic. SF-50% CaS supports the early-stage differentiation of stem cells as compared with SF-50% HA scaffolds, which predominantly increase differentiation at late stage. Thus, we would like to conclude that addition of fillers to SF microparticles provides an easy methodology to tune the performance of the scaffold in BTE with an exceptional control on the mechanical, bioresorption, and osteoregenerative properties.

## Supporting Information

Supporting Information is available from the Wiley Online Library or from the author.

## Acknowledgements

N.P. thanks DST-WOSA grant (grant number SR/WOS-A/CS-144/2017 (G)) for fellowship and financial support. N.P. acknowledges BiolMed Innovations Pvt. Ltd. for providing silk microparticles and scaffolds as per the Materials Transfer Agreement signed with CSIR-National Chemical Laboratory, Pune. The authors also thank Mr. Emmanuel Joseph for help in IR and TGA, and Mr. Ashwini Mishra from IITB for helping in nanoindentation test and indentation facility at IITB.

## Conflict of Interest

S.G.S. and A.A.N. have financial interest in BiolMed Innovations Pvt. Ltd.

## Keywords

bioceramics, bioerosion, osteogenic differentiation, silk fibroin, stem cells

Received: April 15, 2020

Revised: July 14, 2020

Published online:

- 
- [1] R. Langer, J. P. Vacanti, *Science* **1993**, 260, 920.
- [2] C. Gao, Y. Deng, P. Feng, Z. Mao, P. Li, B. Yang, J. Deng, Y. Cao, C. Shuai, S. Peng, *Int. J. Mol. Sci.* **2014**, 15, 4714.
- [3] S. Zwingenberger, C. Nich, R. D. Valladares, Z. Yao, M. Stiehler, *BioDrugs* **2012**, 26, 245.
- [4] S. Midha, S. Murab, S. Ghosh, *Biomaterials* **2016**, 97, 133.
- [5] F. Mottaghitalab, H. Hosseinkhani, M. Shokrgozar, C. Mao, M. Yang, M. Farokhi, *J. Control. Release* **2015**, 215, 112.
- [6] W. Huang, S. Ling, C. Li, F. G. Omenetto, D. L. Kaplan, *Chem. Soc. Rev.* **2018**, 47, 6486.
- [7] N. Kasoju, U. Bora, *Adv. Healthc. Mater.* **2012**, 1, 393.
- [8] B. Kundu, R. Rajkhowa, S. C. Kundu, X. Wang, *Adv. Drug Deliv. Rev.* **2013**, 65, 457.
- [9] S. Das, D. Pati, N. Tiwari, A. Nisal, S. Sen Gupta, *Biomacromolecules* **2012**, 13, 3695.
- [10] S. Sofia, M. B. McCarthy, G. Gronowicz, D. L. Kaplan, *J. Biomed. Mater. Res.* **2001**, 54, 139.
- [11] R. S. Hayden, M. Vollrath, D. L. Kaplan, *Acta Biomater.* **2014**, 10, 486.
- [12] N. Parekh, C. Hushye, S. Warunkar, S. Sen Gupta, A. Nisal, *RSC Adv.* **2017**, 7, 26551.
- [13] A. Nisal, R. Sayyad, P. Dhavale, B. Khude, R. Deshpande, *Sci. Rep.* **2018**, 8, 7235.
- [14] B. B. Mandal, A. Grinberg, E. Seok Gil, B. Panilaitis, D. L. Kaplan, *Proc. Natl. Acad. Sci.* **2012**, 109, 7699.
- [15] F. Ak, Z. Oztoprak, I. Karakutuk, O. Okay, *Biomacromolecules* **2013**, 14, 719.
- [16] B. Yetiskin, C. Akinici, O. Okay, *Polymer* **2017**, 128, 47.
- [17] A. I. Journal, N. Bölgen, P. Korkusuz, İ. Vargel, E. Kılıç, E. Güzel, D. Uçkan, E. Pişkin, *Artif. Cells Nanomed. Biotechnol.* **2014**, 42, 70.
- [18] N. R. Raia, B. P. Partlow, M. McGill, E. P. Kimmerling, E. Ghezzi, D. L. Kaplan, *Biomaterials* **2017**, 131, 58.
- [19] Y. Y. Jo, S. G. Kim, K. J. Kwon, H. Y. Kweon, W. S. Chae, W. G. Yang, E. Y. Lee, H. Seok, *Int. J. Mol. Sci.* **2017**, 18, 858.
- [20] Y. Shen, S. Yang, J. Liu, H. Xu, Z. Shi, Z. Lin, X. Ying, P. Guo, T. Lin, S. Yan, Q. Huang, L. Peng, *Appl. Mater. Interfaces* **2014**, 6, 12177.
- [21] M. Farokhi, F. Mottaghitalab, S. Samani, M. A. Shokrgozar, S. C. Kundu, R. L. Reis, Y. Fatahi, D. L. Kaplan, *Biotechnol. Adv.* **2018**, 36, 68.
- [22] M. V. Thomas, D. A. Puleo, *J. Biomed. Mater. Res. B Appl. Biomater.* **2009**, 88, 597.
- [23] G. Pecora, D. De Leonardi, N. Ibrahim, M. Bovi, R. Cornelini, *Int. Endod. J.* **2001**, 34, 189.
- [24] J. Henkel, M. A. Woodruff, D. R. Epari, R. Steck, V. Glatt, I. C. Dickinson, F. M. Choong, M. A. Schuetz, D. W. Hutmacher, *Bone Res.* **2013**, 1, 216.
- [25] M. H. Kim, B. S. Kim, J. Lee, D. Cho, O. H. Kwon, W. H. Park, *Biomater. Res.* **2017**, 21, 1.
- [26] G. Krishnamurthy, M. Science, C. C. Medicine, *JUMMEC* **2013**, 16, 1.
- [27] P. Wang, B. Pi, J. N. Wang, X. S. Zhu, H. L. Yang, *Mater. Sci.* **2015**, 9, 51.
- [28] M. Kucharska, K. Walenko, M. Lewandowska-Szumieł, T. Brynk, J. Jaroszewicz, T. Ciach, *J. Mater. Sci. Mater. Med.* **2015**, 26, 143.
- [29] J. E. Aubin, *Rev. Endocr. Metab. Disord.* **2001**, 2, 81.
- [30] A. Rutkovskiy, K.-O. Stensløyken, I. J. Vaage, *Med. Sci. Monit. Basic Res.* **2016**, 22, 95.
- [31] E. Canalis, A. N. Economides, E. Gazzero, *Endocr. Rev.* **2003**, 24, 218.
- [32] Z. Huang, E. R. Nelson, R. L. Smith, S. B. Goodman, *Tissue Eng.* **2007**, 13, 2311.
- [33] S. G. Maumita Bhattacharjee, E. Schultz-Thater, E. Trella, S. Miot, S. Das, M. Loparic, A. R. Ray, I. Martin, G. C. Spagnoli, *Biomaterials* **2013**, 34, 8161.
- [34] B. Panilaitis, G. H. Altman, J. Chen, H.-J. Jin, V. Karageorgiou, D. L. Kaplan, *Biomaterials* **2003**, 24, 3079.
- [35] M. Santin, A. Motta, G. Freddi, M. Cannas, *J. Biomed. Mater. Res.* **1999**, 46, 382.
- [36] M. N. Dastjerdi, *Iran. Biomed. J.* **2006**, 10, 133.
- [37] A. T. L. Ghorbanian, R. Emadi, S. M. Razavi, H. Shin, *Int. J. Biol. Macromol.* **2013**, 58, 275.
- [38] S. Khoshniat, A. Bourguine, M. Julien, M. Petit, P. Pilet, T. Rouillon, M. Masson, M. Gatius, P. Weiss, J. Guicheux, L. Beck, *Bone* **2011**, 48, 894.
- [39] M. M. Dvorak, A. Siddiqua, D. T. Ward, D. H. Carter, S. L. Dallas, E. F. Nemeth, D. Riccardi, *Proc. Natl. Acad. Sci.* **2004**, 101, 5140.
- [40] C. B. Khatiwala, P. D. Kim, S. R. Peyton, A. J. Putnam, *J. Bone Miner. Res.* **2009**, 24, 886.
- [41] Y. R. V. Shih, K. F. Tseng, H. Y. Lai, C. H. Lin, O. K. Lee, *J. Bone Miner. Res.* **2011**, 26, 730.